Microstructural and seismic properties of partial melt shear zones

Amicia Lisbeth Lee

Submitted in accordance with the requirements for the degree of
Doctor of Philosophy

The University of Leeds
School of Earth and Environment

October 2019

The candidate confirms that the work submitted is her own, except where work which has formed part of jointly authored publications has been included. The contribution of the candidate and the other authors to this work has been explicitly indicated below. The candidate confirms that appropriate credit has been given within the thesis where reference has been made to the work of others.

The majority of work in Chapters 4 and 5 of this thesis have appeared in the following publications:
Lee, A. L., Torvela, T., Lloyd, G. E. and Walker, A. M., (2018), 'Melt organisation and strain partitioning in the lower crust', *Journal of Structural Geology* 113, 188-199, doi:10.1016/j.jsg.2018.05.016.
Lee, A. L., Walker, A. M., Lloyd, G. E. and Torvela, T. (2017), 'Modeling the impact of melt on seismic properties during mountain building', *Geochemistry, Geophysics, Geosystems* 18(3), 1090-1110, doi:10.1002/2016GC006705.

Chapter 3 is in review in *Journal of the Geological Society* and is available as a preprint on EarthArXiv:
Lee, A. L., Lloyd, G. E., Torvela, T., and Walker, A. M. (2019), 'Evolution of a shear zone before, during and after melting', doi:10.31223/osf.io/ayxj8.

This copy has been supplied on the understanding that it is copyright material and that no quotation from the thesis may be published without proper acknowledgement.

Copyright © **2019** The University of Leeds and **Amicia Lisbeth Lee**
The right of **Amicia Lisbeth Lee** to be identified as author of this work has been asserted by her in accordance with the Copyright, Designs and Patents Act 1988.

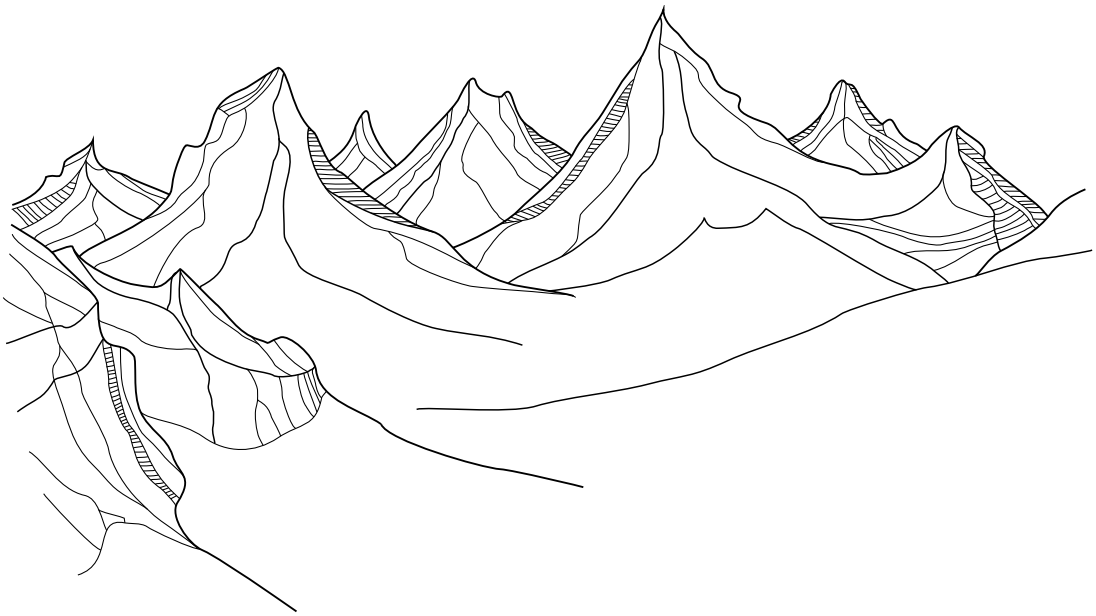

"The mountains are calling and I must go"

–

John Muir

Acknowledgements

This work would not have been possible without the guidance and tremendous supervisory team of Taija Torvela, Geoffrey Lloyd and Andrew Walker. Thank you for seeing the potential in me and giving me the opportunity to pursue my research interests. I am very grateful for your encouragement and support and I could not have completed this research without it. Geoff, the time you give to your PhD students is admirable, our many corridor discussions have yielded lots of ideas to help solve issues within my project. Andrew, thank you for your patience at the beginning of my project when helping me understand programming and tensors, you never made me feel stupid despite how trivial some of my questions were.

I am grateful to Richard Walshaw and Duncan Hedges for their guidance and patience, whilst training and assisting me on the electron microscope and microprobe. Thank you to Harri Wyn-Williams for all the time spent teaching me to prepare my samples and helping to fix the ones that went awry. A big thank you is also given to Andrew Parsons who was a brilliant field assistant in Norway and has since provided many valuable discussions.

I would like to acknowledge the valuable financial support for research and travel to local and international workshops and conferences from University of Leeds, Geological Society of London Timothy Jefferson Research Fund, Edinburgh Geological Society Clough and Mykura Funds, Tectonic Studies Group and Leeds for Life Foundation.

Thank you to all my friends and colleagues for all the good times and support given. Thank you for making my time in Leeds and 8.152 the most memorable and enjoyable experience possible. 8.152 is a fantastic office, we are all hugely supportive of one another. Thanks to Laura Gregory, you are a fantastic friend but also have been a great inspiration, nurturing my enthusiasm for tectonics and academia, despite inducing a coffee addiction. A special mention must go to Ben Craven and Emma Bramham, the impromptu chats were tremendous support when I was juggling my

PhD with teaching assistant duties.

Thank you to Tom with your constant upbeat persona, celebrating my triumphs and comforting me during my failures, without you sticking by my side this thesis would have been significantly more difficult! Thank you to all my running friends, especially Leeds City AC and Doss AC for all our running (and non-running) related shenanigans, having a sport or hobby is essential to maintain a healthy work-life balance during a PhD. Finally, thank you to my family for helping me pursue and achieve my goals and for the unfailing encouragement and support you have given throughout my studies.

Abstract

The coexistence of partial melt with high strain shear zones is a common feature of many continental deformation zones. Partial melt is known to cause a strength decrease but the exact mechanisms and relative timing of the formation is still debated. This thesis provides a field, microstructural and seismic study of syn-melt shear zones for former and actively melting mid to lower crust.

Field and microstructural data was gathered from two field areas, Seiland Igneous Province (SIP), Norway, and Western Gneiss Region (WGR), Norway, with evidence of syn-melt deformation. Both the SIP and WGR showed evidence to indicate partial melt forms an interconnected network even at low melt volumes, thus maximising the weakening effect of partial melt. However, the response to syn-melt deformation does not produce a consistent microstructural signature. Melt migration in the SIP ultimately led to strengthening of the shear zone core, with post-crystallisation deformation focused along shear zone margins where significant heterogeneities are present. In contrast, pervasive open-system melting in the WGR resulted in progressive strain localisation through stress-driven melt organisation and deformation-assisted channelized melt flow, forming fine-grained shear zones with a mylonitic appearance, but lacking subsequent shearing in the solid-state.

Seismic modelling assesses the impact of melt and solid phase properties (melt volume, shape, orientation, and matrix anisotropy) on seismic velocities and anisotropy allowing a comparison of former melt zones with areas of present day partial melting. Seismic properties are non-linear as a result of the variation of these physical properties, which in turn depend on lithology, stress regime, strain rate, pre-existing fabric, and pressure-temperature conditions. Interpretation of seismic data to infer melt percentages or extent of melting should be underpinned by robust modelling of the underlying geological parameters combined with examination of multiple seismic properties in order to reduce uncertainty of the interpretation and geodynamic models.

Table of Contents

List of Figures

List of Tables

List of Abbreviations

List of acronyms

ABQT	$\alpha - \beta$ Quartz Transition
AVs	S-wave Anisotropy
BLG	Bulging recrystallisation
BSE	Back Scattered Electrons
CPO	Crystallographic Preferred Orientations
CQ	Chessboard quartz
DA	Dihedral angle
dEq	Disequilibrium
EBSD	Electron Backscattered Diffraction
EDS	Energy-dispersive X-ray spectroscopy
GBM	Grain boundary migration
GOS	Grain orientation spread
LVL	Low-velocity layer
m.u.d.	Multiples of Uniform Distribution
MCT	Melt Connectivity Threshold
MOR	Mid-Ocean Ridge
MT	Magnetotelluric
myk	Myrmekite
ØSZ	Øksfjord Shear Zone
P	Pressure
perth	Perthite
PPL	Plane Polarised Light
Ps	Vs converted to Vp
qP	Quasi-compressional wave
qS	Quasi-shear wave
RCMP	Rheologically Critical Melt Percentage
rms	Root mean squared
SEM	Scanning Electron Microscope
SGR	Subgrain rotation
SIP	Seiland Igneous Province
SLT	Solid-to-Liquid Transition
SoB	String of Beads
T	Temperature
UHP	Ultra High Pressure
UHT	Ultra High Temperature
V	Velocity
V*L*	Love wave
Vp	Compressional wave (P-wave)
V*R*	Rayleigh wave
Vs	Shear wave (S-wave)
VPSC	Visco-Plastic Self-Consistent
WGR	Western Gneiss Region
XPL	Cross Polarised Light

List of symbols

α	Aspect ratio
γ	Shear strain
$\dot{\varepsilon}$	Strain rate
θ	Dihedral angle
K	Bulk modulus
λ_x	Eigenvalue
μ	Shear modulus
ρ	Density
σ_{1-3}	Differential stress
ϕ	Melt fraction
$\mathbf{G}$	Christoffel tensor
C	Stiffness tensor
S	Compliance tensor
A	Material parameter
D	Recrystallised grain size
M_W	Molecular weight
M_F	Mole fraction
M_T	Peak temperature
Q	Activation enthalpy
R	Ideal gas constant
T	Absolute temperature
$f_{\mathrm{H_2O}}$	Water fugacity
n	Stress exponent
r	Water fugacity exponent
$\parallel$	Parallel to

Mineral abbreviations

$\mathbf{An}_{\boldsymbol{x}}$	Plagioclase with X% Calcium
bt	Biotite
cd	Cordierite
cpx	Clinopyroxene
gt	Garnet
hbl	Hornblende
il	Ilmenite
kf	K-feldspar
opx	Orthopyroxene
pl	Plagioclase
qz	Quartz
sil	Sillimanite

Chapter 1

Introduction

1.1 Overview and rationale

Field evidence from eroded orogens shows the mid to lower crust can be migmatitic (e.g. Brown, 2001a,b), suggesting melt will be present in active orogens (e.g. Vanderhaeghe and Teyssier, 2001, Teyssier and Whitney, 2002), an assumption supported by geophysical observations (e.g. Nelson et al., 1996, Unsworth et al., 2005, Unsworth, 2010). In-situ partial melting is known to cause potentially dramatic strength decreases, even at small melt volumes, affecting models for orogenic deformation and exhumation (e.g. Beaumont et al., 2001, Rosenberg and Handy, 2005, Jamieson and Beaumont, 2013, Levine et al., 2013).

Partial melting adds to the already heterogeneous nature of most rocks (e.g. grain size, mineralogy, microstructure, etc.), and such lithological heterogeneities are important factors in controlling strain partitioning on all scales (Fossen and Cavalcante, 2017). However, comparatively little is known about strain partitioning in partially molten rock volumes. For example, the co-existence of partially molten rock in conjunction with regions of high strain (i.e. shear zones, Figure 1.1) is a common feature of orogenic belts (e.g. the Himalaya-Tibet orogen) however the mechanisms and relative timing of their formation remain poorly understood (e.g. Rosenberg and Riller, 2000, Handy et al., 2001, Viegas et al., 2013, Cavalcante et al., 2016).

There are known theoretical feedback relationships between melting, rheological

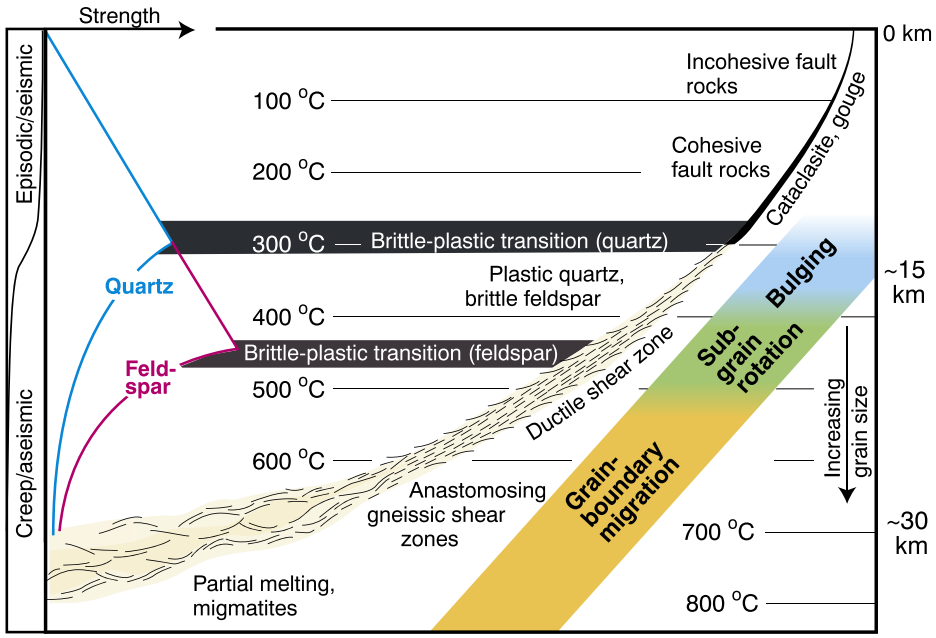

Figure 1.1: Simplified diagram illustrating vertical variations in shear zones and shear zone fabrics (facies). The brittle-plastic transitions for quartz and feldspar and dominant recrystallisation mechanisms (bulging, subgrain rotation and grain-boundary migration) are related to temperature, but also depend on strain rate and the amount of fluids present (After Fossen and Cavalcante, 2017).

weakening (depending on melt fraction and melt connectivity), shear zone nucleation, and melt transport (e.g. Brown and Solar, 1998a, Rosenberg and Handy, 2005, Brown, 2007; and references therein). Thus, syn-melt shear zones are expected to function as effective transport channels for crustal partial melts (Hollister and Crawford, 1986, Brown and Solar, 1998a, Spiegelman et al., 2001). Mid- and lower crustal partial melts infiltrate many shear zones and source many large intrusive bodies (e.g. Brown, 1994, Vigneresse et al., 1996, Petford et al., 2000, Keay et al., 2001), with some areas even showing possible direct evidence of melt removal (e.g. Brown, 1994, Johannes et al., 2003, Stuart et al., 2016, Meek et al., 2019). Additionally, if the melt volume exceeds the rheological threshold, partial melt zones in orogenic systems will form a major zones of weakness that may mechanically detach the overlying crust from the orogenic root and mantle (Schott and Schmeling, 1998, Arnold et al., 2001).

Despite the basic relationships being known, the behaviour of partially molten crust as observed at outcrop is not always easily explained by models and experiments (Rosenberg and Handy, 2005). Many aspects of how partially molten crust actually

deforms therefore remain unknown. For example, it is unclear why very large volumes of melts remain approximately in-situ within the crust in the form of migmatites, despite their sometimes immediate proximity to one or several shear zones that should act as conduits (e.g. Labrousse et al., 2004). Conversely, it remains unclear in many cases what caused the initial strain partitioning into a shear zone within partially molten volume. Non-expulsion of melts might be explained by shear zones forming post-crystallisation (i.e. post-melt), although this contradicts theoretical predictions of formation of syn-melt shear zones (e.g. Holtzman et al., 2003, Walte et al., 2005). Another option is that shear zones formed syn-melt but did not act as effective melt transport channels. If this is true, there are significant implications for how partially molten crust deforms on a large scale.

Improved understanding of mid to lower crustal partial melting is important to the understanding of rheology and stability of mountain belts. The location of partial melt in the lower crust can be identified using geophysical methods, but these methods are not reliable in quantifying melt volume for in-situ melting nor the exact shape, location or connectivity of a melt body. Studying the exposed mid to lower crust in palaeo-orogens can help to quantify the melt volume and understand how shear zones influence or are influenced by partial melt.

1.2 Objectives and research outline

In order to address the above questions regarding the structure, strength and deformation processes that operate in the deforming continental crust, there is a necessity for detailed field and laboratory investigations of exhumed mid to lower crust. Examples of syn-melt shear zones that formed during orogenesis will provide the most information about melting processes and their rheological impact. The objective of this thesis is to provide a study of styles of deformation in such shear zones and quantify their seismic response to be used as an analogue for actively melting mid to lower crust.

To generate robust models for synthetic seismic responses for partial melt it is

important to consider a wide range of inputs. I use representative rock samples from two field areas with differing tectonic settings: Seiland Igneous Province (SIP), Norway, representing the initial stages of continental rifting (Chapter 3); and Western Gneiss Region (WGR), Norway, representing late-stage orogenic exhumation (Chapter 4). By determining how the macroscopic and microscopic structure and strain distribution varies between the field areas, their effect on seismic properties can be assessed. Thus, the thesis rational is as follows.

1. To examine the geology of shear zones to collate data on the structure and deformation processes during partial melting (Chapter 2).

2. To provide detailed descriptions of partial melting and interaction with the rocks microstructure for each of the shear zones, in order to interpret the mechanisms and conditions of deformation and to infer approximate shear strengths during syn-melt deformation:

    - Chapter 3: Øksfjord Shear Zone, Seiland Igneous Province, Norway
    - Chapter 4: Nupen Peninsula, Western Gneiss Region, Norway.

3. To develop models for how melt shape, distribution and orientation effect the seismic response of rocks (Chapter 5).

4. To produce the seismic response of the studied shear zones as if they were actively deforming and melting at present (Chapter 5).

5. To synthesise the geological and seismic data to enable better predictions of partial melt distribution in the crust (Chapter 6).

6. To draw conclusions on how seismic properties can inform us of the architecture, styles of deformation and role in continental deformation of partial melt shear zones (Chapter 7).

Chapter 2

Partial melting and deformation

This chapter establishes a theoretical framework in which to interpret data gathered later in the thesis. For this reason, I include a brief review of shear zones, migmatites and their microtextures, deformation mechanisms and the effect of melt on seismic properties with an aim of examining the geology of shear zones to collate data on the structure and deformation processes during partial melting. In this chapter I also define the use of descriptive terminology as applied in the thesis, so that consistency is maintained in later chapters.

2.1 Ductile shear zones

Shear zones are defined by zones of high deformation surrounded by rocks showing a lower state of finite strain (Ramsay and Huber, 1987), for example they separate unstrained portions of the crust and lithosphere, and are often the deeper portions of upper crustal brittle fault zones (e.g. Sibson, 1977, Scholz, 1988, Fossen, 2010, Cottle et al., 2015). They are rheological and mechanical anomalies that can influence structural evolution during later deformation phases making them important components in understanding plate tectonics (Butler et al., 2008, Bercovici and Ricard, 2012, Bird et al., 2015, Phillips et al., 2016). Shear zones can be subdivied according to the microstructural deformation mechanisms where *plastic*, *viscous* or *ductile shear zones* are dominated by diffusion and crystal-plastic deformation

mechanisms (e.g. dislocation creep and twinning), whilst *frictional* or *brittle shear zones* are dominated by brittle deformation mechanisms (e.g. grain fracture, frictional sliding and grain rotation), shear zones can exhibit components of both brittle and plastic deformation and are known as *brittle-ductile shear zones* (Fossen and Cavalcante, 2017; and references therein). The shear zones analysed in this thesis are deforming in the partially molten ductile lower crust, thus this section focusses on ductile shear zones.

This thesis focusses on the interaction of melt in shear zones, what role does melt play on shear zone evolution through time? The actively deforming area and thickness of shear zones through time is influenced by strain and rheology (Fossen and Cavalcante, 2017). Shear zones with small offset and length are thinner than larger shear zones; this suggests as a shear zone grows and the offset increases, the shear zone must also increase in thickness, contradicting the assumption that shear zones strain soften as strain accumulates (Fossen and Cavalcante, 2017). Many theoretical models have been

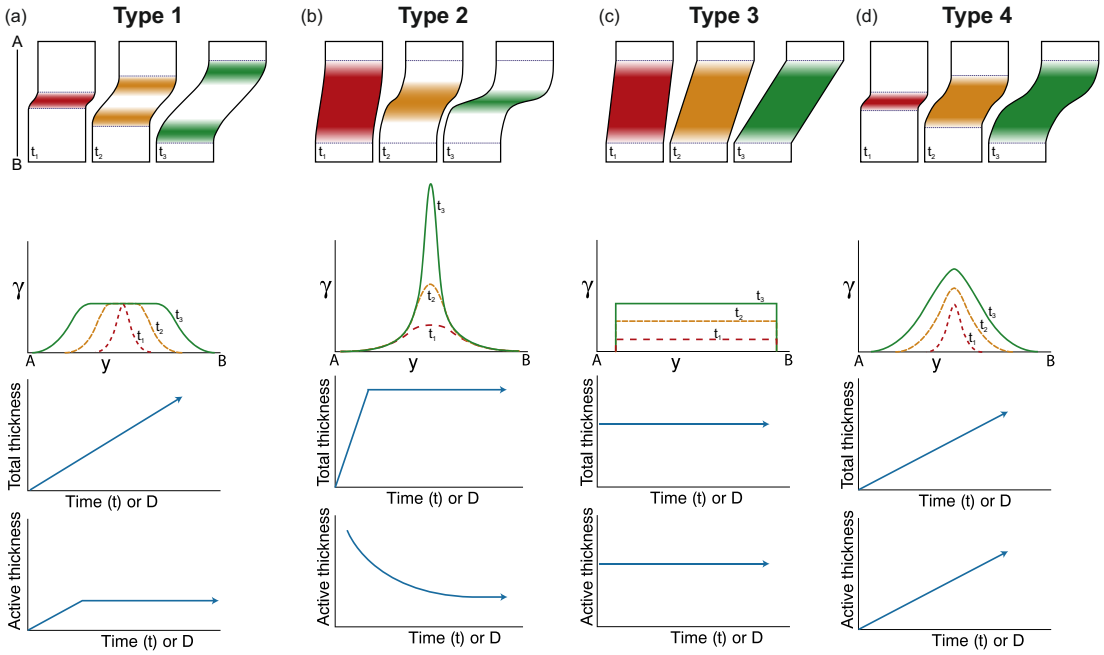

Figure 2.1: Idealised models of shear zone thickness and activity through time where coloured areas represent the actively deforming portions of the shear zone. (a) Type 1, where the zone widens and leaves the central part inactive. (b) Type 2 where strain localises to the central part of the zone. (c) Type 3, which maintains its thickness and is everywhere active at any given time. (d) Type 4, where the zone widens and is everywhere active. Shear strain profiles, thickness-evolution, and thickness of active part of shear zone through time are shown for each case, after Fossen and Cavalcante (2017).

proposed for the evolution of shear zone thickness. Fossen and Cavalcante (2017) summarised these models into the four idealised models that are described as follows and illustrated in Figure 2.1: (1) Type 1 shear zones thicken over time as strain propagates into the walls, leaving an inactive central part behind e.g. plateau-type displacement profiles; (2) Type 2 shear zones form as strain increasingly localises to the central part of the shear zone and a characteristic bell-type develops, evolving into a peak-type profile; (3) Type 3 shear zones are denoted by constant active thickness (also attributable to weakening or confined to a weak preexisting layer); and (4) Type 4 shear zones grow thick while the whole shear zone remains active, and develops a bell-type profile that, unlike Type 2, does not grow into a peak-type profile.

Shear zones often nucleate on small scale defects such as fractures or lithological variations, growing from isolated zones to larger composite shear zones (Ramsay and Graham, 1970, Cobbold, 1977a,b, Poirier, 1980). Mature shear zones form heterogeneous, composite zones that often exhibit anastomosing patterns (e.g. Fusseis et al., 2006, Carreras et al., 2010). The study of small-scale structures in shear zones provides valuable information that can be upscaled to large-scale tectonics. This relies on assumptions that shear zones exhibit simple (translation of material along parallel plains whilst maintaining a constant thickness) or subsimple shear (plane strain; a combination of simple shear with a rotation of the strain axes), but kinematic vorticity estimates suggest that most shear zones deviate from (sub)simple shear and involve combinations of coaxial and non-coaxial deformation such as transpression or transtension (Baird and Hudleston, 2007). Shear zones exhibit progressive deformation but the question still remains on how they may evolve through time especially when containing partial melt.

2.2 Partial melting

2.2.1 Migmatite classification

The term ‘migmatite’ originates from the ancient Greek for ‘mixed rock’. It was first used by Sederholm (1907) who referred to migmatites as originating from a

mixture of melts and solids; an intermediate state between igneous and metamorphic rocks. Mehnert (1968) evolved the definition proposing migmatites as: *"a megascopically composite rock consisting of two or more petrographically different parts, one of which is the country rock in a more or less metamorphic stage, the other is of pegmatitic, aplitic, granitic or generally plutonic appearance"*. Sawyer (2008) found problems with this definition because of the use of genetic terms in a non-genetic definition (e.g. 'pegmatitic', 'aplitic' and 'granitic'). Instead, Sawyer (2008) proposed the following revised definition:

*"**Migmatite:** A rock found in medium- and high-grade metamorphic areas that can be heterogeneous at the microscopic to macroscopic scale and that consists of two, or more, petrographically different parts. One of these parts must have formed by partial melting and contain minerals that are petrographically related to each other (called the neosome) and to their protolith through partial melting or segregation of the melt from the solid fraction. The partially melted part typically contains pale-coloured rocks that are quartzofeldspathic, or feldspathic, in composition, and dark-coloured rocks that are enriched in ferromagnesian minerals. However the partially melted part may simply have changed mineralogy, microstructure, and grain size without developing separate light or dark parts."*

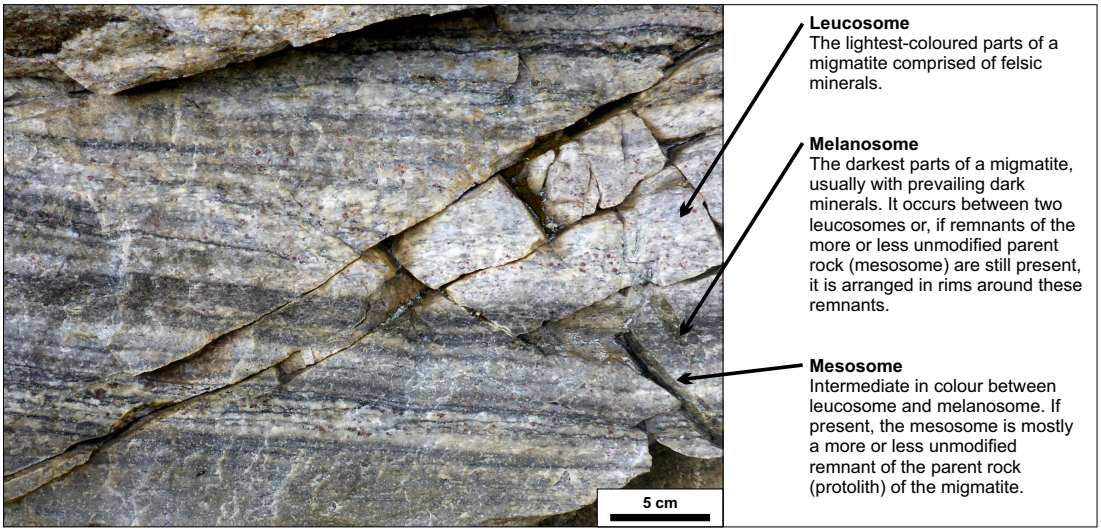

Figure 2.2: Generic classification of a migmatite indicating the leucosome, melanosome and mesosome. This example migmatite formed by partial melting of a paragneiss from the Seiland Igneous Province, Norway (Chapter 3). Definitions after Wimmenauer and Bryhni (2007).

Migmatites are heterogeneous silicate rocks found in areas of high grade metamorphism (Brown, 2012), commonly displaying alternating light and dark layers (Lindh and Wahlgren, 1985), referred to as the leucosome, mesosome and melanosome (Figure 2.2). Leucosomes are the lightest part of a migmatite (Wimmenauer and Bryhni, 2007) comprising the leucocratic fraction of the rock, generally rich in quartz and feldspar (Mehnert, 1968, Robertson, 1999). The melanosome is the melanocratic, mafic-rich fraction of the migmatitic rock, representing the darkest portion (Mehnert, 1968, Robertson, 1999). The mesosome, also known as palaeosome, has an intermediate colour between the leucosome and melanosome; it is the portion of the migmatite that represents the 'unmodified' protolith (Wimmenauer and Bryhni, 2007). The leucosome, mesosome and melanosome are usually all present in the migmatite, with melanosome commonly separating leucosome from mesosome (Kriegsman, 2001). If migmatitic banding is present, the rock is known as a metatexite. If there are higher melt volumes and banding is disrupted, the rock is known as a diatexite (Brown, 1973). Migmatites commonly deform during anatexis, resulting in a rock with a complex morphology (Brown, 2012). Table 2.1 defines some of the key nomenclature used to describe migmatites and Figure 2.3 shows typical structures observed in migmatites.

The heterogeneity is the result of partial melting, melt segregation and recrystallisation that occurs when the rock is subject to high pressures and temperatures (Sawyer, 2008, Brown, 2012). Although migmatites vary enormously, due to the protolith, origin and partial melt conditions, they should all have the same basic characteristics:

1. Migmatites only form during mid to high-grade regional metamorphism (upper amphibolite and granulite facies) and at contact aureoles (pyroxene and sanidinite hornfels facies).

2. They are morphologically complex from the microscopic to macroscopic scale due to varying degrees of melt (completely remelted leucosomes to unmelted mesosomes) and melt migration (Sawyer, 2008).

Table 2.1: Migmatite nomenclature after Ashworth (1985).

Bodies within a migmatite		
Mesosome	Intermediate in colour the portion of the migmatite that represents the 'unmodified' protolith, thus structures pre-melt are persevered and microstructure is unchanged or slightly coarsened (Wimmenauer and Bryhni, 2007, Sawyer, 2008).	
Neosome	Fractions of the migmatite newly formed by partial melting; leucosome and melanosome (Ashworth, 1985, Wimmenauer and Bryhni, 2007, Sawyer, 2008).	
Leucosome	The lightest part of the neosome (Wimmenauer and Bryhni, 2007), generally rich in quartz and feldspar (Mehnert, 1968, Robertson, 1999).	
Melanosome	Mafic-rich fraction of the neosome (Mehnert, 1968, Robertson, 1999).	
Migmatite Structures		Figure
Agmatic	Breccia structure where the mesosome is surrounded by 'veins' of neosome	2.3a
Diktyonitic	Reticulated Structure where the mesosome is interlaced by a network of veins. In contrast to agmatic fabric there are shear movements within mesosome	2.3b
Schollen	Raft structure where blocks or rafts of mesosome floating in neosome.	2.3c
Stromatic	Leucosome and melanosome form layers in mesosome generally parallel to the plane of schistosity but can also be folded.	2.3d
Surreitic	Dilation structure where mesosome forms boudins and neosome is squeezed into the space or neosome fills fissures or cavities formed by dilation.	2.3e
Ptygmatic	Single isolated layers of relatively high competence material are enclosed and folded in a matrix of lower competence and highly shortened.	2.3f
Opthalmitic	Porphyroblasts or lenticular aggregates of several porphyroblasts form 'augens' in mesosome.	2.3g
Schlieren	Streaks of mesosome within the neosome.	2.3h
Nebulitic	Mesosome and neosome are indistinct and largely resembles a magmatic rock.	2.3i

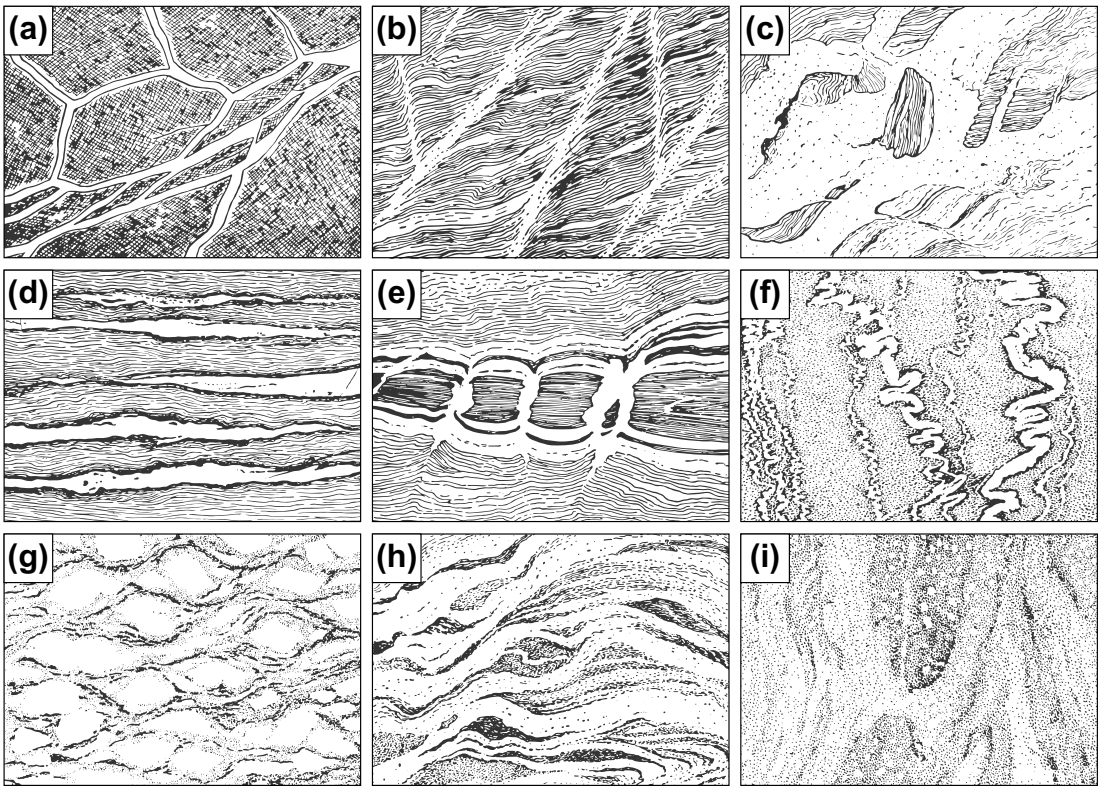

Figure 2.3: Summary of typical migmatite structures: (a) agmatic; (b) diktyonitic; (c) schollen; (d) stromatic; (e) surreitic; (f) ptygmatic; (g) opthalmic; (h) schlieren; (i) nebulitic. See table 2.1 for description of each structure (After Mehnert, 1968).

2.2.2 Character and significance of leucosome

At the outcrop scale it is often assumed that melt is present when there is a high-temperature mineral assemblage alongside quartzofeldspathic lenses, layers or patches (i.e. the leucosome; Mehnert, 1968). However, at the microscale the leucratic material may show evidence of solid-state solution recrystallisation and deformation microstructures as opposed to melt microtextures.

Metamorphic segregation or differentiation is the formation and growth of bands or domains of different bulk compositions within an originally unbanded rock (e.g. Turner, 1941, Robin, 1979, Williams et al., 2000). The segregation typically involves the physical and/or chemical movement of minerals into layers that concentrate similar minerals, resulting in light and dark coloured minerals being concentrated in alternating layers commonly observed in gneisses (Robin, 1979). This segregation commonly separates framework silicates (quartz, feldspar) and chain or layer silicates

(clays, chlorites, micas, amphiboles), where diffusion of silica results in segregation (Durney, 1972, Vidale, 1974, Robin, 1979). It is responsible for metamorphic and structural features such as metamorphic layering, crenulation, spaced and slaty cleavage, quartz rods, mylonite banding, gneissic layering and migmatite layering (Robin, 1979).

There are two main models for compositional segregation in migmatites. The first is via partial melting, migration of melt along grain boundaries and accumulation into leucosomes to form segregated zones of leucratic and melanocratic portions of the rock during crystallisation (Lindh and Wahlgren, 1985). The second model is via diffusion in the solid state possibly enhanced by an intergranular fluid (Lindh and Wahlgren, 1985). The diffusional processes that operate during metamorphic segregation are described described in Section 2.3 on deformation mechanisms. Both processes may operate in migmatites resulting in the observed segregation of leucratic and melanocratic material.

2.2.3 Melt compositions

Migmatites form via partial melting of the protolith during metamorphism at high temperatures (Sawyer, 2008, Brown, 2012). Melting temperature is variable and depends on pressure, rock composition and volume of water. Melt typically forms (1) during decompression in ultra-high-pressure (UHP) terranes; (2) in the zone between peak pressure and peak temperature in medium-temperature eclogite to high-pressure granulite terranes; and (3) by simple prograde heating in granulite facies and ultra-high-temperature (UHT) metamorphic terranes (Brown and Korhonen, 2009). Migmatization processes result in prograde reactions that can produce either a water-rich vapour phase so-called ‘subsolidus migmatites’ (Lindh and Wahlgren, 1985) or melt and are called ‘anatectic migmatites’ (Spear et al., 1999). Thus, migmatites form through partial melting in the presence or absence of a fluid influx (Kriegsman, 2001).

In general, migmatitic melting falls into two melting reactions: granitic wet melt

and dehydration melt. Granitic wet melting occurs via the simple reaction,

$$\text{quartz} + \text{plagioclase} + \text{K-feldspar} + \text{water} = \text{melt}. \quad (2.1)$$

It begins in migmatites with a granitic protolith at approximately 650°C (Wyllie, 1977). Although the melt reaction is simple, the crystallisation products are the same as the reactants (i.e. quartz, plagioclase and K-feldspar), making identification of melt phases and quantification of melt volume difficult.

Biotite-dehydration melting generally occurs at higher temperatures (760-800°C) in anatectic pelites (Spear et al., 1999),

$$\text{biotite} + \text{quartz} + \text{plagioclase} + \text{sillimanite} = \text{melt} + \text{garnet} + \text{K-feldspar}. \quad (2.2)$$

Trace element compositions of melts are controlled by melting reactions, chemical exchange between melt and solid, and differential flow of melt from the solid restite (Sawyer, 1994). Disequilibrium of the melt is preserved when the melt separates or crystallises before chemical equilibrium is reached for trace elements by dissolution and diffusion between melt and solids. Disequilibrium compositions are often preserved in felsic melts from the continental crust (Sawyer, 1991, Watt and Harley, 1993), which implies melt segregation occurs on a more rapid time scale than trace element equilibration between melt and the solid restite (Sawyer, 1994).

2.2.4 Partial melting during continental deformation

Partial melting is common in the middle to lower continental crust due to high temperatures, decompression and/or the influence of volatiles promoting pervasive melting (Sawyer, 1994, Brown, 2001b, Vanderhaeghe, 2009). Partial melt adds to the heterogeneous nature of these rocks (e.g. grain size, mineralogy, microstructure, etc.), and such lithological heterogeneities are important factors in controlling strain partitioning on all scales (Fossen and Cavalcante, 2017). Rheological relationships have been well constrained from experiments; however, experiments do not always explain observed partial melt at outcrop scale in the field (Brown et al., 1995,

Rosenberg and Handy, 2005). For example, if melt localises strain, it is unclear why very large volumes of melt remain in-situ within the crust (crystallising in the form of migmatites), despite their sometimes immediate proximity to one or several shear zones that should act as conduits for melt escape (Labrousse et al., 2004).

It is important to consider how partial melt shear zones evolve through time and what role partial melt plays on their evolution. The active deformation mechanisms and strain localisation in partial melt shear zones vary during their evolution from phases of melt-free to syn-melt and post-melt deformation. Strain localisation is influenced by many parameters within shear zones; for example, pre-existing fractures, weak layers or structures (Passchier, 1982, Austrheim and Boundy, 1994, Pennacchioni and Cesare, 1997), margins of a lithological heterogeneity such as paired shear zones (Pennacchioni and Mancktelow, 2007) and thickness change(s) through time (Hull, 1988, Means, 1995, Vitale and Mazzoli, 2008).

Melt-bearing systems range from solid grain aggregates with minor melt between grains to fully liquid magma with suspended isolated crystals. The volume of melt is a key control on the rheological behaviour of these systems which falls into three categories:

1. Low melt volume: grains form a solid framework and the mechanics are controlled by the solid phase; the viscosity of the solid deforming by diffusion or dislocation creep (e.g. Hirth and Kohlstedt, 1995b,a, Gleason et al., 1999, Mei et al., 2002); or brittle deformation by intracrystalline fracturing (e.g. van der Molen and Paterson, 1979, Dell'Angelo and Tullis, 1988, Rutter, 1997, Renner et al., 2000, Holyoke and Rushmer, 2002).

2. Intermediate melt volume: crystals form an aggregate and rheological behaviour is controlled by granular flow and grain boundary sliding (e.g. Rutter, 1997, Petford and Koenders, 1998, Paterson, 2001).

3. High melt volume: crystals suspended in the melt and the rheology is controlled by the liquid viscosity (e.g. Ryerson et al., 1988).

Partial melting begins to occur when small isolated pockets and tubes of melt form

(Figure 2.4; Mehnert et al., 1973). Melt is likely to be interconnected if the melt-solid dihedral angle is less than 60° (Figures 2.4b, 2.8a, 2.9), but is likely to form isolated pockets when greater than 60° (Figures 2.4a, 2.9; Holness, 2006, Holness et al., 2011). Thus, progressive 'wetting' of grain boundaries results in a connected melt network that reduces the strength of the rock (Vigneresse and Tikoff, 1999). Less than 2% melt is required for the felsic system to become permeable (Dell'Angelo and Tullis, 1988) and almost all grain boundaries are 'wet' at 7% melt content (Rosenberg and Handy, 2005).

For melt volumes <7%, deformation localises around pre-existing weaknesses in the rock or forms fractures (Figure 2.5; van der Molen and Paterson, 1979, Rutter and Neumann, 1995, Rosenberg and Handy, 2005). As melt increases to 7% it forms interconnected films on the grain scale resulting in a strength decrease of the rock and deformation starts to become more distributed (Bruhn et al., 2000, Rosenberg and Handy, 2005). This represents the 'melt connectivity threshold' (MCT), marking the transition from a dry aggregate to an aggregate containing an interconnected melt network, where 90% of grain boundaries host a melt film (van der Molen and Paterson, 1979, Rosenberg and Handy, 2005). When melt volumes exceed 7%, the intergranular films widen, weakening the rock, although the original structure remains largely unchanged (Bruhn et al., 2000, Rosenberg and Handy, 2005).

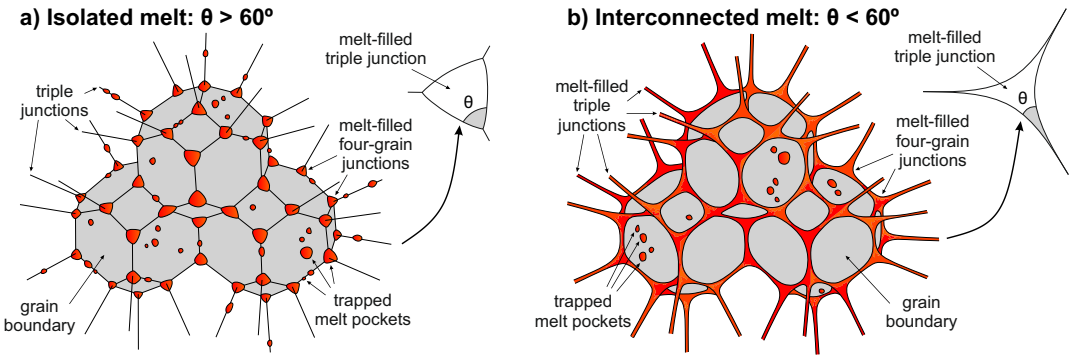

Figure 2.4: Melt distribution for (a) isolated melt-solid system where dihedral angle (θ) is >60°; and (b) interconnected melt-solid system where θ >60°. (a) 3-D view illustrates the presence of melt pockets trapped in grain boundaries, triple junctions and four-grain junctions, whereas (b) shows the presence of an interconnected melt network along triple junctions and through four-grain junctions pockets with melt pockets trapped in grain boundaries. After Lee et al. (1991), Kohlstedt (2002).

At high partial melt volumes between 40 and 60% melt, the solid framework begins to breakdown, and the rock passes through the 'solid-to-liquid transition' (SLT) and region of 'rheologically critical melt percentage' (RCMP; Figure 2.5; Arzi, 1978, van der Molen and Paterson, 1979, Lejeune and Richet, 1995, Rosenberg and Handy, 2005). The microstructure transitions from a solid framework with a network of melt channels to

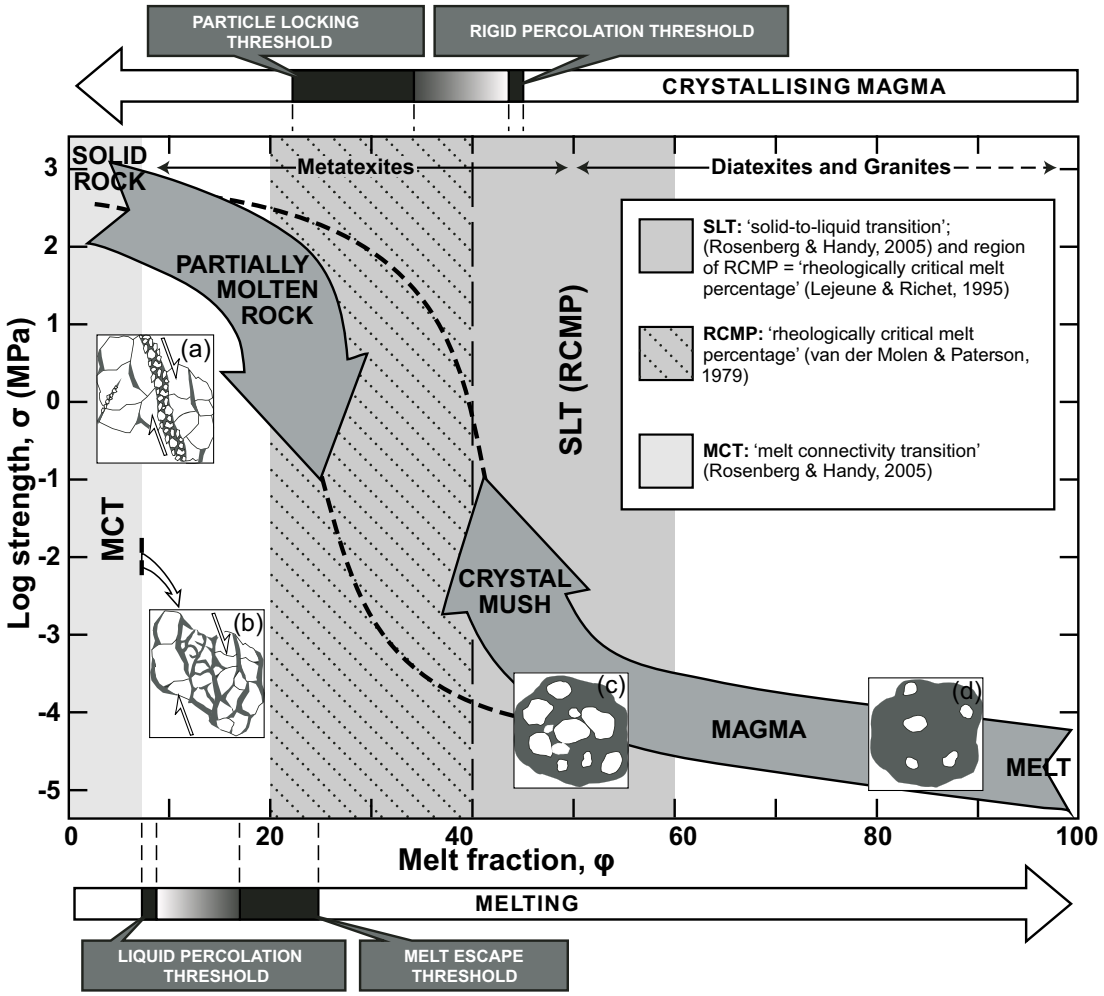

Figure 2.5: Synoptic diagram illustrating the role of melt on rheology and critical thresholds associated with changes in melt fraction. Note that the material properties (i.e. rock strength-viscosity) vary by orders of magnitude and depend on whether a system is melting or crystallising. Corresponding rock types and schematic rock microstructures are shown for clarity; (a) at melt volumes (ϕ) of around 3%, deformation localises along a melt-bearing fracture or fault. (b) At ϕ = 7%, deformation is more distributed on the sample scale, but it is localised along the interconnected network of melt on the grain scale. (c) At 40% to 60% ϕ the solid framework breaks down, but grain interactions still occur. (d) At ϕ = 60% the solid particles are suspended in the melt and do not interact with each other (Modified from Vigneresse and Tikoff, 1999, Burg and Vigneresse, 2002, Rosenberg and Handy, 2005, Vanderhaeghe, 2009, Tikoff et al., 2013; and references therein).

a suspension of grains in melt (i.e. crystal mush). When the melt volume is 60% or greater, grains are suspended in the melt, the original rock structure is fundamentally changed. The MCT yields a much larger strength drop than the SLT, such that the degree of interconnectivity controls the strength of the rock more than the breakdown of the solid framework (Rosenberg and Handy, 2005).

Vigneresse et al. (1996) showed that under static conditions partial melting forms intergranular films of melt, whereas during crystallisation from a melt, the melt is distributed interstitially in pockets. There is a higher melt connectivity during partial melting as opposed to crystallisation, which suggests that the physical properties and microstructures formed during partial melting and magma crystallisation are distinct. However, deformation experiments suggest the melt distribution is controlled by the orientation and magnitude of stress and/or the crystallographic and shape preferred orientations of solid grains when the melt volume is less than 40% (Kohlstedt and Zimmerman, 1996, Daines and Kohlstedt, 1997, Gleason et al., 1999). This implies that when melting or crystallising rocks are subject to stress they likely form the same melt distributions; the MCT therefore is likely to exist at 7% melt for both partial melting and crystallising systems (Figure 2.5; Rosenberg and Riller, 2000, Sawyer, 2001, Rosenberg and Handy, 2005).

Holyoke and Rushmer (2002) showed that melt connectivity varies depending on the rock composition and melt volume. Muscovite-dehydration melting during deformation resulted in the development of highly permeable cataclastic zones at low melt volumes, in contrast, biotite-dehydration melting during deformation resulted in melt migration along grain boundaries. Holtzman et al. (2003) demonstrates that deformation of partially molten ductile rocks produces stress-driven melt segregation (Figure 2.5). In the partially molten lower crust and upper mantle, stress-driven melt segregation may produce melt extraction pathways and localise deformation.

2.2.5 In-situ partial melting vs. melt flux

Anatectic migmatites commonly show both prograde and retrograde reactions between minerals and melt providing evidence for in-situ melting (Kriegsman, 2001).

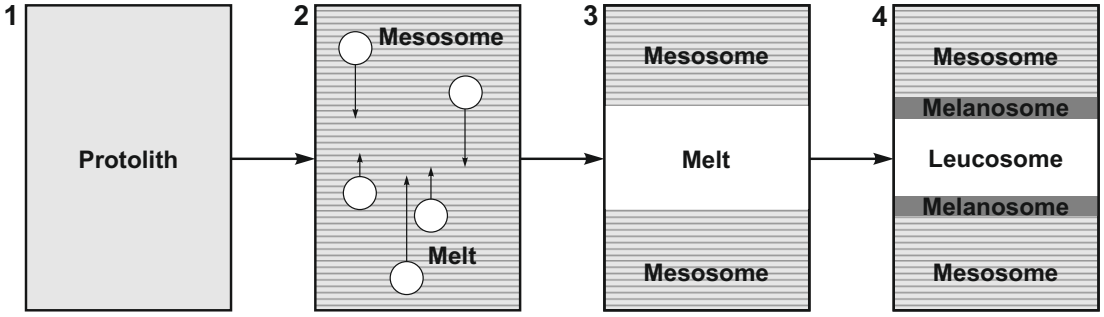

Figure 2.6: In-situ partial melting and migmatite formation in a closed system. Prograde partial melting results in mesosome and melt (1 to 2); melt segregation and collection in specific layers (2 to 3); and back reaction between in-situ melt and adjacent mesosome to form a leucosome-melanosome pair (3 to 4) (After Kriegsman, 2001).

The crystallised rock texture, mineral abundance and mineral chemistry shows evidence for four distinct processes; (1) prograde partial melting and small-scale segregation into melt-rich domains and restitic domains; (2) partial melt extraction; (3) partial retrograde reactions back reaction between in-situ crystallising melt and the restite; (4) crystallisation of remaining melt at the solidus, releasing volatiles (Kriegsman, 2001; and references therein). Figure 2.6 illustrates these processes for partial melting. The protolith is separated into mesosome and melt where a batch melting model assumes segregation of these parts. The segregated melt can be extracted from the system or back react to form a leucosome-melanosome pair (Kriegsman, 2001).

During deformation of a partial melt shear zone, with approximately 4-8% melt, deformation occurs by grain boundary sliding (Sawyer, 1994, 1996, Walte et al., 2005). If the melt is interconnected it allows grains to slide past each other forming rheologically weak layers at grain boundaries (Stuart et al., 2018). This process draws melt into the shear zone, localising melt to actively deforming areas enhancing the flux of melt (Rosenberg and Handy, 2001, Rosenberg and Riller, 2000, Walte et al., 2005, Stuart et al., 2018). The solid framework is maintained within the shear zone but strain is accommodated by the distributed melt.

If water fluxes through a high temperature region, melting can occur (Weinberg et al., 2015). Water-fluxed melt reactions are faster than dehydration melting and the resulting melt has a low viscosity (Behrens and Nowak, 1997, Holtz et al., 1996,

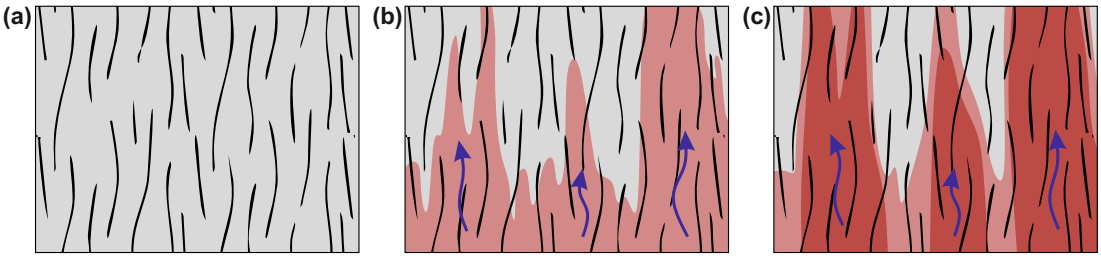

Figure 2.7: Illustration of the process of melt infiltration, metasomatic reactions and melt production through lower crustal rocks. (a) Lower crustal rock with pre-existing structures and no prior evidence of melting. (b) Melt infiltration is initiated in waves, moving upwards along grain boundaries, focusing into a select few channels subparallel to the foliation. (c) Advanced stages of melt migration, involving continued focusing of external melt into channels. Based on illustrations from the Pembroke Granulite by Stuart et al. (2016).

Richet et al., 1996, Schulze et al., 1996). Migmatites can also form by a hydrous melt moving through a previously unmelted rock. Externally derived melt fluxes through the protolith, reacting with the hydrous melt, modifying the mineral assemblage, composition and microstructures (Figure 2.7). A reactive front of porous melt flux propagates through the crust, driven by density contrast between the melt and rock (Stuart et al., 2017). As the melt flux progresses, the flow concentrates into melt channels which continue to focus melt flux.

Melt flux can be distinguished from in-situ melting by the preservation of crystallised melt textures as deformation stops. As the rock approaches and crosses the solidus, the melt volume decreases resulting in a hardening of the shear zone (Stuart et al., 2018). Strain would then localise to a rheologically weaker area, preserving the delicate melt textures that would otherwise be destroyed by further deformation.

2.2.6 Migmatite microtexture

Identification and quantification of melt at the outcrop scale is difficult as not all leucosome represents partial melt. Therefore, it is important to consider the microtexture. If melting occurs under static conditions and there is an absence of deformation in an igneous setting, the crystallised grains will reach textural equilibrium with uniform grain size and grain boundary angles relative to interfacial angles (e.g. 103 to 115° for quartz and feldspars; Vernon, 1968). However, if melting

occurs within a deformation regime or there is chemical disequilibrium due to melt loss or rapid crystallisation, an igneous-like microtexture is unlikely to be preserved.

Partial melting as a result of contact metamorphism is usually short-lived and occurs in the absence of or at low stress (Brown, 2012). Euhedral grains crystallising from partial melt in the metamorphic aureole are often well preserved in comparison to regional metamorphic environments (Vernon, 2011). Microtextures that form in deeper regional tectonic settings are commonly modified by solid-state deformation processes during slow cooling (Brown, 2012). Strain localisation in deformed rocks within the crust is usually characterised by the distribution and geometry of grain boundary melt films, however this evidence is rarely preserved in migmatites (Rosenberg and Riller, 2000). As a result, interpretation of fabrics in partial melt material, in terms of rheology, depends on experimental studies (Rutter, 1997).

Experimental studies by Dell'Angelo et al. (1987) and Dell'Angelo and Tullis (1988) show that partially melted crustal rocks experience cataclastic flow. However, no evidence for this process is seen in naturally deformed granites despite grain-scale fracturing in the presence of melt (Paquet et al., 1981, Gapais and Barbarin, 1986, Hibbard, 1987, Bouchez et al., 1992). Furthermore, deformation of the solid phase(s) associated with low melt percentages (<20%) indicates that dislocation and/or diffusion creep controls deformation (Gapais and Barbarin, 1986, Nicolas and Ildefonse, 1996). Such contrasting observations suggest that experimental studies cannot be used to accurately model microtextures during deformation associated with low melt fractions (Rosenberg and Riller, 2000). Schulmann et al. (2008) suggested melt weakening is the result of both mechanical and chemical processes. Small melt volumes at high strain rates result in weakening at the MCT because of grain boundary sliding causing diffusion creep, which evolves to particulate flow as melt volume increases. Periodic pulses of compaction and dilation in mid-crustal, partially molten rocks contribute to melt migration and ductile flow (Brown, 2007). The transition from submagmatic to magmatic flow coincides with the critical melt fraction (Blenkinsop, 2000) and corresponds to the transition from grain supported to suspension flow (Passchier and Trouw, 2005).

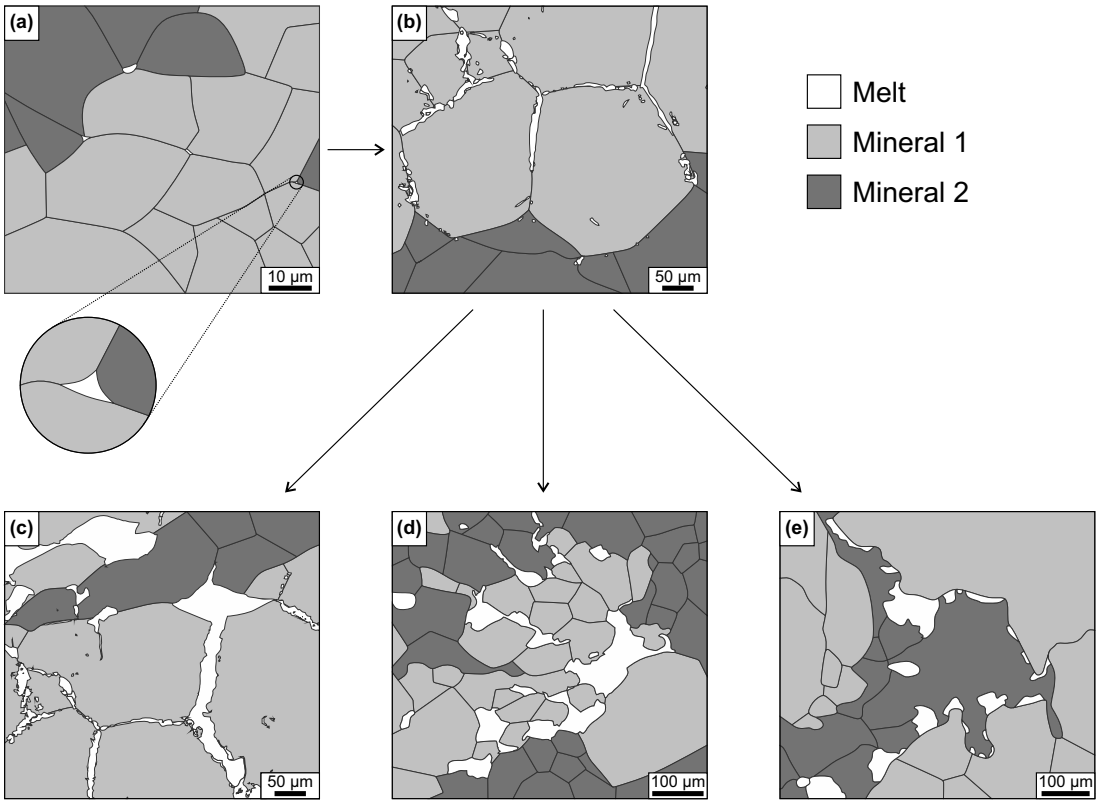

Figure 2.8: Schematic diagrams showing the evolution of possible microtextures produced via grain boundary melting. (a) Dihedral angles where the melt-solid dihedral angle is <60°, thus the melt is interconnected; (b) melt at triple junctions increases and moves along grain boundaries to form melt films; (c) larger melt films form cuspate melt volumes surrounded by non-melt grains; (d) interstitial melt forms an interconnected framework and is pervasive surrounding many non-melt grains; (e) melt films coalesce into multiple 'beads' forming the 'string of beads' texture.

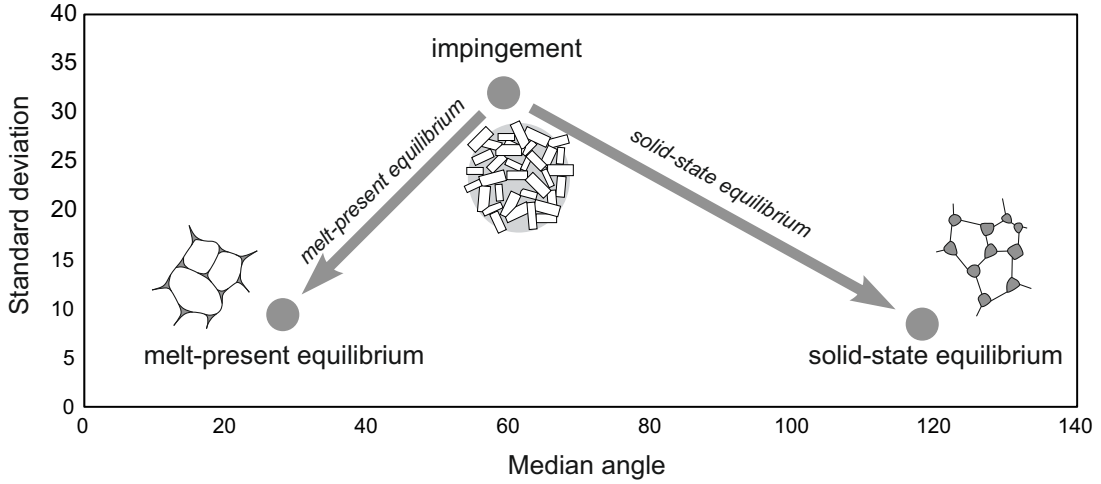

Figure 2.9: Relationship of dihedral angles to melt-present and solid-state equilibrium with schematic diagrams showing end-member solid-solid-melt dihedral angle populations (After Holness et al., 2005).

There are distinctive textures that are diagnostic of crystallisation from melt (e.g. Vernon and Collins, 1988, Vernon, 2011, Holness et al., 2011). These include: cuspate or serrated grain boundaries with low dihedral angles (Figure 2.8a; Harte et al., 1991, Sawyer, 2001, Holness and Sawyer, 2008); pseudomorphs of melt along grain boundaries and at triple/multiple junctions (Figure 2.8 b-e; Rosenberg and Riller, 2000, Holness and Sawyer, 2008); and grains with straight crystal faces (Vernon and Collins, 1988). Dehydration melting reactions are easier to identify because of the melt textures and peritectic products (where a solid and liquid phase react to form a second solid phase at specific conditions). They include: solid products of melting reactions forming euhedral crystal faces against the melt (Sawyer, 1999, 2001); reactant phases exhibiting rounded or corroded boundaries surrounded by melt films (Figure 2.8b; Mehnert et al., 1973, Büsch et al., 1974); small cuspate-shaped melt pools similar to those formed in experimental studies (Figure 2.8c; Harte et al., 1991, Rosenberg and Riller, 2000, Holness and Sawyer, 2008); and inter-growths between quartz and solid products of melting (Figure 2.8d; Waters, 2001, Barbey, 2007).

Melting usually initiates between grains and nucleates at triple junctions (Cooper and Kohlstedt, 1986). This alters the dihedral angle at triple junctions (usually $\sim$120° when rock is texturally equilibrated; Kretz, 1966, Hunter, 1987) and plays a key role in melt connectivity. Melt is likely to be interconnected if the melt-solid dihedral angle is less than 60°, but is likely to form isolated pockets when greater than 60° (Holness, 2006, Holness et al., 2011). Thus, if there is a high dihedral angle the melt connectivity is low and the strength of the partially melted rock is greater than if there is a low dihedral angle where melt connectivity is high. Figure 2.8a shows an example of low dihedral angles observed in melt-present rocks and Figure 2.9 shows the relationship of solid-solid-melt dihedral angles, where the relationship between median angle and standard deviation indicate melt-present or solid-state equilibrium.

If the dihedral angle is low and melt volume increases, melt begins to form an interconnected framework in the rock via grain boundary wetting forming grain boundary melt films (Figure 2.8b). The proportion of grain boundaries that contain melt dramatically increases when the melt volume exceeds 7%, where 90% of

boundaries contain melt (van der Molen and Paterson, 1979), resulting in a strength decrease in the rock marking the MCT.

As the melt volume increases further, grain boundary melt films increase in thickness (Rosenberg and Handy, 2005) and can form a variety of microtextures. Cuspate melt forms concave outward grain shapes, they are commonly comprised of quartz, K-feldspar or Na-rich plagioclase (Figure 2.8c; Vernon, 2011). Cuspate melt is inferred to represent melt that has partly penetrated grain boundaries, especially when surrounded by embayed grains that have partially melted (Holness and Sawyer, 2008, Holness et al., 2011). Cuspate melt patches tend to be pervasively distributed in grain boundaries and in small elongate patches mostly parallel to the foliation (Sawyer, 2001). Another typical microtexture is interstitial melt (Figure 2.8d), infilling the pore space in the rock and forming irregular crystal shapes around the restite and peritectic phases. 'String of beads' texture usually forms during concentration of melt from thick films on grain boundaries into 'beads' (Figure 2.8e; Holness et al., 2011). The texture suggests a slow crystallisation rate to allow nucleation of individual grains from melt films (Holness et al., 2011).

Other melt-indicative microtextures include: simple K-feldspar twins (Vernon, 1986); biotite pseudomorphed by feldspar (Sawyer, 2001); microgranite intergrowths of felsic minerals (Holness and Clemens, 1999, Clemens and Holness, 2000, Cesare et al., 2009); symplectic replacement aggregates explained by reactions between peritectic grains and cooling melt (e.g. Hibbard, 1979, Holness and Sawyer, 2008; and references therein); and zoning of leucosome and melanosome (Sawyer, 1999). Individually these microtextures are weak indicators of melting but when found together significantly strengthen such interpretation (Vernon, 2011). Random mineral distributions (Ashworth and McLellan, 1985), grain-size increase (Sawyer, 2008), corroded relic grains surrounded by felsic minerals (Mehnert et al., 1973, Sawyer, 2001), projections into a mineral (Hasalová et al., 2008a,b), and lobes of myrmekite (Vanderhaeghe, 2001, Hasalová et al., 2008a) are all questionable criteria for melting. These microtextures can be produced during metamorphism as well as melting. However, when present alongside more reliable melt-indicative microtextures they

support a melting origin.

2.3 Deformation mechanisms

In addition to melt distribution, the deformation of solid phases by solid-state process is important for understanding the overall tectonic regime related to partial melting. Deformation mechanisms in shear zones vary with depth (e.g. Figure 1.1; Sibson, 1983, Scholz, 1988, 2002). Fault models and strength profiles for minerals like quartz and feldspar show how the strength of a fault can change with depth. The change in strength is the result of deformation mechanisms transitioning from brittle seismogenic processes, through the brittle-ductile transition to ductile processes such as dislocation creep (e.g. Hirth and Tullis, 1992) and diffusion creep (e.g. Tullis and Yund, 1991).

Dislocation creep is the mechanism to produce crystal plastic deformation through the movement of dislocations through the crystal lattice (Nicolas and Poirier, 1976). Dislocation creep occurs by dislocation glide where the lattice slips on defect planes or by dislocation climb where the dislocation is moved out of the slip plane by migration of vacancies to the dislocation site. Dislocations migrate through the crystal lattice to reduce the density of dislocations and minimize the internal strain energy of the grain (Poirier, 1985). Distributed dislocations form undulose extinction, as recovery ensues, dislocations concentrate in deformation bands, eventually forming subgrain boundaries.

The process of diffusion creep results in solid-state diffusion of atoms (diffusive mass transfer) through a crystal lattice, *Nabarro-Herring creep* (Poirier, 1985), or along grain boundaries, *Coble creep* (Wheeler, 1992). Pressure solution allows material to be transported along grain boundaries in a liquid film rather than the movement of atoms and vacancies (Rutter, 1983). Coble creep and pressure solution occur at lower temperatures than Nabarro-Herring creep (Elliott, 1973, Poirier, 1985) and are more likely to be dominant in crustal materials. Grain-size sensitive creep is the process when diffusion creep occurs and grain-boundary sliding occur together (Passchier and Trouw, 2005; and references therein). This process is dominant in the lower crust and

mantle where fine-grained material deforms at high temperatures with a high strain rate and low differential stress (Karato, 2010). If the deformation mechanism switches from dislocation creep to diffusion creep it suggests a dramatic weakening in the rock (Pearce and Wheeler, 2011).

2.3.1 Grain boundary mobility

Grain boundary mobility allows a reduction of dislocation density in deformed crystals via recrystallisation (Poirier, 1985, Gottstein and Mecking, 1985, Jessell, 1987, Drury and Urai, 1990). Migration and modification of grain boundaries decreases or increases the grain size and in turn the internal free energy of the grain (Urai et al., 1986, Hirth and Tullis, 1992). Three mechanisms of recrystallisation operate during deformation, with increasing temperature and decreasing flow stress these are: bulging, subgrain rotation and grain boundary migration recrystallisation (Figure 2.10; Urai et al., 1986, Wu and Groshong, 1991, Hirth and Tullis, 1992, Stipp et al., 2002).

Bulging (BLG) recrystallisation (Figure 2.10) is the low temperature process that allows local migration of a grain boundary into a neighbouring grain with higher dislocation density (Drury et al., 1985, Shigematsu, 1999, Stipp et al., 2002). These bulges can separate and produce new crystals by the formation of subgrains (Means and Xia, 1981, Urai et al., 1986), or by migration of grain boundaries (Tungatt and Humphreys, 1984, Stipp et al., 2002). BLG recrystallisation commonly occurs along the edges of old grains and at triple junctions. This can produce a core-and-mantle texture where old grains are surrounded by new recrystallised grains.

As temperature increases grains may dynamically recrystallise by subgrain rotation (SGR; Figure 2.10). This process occurs when additional dislocations allow the rotation of subgrains, developing new grains (Hirth and Tullis, 1992, Stipp et al., 2002). This can generally occurs via climb-accommodated dislocation creep, where the dislocation climbs from one lattice plane to another increasing the angle between the subgrain and original grain until the subgrain is classified as a new grain. Old grains are often elongate ribbon-shaped with numerous subgrains. At low

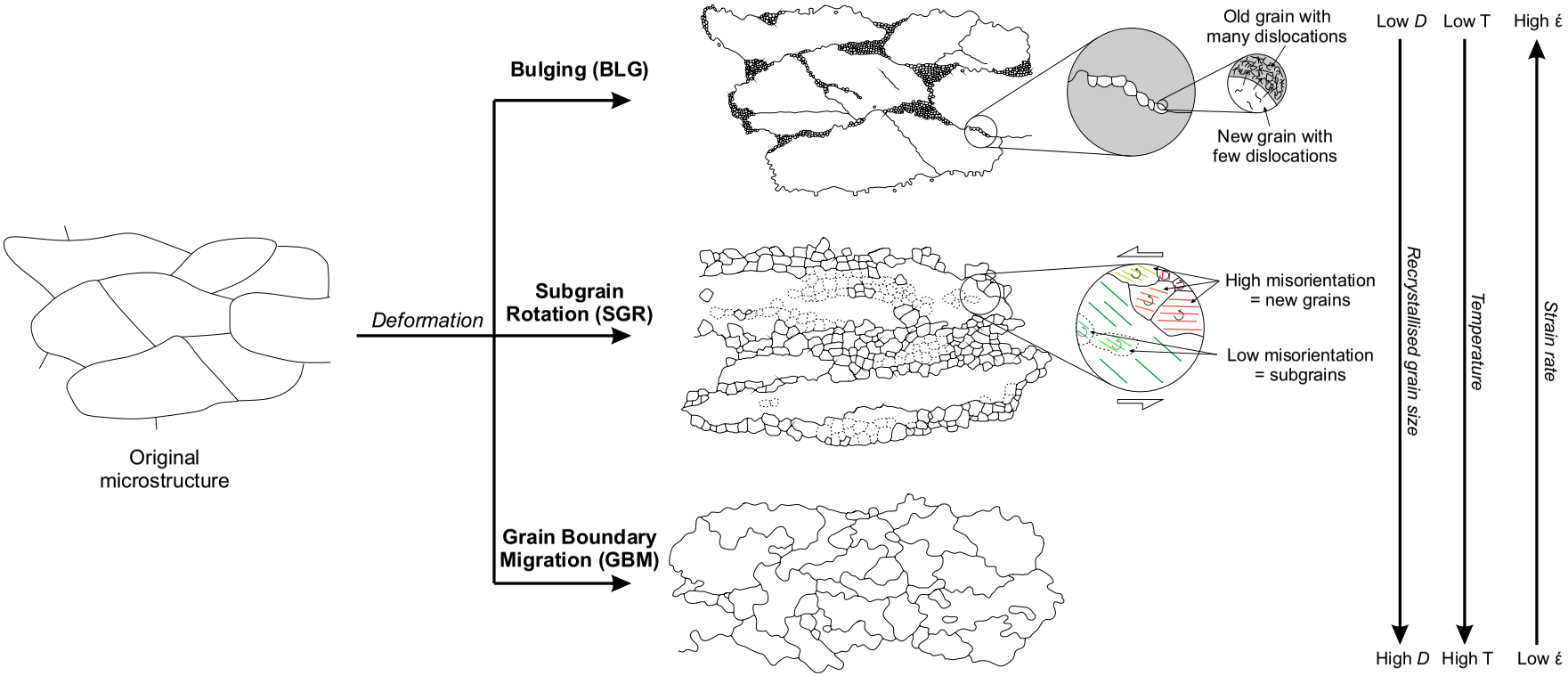

Figure 2.10: Characteristic microstructures of the three dynamic recrystallisation mechanisms of quartz shown at the same relative scale. (a) Bulging recrystallisation (low T): bulges and recrystallised grains are present along grain boundaries and to a lesser extent along microcracks. (b) Subgrain rotation recrystallisation (intermediate T): core and mantle structures or complete subgrain replacement of porphyroclastic ribbon grains and recrystallised subgrains. (c) Grain boundary migration recrystallisation (high T): irregular grain shapes and grain sizes; grain boundaries consist of inter-fingering sutures (Modified from Stipp et al., 2002, Passchier and Trouw, 2005).

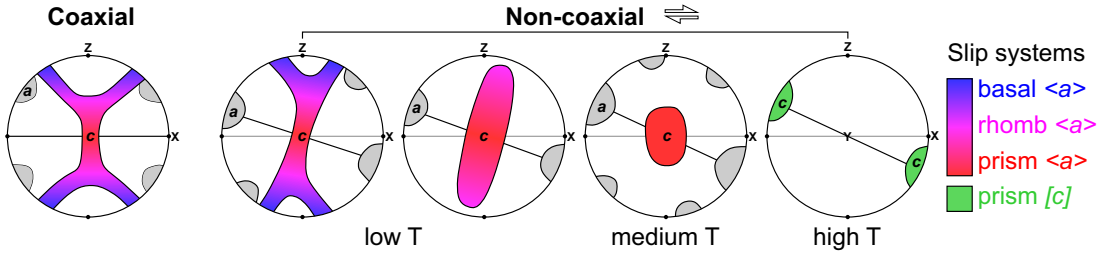

Figure 2.11: Quartz a- and c-axis CPO development. Schematic pole figures showing temperature dependent CPO development of <a> (grey) and [c] (coloured maxima) during coaxial and non-coaxial dextral shearing (Modified from Passchier and Trouw, 2005, Parsons et al., 2016).

temperatures and stresses core-and-mantle textures may form but as temperature and stress is increased, 'sheets' of new subgrains form between or completely replace old grains (Nishikawa and Takeshita, 2000, Nishikawa et al., 2004).

At high temperatures, grain boundary mobility is high and grain boundaries can sweep through a crystal removing all dislocations in a process called grain boundary migration (GBM; Figure 2.10; Guillope and Poirier, 1979, Urai et al., 1986, Hirth and Tullis, 1992, Stipp et al., 2002). Grain boundaries are mobile and grain size is variable, new grains are usually larger than old grains. At high temperatures, grains can be extremely lobate and strain free with no undulose extinction or subgrains.

2.3.2 Quartz slip systems

During crystal plastic deformation of quartz at different metamorphic grades, different slip systems are active. Typically basal <a> slip is common at low temperatures (300-400°C) whilst rhomb and prism <a> slip become active at increasingly greater temperatures (400-650°C; Mainprice et al., 1986, Schmid and Casey, 1986, Lloyd and Knipe, 1992, Lloyd and Freeman, 1994). At high temperatures (650-700°C) prism <c> slip can occur although this may require deformation in the presence of water (Mainprice et al., 1986, Morgan and Law, 2004).

Figure 2.11 shows a- and c-axis crystallographic preferred orientation (CPO) patterns during non-coaxial plane strain deformation (Behrmann and Platt, 1982, Bouchez et al., 1983, Platt and Behrmann, 1986). At low temperatures Type I cross girdles and single girdles inclined to foliation and lineation are common (Burg and

Laurent, 1978, Lister and Hobbs, 1980, Schmid and Casey, 1986). If basal <a> slip is active the CPO may have a strong cluster in the periphery. As temperature increases a single maxima develops around the Y-axis, this indicates prism <a> slip is more prevalent (Wilson, 1975, Bouchez, 1977, Lister and Dornsiepen, 1982, Law et al., 1990), and at high temperatures, a point maxima forms in the direction of the aggregate lineation where prism <c> slip operates (Lister and Dornsiepen, 1982, Blumenfeld et al., 1986, Mainprice et al., 1986). The use of slip systems alongside deformation mechanisms gives an approximate control on the stress and temperature conditions that the rock has been subject to.

2.3.3 Stress and strain estimation

To understand the rheology of the crust during deformation it is important to understand the magnitude of stress that the rock has been subject to. Palaeopiezometers measure the magnitude of differential stress from dynamically recrystallised grain size (e.g. Twiss, 1977, Ord and Christie, 1984, Stipp and Tullis, 2003, Cross et al., 2017). The general relationship is a small mean recrystallised grain size is the result of deformation at low temperatures and high differential stress (e.g. BLG), and a large mean recrystallised grain size is the result of deformation at high temperature and low differential stress (e.g. GBM; Figures 2.10, 2.12). Where there is abundant evidence of partial melt in the microtexture, deformation is inferred to be syn-melt. In this case, it is difficult to determine the palaeostress as melt does not produce microstructures that reflect the deformation regime. However it is important to consider as post-melt deformation may record the retrograde stress-strain path of the rock.

In this thesis recrystallised grain size is calculated from Electron Backscatter Diffraction (EBSD) data via the grain orientation spread (GOS) technique after Cross et al. (2017), where recrystallised and relict grains are isolated to find the root mean squared (rms) recrystallised grain size. There are a range of quartz palaeopiezometers that use thin section grain size; Twiss (1977), Ord and Christie (1984; wet and dry quartz) and the widely accepted Stipp and Tullis (2003) palaeopiezometer. Cross

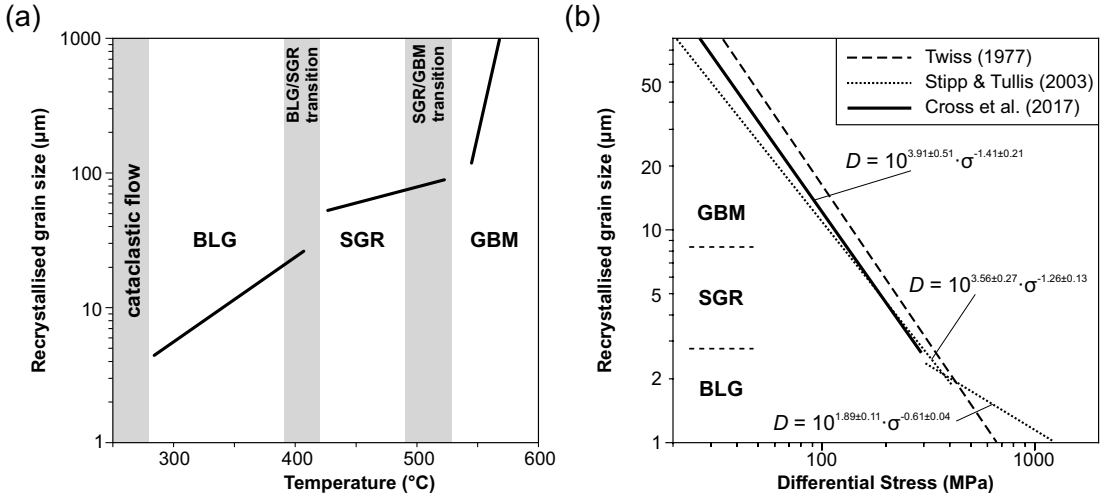

Figure 2.12: Palaeopiezometer for quartz with recrystallised grain size versus temperature and differential stress. (a) Plot of recrystallised grain size versus temperature (After Stipp et al., 2002). (b) Log-log plots of recrystallised grain size (D) versus differential stress (σ_{1-3}) with piezometer relationships (After Twiss, 1977, Stipp and Tullis, 2003, Cross et al., 2017).

et al. (2017) have developed an amendment of the Stipp and Tullis (2003) palaeopiezometer to account for the increased resolution of EBSD data. These palaeopiezometers only consider deformation of monomineralic samples, not accounting for polymineralic or heterogeneous properties and importantly do not consider the effect of partial melt. I use EBSD data to calculate the recrystallised grain size (D), and then apply the Cross et al. (2017) palaeopiezometer to gain a relative understanding of post-melt deformation from the differential stress (σ_{1-3}),

$$D = 10^{3.91\pm0.51} \cdot \sigma_{1-3}^{-1.41\pm0.21}. \tag{2.3}$$

The rheological behaviour of rocks is expressed through flow laws (Poirier, 1985, Hirth et al., 2001). Flow laws describe the dependence of strain rate on parameters such as stress and temperature. In this thesis I apply the quartz power-law flow law for dislocation creep (Table 2.2; Tokle et al., 2019) to understand any relative changes in magnitude of strain rate,

$$\dot{\varepsilon} = A\sigma_{1-3}^{n} f_{\mathrm{H_2O}}^{r} e^{\frac{-Q}{RT}}, \tag{2.4}$$

where $\dot{\varepsilon}$ is strain rate, σ_{1-3} is differential stress, n is the stress exponent, $f_{\mathrm{H_2O}}$ is the water fugacity, r is the water fugacity exponent, Q is the activation enthalpy, R

Table 2.2: Rheological parameters for dislocation creep flow laws in quartz

n	A (MPa^{-n}/s)	f_{H_2O} MPa	r	Q (kJ/mol)	R (kJ/mol)
4	1.75×10^{-12}	200	1	125	0.008314
3	1.1×10^{-12}	55	1.2	115	0.008314

is the ideal gas constant, T is absolute temperature, and A is a material parameter (Tokle et al., 2019). The flow law parameters for dislocation grain boundary sliding are considered when $n = 4$ and parameters for low temperature/high stress dislocation creep are considered when $n = 3$, where the final strain rate is the sum of the dislocation grain boundary sliding component and the dislocation creep component. Calculating relative changes in differential stress and strain rate allows an understanding of how different styles of melting may play a more significant role in reducing the strength of the rock and ultimately the middle to lower continental crust.

2.4 Effect of melt on seismic properties

Seismology is often used to predict present day melt volumes in the crust and mantle (e.g. Hirn et al., 1997, Blackman and Kendall, 1997, Holtzman et al., 2003, Bastow et al., 2010, Cornwell et al., 2010). Laboratory experiments show that partial melt strongly affects seismic velocity and attenuation (Faul et al., 1994), and these experiments can be extrapolated to field-scale seismic frequencies (Garapić et al., 2013). Hammond and Humphreys (2000b) derived a relationship to determine exact melt fractions from seismic velocity anomalies, which has been used to interpret crust and mantle melt volumes (e.g. Goes and van der Lee, 2002, Stixrude and Lithgow-Bertelloni, 2005, Stork et al., 2013). However, the relationship is only valid for specific melt geometries (Hammond and Humphreys, 2000a,b), temperature (Jackson et al., 2002), composition (Karato and Jung, 1998), and attenuation (Goes et al., 2012). In the melt-rich environments of mid-ocean ridges (MORs) and volcanic regimes, it has become clear that melt shape, orientation and distribution are important when predicting melt volume (Mainprice, 1997, Hammond and Kendall,

2016). Melting and tectonic relationships observed in palaeo-orogenies and shear zones feed into seismic models to give more robust results for calculating melt volume in the crust. This type of analysis has not been applied to orogenies, although assessment of the amount and distribution of melt is crucial to understand lithospheric rheology.

Orogenies are different from MORs or volcanic regimes because of their complex deformation mechanisms and chemistry. Metamorphic phase reactions of multicomponent Si-rich crust leads to changes in both solid and melt phase compositions, whereas in MORs melts are essentially formed by decompressional melting of peridotite. Previous studies have analytically modelled seismic velocities and anisotropies of partial melt within an isotropic matrix (e.g. Walsh, 1969, O'Connell and Budiansky, 1977, Mavko, 1980, Schmeling, 1985, Hammond and Kendall, 2016). However, melting in orogens is also predicted to be syn-kinematic with deformation affecting melt shapes, orientation and distribution, and leading to CPO of solid mineral phases. As the partitioning of stress and strain between melt and solid is uncertain, different approximations are used to calculate seismic properties. For solid rock, seismic compressional (Vp) and shear (Vs) wave velocities and anisotropies (AVs) can be calculated from the CPO of mineral phases according to their modal proportions (Mainprice, 1997, Tatham et al., 2008, Lloyd et al., 2009, 2011a,b). Partial melts impact on these estimates (Holtzman et al., 2003, Holtzman and Kendall, 2010), typically causing reductions in velocities (more so in Vs) and increase in anisotropy (Schilling and Partzsch, 2001).

It is suggested that the mid to lower crust in the Himalaya-Tibet orogen is mechanically weak due to partial melting; this is supported by geophysical observations of intra-crustal low-velocity layers/zones (LVL; Yang et al., 2003, Yao et al., 2008, Fu et al., 2010, Zhang and Klemperer, 2010, Bao et al., 2013, Xu et al., 2013, Bao et al., 2015), low electrical resistivity (Lemonnier et al., 1999, Wei et al., 2001, Unsworth et al., 2005, Bai et al., 2010), high heat flow (Hu et al., 2000) and strong attenuation (Bao et al., 2011, Zhao et al., 2013).

The common assumption that seismic velocities decrease linearly after the initial

melting has meant that seismic methods such as Vp/Vs ratios are often used as a tool to quantify both the size of magma chambers/partially molten volumes and/or melt percentages in various tectonic environments (e.g. Schilling and Partzsch, 2001, Caldwell et al., 2009, Lin et al., 2014). However, recent evidence suggests that melt-seismic property relationships are non-linear (Karato, 2010, Hammond and Kendall, 2016), whilst the effect on AVs remains unclear (Xie et al., 2013).

In addition, different geophysical methods yield different results. LVLs observed over the Himalayas and Tibet are usually investigated through inversion of P-wave receiver functions and Rayleigh wave group velocities. The presence of an LVL does not necessarily indicate the presence of partial melt as LVLs occur naturally in granitic crust with a high geothermal gradient (Min and Wu, 1987, Christensen, 1996). However there is evidence from the Himalaya that suggests partial melt is present in some LVLs that are associated with regions of anomalously high temperature (Nelson et al., 1996, Hirn et al., 1997, Makovsky et al., 1999). Zhang and Klemperer (2010) reinterpreted data from the Peigu Tso-Pumoyong Tso (Tibet) deep seismic sounding and obtained the seismic structure of a crustal Vp and Vs model. They found evidence for an LVL which they interpreted to be a partial melt or fluid-rich shear zone dipping 8.5° north, consistent with the Main Himalayan Thrust (Figure 2.13). Yang et al. (2003) studied Himalaya-Tibet LVL, concluding the LVL was the result of intracrustal partial melting. They observed a low Vp of 5.6-5.8 km/s and calculated a melt volume of 7-12% where melt is distributed along grain boundaries to form melt films, which would sufficiently reduce the velocity to form an LVL.

Sheehan et al. (2014) observed the relationship between Vp/Vs and attenuation across Himalaya and Tibet. They found areas of very high attenuation corresponded to an increase of Vp/Vs, interpreting this as evidence for the α-β quartz transition (ABQT; Ohno et al., 2006). Beneath this area the attenuation was much lower and Sheehan et al. (2014) interpreted this as fluid trapped by the porosity and permeability contrast associated with the ABQT. They suggested melt or fluid was present where patches of low to mid attenuation correlated to low Vp/Vs.

Furthermore, as Vs is sensitive to partial melt (Oliver, 1962), Caldwell et al. (2009)

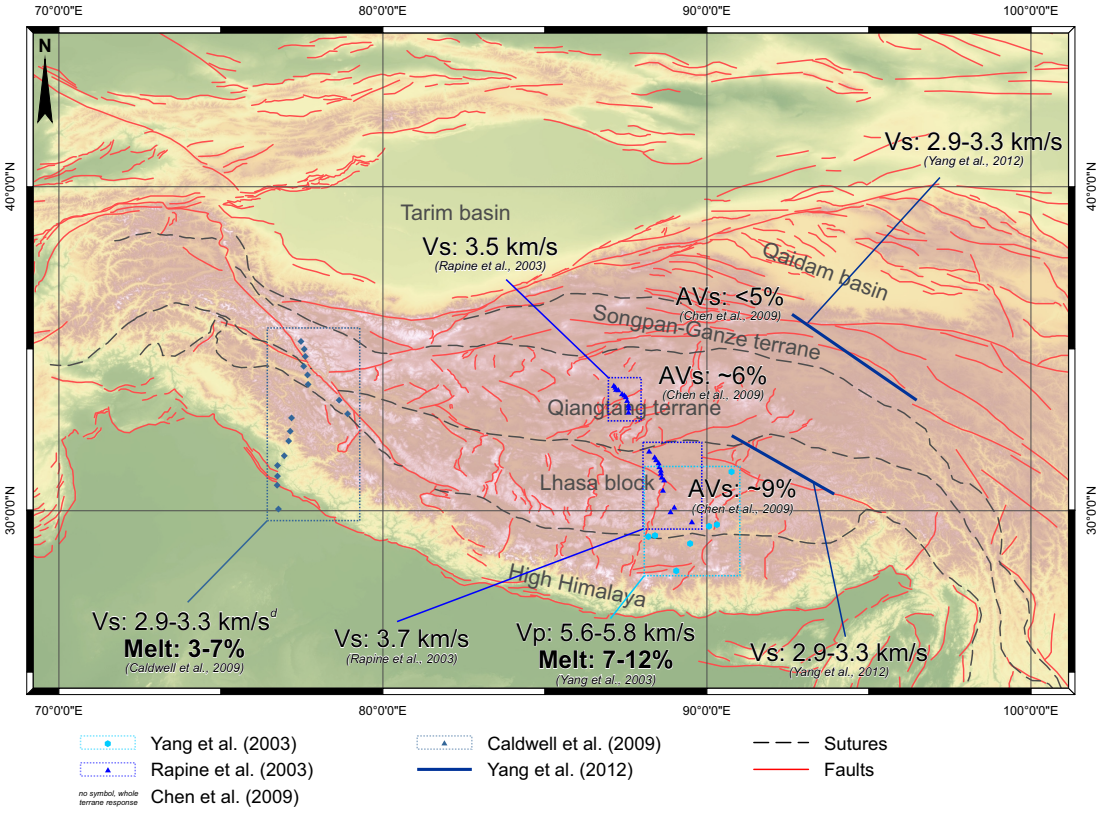

Figure 2.13: Map of the Himalaya-Tibet Plateau with location of seismic surveys (Yang et al., 2003, Rapine et al., 2003, Chen et al., 2009, Caldwell et al., 2009, Yang et al., 2003). Measured seismic velocities and inferred partial melt fractions are shown from the Tibetan Plateau and northwest Himalaya.

measured the dispersion of Rayleigh surface waves and inverted these data to obtain one-dimensional models of shear-wave velocity structure for the northwest Himalaya (Figure 2.13). The LVL, Vs of 2.9-3.3 km/s, was observed to deepen towards the north and continues north of the Karakoram fault, but was absent to the south beneath the Lesser Himalaya. They suggested a low-viscosity ductile layer with 3-7% partial melt is present beneath and north of the South Tibetan Detachment.

Schilling and Partzsch (2001) observed LVLs and high electrical conductivity zones beneath the Tibetan Plateau (Figure 2.13). When combined with additional data from Vp/Vs, seismic attenuation, and thermal and gravity anomalies it suggests that crustal melts are interconnected by networks of dykes and veins. Primarily using results from magnetotelluric (MT) electrical conductivity, they suggest there is 6-12% melt beneath Tibet that is partially interconnected.

Rapine et al. (2003) observed a 5% reduction of Vs in the Tibetan lower crust, giving

velocities of ∼3.7 km/s at 20-30 km in the Lhasa block of southern Tibet beneath and ∼3.5 km/s in the lower crust of the Qiangtang terrane in northern Tibet. A LVL of 2.9-3.3 km/s from 15-40 km depth was observed by Yang et al. (2012) beneath much of Tibet. They also deduce that partial melting is not possible if Vs is >3.45 km/s. Chen et al. (2009) observed Vs reductions and calculated the radial anisotropy beneath the Tibetan Plateau and observed middle crustal AVs up to 9% in the Lhasa block, 6% in the Qiangtang terrane middle crust and less than 5% in the north of the orogen in the Songpan-Ganze and Qaidam terranes. Hacker et al. (2014) took these observations of surface wave tomography over the central Tibetan Plateau to study partial melt. Hacker et al. (2014) compared the surface wave tomography data with modelled wave speeds using values of 3.3 km/s for Vs, and 4% for AVs between depths of ∼20 to 50 km. The observed velocities and anisotropy suggested a subhorizontal, foliated mica-bearing with a much lower silicate melt volume of 2% (Hacker et al., 2014).

MT profiles identify regions of anomalies in resistivity and conductivity, with high conductivity values within the crust known to result from melt, metamorphic fluids and/or brine (Nelson et al., 1996, Wei et al., 2001). Lemonnier et al. (1999) conclude that a high conductivity zone across the Himalaya is caused by metamorphic fluids as temperatures are insufficient to yield melt (Henry et al., 1997). Conversely, Unsworth et al. (2005) suggest there is an increased heat flow within the low resistivity layer, coupled with a viscosity reduction, indicating 5-14% melt is present beneath southern Tibet and 2-4% melt beneath the NW Himalaya. Comparison of seismic and MT data with laboratory experiments measuring electrical resistivity by Hashim et al. (2013) indicates up to 25% partial melt is present beneath the Himalaya-Tibet orogen. Their results suggest a much weaker middle crust with viscosities several orders of magnitude lower than assumed in geodynamic models.

The volume of partial melt beneath the Himalaya-Tibet orogen is extremely varied when interpreting results from different geophysical methods. The examples shown here yield melt volumes from 2-25% (Figure 2.13). The calculated volumes are not consistent along strike, nor do they increase toward either the north or south (Figure 2.13) suggesting a high amount of complexity in the orogen or unreliable

geophysical responses and models. In Chapter 5 I present models for seismic properties and compare these results with active Himalaya-Tibet melting in Chapter 6.

2.5 Experimental and analytical techniques

In order to study the melt and deformation microstructures and acquire CPO data for seismic property calculations, it is necessary to prepare thin sections and polished blocks. This section describes the analytical techniques and procedures employed in this PhD thesis. The aim of this section is to provide the reader with a brief background overview of the analytical instrumentation, with details of sample preparation, of the operating conditions and of data processing.

2.5.1 Sample preparation

Samples were taken from the field areas with the aim of representing typical compositions and structure for the outcrop. Samples were collected ethically according to the Geological Society of London's code of ethics and with the landowner's permission. Field areas were not located within protected areas but sampling was undertaken in accordance with the Norwegian Nature Diversity Act (No.100, 2009). The ideal criteria for sample selection were: a large sized coherent sample (>15x10x10 cm, or similar) to increase the available volume that is unaffected by weathering effects; a sample as undeformed as possible by visible or smaller fracturing, to reduce the chance of the sample disintegrating during preparation; and as representative of the outcrop as possible. All samples were oriented in the field according to the orientation of foliation (strike/dip) and where present stretching lineation (trend/plunge), and these orientations were marked on each sample.

In the laboratory, rock samples were cut perpendicular to foliation and parallel to stretching lineation to make covered thin sections and polished resin blocks for Seiland Igneous Province and Western Gneiss Region samples. Thin sections were oriented with the Z axis pointing towards the pole of the foliation and with the X axis pointing to the

plunging direction of stretching lineation. Samples lacking XYZ strain indicators were cut parallel to geographic horizontal. The X-Z directions from the sample correspond to the X-Z direction of the finite strain ellipsoid.

The scanning electron microscope (SEM) with EBSD is the main apparatus used to determine the CPO in samples, it is required for samples to have a flat highly polished surface to maximise results. For preparation of the polished blocks, rock samples ∼15x15 mm are mounted in a 30 mm resin block. Both the blocks and thin sections are polished with increasingly fine suspended abrasives from 60 μm aluminium oxide to 1/4 μm diamond paste. After which the samples undergo a chemo-mechanical polish using 0.05 μm colloidal silica abrasive suspended in an alkaline fluid (pH 8-9; Lloyd, 1987). This additional polishing step removes lattice damage and distortion caused by the earlier polishing procedures. Geological samples are generally non-conductive, as a result the surface charges when under an electron beam, this can distort the sample image. To prevent this the resin block and sample edges are coated in graphite paint and the sample surface is coated with 10 nm of vacuum evaporated carbon to conduct charge away from the sample.

2.5.2 Electron microscopy

Microstructures in rock samples were observed using optical microscopy and back-scattered electron (BSE) imaging using the SEM. For this work, a beam accelerating voltage of 20 kV, spot size of 5 and a working distance of ∼10 mm was used on the FEI Quanta 650 FEGSEM at the University of Leeds. Optical microscopy was initially used to identify the mineralogy of rocks, but it is necessary to use SEM techniques to image and analyse fine melt textures and melt films not visible optically. Energy-dispersive X-ray spectroscopy (EDS) using Oxford Instruments AZtec software was used to identify phases with a grain size larger than 5 μm in diameter to provide semiquantitative analyses of the phase composition via the resultant spectra. In addition to EDS analyses, the electron microprobe was used for spot analyses on selected samples with the JEOL JXA8230 electron microprobe operated at 15 kV and 15 nA with a defocused beam.

EBSD provides a method of acquiring crystallographic orientation data with known relationships to the rock microstructure (Prior et al., 1999). The technique allows detailed investigations of specific microstructures as well as bulk characterisation of crystallographic fabrics. EBSD data were collected from polished blocks and thin sections using the FEI Quanta 650 FEGSEM equipped with AZtec software and an Oxford/HKL Nordlys S EBSD system. Data were collected using 20 kV accelerating voltage, 5-15 nA specimen current and 69.7° specimen tilt angle. Whole block areas were analysed using combined stage scan-beam scan montage with step sizes of 1-20 μm. Oxford Instruments Channel5 software was used for initial data processing and MTEX open source software toolbox (Bachmann et al., 2010) for MATLAB was used for enhanced data processing, pole figure plotting and seismic property simulations.

2.6 Conclusions

The theoretical discussions presented in this chapter have highlighted the need to gain further information about the seismic response to partial melt and deformation in shear zones. In order to refine the seismic models for melt in the crust, it is necessary to obtain more information about the melting and deformation mechanisms of syn-melt shear zones. It is also important to determine whether there are common features in partial melt shear zones, so that more precise constraints can be utilised when the seismic response is considered to assert the presence or volume of melt. Geological data from exhumed, exposed syn-melt shear zones (Chapters 3 and 4) can provide information about key properties that could result in a specific seismic signature (Chapters 5 and 6). These data are described in the remainder of this thesis, and interpreted in terms of the theoretical concepts that have been discussed in this chapter.

Chapter 3

Evolution of a shear zone before, during and after melting

Øksfjord Shear Zone, Seiland Igneous Province, Norway

The first case study investigates a field example of syn-kinematic partial melting from the Øksfjord peninsula in the Seiland Igneous Province (SIP) of the North Norwegian Caledonides. Deformation of the paragneiss shear zone occurred at the same time as biotite dehydration melting (Elvevold et al., 1994, Menegon et al., 2011), making this an ideal system to study the effects of syn-melt lower crustal deformation. This chapter is in review for publication in the *Journal of the Geological Society* and is available as a preprint through EarthArXiv, doi:10.31223/osf.io/ayxj8.

3.1 Geological setting

The SIP (Figure 3.1a) comprises of a suite of deep-seated, rift-related, mantle-derived magmatic rocks emplaced into paragneisses during the opening of the Iapetus Ocean at 570-520 Ma (Elvevold et al., 1994, Reginiussen et al., 1995, Roberts et al., 2006). It forms part of the Sørøy Nappe of the Kalak Nappe complex, which is the middle allochthon of the Norwegian Caledonides. The Sørøy Nappe comprises paragneiss of the Sørøy Group estimated at between 1.7-1.2 Ga in age (Robins and

Often, 1996). The lowest stratigraphic unit of the Sørøy Nappe is the Eidvågeid Supracrustal Sequence, a paragneiss comprising migmatized pelitic and quartzofeldspathic gneisses, quartzite, marble and calc-silicate rocks (Akselsen, 1982). There is little evidence for the origin of the Eidvågeid Supracrustal Sequence; it is not known whether it is previously deformed basement or the lowest part of the stratigraphic sequence of the Sørøy Group. The structurally overlying Sørøy Group consists of meta-psammites, schists, marble and calc-silicates recording a transition from shallow water clastic deposition to turbidite-type sedimentation (Roberts, 1974, Ramsay et al., 1985).

During the late Proterozoic (829-804 Ma) the Sørøy Group was deformed and metamorphosed. This was followed by intracontinental rifting similar to the current East African Rift, where magmatic rocks ranging in composition from ultrabasic to nepheline syenitic and carbonatitic were emplaced into continental crust of the allochthonous Kalak Nappe (Ramsay et al., 1985, Krogh and Elvevold, 1990, Elvevold et al., 1994, Roberts, 2003, Roberts et al., 2006). The intrusive event was short-lived, between 570-560 Ma, and emplaced during a pre-orogenic extensional phase related to the initial stages of the opening of the Iapetus Ocean (Reginiussen et al., 1995, Roberts et al., 2006). The total extent of magmatism is unknown but was much more voluminous than the current surface exposure of 5400 km^2, which only represents the roots of the intrusions (Roberts et al., 2006). A further phase of deformation and medium to high grade metamorphism was caused by the Finnmarkian Orogeny between 530-490 Ma, an early phase of the Caledonian Orogeny (Sturt et al., 1978, Ramsay et al., 1985, Ramsay and Sturt, 1986, Robins and Often, 1996). This was followed by the thrusting of nappes during the Scandian Orogeny between 420-400 Ma, a later phase of the Caledonian Orogeny (Stephens and Gee, 1989).

The Øksfjord peninsula (Figure 3.1b) consists almost entirely of layered gabbro plutons intruded into paragneiss and metapelites of the Eidvågeid Sequence, which now outcrop c. 50 km northeast of Øksfjord in the Kalak Nappe Complex (Akselsen, 1982, Elvevold et al., 1994, Reginiussen et al., 1995). During the intrusive event, the Eidvågeid gneisses suffered contact metamorphism to peak conditions of T = 930-960°C

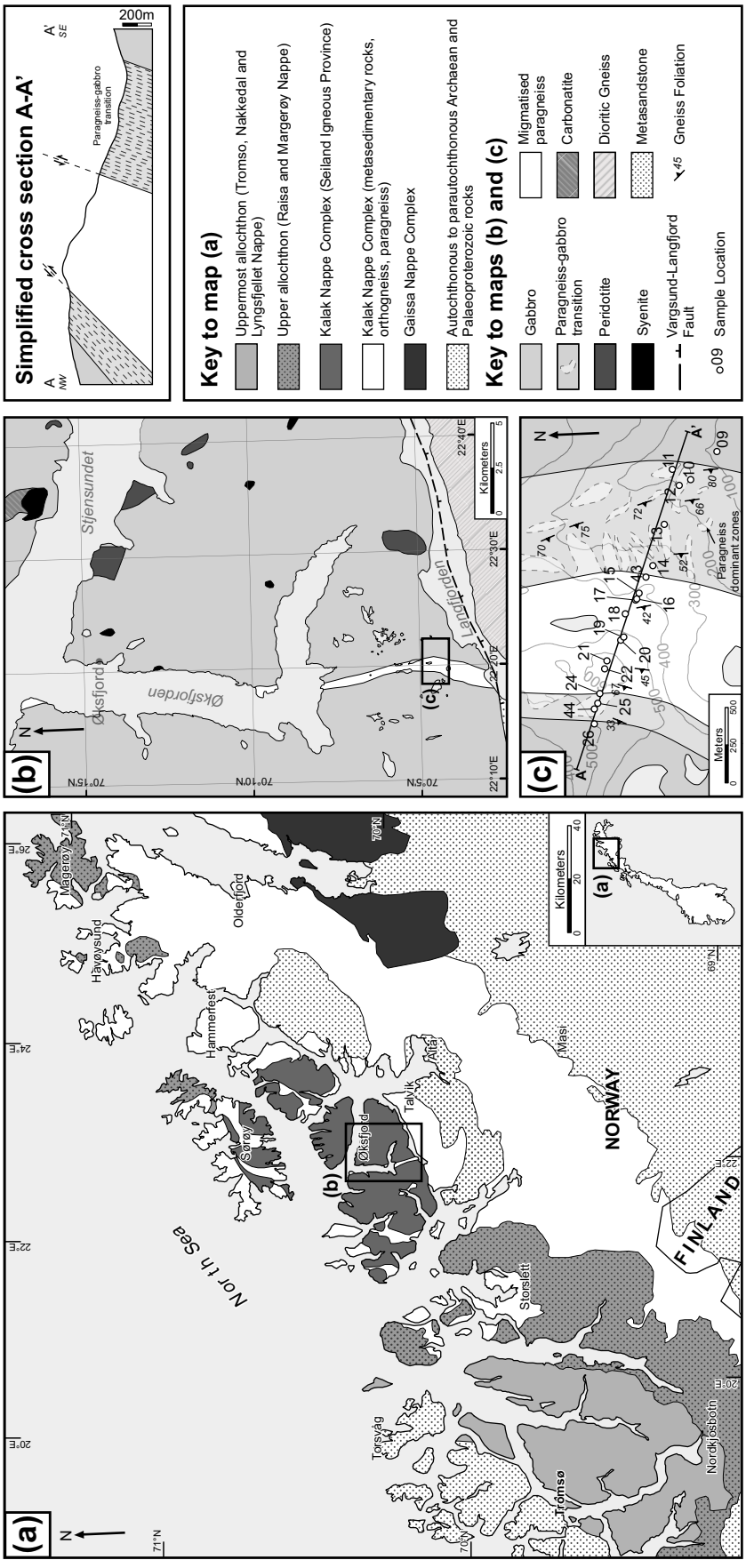

Figure 3.1: Geological map of (a) northern Norway and Seiland Igneous Province with inset detail maps of (b) Øksfjord Peninsula in the Seiland Igneous Province and (c) Øksfjord shear zone transect, additionally (d) shows a simplified cross section through the ØSZ (Geological maps modified from Roberts, 1973, Slagstad et al., 2006).

and P = 0.55-0.7 GPa before cooling and recrystallising at pyroxene granulite facies conditions (700-750°C, 0.5-0.7 GPa; Elvevold et al., 1994). A steeply dipping (∼60° WSW) gneissic to mylonite foliation developed in the metasediments and gabbro during this period of metamorphism, with asymmetric fabrics indicating a top-down-to-NW sense of shear (Menegon et al., 2011). The relationship of magmatic layering with the paragneiss foliation suggests synintrusive deep crustal shearing during lithospheric extension (Elvevold et al., 1994, Roberts et al., 2006). The study area focusses on a 2 km section through a laterally continuous paragneiss Øksfjord shear zone (ØSZ) on the Øksfjord Peninsula. This shear zone can be traced northward to outcrops on the edge of Øksfjorden (Figure 3.1 b-c).

Thermodynamic modelling by Menegon et al. (2011) shows the paragneiss and metapelites have undergone shearing and partial melting at metamorphic conditions of T = 760-820°C and P = 0.75-0.95 GPa via biotite dehydration (bt + pl + sil + qz = kf + gt + melt; Spear et al., 1999). The paragneiss is segregated into leucosome- and melanosome-rich domains visible from outcrop to microscale. It is estimated 5-7% melt was produced during partial melting and shear deformation (Menegon et al., 2011).

Figure 3.2: Outcrop photographs from the ØSZ showing the transition from from localised melt zones within gabbro to highly segregated stromatic migmatites with high temperature mineral assemblages and internal deformation. (a) Gabbro outside transition zone. (b) Transition zone paragneiss, high leucratic proportion in paragneiss pod. (c) Transition zone paragneiss on edge of pod with weak leucosome-melanosome segregation. (d) Paragneiss near shear zone boundary, high leucosome proportion but lacks internal structure and segregation. (e) Schollen-type migmatite near the edge of the shear zone boundary; rafts of mesosome within predominantly leucosome. (f) Stromatic migmatized paragneiss. (g) Stromatic segregation of leucosome and melanosome increases in strength towards shear zone centre. (h) Stromatic layered migmatized paragneiss. (i) Isoclinal folds in stromatic migmatized paragneiss. (j) Migmatized paragneiss with mafic, garnet melanosome layers within a leucratic matrix. (k) Flanking structure with top down to west shearing in paragneiss, outcrop is located outside sample area. (l) Top down to west sheared mafic bands in leucratic paragneiss, outcrop is located outside sample area.

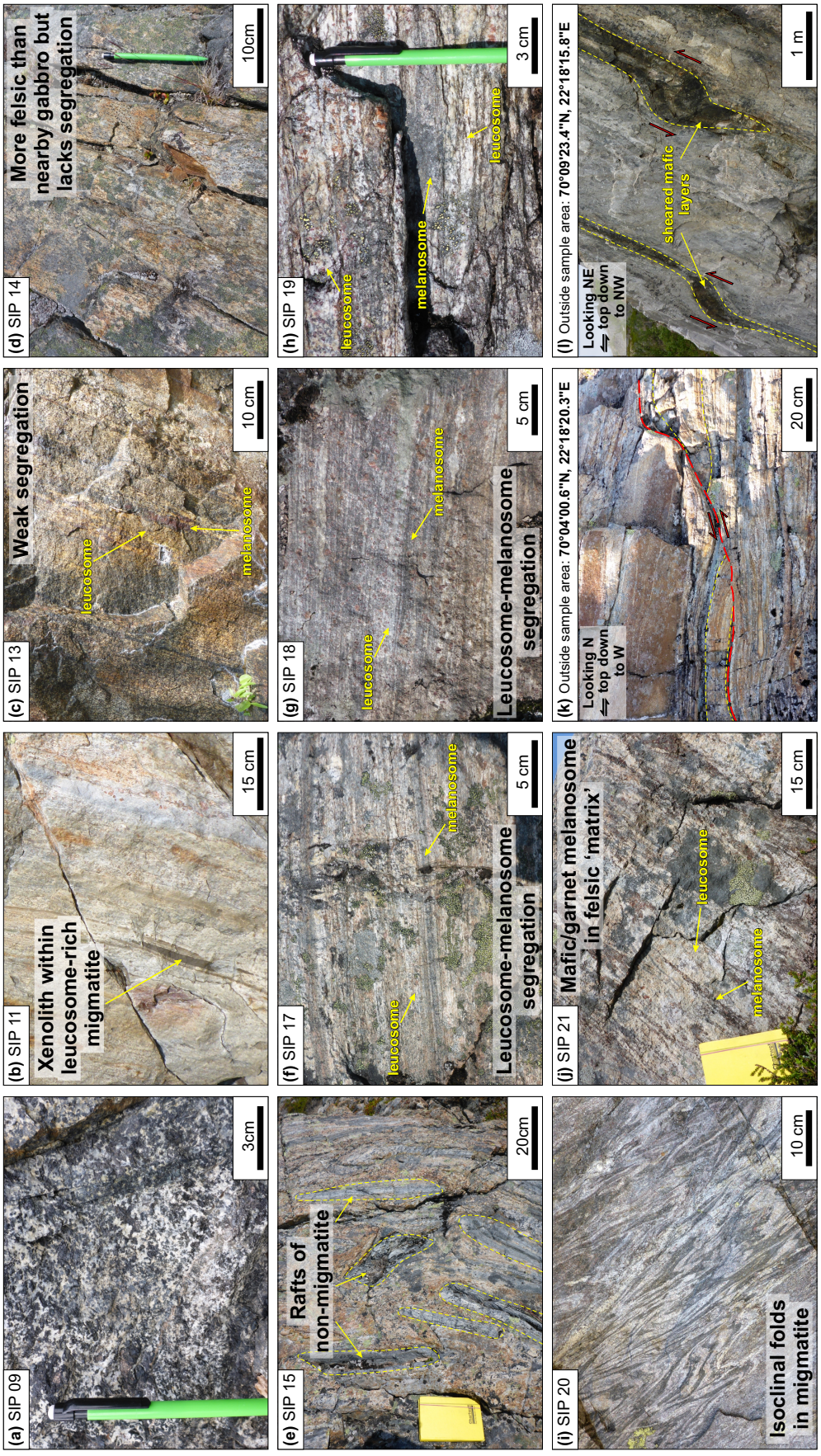

Figure 3.2: Outcrop photographs showing the transition from gabbro to migmatized paragneiss. Full caption opposite.

3.2 Field observations

Approximately 5 km from the shear zone boundary the gabbro has long 3 to 10 cm dendritic pyroxene crystals resembling a Harrisitic texture. Closer to the shear zone boundary (0.5 to 1 km away) the gabbro lacks the Harrisitic texture, the grain size is smaller (up to 1 cm) and it is weakly foliated. The boundary of the gabbro and paragneiss ØSZ is not distinct. There is a transition from gabbro to paragneiss 'pods' hosted in gabbro to paragneiss ØSZ where the dominant lithology is foliated gabbro. The paragneiss 'pods' are also foliated, showing stromatic layering with clear mineral segregation. However, this transition is not a simple linear increase of migmatized paragneiss compared to gabbro. Figure 3.2 shows representative outcrop photographs through this transition and into the centre of the ØSZ. Sample SIP09 is a gabbro in which the foliation is indistinct (Figure 3.2a); it marks the edge of the transition zone from where paragneiss is present. Figure 3.2 b-d show an example of the paragneiss texture where it is surrounded by gabbro. These zones are typically up to 10 to 50 m in size, although they are more common closer to the main ØSZ. The paragneiss pods are isolated and do not exhibit connectivity in the field. The paragneiss exhibits a N-S trending gneissic to mylonitic foliation with a stretching lineation plunging moderately towards the NW. This foliation is parallel to the primary magmatic layering preserved in some areas of the gabbro (Elvevold et al., 1994, Roberts et al., 2006) but more prominent here due to the strain imposed by the shear zone.

Within the ØSZ the rocks have a higher felsic content within a garnet-granulite mineral assemblage. Figure 3.2 e-l show typical outcrop exposures observed in the ØSZ. From the field it is difficult to determine exact areas of melt within the paragneiss, but the presence of a high temperature mineral assemblage, more than one type of migmatite texture, and larger 'pools' of leucosome allow us to infer that the system was melt bearing. The paragneiss typically displays stromatic migmatite textures, with layering observed on a variety of scales (Figure 3.2 f-k). The stromatic layering of the migmatite shows the segregation of the leucosome (felsic) and melanosome (mafic) stroma of various thicknesses from the millimetre to decimetre scale. SIP15, located just

inside the ØSZ boundary, is a schollen-type migmatite where rafts of non-migmatized restite remain intact and the leucosome flows around the rafts (Figure 3.2e). The centre of the paragneiss ØSZ has linear stroma, although in some places tight parasitic folds deform the stromatic migmatite. Layer thickness remains constant in most folded migmatites (Figure 3.2i), but in some localities the leucosome varies in thickness and the fold hinges in the restite have thickened to form similar folds. Where present, kinematic indicators in the paragneiss show normal offset shearing top down to both east and west. However, top down to the west is more common and suggests oblique sinistral-normal faulting of the shear zone (Figure 3.2 k-l).

Macroscale leucosome content is determined via image analysis of outcrop photographs (ImageJ; Schneider et al., 2012). Photographs were simplified with filters to correct for shadows, cracks or vegetation on the outcrop, helping to constrain leucosome vs. restite proportions. Examples of the digitised outcrop drawings are shown in Figure 3.5a with the leucosome and melt volumes from the ØSZ transect (Figure 3.5c). The leucosome content in the Øksfjord area varies from 0 to 90%. However, this does not mean up to 90% of the crust was melt, as the leucosome fraction does not necessarily equal the melt fraction. It is necessary to use microstructures to distinguish if the leucosome formed from melting or solid-state deformation and recrystallisation processes (Figure 3.5b).

3.3 Microstructural analysis

As some of the leucosome can segregate through solid state processes as opposed to melting, it is important to consider the microstructure to understand melting processes and volumes. Melting occurred by biotite dehydration, where K-feldspar, garnet and melt are products of the reaction (bt + qz + pl + sil = melt + gt + kf; Figure 3.3; Spear et al., 1999, Menegon et al., 2011). The melt predominantly crystallises as K-feldspar, plagioclase and ilmenite (Figure 3.3).

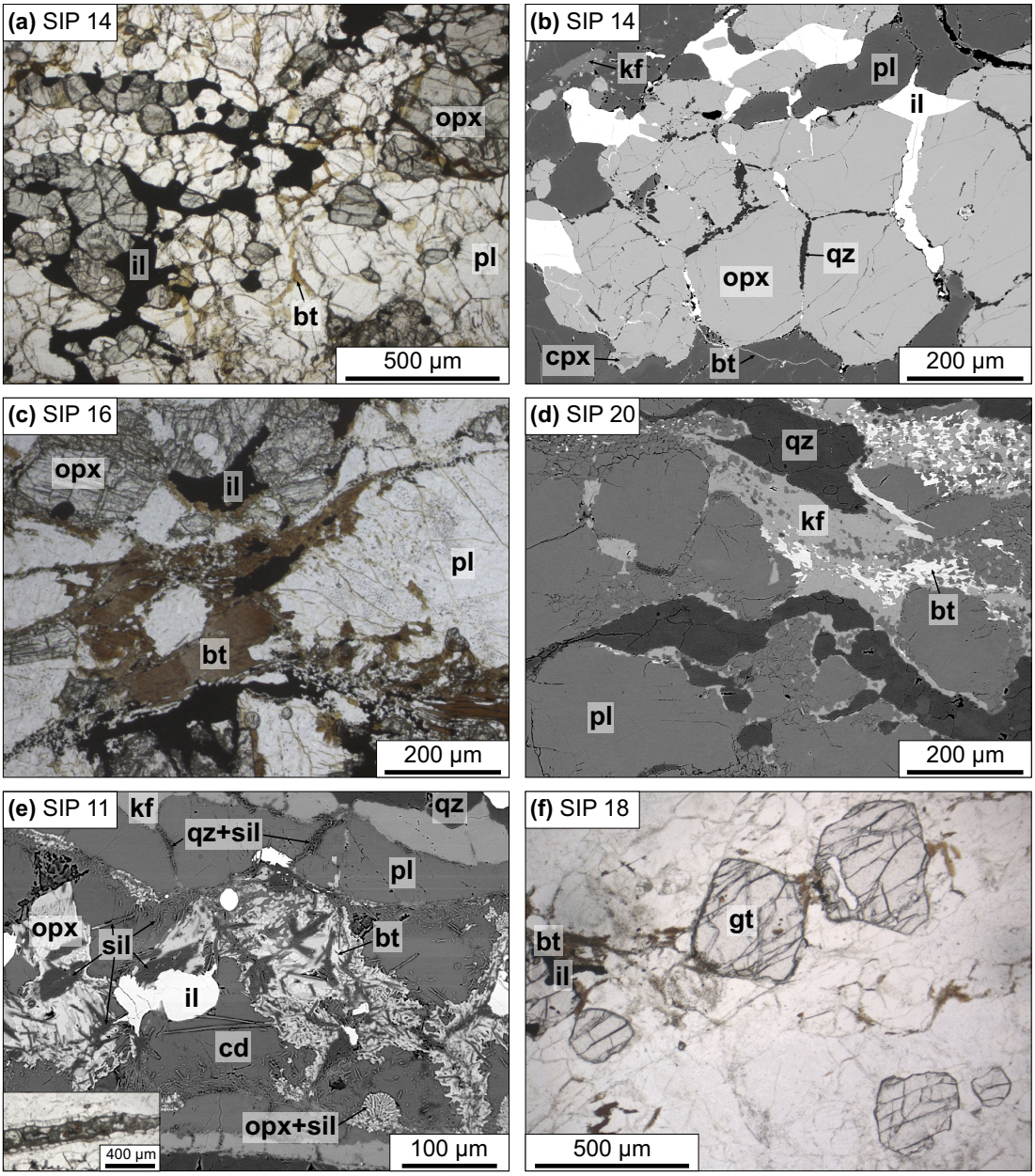

Figure 3.3: Melt textures from the ØSZ from thin section photomicrographs (a, c, g) and backscattered electron images (b, d, e). (a-b) Cuspate and interstitial ilmenite, il, melt. (c-d) Biotite, bt, breakdown to K-feldspar, kf, and plagioclase, pl, forming melt at grain boundaries of quartz, qz, and plagioclase. (e) Melt zone within paragneiss, complex textures of orthopyroxene, opx, sillimanite, sil, cordierite, cd, and ilmenite. (f) Peritectic garnets, gt, produced during biotite dehydration melting reactions.

3.3.1 Melt and leucosome quantification

Grain boundary melt is very common in the ØSZ samples and is generally composed of K-feldspar, plagioclase and ilmenite (Figure 3.3). Reaction textures of plagioclase and biotite are observed to breakdown to form K-feldspar, with ilmenite infilling nearby pore space (Figure 3.3). Figure 3.3b shows fine grained quartz crystallised between orthopyroxene grains. This sample is located in the transition zone, outside the shear zone, and suggests that quartz is a product of melting in this area in addition to K-feldspar, plagioclase and ilmenite. Figures 3.3c and d shows areas between plagioclase grains are filled with fine grained K-feldspar and biotite. These textures could be evidence of 'back reaction' of the melting reaction, melt may have occupied this area and upon crystallisation the biotite-dehydration melting reaction reversed producing the fine grained infill.

In addition to grain boundary melting, 'melt zones' are also observed in SIP11 located outside the main shear zone. Complex melt-rock interaction textures are observed where cordierite and orthopyroxene are replaced by biotite, sillimanite and ilmenite (Figure 3.3e). Orthopyroxene is a major phase in samples located in the transition zone from gabbro to paragneiss; within the shear zone it is either not present or a minor phase. The lack of orthopyroxene within the paragneiss shear zone suggests the transition area may be of a different composition and/or origin to the shear zone.

The melt-solid-solid dihedral angle in the paragneiss ranges from 4° to 85° with a median of 26°, mean of 29° and standard deviation of 17° (Figure 3.4; method after Holness et al., 2005). When the low dihedral angle is considered alongside the abundant presence of grain boundary melt films, it appears that melt connectivity was high in the ØSZ. The solid-solid-solid dihedral angles from ØSZ paragneisses are not in solid-state equilibrium as grain boundary dihedral angles vary from 49° to 179° with a median of 110°, mean of 109° and standard deviation of 31° (Figure 3.4). The large range of dihedral angles is the result of deformation microstructures forming sutured grain boundaries.

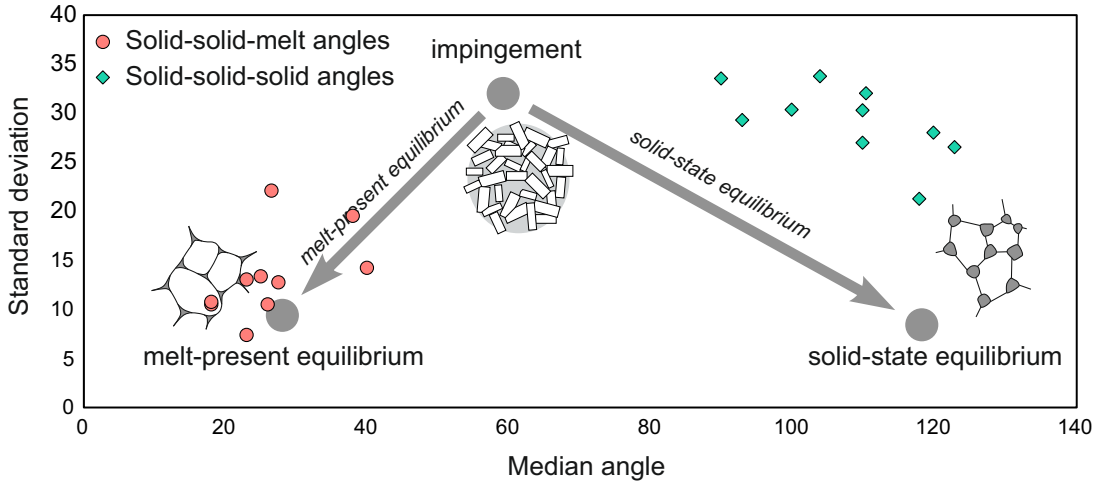

Figure 3.4: Dihedral angles from the ØSZ paragneiss samples for solid-solid-melt boundaries (○) and solid-solid-solid boundaries (◇). Also shown is a schematic diagram showing end-member solid-solid-melt dihedral angle populations (Adapted from Holness et al., 2005).

When considering the rheology and effect of strain localisation in melt present systems, it is important to understand the palaeomelt volume. At the field and outcrop scale the felsic portions of the rock are used to determine the leucosome content. The macroscale leucosome content is determined via image analysis of outcrop photographs (ImageJ; Schneider et al., 2012). Photographs were simplified with filters to correct for shadows, cracks or vegetation on the outcrop, helping to constrain leucosome vs. restite proportions. Examples of the digitised outcrop drawings are shown in Figure 3.5a with the leucosome and melt volumes from the ØSZ transect (Figure 3.5c). The leucosome content in the Øksfjord area varies from 0 to 50%. However, this does not mean up to 50% of the crust was melt, as the leucosome fraction does not necessarily equal the melt fraction.

It is necessary to use microstructures to distinguish if the leucosome formed from melting or solid-state deformation and recrystallisation processes (Figure 3.5b). Microscale melt determination is qualitative as I use microstructures indicative of melt or the former presence of melt (Figures 3.3, 3.5b). With the use of ImageJ I am able to isolate the melt and solid fractions of the rock. Plain polarised light and cross polarised light photomicrographs with and without gypsum plate are used to construct the melt-solid interpretations. Crystallised melt volume is calculated from microstructural and image analysis (Figure 3.5c). The quantification is for the melt

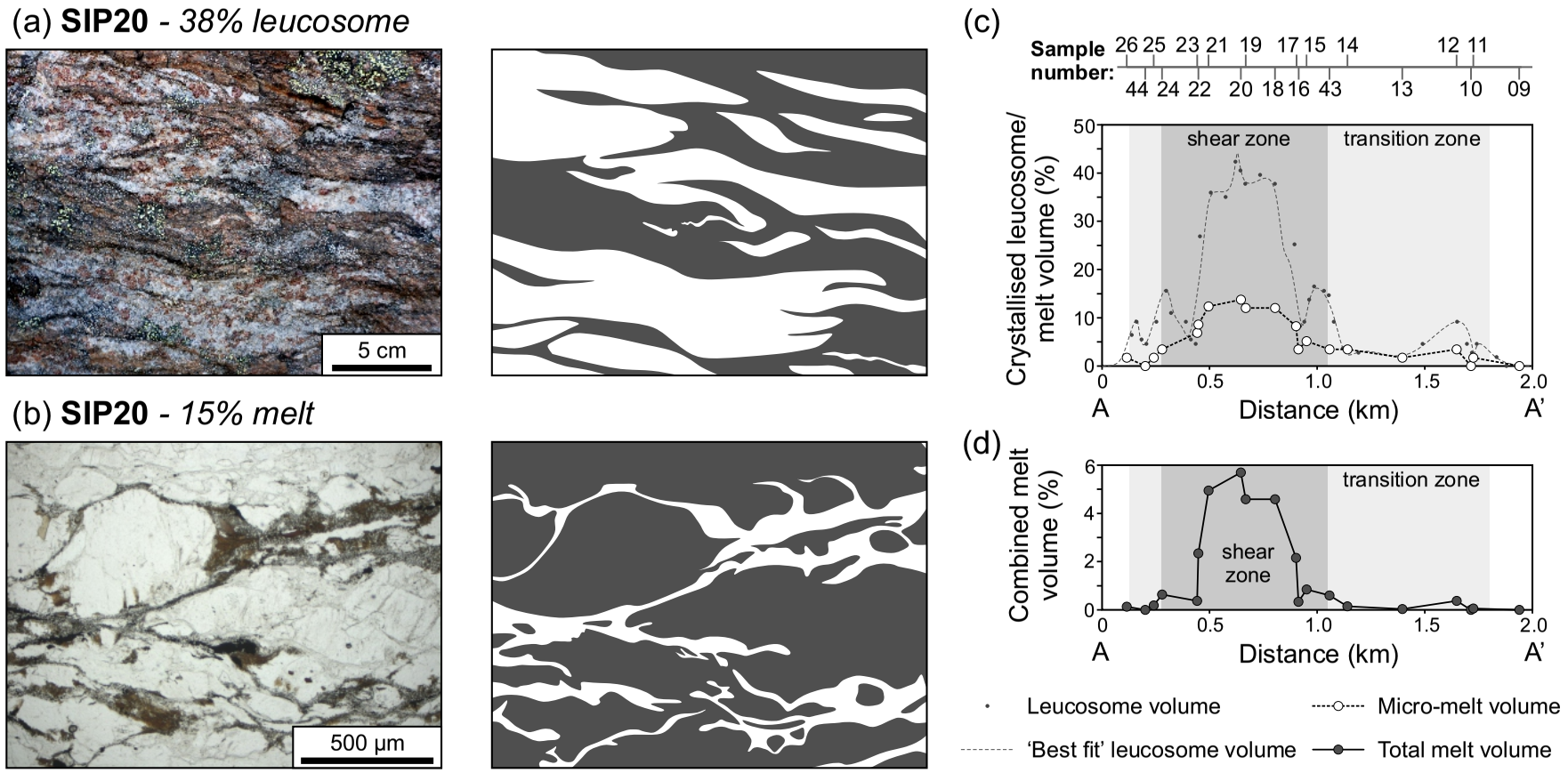

Figure 3.5: Image analysis of field and microstructures to calculate leucosome and crystallised melt volume. (a) Leucosome (white) vs. solid (grey) image analysis interpretations of an example field photograph and (b) melt (white) vs. solid (grey) image analysis interpretations of photomicrograph. Plots of (c) field leucosome and microscale crystallised melt volume across the ØSZ and (d) total melt volume when the leucosome and micro-melt volumes are combined.

textures that remain in the microstructure; therefore, it could be an underestimate if significant melt loss/escape has occurred or overestimated if melt crystallised in the shear zone during multiple melt fluxes.

The total melt volume in figure 3.5d is calculated by attributing the micro-melt volume to the leucosome portion of the rock. For example, SIP20 has 15% melt in its microstructure and 38% leucosome at outcrop, this results in a 5.7% total melt volume as only 15% of the leucosome is comprised of melt. Preserved melt textures suggest a peak crystallised melt volume for SIP20 of <15% and 10-15% for nearby samples SIP 18, 19, 21 and 23. Towards the edges of the shear zone melt textures are poorly preserved where <5% crystallised melt is observed for samples SIP 16, 17, 24 and 43.

Quartz is not a major product of melt within the shear zone (e.g. Figures 3.3 c-e), therefore it is inferred that quartz preserves a deformation history from the ØSZ. During melting, strain localises into the melt, but if shearing is also active after crystallisation, the peritectic phases may show evidence of deformation and melt textures may be destroyed.

3.3.2 Shear zone centre

In the centre of the shear zone, quartz is present as large grains with grain boundaries in disequilibirum. Euhedral garnet grains, 200 to 500 μm in size, are preserved in the centre of the ØSZ (Figure 3.3f) suggesting it is a peritectic product of biotite dehydration melting.

Towards the centre of the ØSZ it is typical to observe chessboard subgrain extinction in large quartz grains (>800 μm; Figure 3.6b), often accompanied by an undulose extinction overprint. Where the grain size is smaller (50-200 μm; Figure 3.6 a-b), quartz exhibits a lobate microstructure with serrated grain boundaries typical of grain boundary migration (GBM) microstructures. Here, rapid grain boundary mobility is favoured by high temperatures, sweeping through grains and removing dislocations (Guillope and Poirier, 1979, Urai et al., 1986, Hirth and Tullis, 1992, Stipp et al., 2002). Figure 3.6a shows a central band where there is evidence for melt reactions in the pressure shadows of plagioclase. This 'melt zone' is

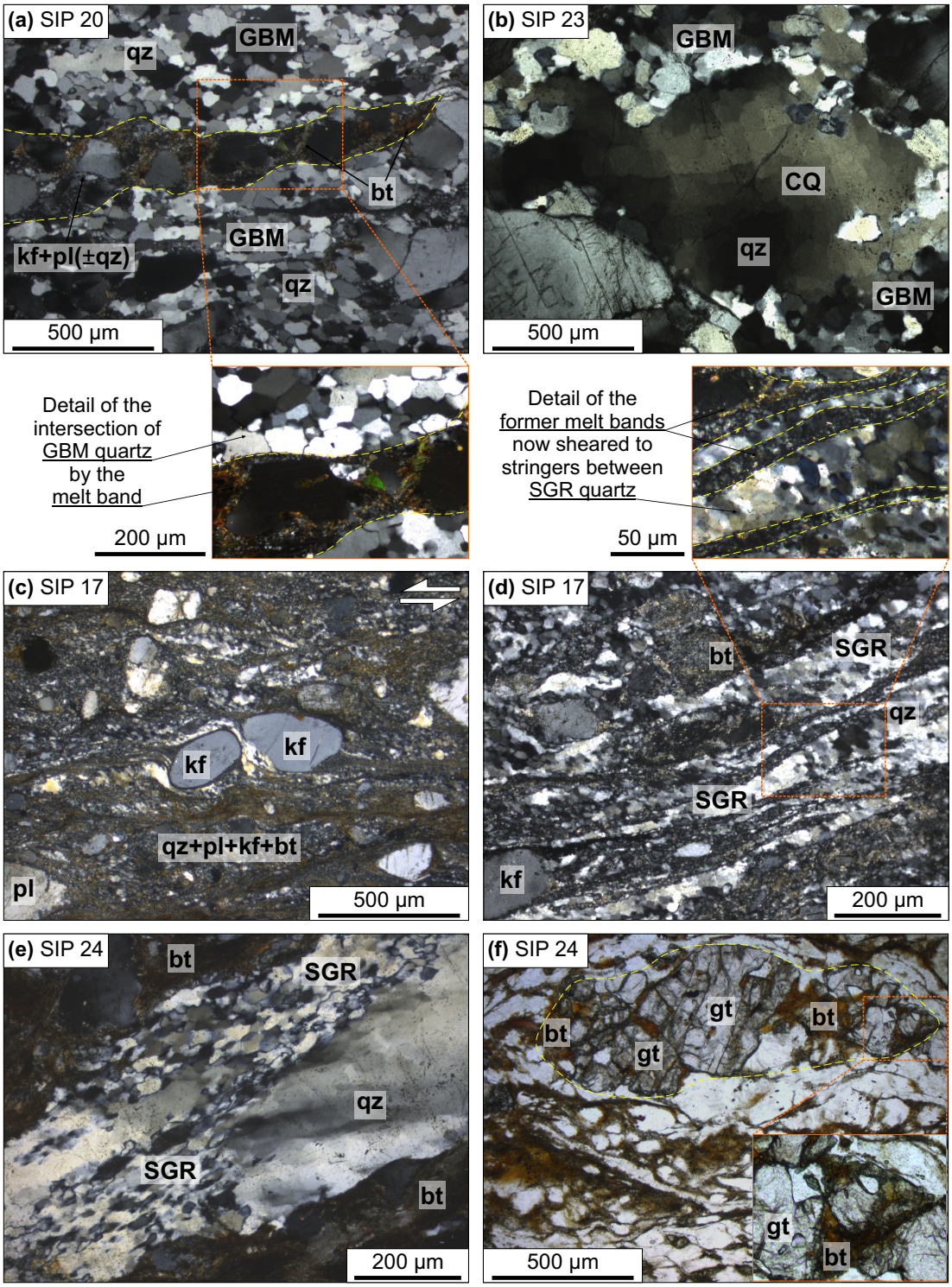

Figure 3.6: Thin section photomicrographs of deformation microstructures from the ØSZ. (a) Lobate/serrated grain boundaries of quartz recrystallising by GBM cut by a K-feldspar, plagioclase and biotite melt band highlighted in yellow, inset shows detail of the intersecting relationship. (b) Large quartz grain showing chessboard extinction (CQ) with an undulose extinction overprint, smaller grains at edge recrystallised by GBM. (c) Sigmoidal feldspar clasts with sinistral sense of shear. (d) Recrystallisation of quartz ribbons and grains by SGR, stringers of biotite, K-feldspar and plagioclase represent former melt bands as observed in (a) but here they are deformed into stringers. (e) Large quartz grain recrystallising by SGR. (f) Fragmented garnet grain breaking down to quartz, feldspars and biotite with detail inset.

cutting quartz zones exhibiting GBM-type recrystallisation. The quartz-plagioclase grain boundaries are straight and preservation of melt next to deformation microstructures suggests the GBM quartz deformation pre-dates melting. The presence of chessboard extinction and GBM suggests the quartz deformed at high temperatures and mid to low stresses (Kruhl, 1996). The undulose extinction overprint suggests minor retrograde deformation at lower temperatures (Figure 3.6b).

3.3.3 Shear zone edges

Grain size decreases towards the edges of the ØSZ (10-80 μm). Here, quartz grains have broken down to subgrains and dynamically recrystallised neoblasts; characteristic of subgrain rotation (SGR) recrystallisation where additional dislocations allow the rotation of subgrains to develop new grains (Figure 3.6 d-e Hirth and Tullis, 1992, Stipp et al., 2002). Figure 3.6a shows evidence of a non-deformation textural relationships between melt and the deformed quartz; in contrast, Figure 3.6 c-d shows that the melt reacting phases (fine grained biotite and k-feldspar) have been sheared and entrained during the formation of the SGR quartz ribbons and shearing of larger sigmoidal K-feldspar clasts. This suggests deformation of quartz at the edges of the ØSZ was active at lower temperatures and higher stresses than the centre of the ØSZ (Hirth and Tullis, 1992, Stipp et al., 2002). Post-crystallisation deformation lead to poor preservation of melt textures in quartz dominant zones. Large K-feldspar grains in these samples are winged mantled σ-type clasts with a sinistral sense of shear. A peritectic texture is expected to be produced from melting but the peritectic phases are deformed with grain mantles at the edges of the shear zone suggesting post-melt deformation.

Garnet grains towards the edges of the ØSZ are 50 to 200 μm with irregular grain shapes. They are breaking down to quartz, K-feldspar, plagioclase and biotite, showing evidence of retrogresion (Figure 3.6f). Deformation at the edges of the ØSZ is likely to have occurred post melting as melt microstructures are not preserved and peritectic phases are deformed.

3.3.4 Crystallographic preferred orientations

The crystallographic preferred orientations (CPO) for quartz-bearing samples within the ØSZ were analysed on the EBSD system at the University of Leeds (see Section 2.5.2 for operating conditions). All samples were run with a 5 μm step size, the maximum step size is constrained by the minimum grain size (20 μm), using the same step size ensures consistency when calculating grain and subgrain relationships.

Figure 3.7 shows the quartz pole figures for ten samples from within the ØSZ. Samples SIP 16, 17, 24 and 43 show similar CPOs with an X-Y girdle in <a> and a maximum at Z in [c]. There is a slight asymmetry, especially in SIP17 where the [c] maxima suggests a sinistral shear component, compatible with field evidence. The CPO in these samples suggests deformation by basal <a> slip (e.g. Law et al., 1990). Samples SIP 20 and 19 in the centre of the ØSZ have a [c] maxima parallel to the Y direction, compatible with prism <a> slip in quartz (e.g. Law et al., 1990). Samples between edges and centre of the ØSZ (SIP 18, 21, 22) have weak CPO's with diffuse poles at Z in [c]. When the weak CPO is considered against their geographic position in the ØSZ, it is suggested that the crystal fabric represents an evolution through fabric overprinting from prism <a> slip in the centre and basal <a> slip at the edges (especially samples SIP18 and 21). SIP15, located at the edge of the ØSZ, is anomalous and shows a similar CPO to SIP20. This sample has large quartz grains with chessboard extinction and GBM in the smaller grains; it also correlates to a secondary peak in leucosome/melt fraction.

3.4 Stress and strain rate estimates

Deformation mechanisms and CPO analysis provide qualitative data for stress and strain, whilst palaeopiezometery allows quantification of differential stress from grain size (e.g. Twiss, 1977, Ord and Christie, 1984, Stipp and Tullis, 2003, Cross et al., 2017). Therefore, it is possible to estimate strain rate via flow laws (e.g. Luan and Paterson, 1992, Gleason and Tullis, 1995, Hirth et al., 2001). Generally, the smaller the recrystallised grain size, the higher the differential stress. However, in a melt

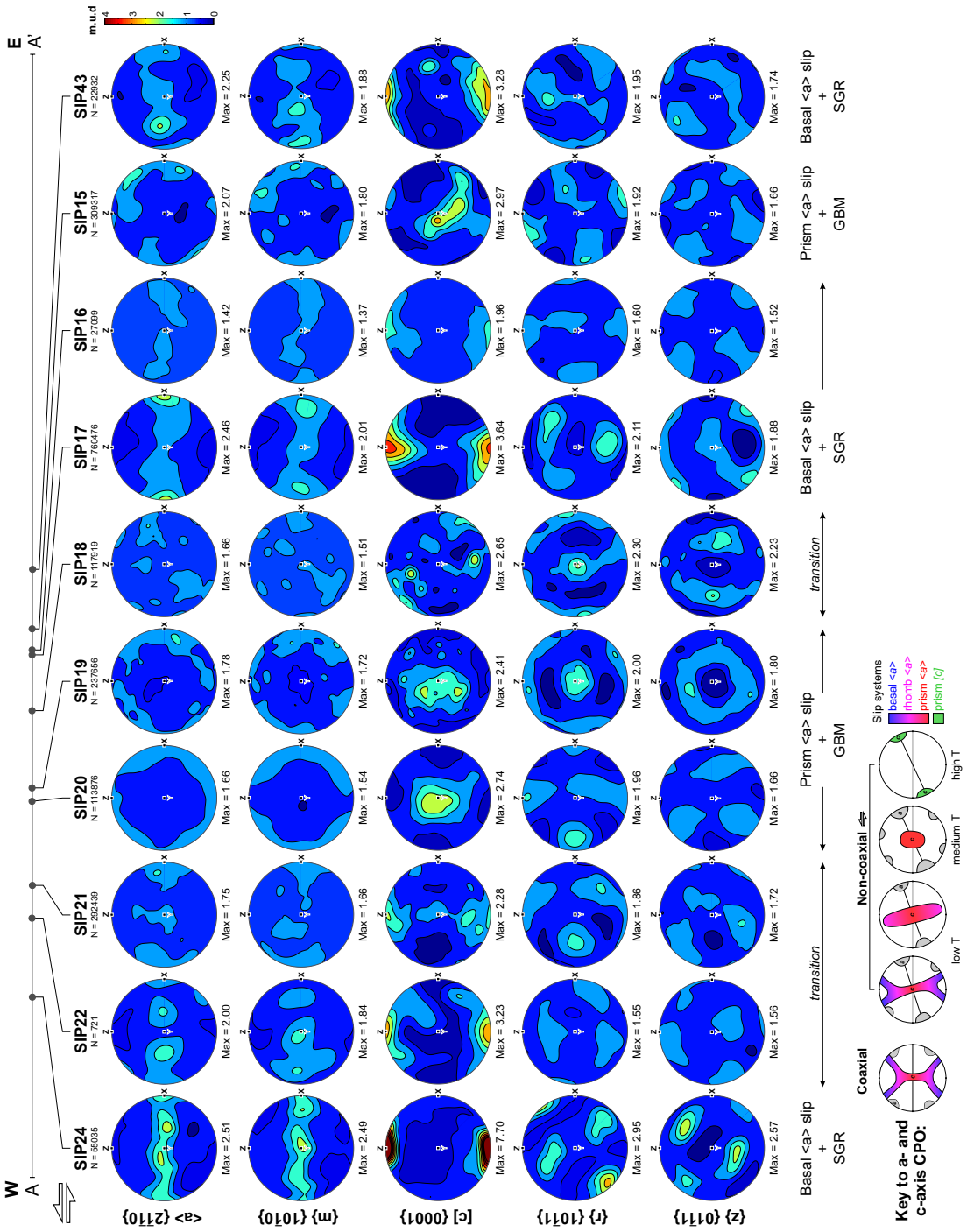

Figure 3.7: CPO pole figures for 10 quartz-bearing samples within the ØSZ. Location on section line A-A' is shown above the pole figures and active slip systems and deformation mechanisms are shown below. Beneath the ØSZ CPO is a key to the a- and c-axis CPO development and active slip systems showing temperature dependent CPO development of <a> (grey) and [c] (coloured maxima) during coaxial and non-coaxial dextral shearing (Modified from Passchier and Trouw, 2005, Parsons et al., 2016).

present system, grains crystallising from the melt are typically larger than grains of the same mineral deformed in solid state. Thus, palaeopiezometers can only be used to quantify deformation post-melting. The results shown here give the relative change in magnitude of stress and strain rate across the ØSZ.

The centre of the shear zone has the highest palaeomelt content, which is problematic for calculation of stress from grain size. At the edges of the shear zone, my interpretation is that SGR deformation and basal <a> slip were active post-crystallisation. Therefore, it is appropriate to apply a palaeopiezometer here. The centre of the shear zone preserved pre-melt deformation of the shear zone and the edges preserve evidence for post-melt deformation, thus the palaeopiezometer will give an estimate of stress pre- and post-melting. The recrystallised grain size is calculated from EBSD data via the grain orientation spread technique after Cross et al. (2017), whereby recrystallised and relict grains are isolated to find the recrystallised grain size

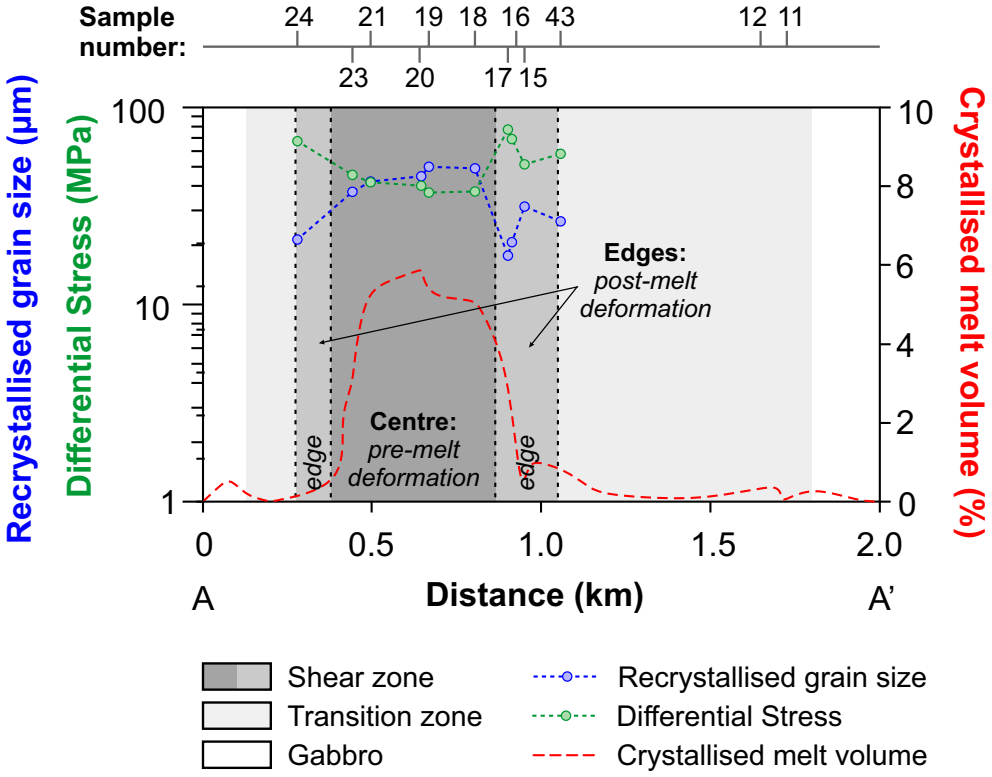

Figure 3.8: Recrystallised grain size and palaeopiezometer for quartz bearing samples from the ØSZ. Recrystallised grain size (blue) calculated from EBSD data using GOS; palaeopiezometer (green) relationship after Cross et al. (2017); and melt volume (red) from Figure 3.5 is shown for reference.

(Figure 3.8). The Cross et al. (2017) piezometer relationship is applied to calculate the differential stress (σ_{1-3}) from recrystallised grain size (D) for quartz bearing samples in the ØSZ,

$$D = 10^{3.91\pm0.51}\sigma_{1-3}^{-1.41\pm0.21}. \tag{3.1}$$

Figure 3.8 shows the variation in recrystallised grain size across the ØSZ. The grain size relationship loosely follows the melt volume trend; both increase towards the centre of the shear zone (e.g. root mean squared recrystallised grain size in the centre is 48.2 ± 7.6 μm, SIP 19, 20, and drops to 21.6 ± 10.2 μm at the edges, SIP 16, 17, 24, 43). The grain size relationship corresponds to samples where GBM is dominant (large, centre) and samples where SGR is active (small, edges).

The palaeopiezometer is applied to the root mean squared recrystallised grain sizes to calculate the differential stresses (Figure 3.8; results are also shown in Table B.1 in the Appendices). The differential stress in the centre of the shear zone is 38 ± 4.3 MPa (SIP 15, 19, 20), increases to 41 ± 11.5 MPa with the evolving quartz fabric (transition from prism <a> to basal <a> slip; SIP 18, 21, 22) and further increases to 68 ± 17 MPa for the shear zone edges (SIP 16, 17, 24, 43). The differential stress variation within the shear zone therefore suggests faster strain rates at the edges of the shear zone and slower strain rates in the centre.

The rheological behaviour of rocks is expressed through flow laws (Poirier, 1985, Hirth et al., 2001). Flow laws describe the dependence of strain rate on parameters such as stress and temperature. In this chapter I apply the quartz power-law flow law for dislocation creep (see Section 2.3.3; Tokle et al., 2019) to understand any relative changes in magnitude of strain rate,

$$\dot{\varepsilon} = A\sigma_{1-3}^{n} f_{\mathrm{H_2O}}^{r} e^{\frac{-Q}{RT}}, \tag{3.2}$$

where $\dot{\varepsilon}$ is strain rate, σ_{1-3} is differential stress, n is the stress exponent, $f_{\mathrm{H_2O}}$ is the water fugacity, r is the water fugacity exponent, Q is the activation enthalpy, R is the ideal gas constant, T is absolute temperature, and A is a material parameter. The

dislocation creep flow law is a combined flow law of a power-law stress exponent and a low temperature/high stress exponent that are summed to give a strain rate accounting for both exponents. The flow law parameters for a power-law stress exponent of $n = 4$ are: $Q = 125$ kJ/mol, $r = 1$, $f_{H_2O} = 200$ MPa, and $A = 1.75{\times}10^{-12}$ MPa^{-n}; and parameters for low temperature/high stress data with a stress exponent of $n = 3$ are: $Q = 115$ kJ/mol, $r = 1.2$, $f_{H_2O} = 50$ MPa, and $A = 1.1{\times}10^{-12}$ MPa^{-n}/s. If the quartz power-law flow law for dislocation creep is applied to the calculated stresses, it yields strain rates of 4.6×10^{-12}, 3.7×10^{-12} and 2.8×10^{-11} for the ØSZ centre, transitioning fabric and edges respectively.

These estimates do not represent the true deformation conditions of the ØSZ, as they only account for the quartz deformation. Quartz deformation is important, Menegon et al. (2011) postulated that the quartz formed a load-bearing framework in these migmatitic gneisses, controlling the behaviour of the lower crust. This indicates that the post-melt deformation of the shear zone edges deformed at a magnitude faster strain rate than the shear zone centre deformed pre-melting.

3.5 Discussion

The ØSZ is a high strain deformation zone of migmatized paragneiss, which transitions to foliated gabbro with pockets of paragneiss to foliated gabbro with no evidence for partial melting. It is part of a series of thin ductile paragneiss shear zones within the gabbro that formed by synintrusive deep crustal shearing during lithospheric extension (Elvevold et al., 1994, Roberts et al., 2006). The paragneiss is strongly sheared and kinematic indicators suggest oblique sinistral-normal faulting, supporting the extensional rifting model for the SIP (Reginiussen et al., 1995). The pockets of paragneiss in the gabbro are richer in orthopyroxene than samples in the main shear zone, suggesting a different protolith. During the percolation of melt through the system, it is possible that the melt infiltrated into the gabbro wall rock and the paragneiss pods could be the result of metasomatism of the gabbro. The melt zones in SIP11 show complex melt-rock interaction textures not observed in samples

within the shear zone. The presence of sillimanite and cordierite suggest an Al-rich fluid fluxed through these rocks to allow replacement of the gabbro.

Typically palaeo shear zones have a grain size distribution of coarse grains at the edges and fine grains in the centre where the strain was higher (Figure 3.9a; Ramsay and Graham, 1970, White, 1979, Olgaard and Evans, 1988). In the ØSZ the reverse is the case, with large grains in the centre and small grains at the edges (Figure 3.8). The normal grain size distribution is only observed in melt-free areas. Therefore, it seems that the inverse grain size distribution in the ØSZ is the result of the influence of melt in the system. Grain growth is promoted from the high temperatures and transport of melt through the system, which can occur in two ways: static recrystallisation outpacing active recrystallisation (Evans et al., 2001), or crystallisation of grains directly from melt where crystallisation rate outpaces strain rate (Jurewicz and Watson, 1985). In the ØSZ it is likely that both processes were active, resulting in grain growth of solid and peritectic phases. The melt textures present indicate up to 15% melt crystallised in-situ in the centre of the system, decreasing in volume through to the edges of the ØSZ and within the transition zone. This does not suggest 15% melt was present at any one time but does suggest melt may have pooled and crystallised if unable to escape the system. Higher melt volumes may have been present at the shear zone edges but it may have been transported to the centre or completely escaped the shear zone. As a result of the enhanced melt presence, grain growth is greater in the centre of the ØSZ.

Menegon et al. (2011) suggested 5-7% melt was located in isolated pockets and did not control the mechanical strength of the ØSZ. However, in the shear zone samples studied here, located ∼10 km south of those sampled by Menegon et al. (2011), melt has low dihedral angles and forms grain boundary melt films forming an interconnected melt framework. An interconnected melt network would result in mechanical weakening during melting and cause a dramatic strength decrease if 5-7% melt was present at any time (Figure 3.9b; Rosenberg and Handy, 2005, Llorens et al., 2019). Degli Alessandrini et al. (2017) analysed dry mafic dykes from the same area as Menegon et al. (2011); they suggest that melt-induced chemical reactions may be a common feature in the lower crust and responsible for weakening dry, strong mafic rocks. As a result melt-assisted

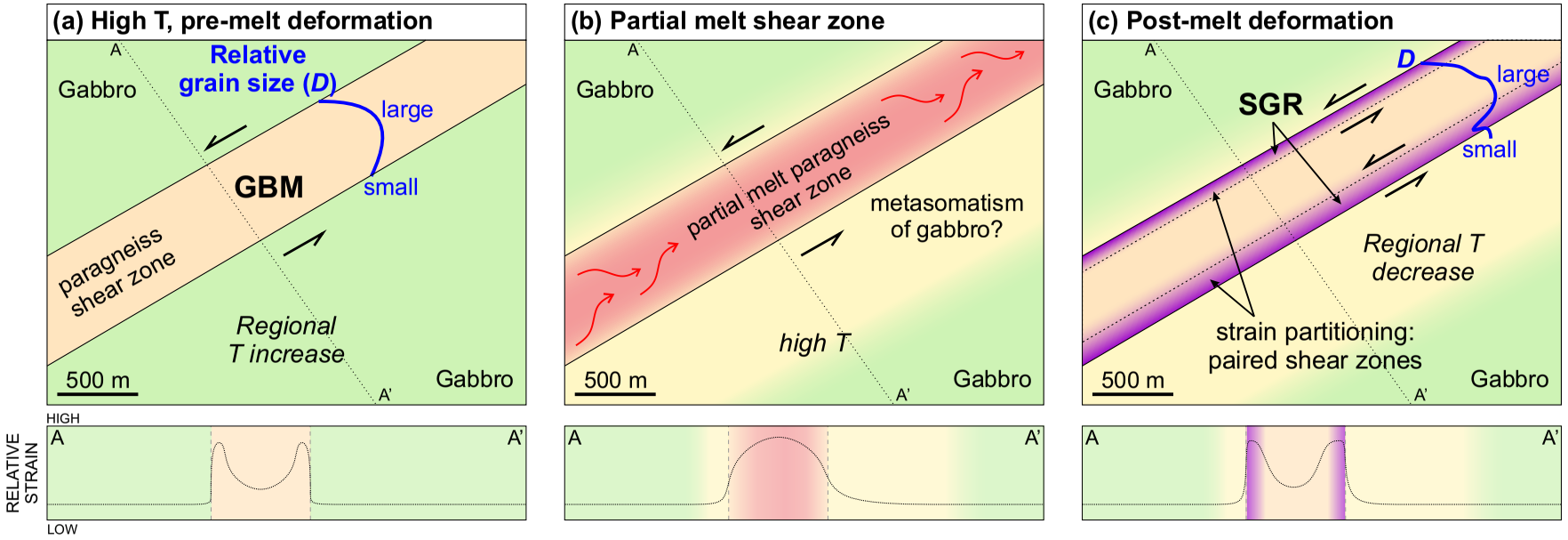

Figure 3.9: Schematic diagrams of pre-, syn-, and post-melt shear zones to the ØSZ, relative strain rate is shown beneath each schematic. (a) A 'typical' non-melt shear zone will have a recrystallised grain size (D) distribution of large grains at the edges and small grains in the centre where stress and strain rate is greatest, but if it is deforming at high temperatures and GBM is the active deformation mechanism, deformation will result in solid state, static grain growth. Relative strain: low in centre, high at edges. (b) Syn-melt deformation in the ØSZ; higher melt volume towards shear zone centre promotes a grain size increase in crystallisation of peritectic phases, at this stage solid phases do not deform as melt localises the strain. Relative strain: high in centre, low at edges. (c) Crystallisation of shear zone and post-melt deformation; upon regional temperature decrease the shear zone crystallises forming a 'strong' centre, pre-melt GBM deformation and melt-induced grain growth produces a grain size distribution from small to large from edges to centre. Post-melt deformation results in a partitioning of strain to shear zone edges where grain size is smaller, the deformation forms a set of paired shear zones deforming by SGR at lower temperature and higher stress, overprinting evidence for melting at shear zone edges. Relative strain: low in centre, high at edges.

deformation in the lower crust is likely to have a dramatic effect on the strength of dry, strong mafic rocks.

From microstructural and CPO analysis, there were two deformation phases active in the ØSZ; (1) high-temperature deformation (GBM and prism <a> slip) observed in the centre of the shear zone; and (2) mid-temperature deformation (SGR and basal <a> slip) observed at the edges. The slip systems and deformation mechanisms responsible for the recorded CPOs and microstructure in the ØSZ are likely to have been active at different times as a sharp temperature gradient over the narrow shear zone is unlikely. This is supported by evidence of deformation microstructures overprinting melt microstructures at the edges of the ØSZ (Figures 3.6d, 3.9c), suggesting the edges deformed later than the centre.

During prograde metamorphism before melting, quartz begins to deform by GBM and prism <a> slip (Figure 3.9a). Experiments suggest GBM and prism <a> slip is favoured by high temperature and low stress deformation (Nachlas and Hirth, 2015, Richter et al., 2016). Partial melting in the ØSZ occurred at high temperatures (760-820°C; Menegon et al., 2011) and during this evolution phase, stress was absorbed by the melt (Figure 3.9b). Percolation of partial melt through the shear zone resulted in an overprinting of the GBM deformation microstructure by melt textures (Figure 3.9b).

Upon crystallisation of the system and subsequent cooling, there is no melt to localise strain (Brown, 2001b, 2007, Yakymchuk and Brown, 2014). Where melt crystallises, the rock is strengthened as pre-existing dislocations will have been removed during the recovery process of GBM recrystallisation, as well as the relative grain size increase during crystallisation (Walte et al., 2003, 2005, Otani and Wallis, 2006). Subsequent post-melt deformation is localised to the finer-grained edges of the ØSZ as it is easier to deform finer grains by diffusion-accommodated grain boundary sliding and diffusion creep than coarser grains (Figure 3.9c; Karato et al., 1986, Nixon et al., 1992). This produces the SGR microstructures and basal <a> slip CPO observed at the ØSZ edges where deformation occurs at lower temperatures and higher stresses than GBM.

Microstructural evidence from the ØSZ shows evidence for different deformation

conditions. The first phase was active pre-melt, deforming at high temperatures. This was followed by syn-melt deformation of the shear zone causing a relative strength increase towards the shear zone centre upon crystallisation. The second phase nucleated two parallel shear zones at the edges of the larger ØSZ. There is a lack of evidence to determine if the post-melt deformation of the shear zone by SGR and basal <a> slip is part of the same deformation event or if it is related to a later deformation phase. If it is a later deformation phase it could be part of the Finnmarkian orogeny, an early Caledonian deformation phase. This would mean crystallised areas of partial melt are not 'dry and strong' if there are significant heterogeneities (e.g. grain size).

The 'flanking shear zones' from the post-melt deformation phase are similar to paired shear zones observed at the mm to cm scale in ductile mid to lower crust, such as the Neves area, Eastern Alps (Mancktelow and Pennacchioni, 2005, Pennacchioni

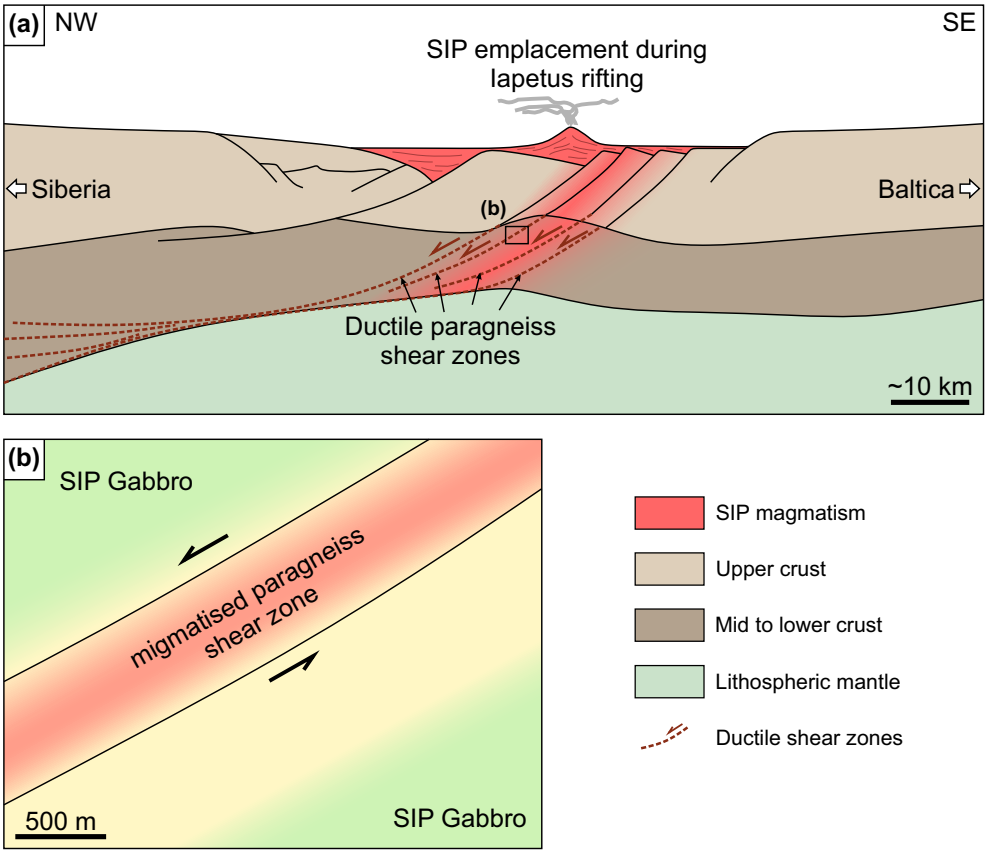

Figure 3.10: (a) Tectonic model for SIP emplacement and shear zone development adapted from models by Clerc et al. (2015), Abdelmalak et al. (2017), Kjøll et al. (2019). (b) The ØSZ represents a ductile shear zone within the middle to lower crust.

and Mancktelow, 2007) and Fiordland, New Zealand (Smith et al., 2015). The central syn-melt deformation zone of the ØSZ is 500m wide with 100 to 150m wide post-melt shear zones flanking the partial melt shear zone. The ØSZ is 4-5 orders of magnitude wider than those observed by Mancktelow and Pennacchioni (2005), Pennacchioni and Mancktelow (2007) and Smith et al. (2015). I suggest that the ØSZ is a large-scale manifestation of the same mechanisms where paired shear zones flank mm to cm scale strong heterogeneities in the rock. During syn-melt deformation, strain localised towards the centre of the ØSZ where the melt fraction was highest. Upon crystallisation and formation of the paired shear zones flanking the former syn-melt shear zone, strain partitioned to the edges.

The SIP represents a former rift zone where the paragneiss shear zones formed during synintrusive deep crustal shearing (Elvevold et al., 1994, Roberts et al., 2006). Evidence for these shear zones has been observed in present day rifted margins (e.g. Atlantic rifting; Clerc et al., 2015, 2018) as well as older, former Iapetus margins (e.g. Kjøll et al., 2019). When considering SIP emplacement alongside the shear zones it suggests the SIP was part of a magma-rich continental rift zone where the paragneiss formed ductile mid crustal shear zones as demonstrated in Figure 3.10. When this tectonic model is combined with U-Pb age data (∼565 Ma after Roberts et al., 2006) and the microstructural analysis from this study, it indicates the ØSZ partial melting occurred after emplacement of the SIP gabbro but was short-lived, with deformation contining post-melt to accommodate extension on the Baltica margin.

A summary of the geological events that lead to the formation and structure of the ØSZ are summarised below.

1. Eidvågeid gneiss is present in the lower crust of Baltica.

2. Iapetus rifting resulting in the break up of Baltica and Siberia and emplacement of the SIP (570-560 Ma Roberts et al., 2006). Synintrusive deep crustal shear zones form from the Eidvageid gneiss as gabbro of the SIP intrudes the Baltica lower crust.

3. Temperature increase due to gabbro emplacement results in microstructural

deformation of the shear zone gneiss. Deformation is preserved as GBM recrystallisation and chessboard subgrains in the quartz.

4. Temperature increases further and the gneiss starts to melt. In-situ melting of the gneiss through biotite dehydration melting results in growth of garnet and larger K-feldspar grains.

5. Melt crystallises predominantly as ilminite and K-feldspar, with plagioclase and biotite showing evidence of a 'back reaction' of the melt adjacent to K-feldspar grains.

6. Post-SIP regional temperature decreases but the shear zones continue to deform at the shear zone edges. Quartz records the deformation event through SGR recrystallisation and melt bands are sheared to form stringers.

3.6 Conclusions

Coexistence of deformation and melt microstructures suggests a complex geological history for the ØSZ. In contrast to conventional expectations for melt-free shear zones, a reverse grain size distribution is observed with finer grains at the shear zone edges and coarser grains in the centre. In addition, high-temperature, low stress deformation microstructures (GBM, prism <a> slip) are recognised in the shear zone centre, with mid-temperature, high stress deformation microstructures (SGR, basal <a> slip) at the shear zone edges.

I argue that strain localised towards the centre of the shear zone during a regional temperature increase, which ultimately led to partial melting. During the pre-melt phase, the shear zone deformed at high temperatures resulting in grain growth from GBM deformation. During partial melting, melt localised strain during this time and absorbed the majority of the stress. The percolation of melt and formation of melt textures dissect the pre-melt deformation and overprint some of these microstructures. The high temperatures and crystallisation from partial melt promoted further grain growth of already relatively coarse grained restite phases in the shear zone. Once all the

melt had crystallised and/or escaped from the system and the temperature decreased, the centre of the shear zone was 'strong' relative to the finer grained margins. As the temperature decreased further, and the stress absorbed by the solid phases increased, the finer grains proved easier to deform and hence strain partitioned to the shear zone boundaries forming the paired shear zones observed today. Unlike the partial melt shear zone described in the next chapter, where melt organisation and pinning of grain growth promotes grain size reduction, grain growth during crystallisation of the ØSZ centre transferred stress to shear zone edges to permit continued deformation and extension of the Baltica margin, suggesting syn-melt shear zones form significant heterogeneities to continue reduce the strength of the crust upon crystallisation.

Chapter 4

Melt organisation and strain partitioning in the lower crust

Nupen Peninsula, Western Gneiss Region, Norway

The second case study investigates how mylonite shear zones form in an area of distributed melt from the Western Gneiss Region (WGR), Norway. In contrast to the well-defined and comparatively wide ØSZ, the Nupen Peninsula hosts multiple narrow shear zones within a much larger partial melt regime, making it an ideal candidate to understand how melt self-organises to allow strain partitioning in the lower crust. This study has been published in the *Journal of Structural Geology* as Lee et al. (2018), thus most of the content of this chapter is shared with the publication. All scientific content was produced by myself with coauthors providing opportunities for discussion and editorial corrections.

4.1 Geological setting

The Caledonian orogeny was a major mountain building event across northern Europe and eastern North America. During the Ordovician and Early Devonian the closure of the Iapetus Ocean resulted in the collision of Baltica with Laurentia to from the Scandinavian Caledonides (Roberts and Gee, 1985, Roberts, 2003). The

WGR is comprised of subducted and subsequently exhumed Baltica shield forming the deepest structural level of the Scandinavian Caledonides (Figure 4.2a; Andreasson and Lagerblad, 1980). The formation of the mountain belt was preceded by ophiolite obduction and succeeded by orogenic collapse and formation of Devonian sedimentary basins.

The Baltica shield is dominated by tonalites of 1686 to 1650 Ma, subsequently intruded by granite, gabbro and diabase from 1640 to 900 Ma (Tucker et al., 1990). At 950 Ma, the igneous basement underwent granulite facies metamorphism at 900°C and 1 GPa associated with extensive plutonism (Tucker et al., 1990, Krabbendam et al., 2000, Corfu and Andersen, 2002). During the early Palaeozoic and initiation of the Caledonian orogeny (480-430 Ma), deformation and metamorphism of the Proterozoic basement gneiss and oceanic allochthons occurred at 725°C and 1.2 GPa (Hacker et al.,

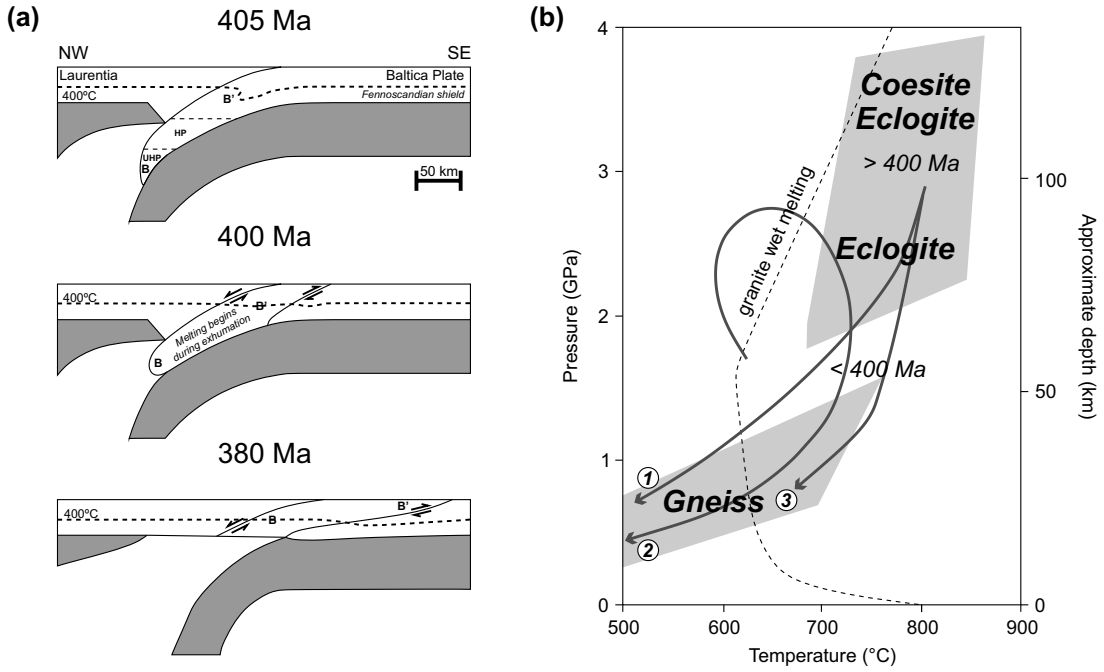

Figure 4.1: (a) Crustal Cross section through the Baltica-Laurentia collision at peak metamorphic conditions (405 and 400 Ma) and following cooling through 400°C of the UHP regions (380Ma), note the change in position of section line B-B' (shown in Figure 4.2) as the Baltica slab is exhumed (After Kylander-Clark et al., 2008). (b) P-T diagram showing the relationship of WGR metamorphic conditions recorded by eclogites and gneiss in the Nordfjord-Stadlandet and Sørøyane UHP domains and surrounding HP domains. P-T paths from (1) Gordon et al. (2016), (2) Labrousse et al. (2002), and (3) Gordon et al. (2013), and granite solidus from Auzanneau et al. (2006). Timing of peak UHP and HP metamorphism from Hacker et al. (2010). Note that although both the eclogite and gneiss likely experienced UHP conditions, the gneiss equilibrated at much lower PT conditions during decompression.

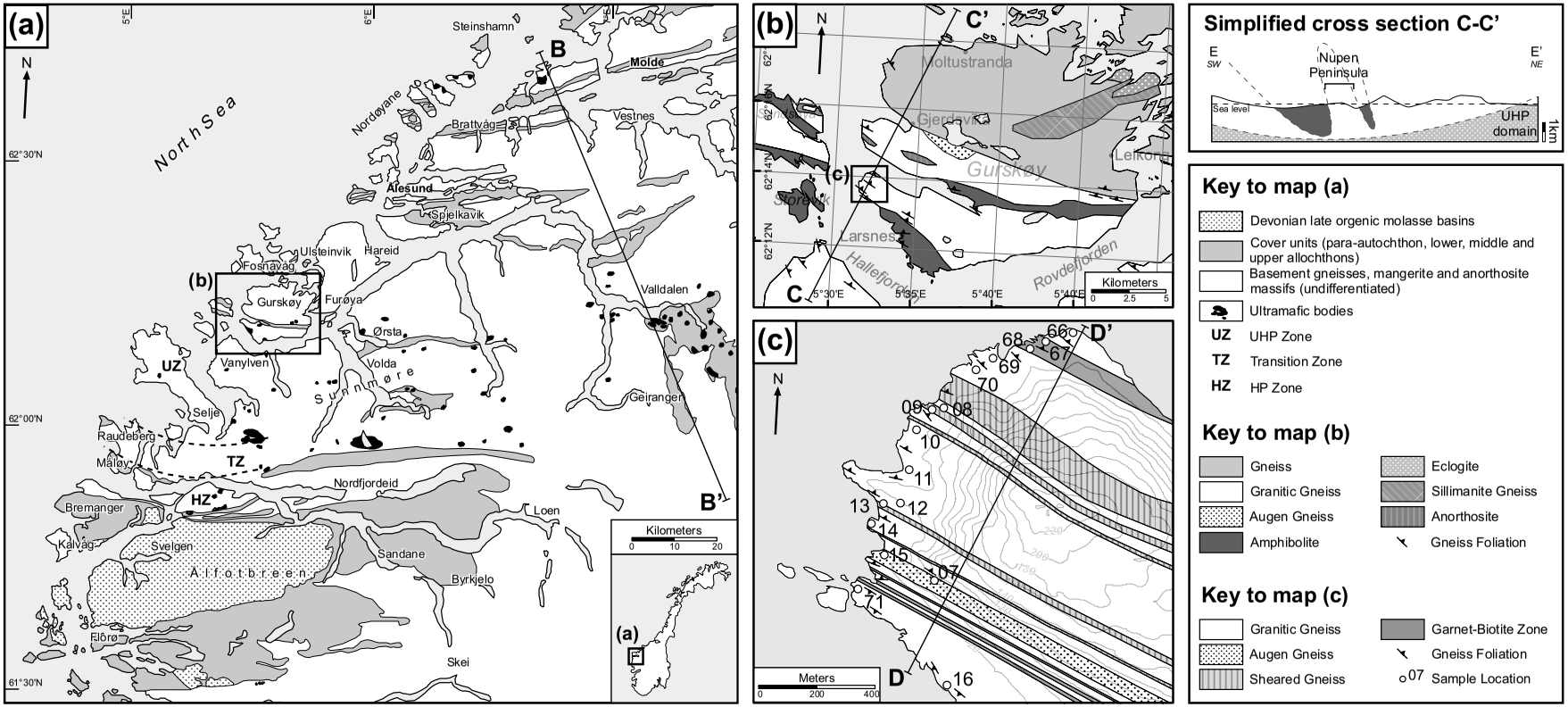

Figure 4.2: Geological map of (a) Western Gneiss Region and section line B-B' shown in Figure 4.1 with inset detail maps of (b) Gurskøy with section line C-C' and (c) Nupen Peninsula with sample locations and section line D-D' shown in Section 4.2.2. Geological cross section from northern Vanylven through Gurskøy shown in section line C-C' (Geological maps modified from Kildal, 1970, Lutro et al., 1997, Lutro and Tveten, 1998, Tveten et al., 1998, Carswell et al., 2003, Root et al., 2005).

2010). The final stage of the Caledonian Orogeny, the Scandian, resulted in the closure of the Iapetus Ocean and emplacement of oceanic allochthons onto Baltica between 430 and 410 Ma (Tucker et al., 2004, Hacker and Gans, 2005). Later collision of Baltica and Laurentia between 425 and 400 Ma resulted in the westward subduction of the Proterozoic Baltican basement and portions of the allochthon to ultrahigh-pressures (UHP) of 1.8-3.6 GPa and temperatures of 600-800°C (Figure 4.1; Andersen et al., 1991, Schärer and Labrousse, 2003, Tucker et al., 2004, Hacker and Gans, 2005, Kylander-Clark et al., 2008, Hacker et al., 2010).

From 400 to 385 Ma the WGR exhumed to shallow crustal levels (Figure 4.1a; Andersen, 1998, Terry et al., 2000, Tucker et al., 2004, Hacker, 2007, Walsh et al., 2007, Hacker et al., 2010), during exhumation, an E-W horizontal stretching fabric was imprinted alongside in-situ partial melting of the gneiss via post-UHP decompression-related retrograde amphibolite metamorphism as the pressure decreased from 2.8 to 0.5 GPa at temperatures of 600 to 800^{o}C (Figure 4.1b; Krogh, 1980, Chauvet et al., 1992, Andersen, 1998, Straume and Austrheim, 1999, Hacker et al., 2003, Labrousse et al., 2002, 2004, Schärer and Labrousse, 2003, Walsh and Hacker, 2004, Root et al., 2005, Engvik et al., 2007, Gordon et al., 2013, 2016). Evidence for (U)HP metamorphism was almost completely overprinted during the open-system partial melting event, as the UHP rocks were exhumed from 100 km depth to 15-20 km (Schärer and Labrousse, 2003, Root et al., 2005). Exhumation occurred from 394 to 389 Ma at a rate of 5 mm/year, followed by rapid cooling to reach 300°C by 357 Ma (Schärer and Labrousse, 2003, Root et al., 2005).

This chapter focuses on the Nupen Peninsula in the southwest of the island Gurskøy (Figure 4.2 b, c). The primary lithology is amphibolite-facies quartzofeldspathic gneiss that has undergone varying degrees of partial melting. The gneisses show layers of melanosomes and leucosomes that were stretched and sheared at a later stage, indicating that the migmatization commenced early in the exhumation-related deformation history (Labrousse et al., 2002). Gurskøy was exhumed via thrusting and formed a NW-SE trending isoclinal fold verging southwest on the peninsula (Figure 4.2; Labrousse et al., 2004). Geothermometry from the

nearby Vanylven migmatized gneiss (approx. 5 km south of Nupen) indicates an influx of H_2O-rich fluids, allowing decompression melting to begin at 600-650°C and not exceeding 800°C (Labrousse et al., 2002, 2004, Ganzhorn et al., 2014).

Over a 1.2 km section (Figure 4.2c), there is a diverse deformation sequence of migmatized gneiss, mylonitic shear zones, sillimanite bearing garnet-biotite zones, augen gneiss and boudinaged amphibolite dykes. The strongly deformed mylonitic shear zones extend from 5 to over 100 m in width, but deformation is widespread over the peninsula, the migmatitic layers exhibit S-C fabrics and isoclinal folding of leucosome, mesosome and melanosome. Sixteen samples representitive of leucosome:melanosome ratio at the outcrop were taken from the different lithologies. The leucosome abundance and the degree of strain varies between different sample locations (Figure 4.2c).

4.2 Melt characteristics

Here I examine the rocks microstructure using optical, SEM, image analysis and EBSD to determine melt properties and crystallised volume of a section of migmatized and sheared gneiss from the WGR where partial melting occurred during the formation of the Scandinavian Caledonides (Hacker et al., 2010; and references therein). Through analysis of textures in the migmatites and shear zones I demonstrate that even in volumes with high melt percentage, deformation may partition away from the highly molten volumes into discrete shear zones.

4.2.1 Macroscale evidence for melt

The Nupen peninsula is comprised of migmatized gneiss, mylonitic shear zones, sillimanite bearing garnet-biotite zones and augen gneiss, all having undergone varying degrees of partial melting. Figure 4.3 shows the characteristic outcrop scale variation across the peninsula. The migmatites are typically stromatic in structure accompanied by intense folding but the leucosome content is varied (Figure 4.3 a, d). The next most common lithology is the mylonitic shear zones, which are strongly lineated with

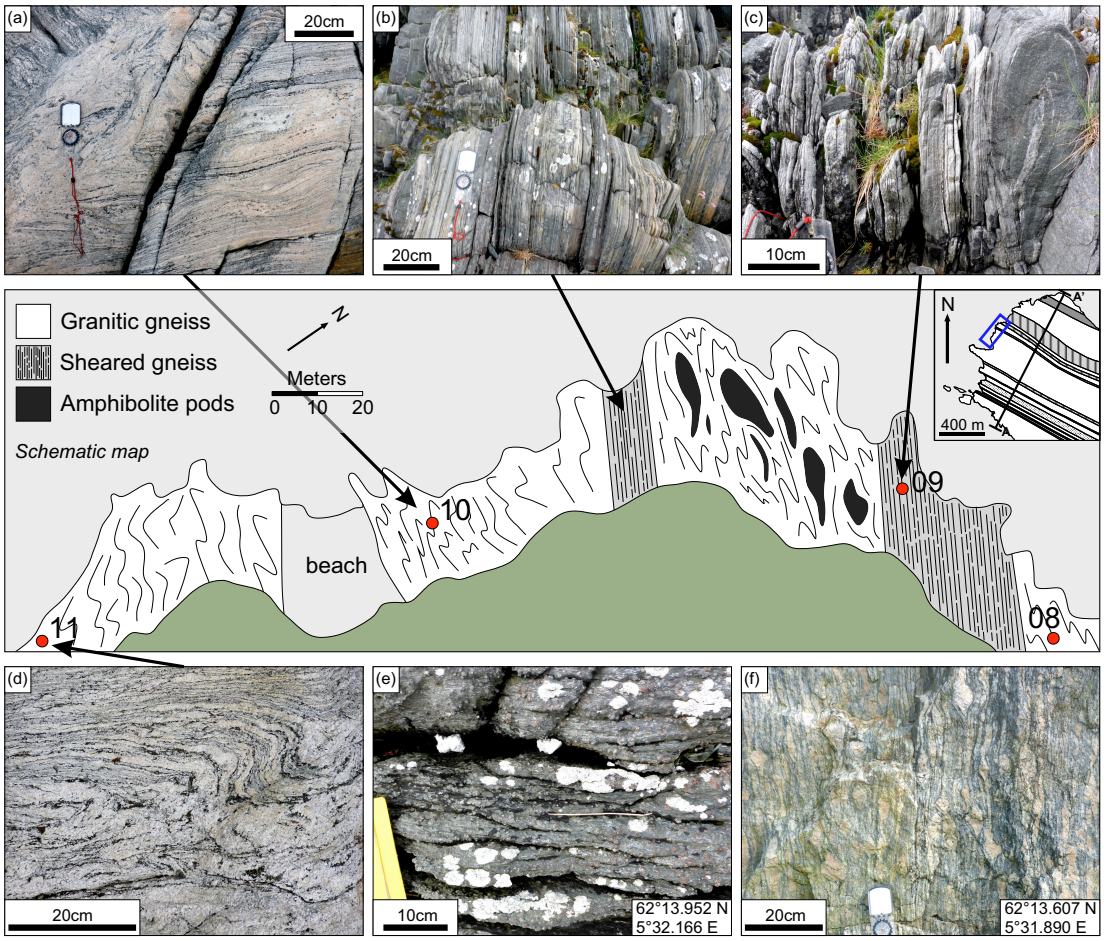

Figure 4.3: Detailed geological field map showing variation of the gneiss at Nupen, foliation pattern and amphibolite pod location is representative. Photos (a-f) are characteristic outcrop photos of the (a, d) migmatized gneiss and (b, c) sheared gneiss and not shown on detailed field map (e) garnet-biotite zone and (f) augen gneiss.

segregation of felsic and mafic layers (Figure 4.3 b, c). Foliation parallel zones of garnet and biotite are common in the north and south (Figure 4.3e). The garnet-biotite zone contains garnet porphyroblasts (0.5 to 5 cm) with the foliation defined by bands of biotite and sillimanite, hornblende, and felsics. A zone of augen gneiss is observed in the south of the Nupen Peninsula; the augen (3 to 10+ cm) are mostly K-feldspar and occasionally plagioclase (Figure 4.3f).

Figure 4.4 shows examples of the variation in the migmatized gneiss at the outcrop scale. Stromatic migmatites are most common but the leucosomes can also appear patchy, indicating the migmatite texture is surreitic or ophthalmic. Stromatic-type migmatites have the highest leucosome content (Figure 4.4a) and surreitic migmatites have the lowest (Figure 4.4c). The variation in melt fractions and migmatite structures

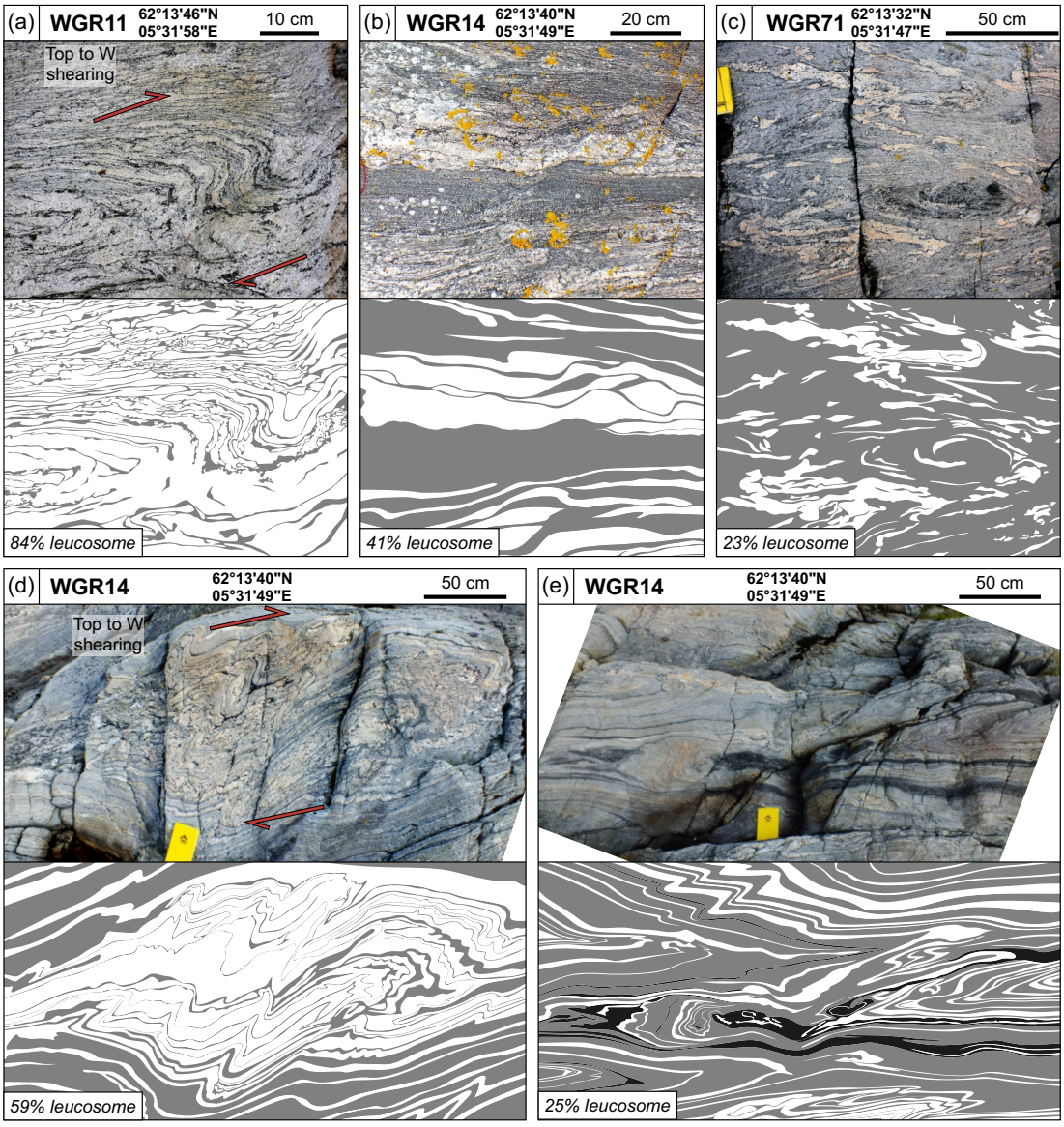

Figure 4.4: Field photographs with schematic drawings to emphasise the leucosome and melanosome segregation at outcrop scale. Examples shown from the WGR; (a) Leucosome-rich outcrop with top to the west shearing; (b) Ophthalmic layers in leucosome; (c) Surreitic/dilational migmatite; (d) Folded stromatic migmatite with top to the west shearing; (e) Folded stromatic migmatite with leucosome, mesosome and melanosome. Migmatite nomenclature after Ashworth (1985).

are expected to reflect strain partitioning due to internal rheological variations.

Macroscale leucosome content is determined via image analysis using ImageJ of digitised outcrop photos (Schneider et al., 2012). Digitising photographs and correcting images for shadows or cracks on the outcrop helps to constrain leucosome vs. restite proportions. Examples of the digitised outcrop drawings are shown in Figure 4.4. The leucosome content in the Nupen area varies from 0 to 90%. However, this does not mean up to 90% of the crust was melt, as the leucosome fraction does not equal the melt fraction. The leucosome content gives the maximum melt proportion left in-situ. It is necessary to use microstructures to distinguish if the leucosome formed from melting or solid-state deformation and recrystallisation processes.

4.2.2 Microstructural evidence for melt

At the microscale I am able to determine how much of the leucosome is representative of melt and the type of migmatitic melting that occurred. The typical melt textures observed in the migmatites are peritectic melt products, euhedral crystal faces, cuspate-shaped melt pools, felsic compositional zoning (quartz and feldspar bands), low dihedral angles (e.g. <60°), disequilibrium grain boundaries, 'string of beads' texture, interstitial quartz, and myrmekite lobes (Figure 4.5; Sawyer, 1999, 2001, Holness et al., 2005, Vernon, 2011, Holness et al., 2011). On their own, these microstructures would be weak indicators of melting, but when found together significantly strengthen the interpretation of partial melt across the Nupen peninsula (Vernon, 2011).

Fluid-present granitic eutectic melting starts to occur at lower temperatures (∼650°C; Wyllie, 1977) than biotite-dehydration melting (760-800°C; Spear et al., 1999). Decompression related partial melting in the WGR began at 600-650°C and did not exceed 800°C (Labrousse et al., 2002, 2004, Ganzhorn et al., 2014). Thin quartz films along grain boundaries between plagioclase and K-feldspar and occasionally biotite and K-feldspar are observed in the migmatized gneiss (Figure 4.5f). When the presence of quartz films is combined with the lack of garnet, the peritectic product from biotite-dehydration melting, and absence of chessboard

extinction within quartz grains, they together suggest melting of the migmatites occurred at the lower end of the temperature range via granitic wet melting rather than biotite-dehydration melting. Thus, the primary reaction system is:

$$\text{quartz} + \text{plagioclase} + \text{K-feldspar} + \text{water} = \text{melt}, \tag{4.1}$$

However the garnet-biotite zones contain both the reactants and products of biotite-dehydration melting (Equation 2.2, Figure 4.5i-l). This suggests either the granitic migmatite and the garnet-biotite zone were different protoliths of the partially melted rocks, most likely a granitoid protolith for the migmatized gneiss and a pelitic protolith for the garnet-biotite zone (Bucher and Grapes, 2011), or the melt source varied from an A-type to an S-type composition resulting in different peritectic phases crystallising in the garnet-bioite zone. There are two generations of biotite present in the garnet-bioite zone (Figure 4.5j), the first (bt^1) forms short stubby anhedral grains and its strong mineral colour masks the interference colours, the second generation (bt^2) forms long euhedral grains with brighter interference colours. The abundance of the secondary biotite and presence of minor sillimanite suggests that not all the biotite and sillimanite were consumed during biotite-dehydration melting and/or the biotite and sillimanite are retrograde phases (Figure 4.5 i-l). The consumption texture suggests two phases of melt/fluid flux; during the initial phase garnet was stable and grew large peritectic garnets, during the second phase garnet was no longer stable and underwent retrogression to quartz and biotite. This two phase fluid flux suggests the WGR underwent open-system melting and was fed from an external melt source. Here I primarily focus on the fluid-present granitic eutectic melting of the migmatitic gneiss to determine the melt fraction and styles from microstructures.

If melting occurs under static conditions and absence of deformation in an igneous setting, the grains crystallised from melt will reach a textural equilibrium with a uniform grain size and grain boundary angles relative to interfacial angles (e.g. 103-115° for quartz, plagioclase or K-feldspar; Vernon, 1968). This does not apply to the migmatites from the Nupen Peninsula as partial melting occurred under a deformation regime

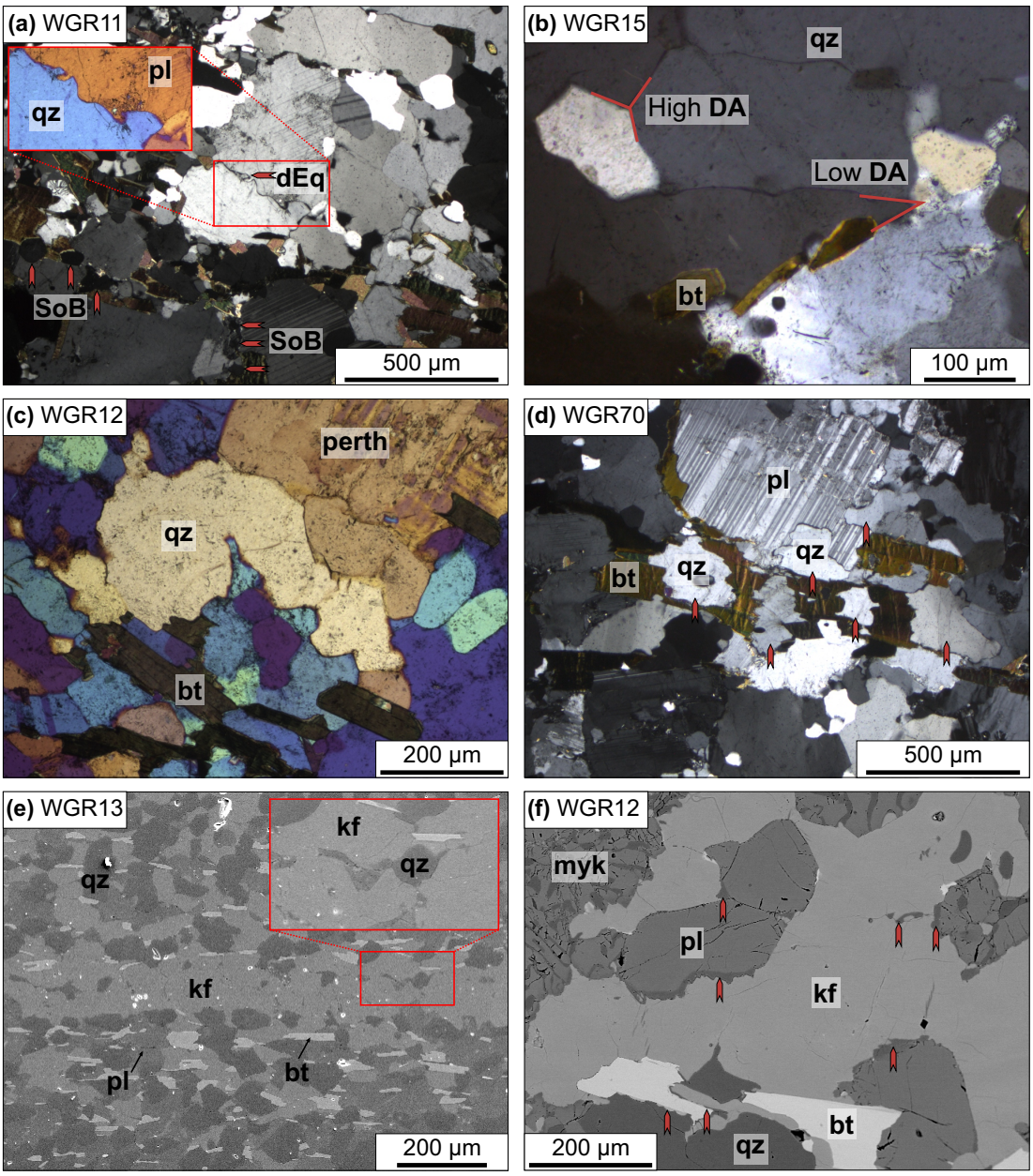

Figure 4.5: Microstructures from Nupen Peninsula samples from photomicrographs in cross-polarised light (a, b, d), cross-polarised light and gypsum plate (a-inset, c) and SEM-BSE images (e, f). (a) Migmatite with plagioclase (pl) and quartz (qz) grain boundaries in disequilibrium (dEq), string of beads texture (SoB) in quartz along plagioclase grain boundaries indicated by arrows. (b) Augen gneiss with high and low dihedral angles (DA) between quartz grains. (c-d) Migmatite with interstitial quartz melt infilling pore space. (e) Shear zone sample with interstitial quartz melt infilling pore space. (f) Migmatite with quartz (qz) films along grain boundaries of plagioclase, K-feldspar (kf) and biotite (bt) with qz-pl myrmekite (myk).

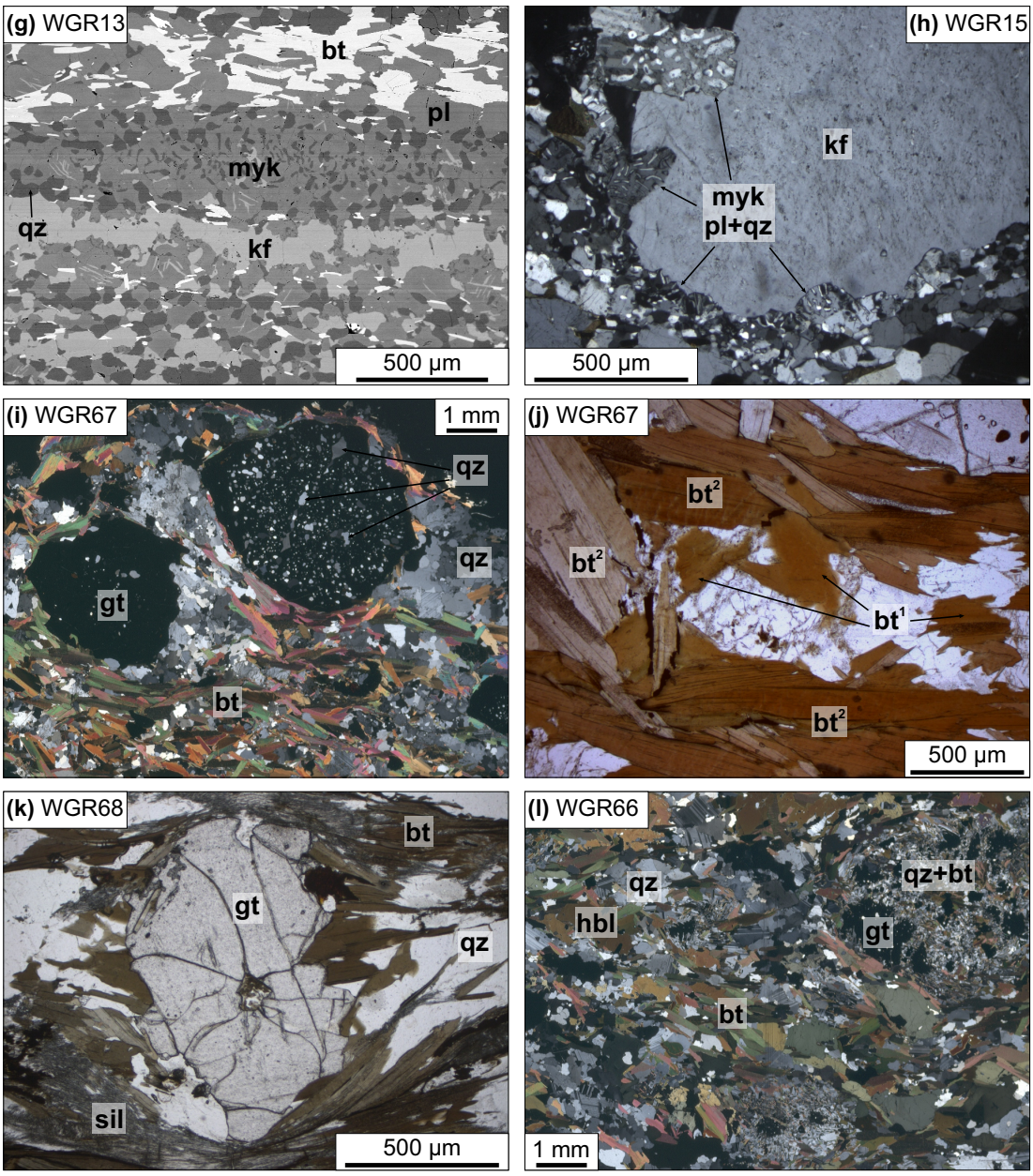

Figure 4.5: Microstructures from Nupen Peninsula samples from photomicrographs in plain-polarised light (j), cross-polarised light (h, i, k), and SEM-BSE images (g, l). (g) Shear zone sample with myrmekite and disequilibrium grain boundaries. (h) Augen gneiss with quartz-plagioclase myrmekite surrounding large K-feldspar grain. (i) Garnet-biotite zone with peritectic garnet (gt) and secondary 'igneous-like' biotite. (j) Detail of biotite generations from (i), original biotite (bt^1) and secondary 'igneous-like' biotite (bt^2). (k) Garnet-biotite zone with peritectic garnet surrounded by sillimanite (sil), biotite and quartz. (l) Retrograde breakdown of garnet in garnet-biotite zone to quartz, new biotite with albite infill and oxides.

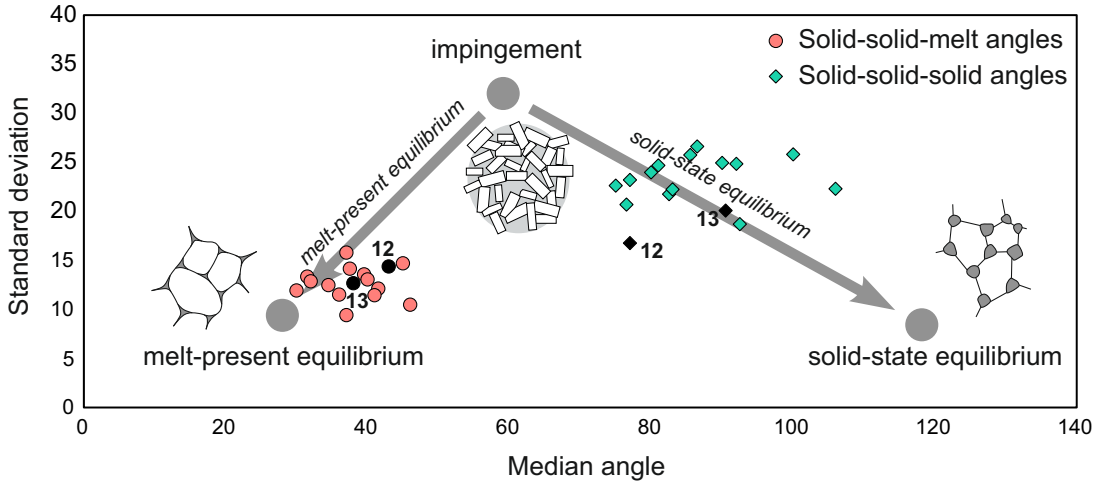

Figure 4.6: Dihedral angles from the WGR samples for solid-solid-melt boundaries (○) and solid-solid-solid boundaries (◇). Results for samples WGR12 (migmatite) and WGR13 (shear zone) are identified and shown with filled in black symbols. Also shown is a schematic diagram showing end-member solid-solid-melt dihedral angle populations (Adapted from Holness et al., 2005).

via decompression related retrograde metamorphism as Baltica exhumed. As a result I mainly observe irregular grain boundaries and low dihedral angles (<60°) as the migmatite crystallised in textural disequilibrium (Figure 4.5a).

Dihedral angles play a key role in melt connectivity: melt is likely to be interconnected if the melt-solid dihedral angle is less than 60°, but is likely to form isolated pockets when greater than 60° (Section 2.2.6; Holness, 2006, Holness et al., 2011). Thus, if there is a high dihedral angle the melt connectivity is low and the strength of the partially melted rock would be greater than if there is a low dihedral angle where the melt connectivity is high. Figure 4.5b shows examples of both high and low dihedral angles observed in these samples. Following the method of Holness et al. (2005) a sample of >50 dihedral angles were measured for each thin section. Figure 4.6 shows results of solid-solid-melt and solid-solid-solid dihedral angles, where the relationship between median angle and standard deviation indicate melt-present or solid-state equilibrium. I observe a median dihedral angle of 53° for all boundaries, 37° for solid-solid-melt boundaries and 88° for solid-solid-solid boundaries (Figure 4.6). Where melt is present it is observed to be connected and thus the strength of the migmatite during melting is low.

The 'string of beads' texture of quartz grains is observed in some WGR samples

(Figure 4.5a). This texture usually forms during concentration of melt from thick films on grain boundaries into 'beads' (Holness et al., 2011). The texture suggests a slow crystallisation rate to allow nucleation of individual grains from melt films (Holness et al., 2011). Interstitial melt can appear similar to the 'string of beads' texture and is more commonly observed. This texture represents larger collections of crystallised melt that did not coalesce into individual beads. Irregular grains of quartz with lobate (Figure 4.5c) and cuspate (Figure 4.5 b, d, e) grain boundaries are also commonly present. Figure 4.5d shows embayed biotite and plagioclase where quartz has penetrated into the non-melt grains. Fingers of inferred former melt with small dihedral angles are shown in Figure 4.5b and commonly align parallel to foliation. The shear zone samples also show interstitial quartz infilling pore space implying they have also melted (Figure 4.5e).

Lobes of myrmekite are very common in the migmatized gneisses and are also present in small amounts in the shear zone samples; however, their origin is controversial. It has been proposed that they originated either from a quenched fluid-rich melt (Hibbard, 1979, 1987) or that they represent solid-state reactions in the presence of hydrous fluid (e.g. Ashworth, 1972, Phillips, 1974, 1980, Simpson and Wintsch, 1989, Vernon, 1991, Yuguchi and Nishiyama, 2008, Vernon, 2011). Figure 4.5h shows a large K-feldspar grain mantled by myrmekite lobes, which could be of melt origin as they co-exist with other melt microstructures. Figure 4.5f shows evidence for the initiation of myrmekite formation in plagioclase grains. Myrmekite is also observed in the shear zone samples, Figure 4.5g shows a coarse myrmekite band as well as finer myrmekite mantling K-feldspar grains. Conversely if they are a solid-state texture, they indicate deformation occurred post-melt in a fluid-rich system. When we combine the observed myrmekite with other evidence for partial melting, I propose the myrmekite is evidence for partial melting at the Nupen Peninsula.

To understand the effects of melt on rheology, it is important to quantify the melt fraction. Microscale melt determination is qualitative as I use microstructures indicative of melt or the former presence of melt (Figures 4.5, 4.7). With the use of

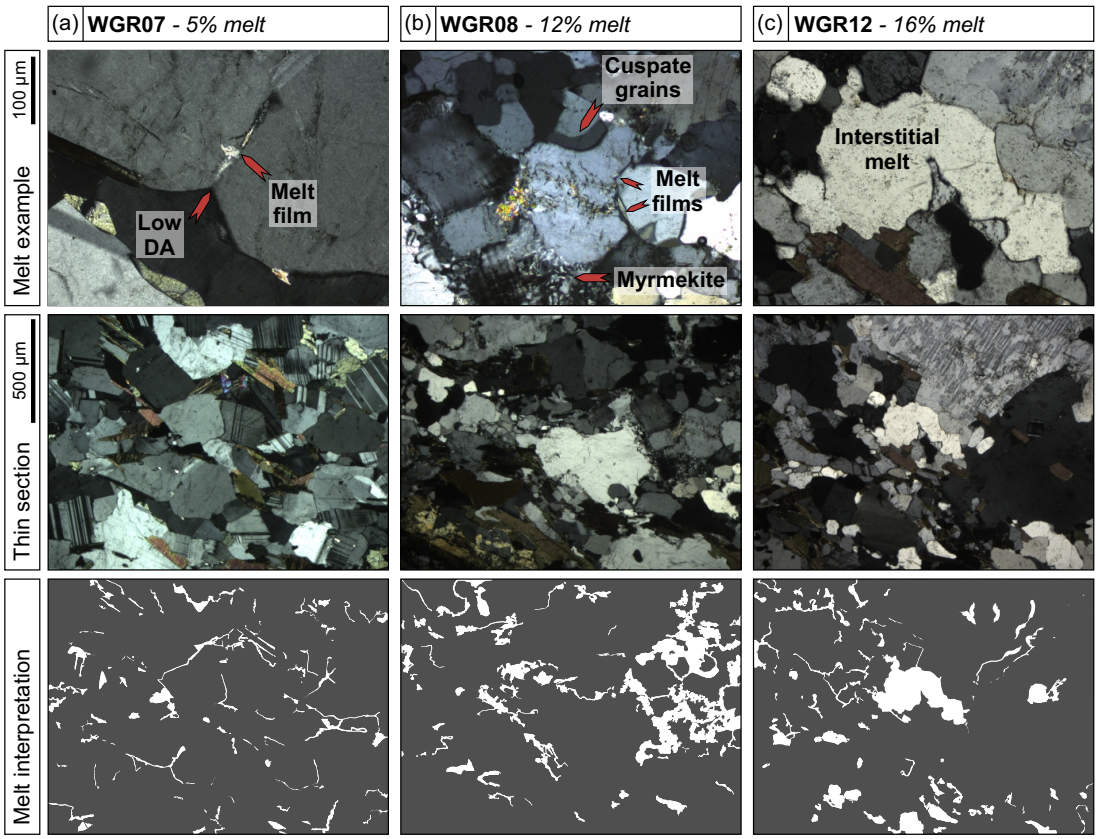

Figure 4.7: Photomicrographs and image analysis of melt microstructures. Top: Example of melt textures used to determine crystallised melt volume. Middle: Photomicrographs of melt on grain boundaries in WGR migmatites in plane polarised light. Bottom: Melt (white) vs. solid (grey) image analysis interpretations of each photomicrograph.

ImageJ I am able to isolate the melt and solid fractions of the rock. Plain polarised light (PPL) and cross polarised light (XPL) photomicrographs with and without gypsum plate are used to construct the melt-solid interpretations. Figure 4.7 shows examples of the quantification of the migmatized gneiss via photomicrographs and corresponding interpretations of melt (white) vs. solid (grey).

The leucosome volumes quantified in figure 4.4 represent the felsic portion of the rock, micorstructural analysis shows that these felsic portions are not solely comprised of melt as they are also formed through solid state segregation. In the Nupen area, the leucosome volume is more than twice the interpreted microstructural melt content, leading to a possible overestimation and an unreliable method of calculating accurate melt volumes in the field (Figure 4.8a). The total melt volume in figure 4.8b is calculated by attributing the micro-melt volume to the leucosome

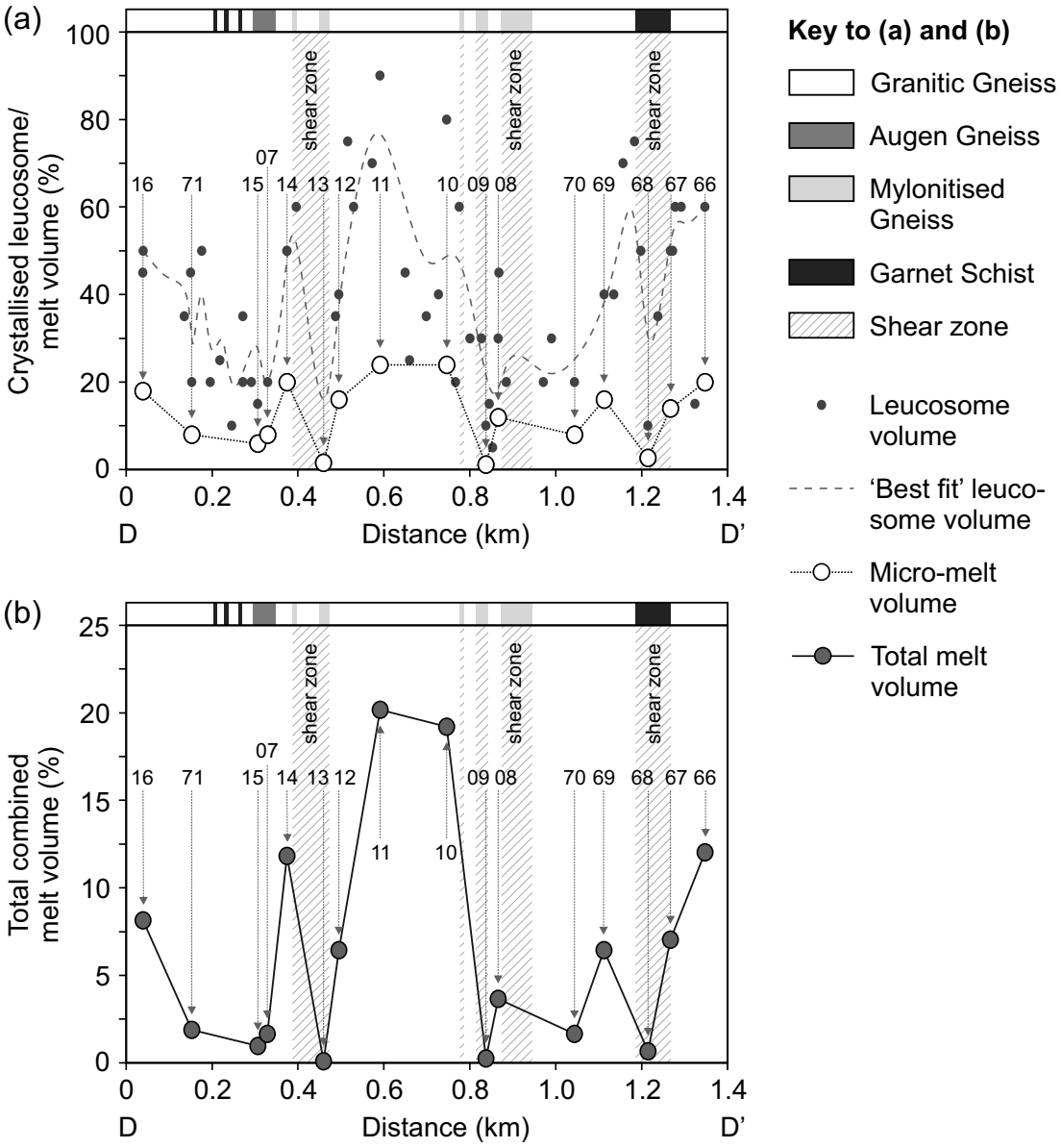

Figure 4.8: Leucosome and melt volume over the Nupen Peninsula (Figure 4.2c, section line D-D'). (a) Macroscale leucosome volume calculated in the field and via image analysis at the outcrop scale and microscale melt volume calculated from image analysis of thin sections and SEM images. (b) Total melt volume when the leucosome and micro-melt volumes are combined.

portion of the rock. For example, WGR12 has 16% melt in its microstructure and 40% leucosome at outcrop, this results in a 6.4% total melt volume as only 16% of the leucosome is comprised of melt. This calculation assumes all melt was liquid at the same time, which is unlikely, nevertheless the total melt fraction is higher in the migmatite gneisses outside the shear zones.

4.3 Mineral assemblages and compositions

In the WGR there is field evidence for fine grained shear zones in the migmatized gneiss, and it is important to understand the timing of melting with respect to the shear zones. To investigate how the shear zones are related to the migmatites, I use microanalytical techniques to compare migmatite and shear zone samples. WGR12 is a migmatized gneiss with ~6% melt crystallised in the microstructure and WGR13 is a mylonitized gneiss with <1% melt in the crystallised microstructure. Figure 4.9 shows backscattered electron maps of both samples where there is a grain size variation of 0.2 to 5 mm in the migmatite and 0.05 to 0.3 mm in the shear zone.

If the shear zone has not undergone partial melting or was originally a different

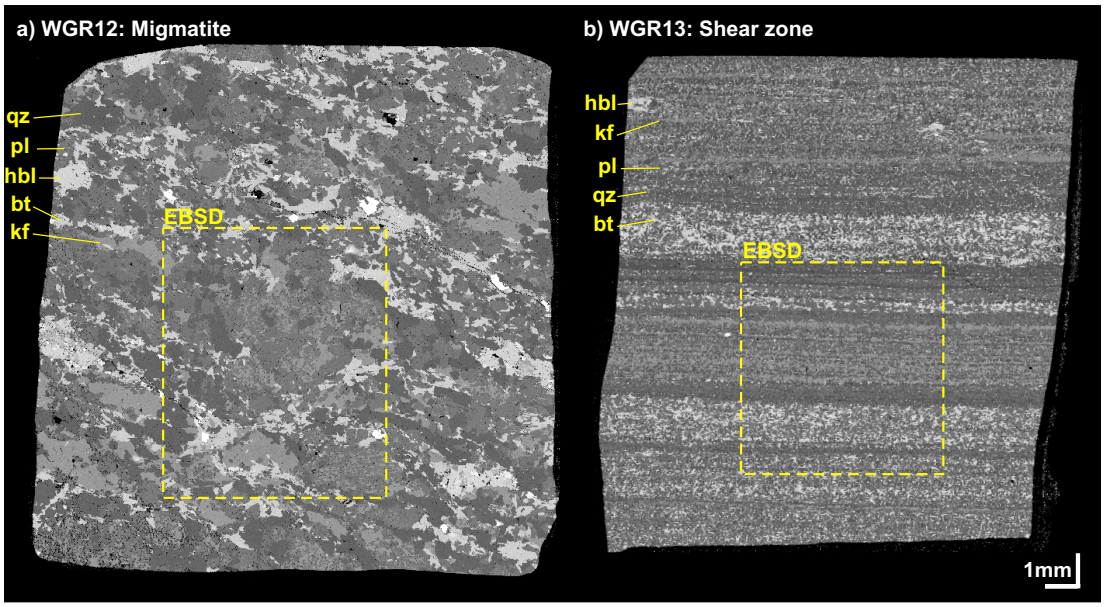

Figure 4.9: Backscattered electron maps of (a) migmatite sample WGR12 and (b) shear zone sample WGR13. Maps are at the same scale with 1 mm bar shown for scale. Dashed yellow boxes indicate area of EBSD analysis.

Table 4.1: Microprobe data of plagioclase (pl), K-feldspar (kf), biotite (bt) and hornblende (hbl) compositions for migmatite sample WGR12 and shear zone sample WGR13[a].

	WGR12: Migmatite					**WGR13: Shear zone**				
Mineral	Qz	Kf	Pl	Bt	Hbl	Qz	Kf	Pl	Bt	Hbl
wt%	35%	33%	16%	14%	2%	46%	28%	17%	8%	1%
N		16	19	6	11		13	17	11	3
SiO_2		64.242	61.001	36.310	39.275		64.647	60.828	35.806	38.879
TiO_2		0.009	0.005	3.037	1.075		0.018	0.008	3.066	1.076
Al_2O_3		18.835	24.165	17.704	11.609		18.656	24.539	18.552	11.565
Cr_2O_3		0.006	0.005	0.025	0.015		0.007	0.009	0.031	0.016
FeO		0.049	0.114	19.243	21.173		0.034	0.104	19.096	20.949
MnO		0.003	0.008	0.506	0.827		0.008	0.007	0.297	0.834
MgO		0.005	0.007	8.619	7.105		0.004	0.006	8.993	7.012
CaO		0.051	5.987	0.018	11.484		0.058	6.177	0.033	11.452
BaO		0.699	0.015	0.090	0.008		0.671	0.024	0.144	0.000
Na_2O		0.973	8.310	0.075	1.455		1.014	8.074	0.052	1.460
K_2O		15.136	0.338	9.721	1.971		15.112	0.245	9.725	1.976
Total		100.009	99.955	95.348	95.997		100.228	100.021	95.794	95.218
No. of O		8	8	22	24		8	8	22	24
Si		2.974	2.740	5.539	6.640		2.984	2.729	5.432	6.630
Ti		0.000	0.000	0.348	0.137		0.001	0.000	0.350	0.138
Al		1.028	1.279	3.183	2.313		1.015	1.298	3.317	2.324
Cr		0.000	0.000	0.003	0.002		0.000	0.000	0.004	0.002
Fe		0.002	0.004	2.455	2.993		0.001	0.004	2.422	2.987
Mn		0.000	0.000	0.065	0.118		0.000	0.000	0.038	0.120
Mg		0.000	0.000	1.960	1.791		0.000	0.000	2.034	1.783
Ca		0.002	0.224	0.002	1.619		0.002	0.231	0.004	1.628
Ba		0.014	0.000	0.006	0.001		0.014	0.000	0.010	0.000
Na		0.087	0.724	0.022	0.477		0.091	0.702	0.015	0.483
K		0.894	0.019	1.892	0.425		0.890	0.014	1.882	0.430
Total		5.002	4.992	15.476	16.516		4.998	4.980	15.507	16.525

No analyses

[a]Modal proportions for each mineral, including quartz (qz) are shown by weight % (wt%). *N* is number of spot analyses per mineral, analyses were reject where totals are outside 99.0-101.0% for feldspars and below 95% for biotite and hornblende.

layer of rock, I would expect to see variation in the mineralogy due to melt reactions that would have occurred in the migmatite. However, if the protolith was fairly homogeneous and the mylonite-like fabric formed via syn-melt shearing, the melt reactions will produce the same mineralogy for the migmatized and mylonitized gneisses. In detail, there may be small differences between the migmatite and shear zone as more melt loss is likely to have occurred via transport through the shear zone than in the migmatized wall rock as indicated in Figure 4.8.

The mineral compositions in the migmatites and shear zones are the same; quartz,

K-feldspar, plagioclase, biotite and minor hornblende. The modal proportions are calculated via the number of points indexed from EBSD and shown in Table 4.1. Quartz is the most abundant mineral in both samples followed by K-feldspar. K-feldspar makes up more of WGR12 than WGR13 but this is due to large K-feldspar grains dominating the sample. As the modal compositions are similar it suggests there has not been a significant change in mineralogy due to melt reactions or melt loss between the two samples. The observed leucosome and interpreted melt volume are much lower in the shear zone than in surrounding migmatites, mineralogical proportions suggest the leucosome is underestimated greatly in the shear zone due to the small grain size.

Spot analyses for plagioclase (pl), K-feldspar (kf), biotite (bt) and hornblende (hbl) were measured with the electron microprobe at the University of Leeds (Table 4.1; see Section 2.5.2 for operating conditions). The results show there are no significant variations in the major or minor elements. Plagioclase and some K-feldspar represent the melt phase and the element totals are similar between the migmatite and shear zone samples. Both samples indicate the plagioclase is andesine in composition (An_{32-48}), although some analyses indicate a more sodic composition, due to the perthitic relationship between plagioclase and K-feldspar where albite forms the perthite. Mineral compositions and abundances suggest a protolith of a granitic composition such as felsic gneiss (Bucher and Grapes, 2011). The similarities in element totals suggest the shear zone was involved in melting and did not permit increased melt loss when compared to the migmatites.

4.4 Crystallographic preferred orientations

If the shear zones have not undergone melting they should preserve a record of pre-, syn- and post-melt deformation(s). In particular, the lack of pervasive melting would mean the crystal microstructure is not 'reset' in non-melt zones and hence should be observed in CPO. In contrast, if all of the gneiss is involved in melting and the shear zone forms syn-melting, any pre-existing fabric will have been 'reset' with crystallisation under the same stresses for the migmatite and shear zone. Subsequent deformation may

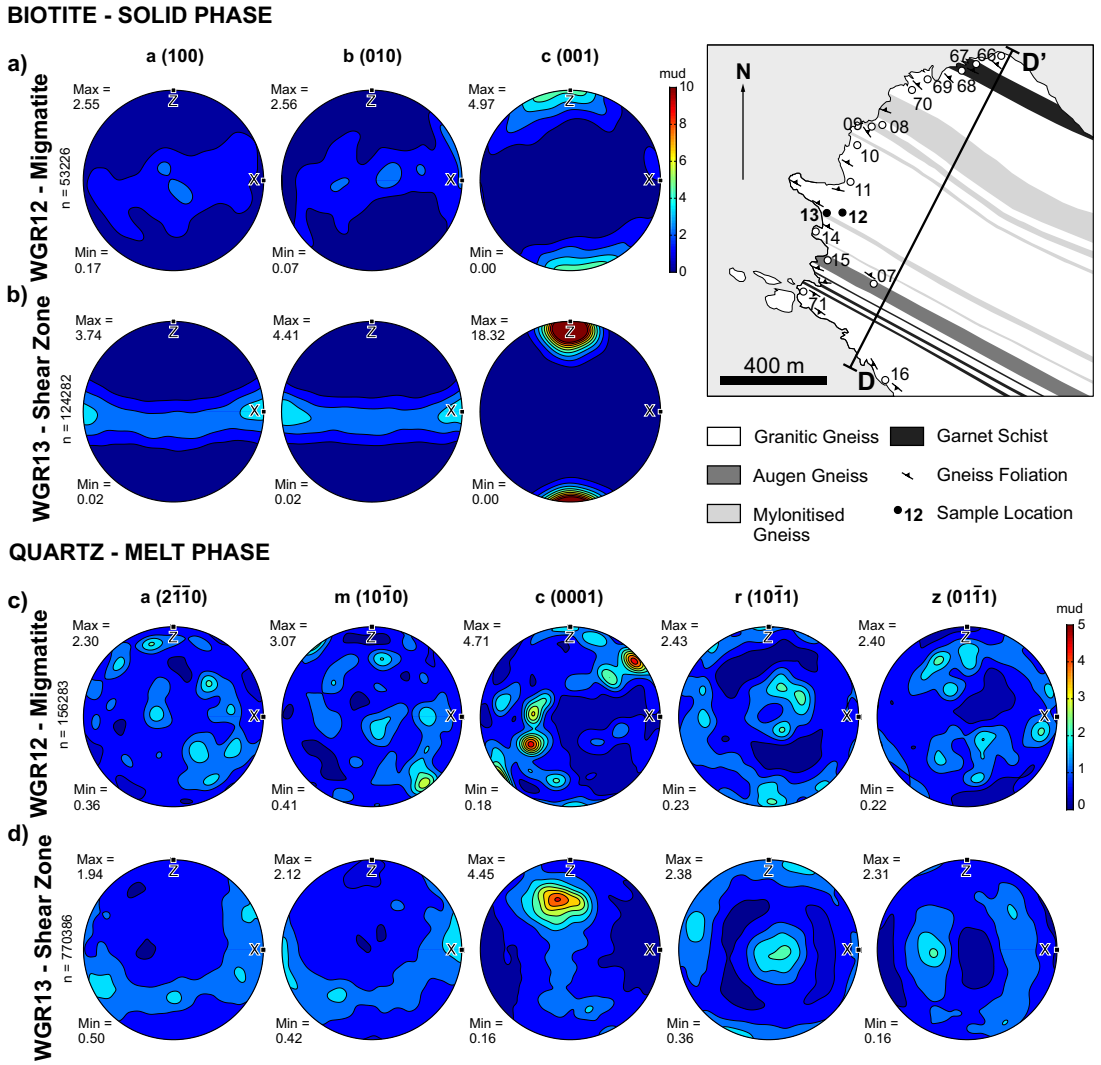

Figure 4.10: EBSD-derived CPO of biotite (a, b) and quartz (c, d) in kinematic coordinate system for migmatized gneiss sample WGR12 (a, c) and mylonitized gneiss sample WGR13 (b, d). All stereographic projections are lower hemisphere and CPO are contoured in terms of multiples of the uniform distribution (m.u.d.). Inset map shows locations of adjacent mylonitized and migmatized gneiss samples.

occur but the post-melt CPO from the migmatite should be recognisable in the shear zone CPO which would be strong to reflect the deformation fabric observed in the field. I compare the CPO for the adjacent migmatite, WGR12, and shear zone, WGR13, to identify timing of deformation relative to melting.

CPO results were measured via EBSD at the University of Leeds (mapped areas are shown in Figure 4.9; see Section 2.5.2 for operating conditions). Figure 4.10 shows the CPO for biotite and quartz in samples WGR12 and WGR13 (additional phases and samples are availables in Appendix A.2). The biotite represents a solid phase whereas

the quartz represents one of the melt phases.

Figure 4.10 a, b shows the biotite CPO for both samples, they are somewhat similar both exhibiting strong c-axes maxima parallel (||) to Z, although more dispersed in WGR12 (e.g. Ji et al., 2015). Similarly, single girdles parallel to basal plane for $< a >$ and $< b >$, again, less well-defined for WGR12 with distinct a-max||X and b-max||Y in WGR13. The presence of the girdles and a/b-max suggest gliding on the $< 001 >$ parallel to $< 100 >$ or perhaps $< 110 >$, which is the average of $< 100 >$ and $< 010 >$ in WGR13. However, the dispersion of a and b in a girdle parallel to XY for WGR12 plane could indicate 'floating' in a melt. The dispersed c-max is compatible with this idea as it indicates slight 'floating' induced undulation. As a result, the WGR12 biotite CPO is more likely the effect of a syn-melt fabric and controlled by the shape preferred orientation of biotite aligned by flow of the melt instead of a deformation induced CPO present in the shear zone.

The quartz CPO are generally weak for both the shear zone and especially migmatite samples (Figure 4.10 c, d). If deformation to form the shear zone occurred pre- or post-melt producing a mylonite, I would expect to see a strong CPO in WGR13. However, the weak CPO is atypical for a mylonite (Toy et al., 2008, Barth et al., 2010) suggesting there was little deformation in solid-state (Figure 4.10d). Additionally preservation of delicate melt textures in the shear zone sample microstructures suggest diffusion creep was not a dominant deformation mechanism for solid-state deformation. Furthermore, whilst both samples indicate r||Y as a possible vorticity axis in quartz, the biotite CPO's imply no such rotation. This suggests any deformation is preferentially irrotational (i.e. 'pure shear') for biotite whereas it is rotational (i.e. 'simple shear') for quartz. By comparison with VPSC models (Morales et al., 2014), the quartz CPO correlates with amphibolite facies r-slip simple shear simulations ($\gamma = 1.73$). Implying both melt and crystallisation occurred within the amphibolite facies (Chauvet et al., 1992, Andersen, 1998, Schärer and Labrousse, 2003, Labrousse et al., 2011). In summary, the similarities between the CPO for the migmatite, WGR12, and the shear zone, WGR13, suggest the CPO was reset during the melting event; the lack of strength in the shear zone CPO and similarities with the migmatite CPO suggests deformation was transient or even

absent post-melting.

4.5 Discussion

Searle (2013) posed the question "do shear zones control the generation and ascent of magmas (Brown and Solar, 1998a, Brown, 2007) or do magmas trigger nucleation of shear zones?". The Nupen Peninsula has fine grained shear zones within migmatized gneiss. However, there is no evidence for significant mineral chemistry variations or post-crystallisation strain in the shear zone. I propose a hypothesis that grain size reduction is a result of initial syn-melt shearing which results in the observed geometry of the bodies (thin laminae/sheets of melt). The layering constrained grain growth and increased heterogeneous nucleation rates to maintain a small grain size.

Low dihedral angles, interstitial quartz infilling pore space and myrmekite are present in shear zone samples from Nupen (Figure 4.5e). Individually these microstructures are not strong evidence of melting, but when taken together and considering the close proximity to the migmatites it is likely melt was present in the shear zones. If the shear zones were active post-melting, the delicate melt textures are likely to have been overprinted and erased by solid-state processes. I do not see deformation of the melt textures in solid-state (Figure 4.5e), suggesting the shear zone was active pre- or syn-melt. As well as the shear zone microstructures, the alignment of the foliation, shear zones and melt 'fingers' in the migmatite is evidence for a single pattern of strain for the formation of all three features, suggesting a syn-melt fabric.

The absence of significant variations in mineralogy or mineral chemistry between the migmatite and shear zone suggest the protolith and melt source was the same (Figure 4.1), most likely a felsic gneiss to allow for fluid-present granitic melting (Equation 4.1). This suggests melt was pervasive through the migmatite and shear zone. The shear zone may have been used as a pathway for melt loss but the mineralogy suggests no evidence for increased melt loss or gain in the shear zone relative to the migmatite, however granitic-wet melting of a granitic protolith may mask the effects of melt loss/gain. This suggests the shear zone was short-lived as the

migmatite was not 'drained' of melt relative to the shear zone.

The strong biotite CPO is expected for the shear zone sample with strong c-axes maximum and normal to foliation in <a> and <b>. The biotite CPO for the migmatite is similar to the CPO from the shear zone but more diffuse. The similarity between the CPOs suggests deformation and formation of the foliation occurred under the same stress field which resulted in passive rotation of the biotite grains sub-perpendicular to the maximum normal stress component. Although the shear zone sample appears to have a mylonitic fabric in the field, the quartz CPO is not typical for a mylonite (Toy et al., 2008, Barth et al., 2010). I suggest syn-melt deformation of the quartz with progressive crystallisation results in a weak CPO regardless of deformation intensity. As there is little evidence for post-melt deformation in the CPO, I suggest grain size reduction through pinning gives the appearance of a mylonite that formed syn-melt.

As a result of the microstructural and petrology data, I propose a model for melt organisation, strain localisation and formation of a fine grain size during partial melting. The model starts with a homogeneous solid gneiss where strain is distributed evenly (Figure 4.11a). Melting is generally evenly distributed throughout the leucosome; however, where melt connectivity is slightly higher, the melt organises into layers whereas elsewhere it remains as disorganised 'pools' (Figure 4.11 b, c).

The organised melt system results in a viscosity reduction compared to the disorganised melt system and in turn results in a higher strain for a lower shear stress as shown by Rosenberg and Handy (2005). Increased shearing of the melt thins the melt layers (Figure 4.11d). Strain localises into the melt zones resulting in a stress-driven organisation of melt (Brown and Solar, 1998a, Rosenberg and Handy, 2005, Vanderhaeghe, 2009). The melt drains from the nearby migmatite into the shear zones and forms the initial stages of a melt pathway and the mylonite-like fabric. The localisation of strain into the isolated mylonite-like units suggest Type 2 shear zones were active at Nupen (Figure 2.1; Fossen and Cavalcante, 2017). Strain progressively localises from the whole migmatite into central portions that form the apparent mylonites. I suggest the shear zones at Nupen are short-lived and do not develop melt pathways to expel significant melt from the system.

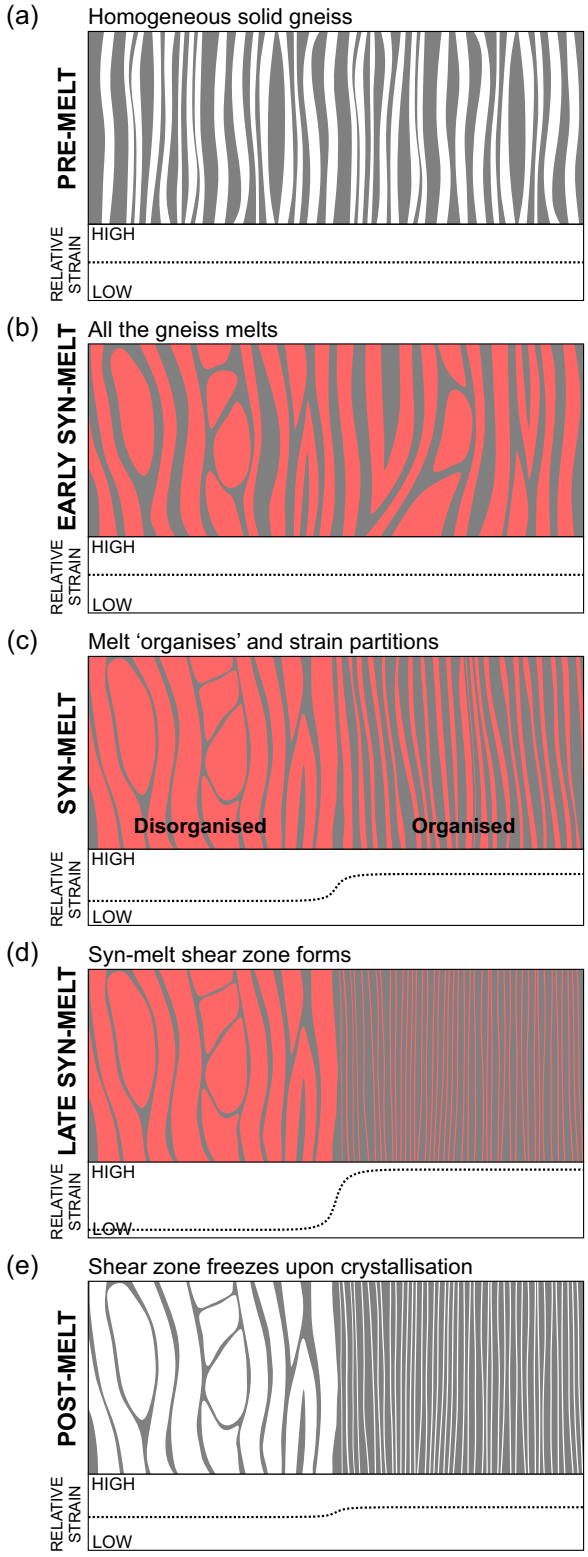

Figure 4.11: Schematic diagrams to show how strain localisation can vary during syn-melt shearing of a migmatized gneiss. Under each stage of the models are relative strain profiles indicating areas of strain localisation. (a) Homogeneous solid gneiss where strain is distributed evenly; (b) melting is pervasive throughout the leucosome; (c) melt organises into layers whereas elsewhere it remains as disorganised 'pools'; (d) runaway organisation effect produces syn-melt shear zones; (e) structure freezes upon crystallisation giving a mylonite-like outcrop style in the field.

The shear zones formed thin melt bands due to higher strain accommodation when the rocks were partially molten. This layering constrained grain growth and increased heterogeneous nucleation rates in the fine grained rocks. When the melt crystallised the grains do not have the space (or surface energy) to grow. This resulted in the small grain size in the organised melt layers giving the mylonitic appearance seen at outcrop scale today (Figure 4.11e). This process induces a mylonitic macroscale appearance of the shear zone without the solid-state deformation fabric expected of a mylonite. The melt organisation process generates (or preserves) grain size heterogeneity without significant solid-state deformation in shear zones after solidification of the migmatite. This means a mechanism for later strain localisation is preserved in a system which has not undergone later deformation. The resulting heterogeneity allows formation of shear zones in areas such as South Armorican Shear Zone, Brittany (Brown and Dallmeyer, 1996), Wet Mountains, Colorado (Levine et al., 2013), and the Himalayas and Karakoram (Searle, 2013) where there is a longer history of post-solidification deformation.

The multiple mylonite-like shear zones across Nupen may be explained by short-lived melting. Deformation-assisted, channelized melt flow occurs when a unit resembles a shear zone in the field but lacks the microstructural evidence for deformation (e.g. Carter and Dworkin, 1990, Streit and Cox, 2002, Cartwright and Barnicoat, 2003, Meek et al., 2019). The weak, disorganised CPOs from the Nupen Peninsula (Figures 4.10, A.2) and preservation of delicate melt textures indicates deformation did not continue post-crystallisation supporting the occurrence of deformation-assisted channelized melt flow. Figure 4.12 demonstrates how these short-lived melt shear zones may occur. During exhumation, partial melting occurred by decompression melting, this partial melting formed the migmatites observed at Nupen and organisation of the partial melt results in the formation of the mylonite-like shear zones. In this model, the partial melt zones are short-lived, transient features within the crust and upon melt loss and/or crystallisation they have a much stronger crystal framework than the actively melting and non-melt crust (Figure 4.12b). Strain localises into the melt zones whilst active but jumps to a new melt area upon melt loss/crystallisation of the former system. This

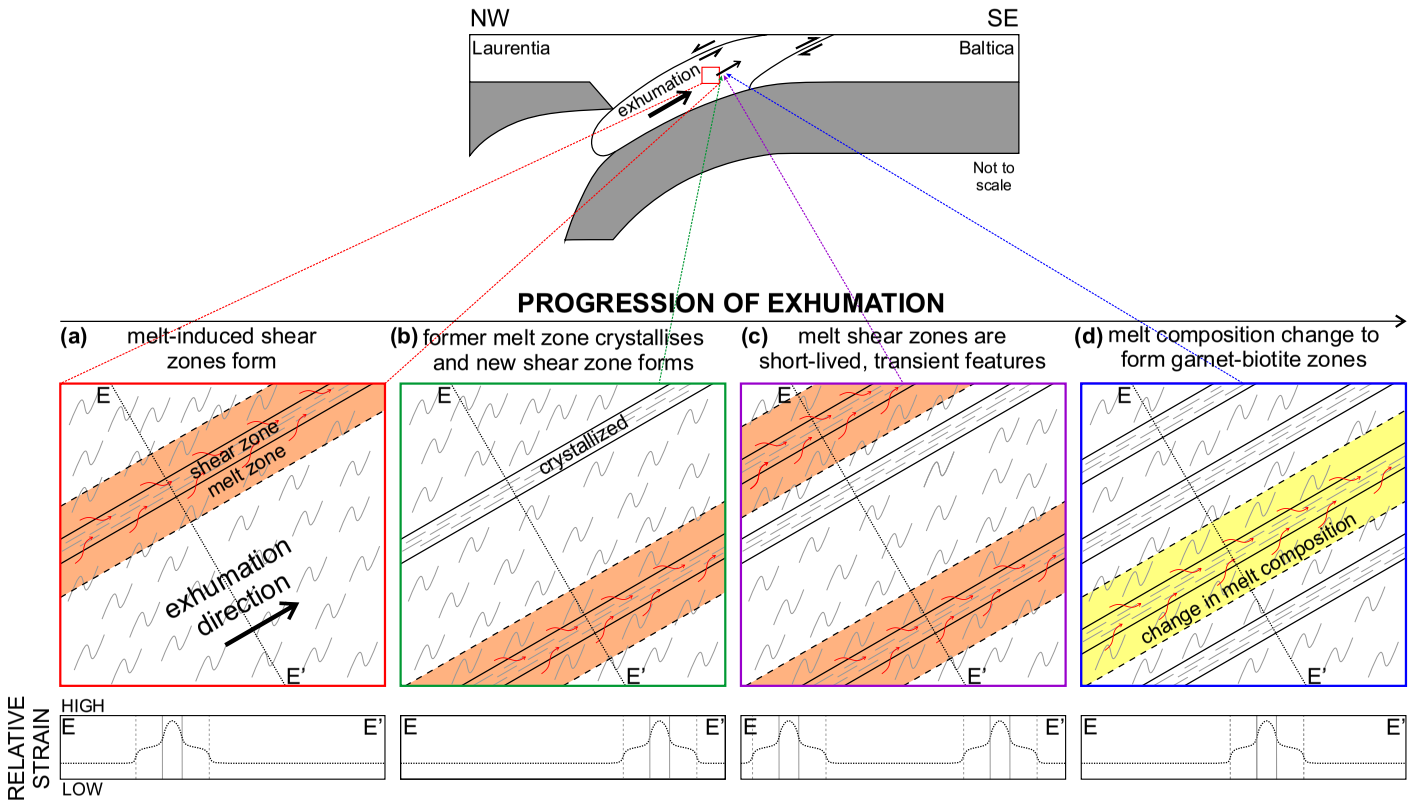

Figure 4.12: Schematic model for formation of multiple syn-melt shear zones in the Nupen Peninsula. (a) Melting initiates and forms an 'organised' shear zone with apparent mylonite-structure in the field (e.g. Figure 4.11); (b) as exhumation progresses the former syn-melt shear zone crystallises to form a strong mineral framework and a new syn-melt shear zone forms; (c) syn-melt shear zones are short-lived, transient features and continue to re-localise strain each time they form, more than one shear zone may be present at any time and repositioning can be non-sequential; (d) melt composition varies allowing formation of garnet-biotite shear zones in addition to granitic melting. Below each diagram is a relative strain estimate for each time step through section E-E'.

jump can be non-sequential and more than one melt shear zone may be active at a time (e.g. Figure 4.12c; Gardner et al., 2017). The Nupen area was predominantly infiltrated by granitic melt but the garnet-biotite zones are evidence for a different melt source, the open-system partial melting in the WGR was likely fed by a major melt source and the melt composition may change during evolution of this syn-melt deformation system (Figure 4.12d). The syn-melt shear zones at Nupen result in a shear zones that lack a mylonite-like microstructure and crystal fabric despite their field appearance.

A summary of the geological events that lead to the formation and structure of the Nupen Peninsula are summarised below.

1. Collision of Baltica and Laurentia during the Caledonian Orogeny (430-410 Ma; Hacker and Gans, 2005).

2. Proterozoic Baltica basement subducted to Eclogite facies conditions (425-400 Ma; Hacker et al., 2010).

3. Western Gneiss Region exhumed from 100 km to shallow crustal levels (400-385 Ma; Hacker et al., 2010).

4. During exhumation, in-situ partial melting of the gneiss occurred via post-UHP decompression-related retrograde amphibolite metamorphism (Gordon et al., 2016). In-situ partial melting occurs at Nupen.

5. Melt begins to 'organise' to for finer layers whilst elsewhere it remains in disorganised pools.

6. Runaway organisation effect produces progressively finer layers and eventually forms the shear zones.

7. Structure freezes upon crystallisation giving a mylonite-like outcrop style in the field.

8. Melting to form the organised shear zones may have been active at different times or synchronously.

9. The WGR was exhumed to 15-20 km followed by rapid cooling (357 Ma; Root et al., 2005).

4.6 Conclusions

In this study I have interpreted the mechanisms for strain partitioning at Nupen in the WGR, Norway. I observe a feedback process where reorganisation of the melt leads to strain localisation and grain size reduction, which in turn results in increased strain partitioning. Whereas mylonite-like fine grained rocks are normally interpreted to have formed due to shearing in the solid-state, here I observe a mylonite-like rock that probably formed while partially molten and, therefore, lack the deformed microstructure of a mylonite. This situation implies that while partially molten volumes are weaker than completely solid rock, internal heterogeneities may result in significant differences in relative, effective rheology and therefore strain partitioning.

Fine grained shear zones are not necessarily post-melt or retrograde mylonites. The once-molten rocks do not necessarily accumulate further strain once crystallised. However, the organisation of partial melt forming syn-melt shear zones could be the origin of the mechanical heterogeneity needed to allow later strain localisation. If the shear zones continued to deform post-melting in the solid-state I would expect to see strain localise into the shear zones with evidence for solid-state deformation and the loss of melt microstructures. This process would produce the mylonitic fabrics observed in shear zones.

Chapter 5

Modelling the impact of melt on seismic properties during mountain building

This chapter defines the methodology for seismic modelling of melt in the crust. In contrast to Mainprice (1997) and Hammond and Kendall (2016), this study uses the real rock properties of the migmatites from Chapters 3 and 4. This study has been published in the journal *Geochemistry, Geophysics, Geosystems* as Lee et al. (2017), thus most of the content of this chapter is shared with the publication. All scientific content was produced by myself with coauthors providing opportunities for discussion and editorial corrections. This chapter features updated results after improved melt calculation in Chapter 3, and additional results to include the field area from Chapter 4. The comparison with active melting in the Himalaya-Tibet orogeny is found in Chapter 6.

5.1 Background

Large volumes of partial melt have been suggested to exist in the middle and lower crust of orogens where they can significantly affect the crustal rheology and may enable processes such as strain localisation, channel flow, melt channelling into shear zones, and post-orogenic collapse (e.g. Arzi, 1978, McKenzie, 1984, Hollister and Crawford,

1986, Brown and Solar, 1998b, Rutter and Neumann, 1995, Brown, 2007, Kohlstedt et al., 2009, Sawyer et al., 2011, Jamieson et al., 2011, Brown et al., 2011). The stability and rheology of active orogenies (e.g. Himalaya-Tibet orogen) is thought to be in part controlled by crustal melts. Seismology has been used to predict melt volumes in the crust and mantle in orogenic systems as well as volcanic environments (e.g. Hirn et al., 1997, Blackman and Kendall, 1997, Holtzman et al., 2003, Bastow et al., 2010, Cornwell et al., 2010). In the melt-rich environments of MORs and volcanic regimes, it has become clear that melt shape and distribution is important when predicting melt volume (Mainprice, 1997, Hammond and Kendall, 2016). However, this type of analysis has not been applied to orogenies that are more chemically and structurally complex than MORs (see Section 2.4). Nevertheless, an assessment of the amount and distribution of melt is crucial to understand lithospheric rheology.

The partitioning of stress and strain between melt and solid is uncertain and different approximations are used to calculate seismic properties. For solid rock, Vp, Vs and AVs can be calculated from the CPO of mineral phases according to their modal proportions (Tatham et al., 2008, Lloyd et al., 2009, 2011a,b). Partial melts impact on these estimates (Holtzman et al., 2003, Holtzman and Kendall, 2010), typically causing reductions in velocities (Schilling and Partzsch, 2001). It is commonly assumed that seismic velocities decrease linearly with increasing melt volume (e.g. Schilling and Partzsch, 2001, Caldwell et al., 2009, Lin et al., 2014), however, recent evidence suggests that melt-seismic property relationships are non-linear (Karato, 2010, Hammond and Kendall, 2016), whilst the effect on AVs remains unclear (Xie et al., 2013).

In this chapter, I adapt and further develop modelling methods used to estimate melt in volcanic regimes and MORs (Mainprice, 1997, Hammond and Kendall, 2016) and apply them to field examples of migmatitic shear zone. This approach incorporates the CPO, chemistry, melt shape, and melt body orientation with respect to the seismic wave propagation direction, in order to evaluate expected uncertainties and possible signatures of the combined effect of these parameters on seismic velocities and anisotropies. EBSD is used to measure CPO in the sheared migmatites,

from which models invoking varying amount, shape, distribution and orientation of melt give an assessement of their impact on seismic properties. I explain how the models are built and work for a simple case, I then apply the modelling to geological and geophysical systems. I show that the interaction of all of the modelled geological parameters play a key role in the seismic wave behaviour which, as a consequence, is non-linear across the examined mid-crustal shear zone analogues.

5.2 Seismic modelling

I have developed four melt models that incorporate shape and crystal fabrics to model the seismic properties of mid to lower crustal melt (Figure 5.1): (a) 'no fabric', (b) 'shape fabric', (c) 'layered fabric' and (d) 'crystal fabric'. The starting point for the creation of models of seismic properties for partially molten rocks is to acquire EBSD data to give the mineral phase proportions as well as the CPO. The CPO and, consequently, its effect on seismic properties can be both strengthened or reduced during shear induced melting or anatexis, depending on the starting lithology and fabrics, associated phase reactions, and deformation style and magnitude. The inclusion of CPO into the models emphasises the importance of the mineral composition and crystal fabric that can be up scaled to infer the seismic-scale crustal fabric, which in turns controls the seismic behaviour (Lloyd et al., 2011a). The modelling approach builds on previous studies modelling the effect of melt shapes, distributions and orientations on seismic properties on one hand (e.g. Watanabe, 1993, Hammond and Humphreys, 2000b, Taylor and Singh, 2002, Hammond and Kendall, 2016), and the CPO-based modelling method of Mainprice and Humbert (1994) and Lloyd et al. (2011a) on the other hand. The approach aims to examine the combined effect of the key parameters which affect seismic behaviour: melt body shapes and orientations, and the CPO of the solid phase.

The elasticity of the solid phase is based on CPO determined via EBSD at the University of Leeds (see Section 2.5.2 for operating conditions). The seismic properties of the constituent minerals and hence the bulk rock were predicted from

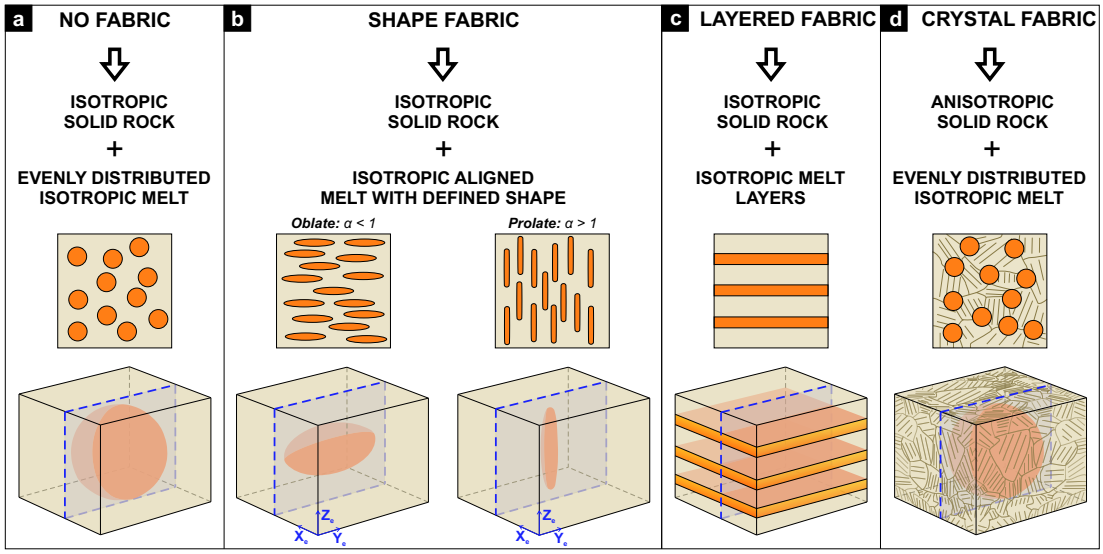

Figure 5.1: Melting models to calculate the seismic properties with variation in melt fraction: (a) no fabric, (b) shape fabric based on Tandon and Weng (1984), adaptation of Eshelby (1957), (c) layered fabric based on the theory of Backus (1962) and (d) crystal fabric models.

the CPO according to the modal composition (Mainprice and Humbert, 1994). The model methodology, therefore, takes into account the anisotropy induced by the measured mineral properties in the solid phase (see Table C.1 for solid crystal properties; Lloyd et al., 2009). I take this relatively standard approach further by then assigning melt fractions into the model in order to study how the combination of CPO-induced anisotropy and melt affects the seismic properties. Any melt fraction can be specified in the models, allowing the calculation of the seismic properties of the resulting rock-melt aggregate. In this initial simple approach, I have 'melted' all the phases without considering metamorphic phase reactions as the melting progresses (e.g. phase reactions from biotite or hornblende to pyroxene).

For the melt phase I assume isotropic elasticity with a small but finite shear modulus. I assume a bulk modulus, K, of 16.1 GPa, appropriate for andesitic composition (Rivers and Carmichael, 1987, Bass, 1995) and set the shear modulus, μ, of 0.01 GPa. For reference, K = 13.5 GPa and 19.4 GPa for rhyolitic and basaltic melts respectively (Rivers and Carmichael, 1987, Bass, 1995). These values give isotropic properties to the elasticity and to allow calculation of the Reuss bound where a shear modulus >0 GPa is required (Kushiro, 1976, Karato, 2012). A melt with zero shear modulus can be used to calculate the shear wave velocities

propagating parallel to the layers and polarised such that the particle motion is parallel to the layers (i.e. physically this is a wave in the solid layers).

The same elastic stiffness matrix is used for all melt phases. However, the density of melt varies according to melt composition (Bottinga and Weill, 1970), which is calculated via the 'Magma-Density' spreadsheet (Preston, 2006). A melt density is calculated for each 'melted' mineral using the molar weight percent of oxides, wt%, molecular weight, M_W, giving the mole fraction, M_F (Equation 5.1), and molar volume at 800^{o}C, M_T (The peak temperature for leucosome-rich domains in the natural example considered later, Menegon et al., 2011), from which a melt density, ρ, is calculated (Equation 5.2). Individual mineral melt densities are averaged according to modal proportion to give the whole melt composition assuming the same mixing laws as for solids.

$$M_F = \frac{wt\%/M_W}{\sum wt\%/M_W} \tag{5.1}$$

$$\rho = \frac{\sum M_F/M_T}{\sum M_F/M_W} \tag{5.2}$$

The first and simplest model developed is the 'no fabric' model (Figure 5.1a), which constrains an isotropic end member case. It uses an isotropic solid rock aggregate with isotropic melt evenly distributed as spheres, such that there is no shape or fabric effect for melt or solid phases in this model. To calculate the isotropic elastic stiffness tensor, an upper bound Voigt aggregate tensor is calculated for the individual minerals in the sample using functions within the MTEX toolbox (Bachmann et al., 2010, Mainprice et al., 2015). The Voigt average stiffness tensor of the solid rock aggregate, C, is given by averaging the elements of the rotated single crystal tensor giving the anisotropic elasticity (after Walker et al., 2011):

$$\mathsf{C}^{V}_{ijkl} = \sum_{n=1}^{N} g^n_{i\alpha} g^n_{j\beta} g^n_{k\gamma} g^n_{l\delta} c_{\alpha\beta\gamma\delta} \tag{5.3}$$

where Bunge Euler angles describing the orientation of each crystal are converted into a rotation matrix, $g(\varphi_1, \Phi, \varphi_2)$, limits of summation (1 and N) bound the number

of EBSD points and assumed to represent volume of sample, and repeated indices imply a summation. Similarly, the Reuss average compliance tensor, S, is found using Equation 5.4:

$$\overset{R}{\mathsf{S}}_{ijkl} = \sum_{1}^{N} g^n_{i\alpha} g^n_{j\beta} g^n_{k\gamma} g^n_{l\delta} s_{\alpha\beta\gamma\delta} \tag{5.4}$$

The elastic stiffness tensor of the aggregate is calculated by Voigt-Reuss-Hill averaging of the single crystal elastic stiffness tensor, C, and compliance tensor, $\mathsf{S} = \mathsf{C}^{-1}$. The elastic properties of each mineral are calculated using the single crystal elastic stiffness matrix (c_{ij}, see Appendix).

$$\overset{H}{\mathsf{C}}_{ijkl} = \frac{\overset{V}{\mathsf{C}}_{ijkl} + \left[\overset{R}{\mathsf{S}}_{ijkl}\right]^{-1}}{2} \tag{5.5}$$

Individual Voigt estimate of the elastic stiffness tensors are compiled into an aggregate Voigt tensor according to the modal fraction of each mineral, alongside calculation of an aggregate density of the solid rock (Anderson, 1989). A separate elastic stiffness tensor for melt is defined with a new melt density (Preston, 2006). The bulk and shear moduli are defined for the solid and melt fractions and when combined, these return an isotropic elasticity matrix for the aggregate and the melt. The solid rock matrix is then combined with the melt matrix and converted to an elastic stiffness tensor (Equation 5.6). Aggregate elastic stiffness tensors (C) and densities (ρ) for solid rock and melt fractions are calculated using the following equations within the no fabric model:

$$\mathsf{C} = \mathsf{C}_{\mathsf{agg}}(1-\phi) + \mathsf{C}_{\mathsf{melt}}\phi) \tag{5.6}$$

$$\rho = (\rho_{agg}(1-\phi) + \rho_{melt}\phi) \tag{5.7}$$

where $\mathsf{C}_{\mathsf{agg}}$ is the solid rock aggregate elasticity tensor, $\mathsf{C}_{\mathsf{melt}}$ is the isotropic melt elasticity tensor, ϕ is the melt fraction, ρ_{agg} is the solid rock density and ρ_{melt} is the isotropic melt density.

A development of the no fabric model is the 'shape fabric' model (Figure 5.1b), this model uses effective medium theory to build analytical models of the macroscopic properties of composite materials. Tandon and Weng (1984) adapted Eshelby (1957) inclusion theory for an isotropic inclusion in an isotropic matrix. The shape fabric model incorporates a shape variant for the aligned melt inclusions within the isotropic rock aggregate, applied using the MSAT toolbox (Walker and Wookey, 2012). Melt shape is modelled with a defined aspect ratio (α). For oblate ellipsoids $\alpha < 1$ (e.g. $\alpha = 0.1$ when X_e:Y_e:Z_e = 10:10:1), and are used to represent isolated melt pockets, sheets and pillows. Spheres have an $\alpha = 1$ (X_e:Y_e:Z_e = 1:1:1) and produce an identical model to the no fabric model. Prolate ellipsoids, $\alpha > 1$ (e.g. $\alpha = 10$ when X_e:Y_e:Z_e = 1:1:10), represent elongate magma tubes or tunnels as well as smaller pockets. Here α is modelled between 10^{-4} and 10^{4}, with a value of 10^{-2} used as an analogue for crustal melt layers or lenses as this is the minimum aspect ratio estimated from field examples (see section 5.4).

The layered fabric model (Figure 5.1c) also builds on functions within the MSAT toolbox, but this time applying the theory of Backus (1962) via an effective medium framework. Backus theory shows when isotropic layering is finer than the seismic wavelength, it can be replaced by a homogeneous transversely isotropic medium that behaves identically to the actual medium under static load in the infinite wavelength limit. In this case, the model is built by thin horizontal layers of isotropic rock aggregate and isotropic melt, with melt volume assigned by varying the layer thickness. As this model includes layers of liquid melt, shear waves should not be transmitted through this model. However the elastic stiffness matrix for melt has a finite shear modulus allowing the shear waves to pass through the layered fabric model.

In the aforementioned models, the solid aggregate is isotropic but in nature this is rarely the case. The crystal fabric model (Figure 5.1d) uses an anisotropic solid phase aggregate with a mineral CPO. The fabric is combined with an evenly distributed isotropic melt with the aspect ratio of a sphere. Therefore, the solid phase fabric is taken into consideration here but melt shape is not modelled. The upper bound Voigt aggregate tensor is calculated from the mineral CPO and the elastic stiffness tensors and individual densities for both the solid rock and melt are combined in accordance

with the modal and melt fractions (Equation 5.6, 5.7).

Once the density and elasticity of the melt-rock aggregate has been established, the next step is to find the velocities of seismic waves passing through each model. As these models are anisotropic the phase velocities vary with propagation direction and for any general direction three elastodynamic plane waves can be supported: a fast quasi-compressional wave, qP, with particle motion close to the wave propagation direction, and two quasi-shear waves, qS1 and qS2, with different velocities and mutually orthogonal particle motion normal to that of qP. As most of the models exhibit hexagonal symmetry, I drop the quasi- prefix and name these phases P, S1 and S2, and their phase velocities Vp, Vs1 and Vs2, respectively (Vp>Vs1≥Vs2). For a given propagation direction, these velocities are found from the three eigenvalues, λ_1, λ_2 and λ_3 of the Christoffel tensor, $\mathbf{G}$ or $G_{ik} = C_{ijkl}n_j n_l$ where n is the unit vector pointing in the propagation direction. Once the eigenvalues are sorted the phase velocities are given by:

$$Vp = \sqrt{\frac{\lambda_1}{\rho}}, \quad Vs1 = \sqrt{\frac{\lambda_2}{\rho}}, \quad Vs2 = \sqrt{\frac{\lambda_3}{\rho}}. \tag{5.8}$$

The eigenvectors of $\mathbf{G}$ give the particle motion directions for the three phases. In practice, I either evaluate the three phase velocities for a propagation direction accessible to seismological observation or calculate the phase velocities on a grid of directions to allow contouring the phase velocity surfaces as stereographic projections. The calculations and plotting make use of the MTEX toolbox (Bachmann et al., 2010, Mainprice et al., 2011). I also calculate derived seismic properties based from the phase velocities. In particular, for each propagation direction I estimate the magnitude of shear wave splitting expressed as a percentage shear wave anisotropy, AVs, from:

$$AVs = 200\frac{Vs1 - Vs2}{Vs1 + Vs2}, \tag{5.9}$$

and evaluate the ratio of P- and S-wave velocities (Vp/Vs1 and Vp/Vs2), which can be compared to receiver function analysis.

The penultimate step is to relate the velocities calculated in an abstract model to a

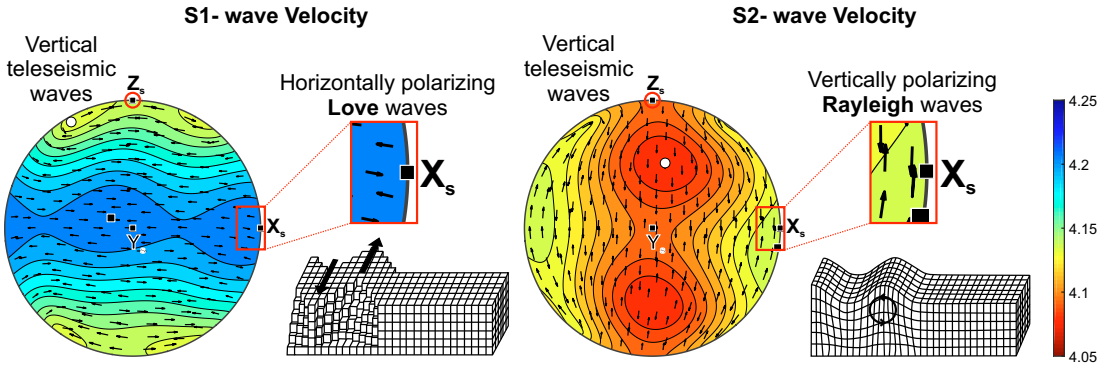

Figure 5.2: Example stereographic projections of Vs1 and Vs2 indicating where analogue teleseismic and surface wave data are taken from. Surface wave data are taken from the X_s-Y_s plane and teleseismic data are taken from X_s. The Vs1 plot shows horizontal polarisation representing Love waves, whereas Vs2 polarises vertically and represents Rayleigh waves.

geographic reference frame that can be related to the Earth. The modelling and sample reference frame, X_m:Y_m:Z_m, relates to the orientation of the symmetry axis. In the case of an oblate melt inclusion, the symmetry axis is in the Z_e direction. Samples are analysed via EBSD in the kinematic reference frame where the X_m-Y_m plane is parallel to the foliation plane and X_m is parallel to the stretching lineation.

Seismic waves propagate in a geographic reference frame, X_s:Y_s:Z_s. P- and S-waves are body waves that propagate through the Earth's interior and are of higher frequency than surface waves (Milsom, 2003). Receiver function analysis is used to image the internal structure of the Earth, using the information from teleseismic earthquakes recorded at a three-component seismograph. Teleseismic body waves are assumed to be propagating (near) vertically when recorded at the seismic station, thus can be derived from the Z_s direction which is vertical in the models (Figure 5.2). P-waves generate P-to-S conversions at boundaries; deconvolution of the incoming vertical and longitudinal components of the seismogram result in a receiver function resolving the detailed structure (Vinnik, 1977, Frederiksen and Bostock, 2000). Polarised shear waves 'split' when entering an anisotropic medium and produce two polarised S-waves (Vs_1 and Vs_2). Here it is assumed that shear waves are the result of SKS shear wave splitting (S-to-P and P-to-S conversions when the ray enters and leaves the outer core) and propagate near vertically through the crust (Z_s direction). The body wave velocity is a measurement of arrival time that is spread along the ray path, this means the

seismic signal for a partial melt layer is an integrated signal (Stein and Wysession, 2003). Analysis of geophysical data gives estimates of phase velocities and anisotropy which are used to compare with my models.

Surface waves propagate horizontally and hence can be derived from the horizontal X_s-Y_s plane in the models. Love and Rayleigh waves are distinguished by the shear wave polarisation direction (Figure 5.2). Love waves are purely transverse in their motion, polarise horizontally and are typically faster (usually Vs1 or defined as VL) than vertically polarising Rayleigh waves (usually Vs2 or defined as VR) in most models (Shearer, 2009). Surface waves represent the apparent velocity which is is frequency dependent and depends on the vertical velocity structure, whereas I calculate the intrinsic velocity of the medium (Stein and Wysession, 2003). For the simplest case (a homogeneous isotropic Poisson half-space) Love waves cannot propagate and Rayleigh waves propagate at 0.92 times the shear wave velocity (Stein and Wysession, 2003). However the Earth is not this simple and surface waves give an estimate of vertical and horizontal S-waves with depth. Rayleigh and Love waves give an estimate of anisotropy for a particular propagation direction parallel to the surface, while both give an estimate of the azimuthal anisotropy (Stein and Wysession, 2003).

5.3 Model results

In order to show the general behaviour of each model I have used sample SIP20 (see Chapter 3, Figures 3.2c, 3.5) to consider cases from 0 to 40% melt, after which value the crystal framework for an effective medium breaks down (Lejeune and Richet, 1995). The seismic results for the four models (no fabric, shape fabric, layered fabric and crystal fabric) are plotted in 3D via stereographic projections for a 20% melt volume (Figure 5.3) and also as analogues for surface waves, X_m-Y_m, and teleseismic, Z_m (Figure 5.4).

5.3.1 3D seismic projection

Stereographic projections of seismic properties for each model show the elastic stiffness relationship when 20% melt is introduced to the solid rock (Figure 5.3). As expected, the no fabric model has no variation in 3D space, yielding identical values for the maximum and minimum in each seismic property, it is isotropic. The impact of the alignment of melt can clearly be recognised in the shape and layered fabric models. When the melt inclusion symmetry axis is parallel to Z_m (e.g. layered fabric

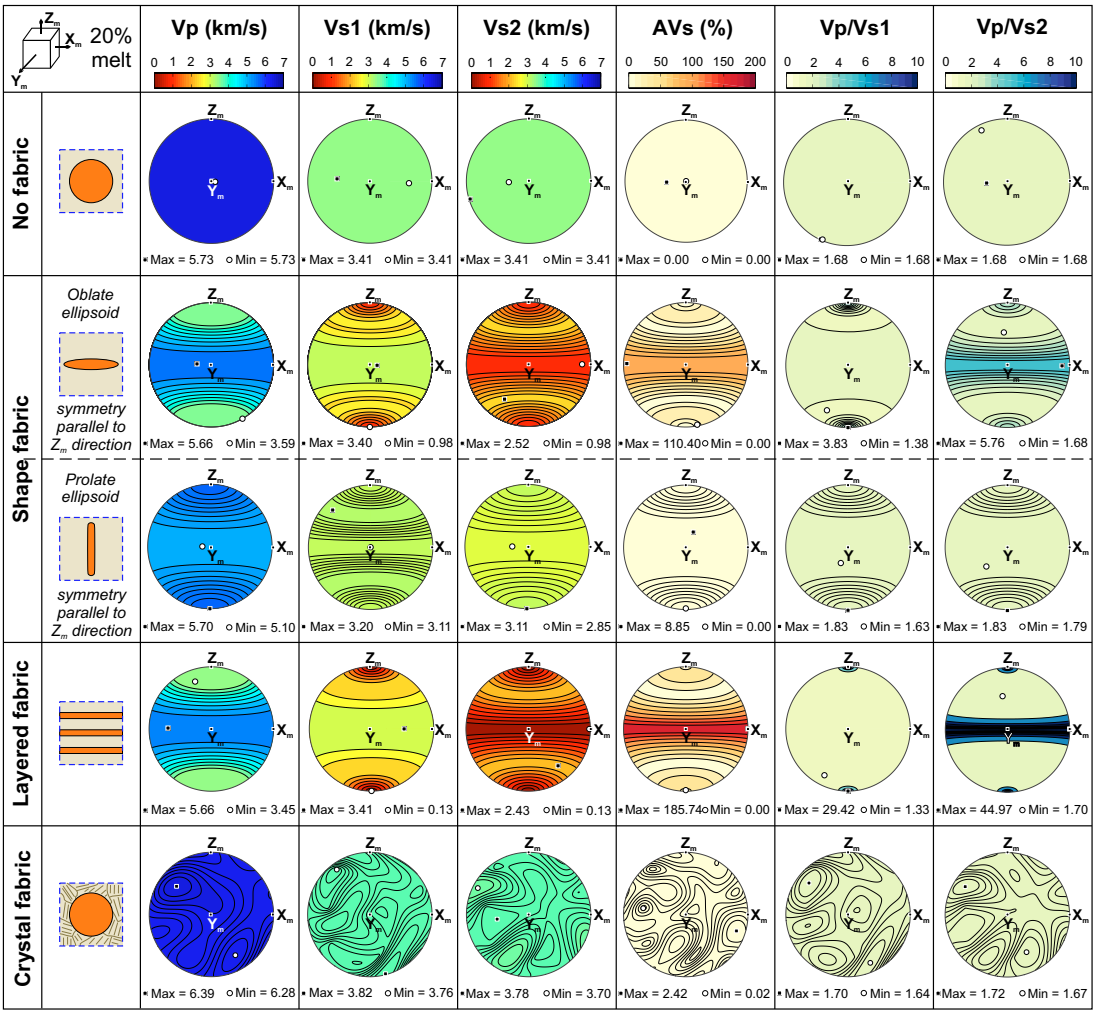

Figure 5.3: Antipodal stereographic projections of the seismic properties at 20% melt for each model. The projections show the relationship of the seismics in 3D. Analogues to teleseismic data is taken from the vertical Z_m direction, surface wave data is taken from the horizontal X_m-Y_m plane. The symmetry axis for all models is in the Z_m direction. Common scales for Vp, Vs1 and Vs2, AVs and Vp/Vs for all models. Black squares and white circles indicate the maximum and minimum points respectively.

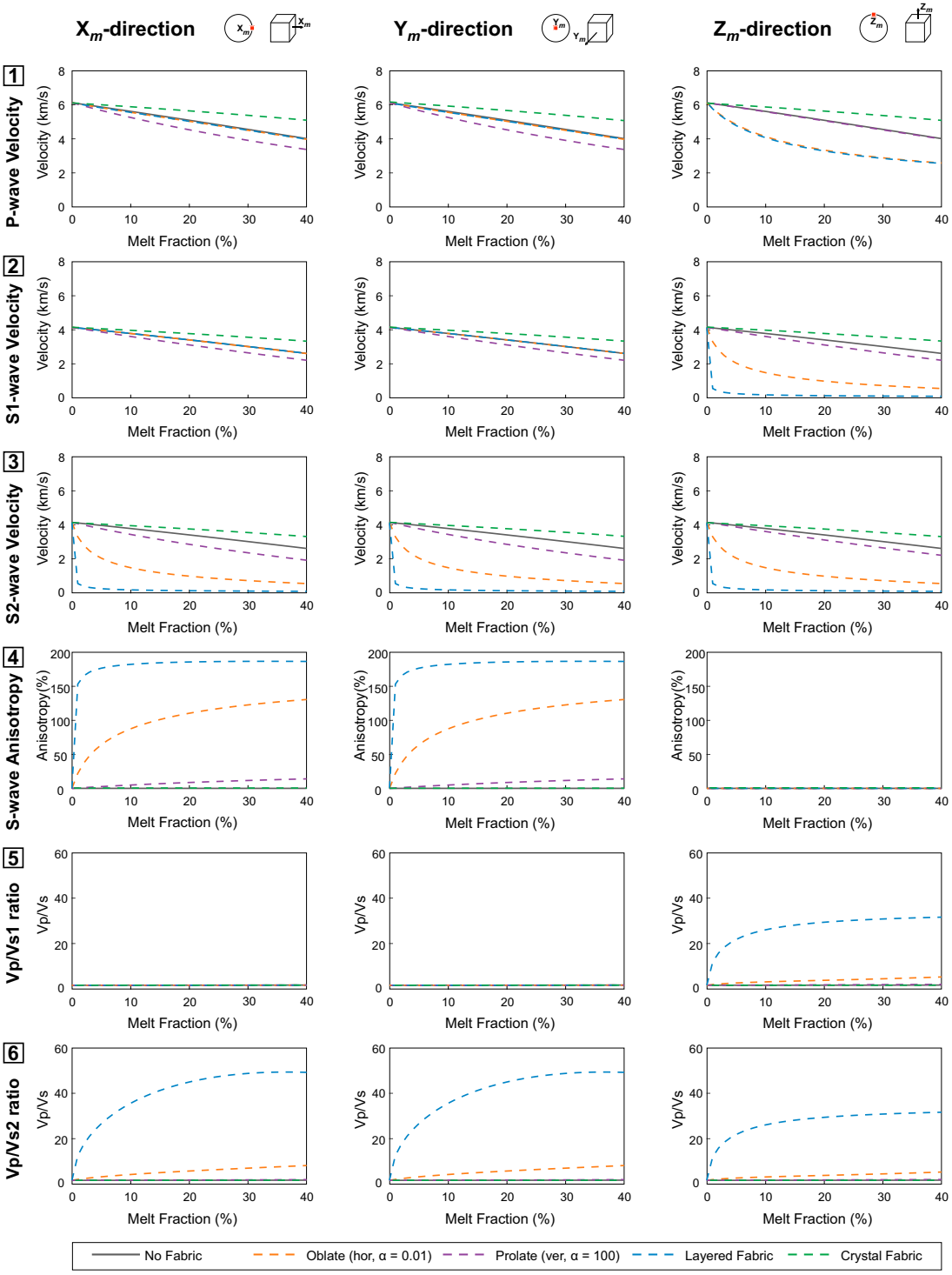

Figure 5.4: Seismic properties for each model with variations in the shape fabric model. Calculated seismic results (1-6) are shown for waves propagating in the X_m, Y_m and Z_m directions. The aspect ratios used in the shape fabric are $\alpha = 10^{-2}$ for oblate ellipsoids and $\alpha = 10^{2}$ for prolate ellipsoids and the symmetry axis is in the Z_m direction.

model, horizontally aligned oblate ellipsoids and vertically aligned prolate ellipsoids in the shape fabric model) velocity lows are parallel to X_m and Y_m. This behaviour switches if the melt inclusions are rotated and the symmetry axis is in the X_m direction, where velocity lows parallel to Y_m and Z_m. The stiffness matrices for the layered fabric model are similar to those for horizontal oblate ellipsoids in the shape fabric model melt, and hence produce similar seismic velocity behaviour. The crystal fabric model considers the mineral CPO and results in a non-uniform seismic projection, which indicates that the CPO induces an anisotropy into the solid phase and, therefore, to the bulk solid-melt aggregate. Variations in orientation within the shape fabric model simply alter the alignment of the symmetry axis, as the minimum and maximum are identical for each variation.

Large difference between Vs1 and Vs2 for oblate ellipsoids and layered melts produce large S-wave anisotropies. Here I show the results for oblate ellipsoids with an α of 10^{-2}, the layered fabric model and oblate ellipsoids give similar results if $\alpha = 10^{-4}$ as this aspect ratio is large enough to be comparable with continuous ('infinite') layers. The large differences between Vs1 and Vs2 also result in large Vp/Vs ratios as Vs1 $\gg$ Vs2. For horizontal oblate ellipsoids in the shape fabric model, the Vp/Vs1 ratio is 60% lower than the Vp/Vs2 ratio. Similarly, Vp/Vs1 is also 60% lower than Vp/Vs2 for the layered fabric model, although the maximum ratio is much larger at 27.76 for Vp/Vs1 and 43.46 for Vp/Vs2.

5.3.2 Surface waves

Surface waves propagate in the X_m-Y_m plane and are sensitive to the S-wave velocity. Where Vs polarises horizontally the surface wave signal would represent Love waves, Vs1 polarises horizontally for all models except prolate ellipsoids with a symmetry axis parallel to Z_m (Figures 5.2, 5.4 X-Y2). Whilst Vs2 polarises vertically and represents Rayleigh waves (Figures 5.2, 5.4 X-Y3). The no fabric, crystal fabric and prolate ellipsoids in the shape fabric models give a linear decrease for both Love (Vs1 or VL) and Rayleigh (Vs2 or VR) waves, decreasing at different rates between models. In the X_m direction for Love waves for the layered fabric and the horizontal

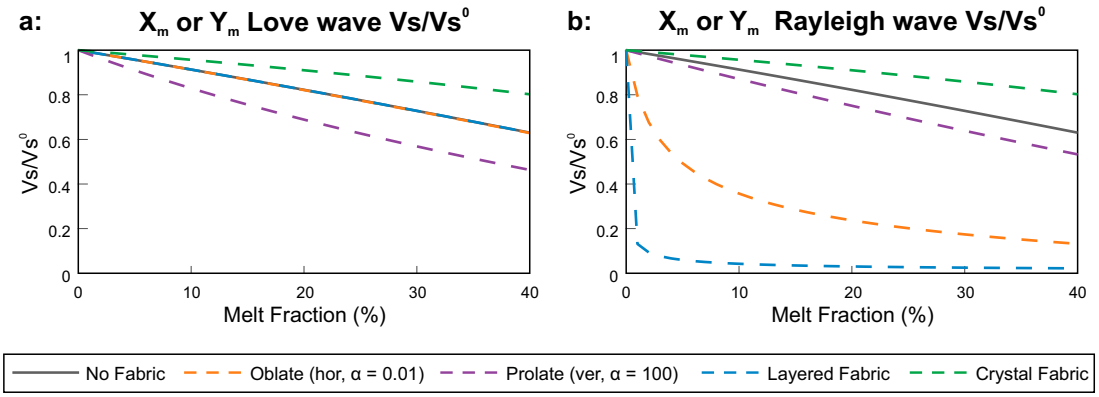

Figure 5.5: Shear wave velocity reduction (Vs/Vs^0) for each model for (a) Love and (b) Rayleigh waves from the X_m or Y_m directions.

oblate ellipsoids in the shape fabric models, the decrease is also linear but variable between models (Figure 5.4 X2). Whereas it is non-linear for Rayleigh waves for the same models, with a rapid decrease in velocity to 25% melt, followed by a more gradual decrease to near 0 km/s at 40% melt (Figure 5.4 X3). A similar behaviour is observed in the Y_m direction for these models (Figure 5.4 Y2-3).

The variations in Vs are reflected in the AVs behaviour (Figure 5.4 X-Y4): AVs is 0% where there is no difference between Love and Rayleigh waves, but equally very large anisotropies are induced when there are differences between Love and Rayleigh waves. The greatest AVs observed is for the layered fabric model, where AVs increases rapidly to ∼180%. This same behaviour but increasing up to ∼120% is seen for horizontal oblate ellipsoids in the X_m and Y_m directions. Prolate ellipsoids also show an AVs increase up to 20% at 40% melt in the X_m and Y_m directions. The crystal fabric model has a constant AVs between 0 and 4% depending on initial mineralogy of the sample.

Figure 5.5 shows the results for the reduction of shear wave velocities that would be inferred from measurements of surface wave dispersion where Vs/Vs^0 is the Vs at the specified melt fraction divided by the Vs^0 at 0% melt. Love and Rayleigh waves are calculated for the X_m and Y_m directions. All models show a reduction of Vs/Vs^0, but this reduction is not linear for models which include low aspect ratio melt inclusions. For Love waves, Vs/Vs^0 decreases linearly for the no fabric and layered models and horizontal oblate ellipsoids in the shape fabric model. The crystal fabric model also decreases linearly but at a slower rate, whereas vertical prolate ellipsoids decrease faster.

For Rayleigh waves, Vs/Vs^0 behaves identically to Love waves for the no fabric and crystal fabric models as well as horizontal prolate ellipsoids in the shape fabric model. Prolate ellipsoids show a slower rate of decrease for Rayleigh wave reduction than they did for Love wave reduction. Oblate ellipsoids show a rapid decrease in Vs/Vs^0 and the layered fabric exhibits an even faster reduction. The symmetry axis of all the models is orientated in the Z_m direction, thus surface waves for the X_m:Y_m plane is non-direction dependent.

5.3.3 Teleseismic waves

Seismic waves travelling in the Z_m direction (approximate analogue for sub-vertical teleseismic waves) are shown in Figure 5.4 (Z1-6). For most models Vp shows a linear decrease, but at differing rates depending on the model, with the layered fabric model and the horizontally orientated oblate ellipsoids in the shape fabric model showing an initial rapid decrease, before decreasing at a slower rate after ∼25% melt is introduced (Figure 5.4, Z1). Vs decreases linearly for most models (Figure 5.4, B-C3), however the layered fabric and oblate ellipsoid models show initial non-linear behaviour.

AVs can be measured from teleseismics via shear-wave splitting where the shear wave window limits the use of Vs to within 35 degrees of vertical, here I calculate the AVs to illustrate the model properties. A 0% anisotropy is observed for the no fabric, shape fabric and layered fabric models (Figure 5.4, Z4). Vs1 and Vs2 are equal in the Z_m direction for these models as the symmetry axis is also orientated in the Z_m direction. The crystal fabric model has a constant AVs of 1.67% due to small variations in Vs caused by the solid rock anisotropy.

Vp/Vs can be measured via receiver functions where back azimuthal variations are used to acquire two Vp/Vs values (Hammond, 2014). Here Vp/Vs is 1.66 at 0% melt for all models increasing to 1.73 at 40% melt for the no fabric and crystal fabric models and 2.03 at 40% melt for prolate ellipsoids in the shape fabric model. Oblate ellipsoids exhibit a faster rate of increase in Vp/Vs1 and Vp/Vs2 increasing up to 5.32 at 40% melt (Figure 5.4 Z5-6). The layered fabric model increases rapidly and non-linearly to Vp/Vs of ∼30 where it remains approximately constant after ∼15% melt.

Vp would not be measured in the X_m-Y_m direction via surface wave data but could be interpreted from tomography. Vp shows similar behaviour for most models, with a linear decrease for increasing melt fraction (Figure 5.4 X-Y1). Even in the case of linear decrease, it is not identical for all models: the crystal fabric model decreases in Vp at a slower rate than the no fabric and layered fabric models, whereas prolate ellipsoids in the shape fabric model decrease at a faster rate.

For the Vp/Vs1 in the X_m and Y_m directions, all models show low ratios (1.66 at 0% melt to 1.71-1.73 at 40% melt), reflecting the Vp and Vs1 behaviours described above (Figure 5.4 X-Y5). This relationship is also observed in the X_m and Y_m directions for Vp/Vs2 for the no fabric, prolate ellipsoids and crystal fabric model. Vp/Vs2 for oblate ellipsoids shows a gradual increase up to 8.18 at 40% melt and reaches $\sim$50 for the layered fabric model.

5.3.4 Rotation of melt inclusions

An oblate ellipsoid can be used as an application for sheets or layers with low aspect ratios, reflecting an overall flattening of the rock volume during melting (e.g. lenses of melt parallel to foliation in orogenies) is an analogue for an interconnected melt network. Melt shaped like prolate ellipsoids can be used as an analogue for elongate magma tubes or smaller melt pockets with finite dimensions and high aspect ratios where the rock is subjected to overall constriction during melting (e.g. magma tubes to transport melt in low strain regions). In both cases, the melt volumes often, although not always, follow pre-existing geological features such as bedding, foliation, or shear zone/fault planes. These geological features are usually not at perfect right angles to the seismic wave propagation direction, whereas the models above and those often used in literature presume this to be the case. However, the angle of incidence of the seismic wave with respect to the feature being imaged greatly affects the observed seismic signal.

Figure 5.6 illustrates the results for each seismic property at 20% melt when the ellipsoids are rotated with respect to the wave propagation direction. As the symmetry axis for oblate melt inclusions is in the Z_m direction, therefore rotations of 90° are shown around the X_e or Y_e planes and measured from Z_m. The symmetry axis for vertically

orientated prolate ellipsoidal shaped melt inclusions is also in the Z_m direction and seismic properties are measured from this direction when rotated around the X_e or Y_e planes. Below each graph is a stereographic projection at 15° intervals of the Vp, Vs1 and Vs2 to show how they change as the inclusions are rotated. For oblate ellipsoids, there is a large variation in seismic velocity as the inclusions are rotated. The velocity changes are not linear as shown by the velocity and Vp/Vs ratios. Where Vs1 and Vs2

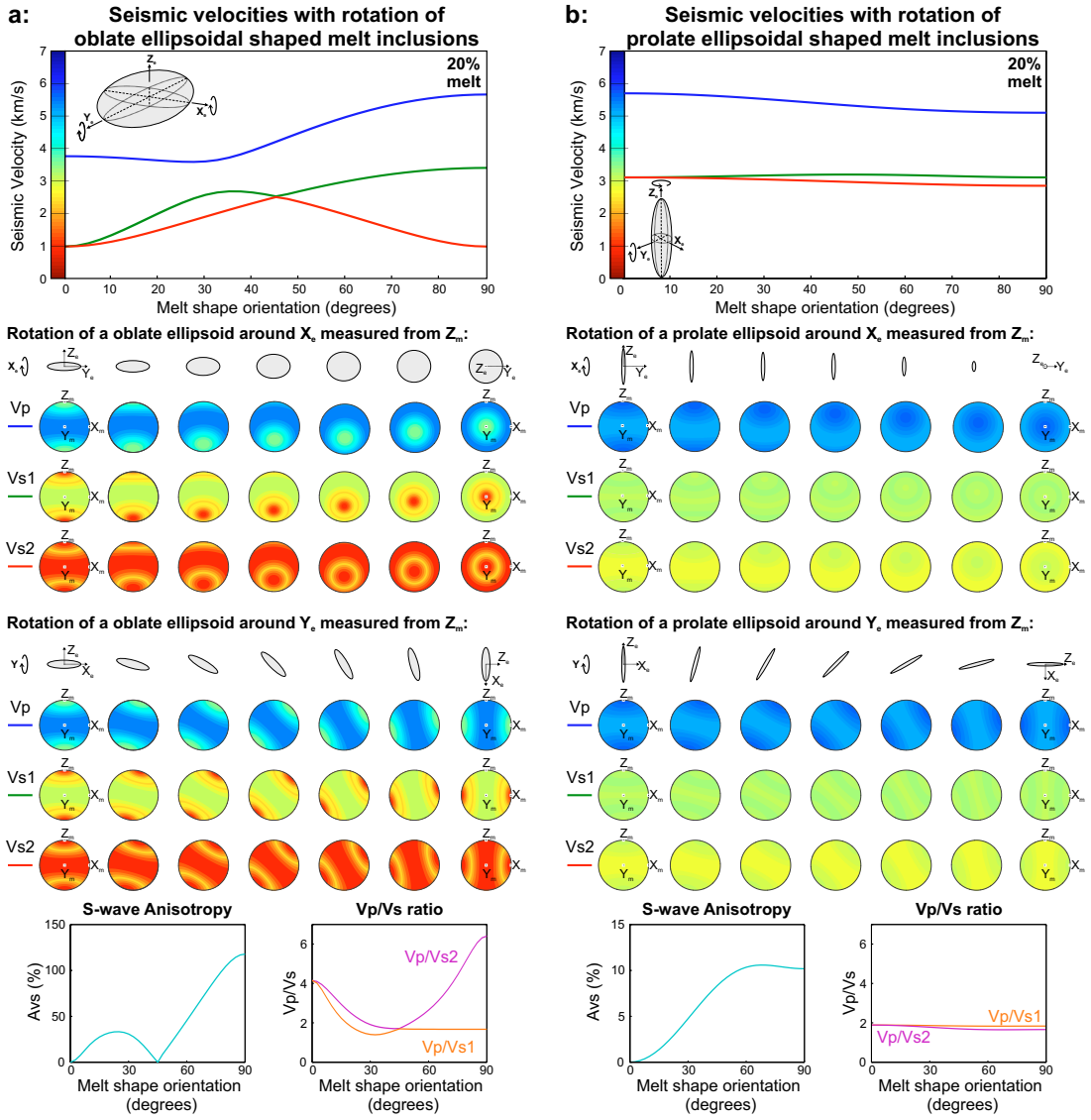

Figure 5.6: Change in Vp, Vs1 and Vs2 with rotation of melt inclusions at 20% melt volume. a) Rotation of oblate melt inclusions ($\alpha = 10^{-2}$) around the X_e or Y_e, measured from the Z_m direction; b) rotation of prolate melt inclusions ($\alpha = 10^{2}$) around the X_e or Y_e axis, measured from the Z_m direction. AVs and Vp/Vs relationship with melt inclusion orientation is shown and seismic stereographic projections of Vp, Vs1 and Vs2 for the rotated melt inclusions are shown beneath the graphs.

are equal there is no shear wave splitting, and hence no anisotropy is observed at 0° and the inflection point at 45°. For prolate ellipsoids, velocity change with rotation is not as pronounced. Variation between Vs1 and Vs2 between 60° and 90° induces a 10% anisotropy and the Vp reduces only slightly between ∼20-60° rotation.

5.4 Application to natural migmatites

To test the seismic melt models defined in this chapter in a geological setting, I input the conditions observed in the Øksfjord (Chapter 3) and Nupen (Chapter 4) partial melt shear zones to explore the range of results before finally comparing with results from an active orogeny. The melting models are applied to samples collected across the migmatized shear zones, in order to investigate how the observed changes in melt fraction, melt pocket/layer shape and orientation, and the CPO of the solid phase affect the seismic wave behaviour across a deep crustal, partially molten layer. The two field areas have different styles of partial melting allowing various complexities to be modelled. Therefore, the field examples serve as an analogue for a deep crustal partially molten shear zone/layer that which has been assumed to exist under the Himalayan-Tibetan crust. The results underline the difficulty of predicting melt fractions from seismic data.

5.4.1 Seismic properties of a syn-melt Øksfjord Shear Zone

Seismic properties were calculated for multiple samples from a traverse across the ØSZ for the four models: no fabric, shape fabric, layered fabric and crystal fabric. The palaeomelt fraction varies for each sample and has been quantified by microstructural analysis of the sample (see Chapter 3 for detail on melt quantification). Results shown in Figure 5.7 are for waves propagating in the horizontal X_s and Y_s directions and vertical Z_s direction, giving analogues to surface and teleseismic waves respectively at the time of melting. Therefore, these models assume the melt pockets are either vertical or horizontal in the crust, in order to provide a simplified example of the effect of the different melt configurations alone. It should be noted that additional complexity, as

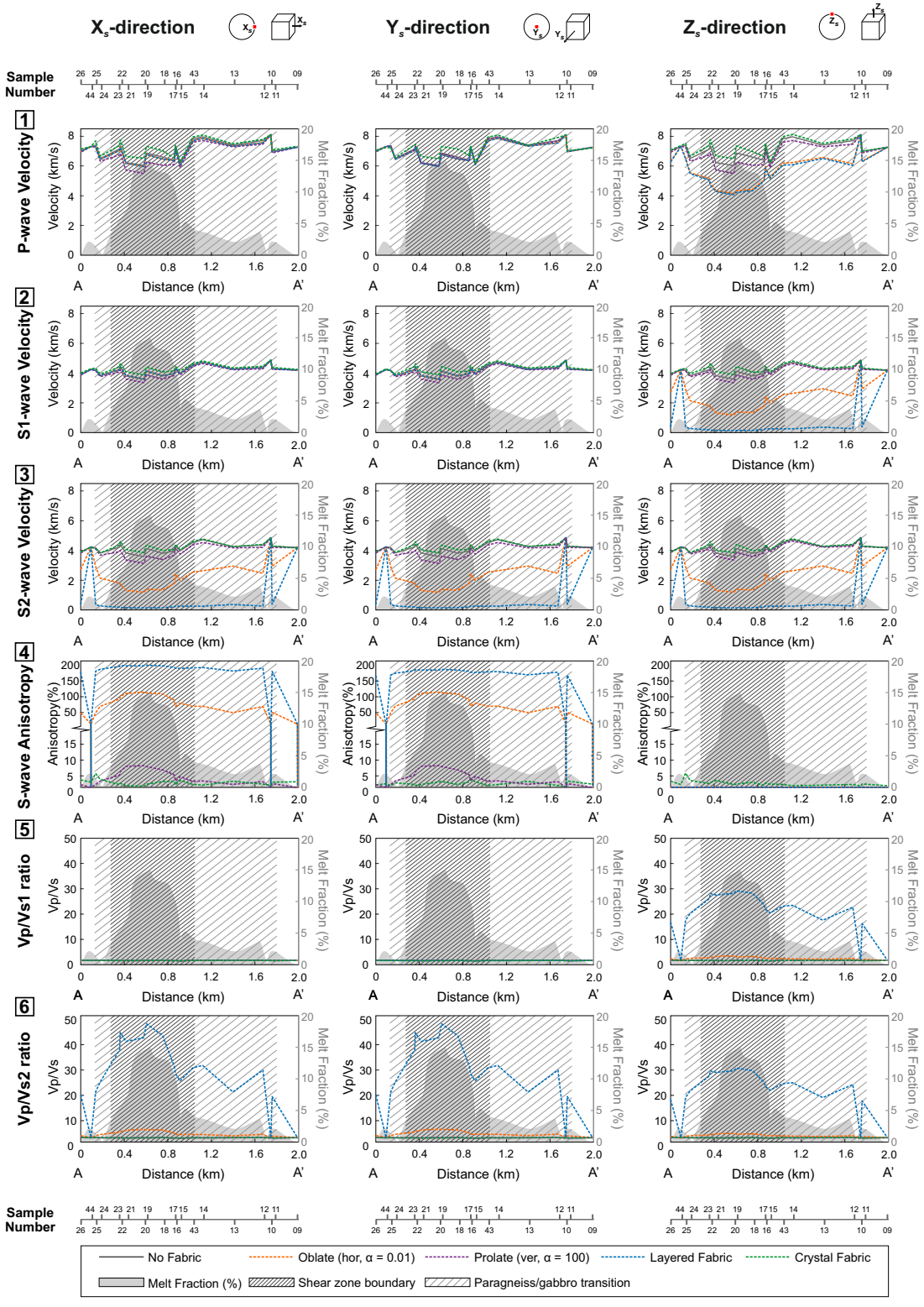

Figure 5.7: Change in seismic properties across the ØSZ for each of the four models with additional variation in the shape fabric model. Seismic property results (1-6) are shown for waves propagating in the X_s, Y_s and Z_s directions (Figure 5.3, 5.4). Relative sample location along the section line is shown in the bottom left diagram. Melt fraction calculated from the field and microstructural studies in Chapter 3 and indicated by the grey polygon.

shown in Figure 5.6, would result from the equally realistic case of an anatectic layer that is inclined (i.e. at an angle to the seismic wave propagation direction).

All models show the expected general trend of a velocity reduction with increasing melt fraction but it is not a simple linear trend and there are significant differences between models. Mineral properties (matrix density and elastic stiffness) and CPO strength have a significant effect on the seismic velocities, although the latter is only present for the crystal fabric model. For example, the strongly orientated minerals in sample SIP43 cause a greater increase in the velocity for this sample compared to others at the same melt fraction of 15%. The layered fabric model show a much larger reduction of Vs compared to the other models (Figure 5.7 XYZ2-3), especially when seismic waves propagate in the Z direction where they travel perpendicular to the melt layers as opposed to parallel in the X and Y directions. The horizontally layered oblate melt inclusions in the shape fabric model show similar results to velocities calculated from the layered fabric model (Figure 5.7 XYZ1-3).

When Vs1 and Vs2 are equal, AVs is zero, as shown for the no fabric, shape fabric and the layered fabric models in the Z propagation direction (Figure 5.7 Z4). When seismic waves propagate parallel to the orientation of the oblate melt ellipsoids in the shape fabric model AVs increases up to 120% with greater melt volumes compared to 12% for vertically orientated prolate ellipsoids. This is due to the isotropic melt shape component inducing strong anisotropy. The small differences between Vs1 and Vs2 in the crystal fabric model yields a decreasing AVs with increasing melt volume, but the AVs variation is minimal when compared with the large increase in AVs caused by the vertical inclusions in the shape fabric model.

Vp/Vs results for the no fabric model, prolate ellipsoidal melt inclusions in the shape fabric model and crystal fabric models are similar (Figure 5.7 XYZ5-6). They remain constant at just below 2, indicating that isotropic material, tubular melts, or CPO have very little effect on the Vp/Vs ratio. When oblate melt inclusions and/or melt layers are considered, Vp/Vs1 is similar to results from the other models, however, results for Vp/Vs2 reflect an overall increase in melt fraction, but the relationship is not linear (Vp/Vs does not increase at the same rate as melt fraction). In the X and

Y propagation directions, Vp/Vs2 is increased compared to the other models, in the Z direction it is ∼30% lower but is also equal to Vp/Vs1. The layered melt model shows very large Vp/Vs ratios compared to the other models. Thus a significant increase of Vp/Vs2 is likely to be a good indicator for the presence of melt layers or large aspect ratio melt ellipsoids.

5.4.2 Seismic properties of a syn-melt Nupen Peninsula

Seismic properties were calculated for samples from the traverse across Nupen Peninsula for the four models: no fabric, shape fabric, layered fabric and crystal fabric. The palaeomelt fraction varies for each sample and has been quantified by microstructural analysis of the sample (see Chapter 4 for detail on melt quantification). Results shown in Figure 5.8 are for waves propagating in the horizontal X_s and Y_s directions and vertical Z_s direction, giving analogues to surface and teleseismic waves respectively at the time of melting. These models, therefore, assume the melt pockets are either vertical or horizontal in the crust, in order to provide a simplified example of the effect of the different melt configurations alone.

Similarly to results from the ØSZ, all models show the expected general trend of a velocity reduction with increasing melt fraction. However the Nupen Peninsula is more complex than the other case studies and melt volume decreases into the shear zones as opposed to increasing as seen at ØSZ. The effects of melt volume, shape, orientation and mineral CPO is best summarised in the AVs and Vp/Vs2 plots (Figure 5.8 XYZ4,6).

AVs results for the shape and layered fabric models are emphasised when seismic waves propagate parallel to the long axis of the melt inclusion (Figure 5.8 XY4). AVs for prolate ellipsoidal melt inclusions ranges from 1% in the shear zones to 10% in areas of higher melt volume outside the shear zones. This trend in AVs is also observed for oblate ellipsoid shaped melt inclusions (36 to 116%) and melt layers (163 to 185%) at an order of magnitude greater than results for other models. The CPO at Nupen strongly effects the AVs results. There is significant shear wave splitting when seismic waves propagate in the X and Z directions where AVs varies from 2 to 12% in X and 2 to 11% in Z. However, AVs in the Y direction is much lower, ranging from 0.6 to 5%

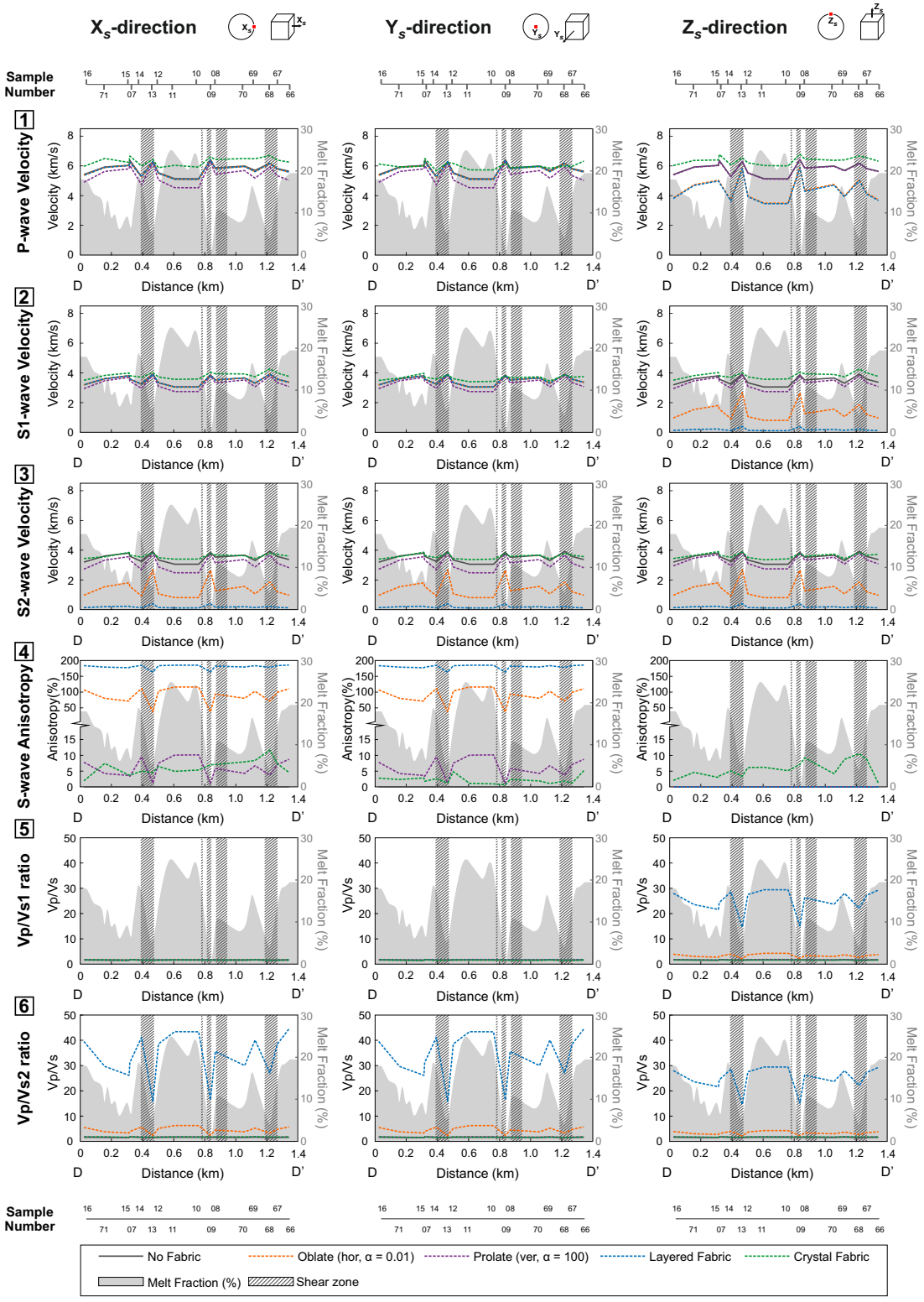

Figure 5.8: Change in seismic properties across the migmatized Nupen Peninsula where a series of shear zones yield lower melt volumes. Seismic property results (1-6) are shown for waves propagating in the X_s, Y_s and Z_s directions (Figure 5.3, 5.4). Relative sample location along the section line is shown in the bottom left diagram. Melt fraction calculated from the field and microstructural studies in Chapter 4 and indicated by the grey polygon.

indicating the crystal fabric is orientated parallel to Y.

As the melt volume decreases into shear zones, Vp/Vs2 also decreases (Figure 5.8 XYZ6). The shear zones are proposed to have acted as conduits for melt to leave the system, thus seismic properties calculated using the low palaeo-melt volumes would not reflect seismic properties from active syn-melt shear zones.

5.5 Conclusions

Using the experience gained in the present study, future modelling efforts should aim at combining the CPO approach with melt body shapes, orientations, and connectivity. Nevertheless, the models presented here are geologically realistic and can be used to inform geophysical data interpretation and other modelling efforts: the four numerical melt models in this study use real geological data to calculate seismic properties. The solid phase properties and the mesosome (paleo melt) volume are estimated from microstructural analysis and input into the models. The progression of partial melt is assumed to initiate with melt at triple junctions (Holness, 2006). Such very small melt volumes, cannot be modelled as spheres or ellipsoids as they are cuspate in shape (Hammond and Humphreys, 2000b). At present no model incorporates cuspate melt inclusions, but the crystal fabric model may be appropriate when melt volume is low and the CPO is the more dominant factor.

As melt volumes increase, melt body shape has a much larger impact on the seismic properties; melt wets grain boundaries (Garapić et al., 2013) and as volumes increase further, they form lenses, layers and channels, allowing transport of the melt (Kelemen et al., 1997, Berger and Kalt, 1999, Vanderhaeghe, 2009, Holness et al., 2011). This suggests that oblate ellipsoids in the shape fabric model and layered fabric model are most appropriate analogues for larger melt fractions. However, local geological fabric can be expected to have influence in the spatial orientation of these oblate ellipsoids and layers and they cannot be assumed to be either horizontal or vertical. Hammond (2014) shows how back azimuth variations from receiver functions can be used to determine the symmetry axis and thus orientation of melt layers in the crust via anisotropic H-κ

stacking. Exposed sections of migmatitic middle and lower crust clearly indicate that non-horizontal migmatitic layering (e.g. due to shear zone formation or metamorphic dome formation) is a common phenomenon (e.g. Torvela et al., 2013, Platt et al., 2015). In the next chapter I test the models developed in this chapter with seismic responses from the actively melting areas.

Chapter 6

Discussion and synthesis

This chapter contains a synthesis of the main contributions of this thesis, which are divided into two parts: (1) first I compare the partial melt microtextures and deformation microstructures between the two field areas (Chapters 3, 4); (2) I then compare the modelled seismic properties (Chapter 5) from the field areas with data areas of partial melting in the Himalaya-Tibet orogen. The comparison of the palaeomelt shear zone with responses observed in the Himalayas shows which geological parameters are important to consider when interpreting the Himalaya-Tibet crust via teleseismic or surface wave analysis.

6.1 Controls on syn-melt deformation

The two field areas analysed in this PhD thesis provide a window on natural processes occurring in the ductile mid to lower crust and contribute evidence to the link between partial melting and deformation. The contrasting deformation styles between the two field areas addresses the complexities of syn-melt deformation.

The deformation and melting phases in the two field areas are related to different deformation events. The ØSZ formed in an extensional setting via synintrusive deep crustal shearing during the initial stages of the opening of the Iapetus Ocean (570-550 Ma; Chapter 3; Elvevold et al., 1994, Roberts et al., 2006), whereas melting at the Nupen Peninsula and in the wider WGR represents one of the final phases of the

Caledonian orogeny (430-385 Ma; Chapter 4; Schärer and Labrousse, 2003, Tucker et al., 2004, Hacker and Gans, 2005, Walsh et al., 2007, Hacker et al., 2010).

It is important to note the difference in scales of melting between the two field areas. The ØSZ is a localised partial melt paragneiss that formed to accommodate extension of the Baltica margin. The Nupen Peninsula is part of the much larger WGR which forms the lowest structural level of the Caledonian orogeny. It represents a major HP/UHP zone of the subducting Baltica plate where partial melting was pervasive over the whole area (Hacker et al., 2003, Labrousse et al., 2002, 2004, Schärer and Labrousse, 2003, Gordon et al., 2013, 2016). The scale of partial melting in the paragneiss shear zones in SIP (Menegon et al., 2011, Degli Alessandrini et al., 2017) is much smaller than that in the WGR (Labrousse et al., 2002, 2004, Ganzhorn et al., 2014). This contrast makes them perfect case studies to aid our understanding of the range of deformation styles present in partial melt shear zones.

The greatest difference between these two field areas is the effect of post-melt deformation. The ØSZ experienced post-melt deformation at the edges of the shear zone, which contributed to a loss of preserved melt textures and a strong deformation fabric. From the field, the Nupen Peninsula appears to have undergone post-melt deformation in the mylonite-like shear zones but upon microstructural analysis, it is apparent the mylonite-like fabrics were developed during melting (e.g. Brown and Dallmeyer, 1996, Levine et al., 2013, Searle, 2013). As the Nupen Peninsula is part of much larger open-system melting, I propose melting was short-lived and transient (e.g. Schärer and Labrousse, 2003, Stuart et al., 2016, Meek et al., 2019).

The gneiss at Nupen melted to form the migmatites. Self-organisation of the melt and solid phases formed the strongly foliated fabric, the system crystallised when the melt source depleted or moved to a different part of the WGR (Chapter 4). Deformation-assisted channelized melt flow is suggested to be the process operating at Nupen, where the shear zones appear strongly deformed in the field but lack the microstructural evidence for deformation (e.g. Carter and Dworkin, 1990, Streit and Cox, 2002, Cartwright and Barnicoat, 2003, Meek et al., 2019). Weak CPOs support this process (Figures 4.10, Appendix A.2) and indicate deformation ceased before the

melt crystallised. The mylonite-like shear zones are suggested to be short-lived, transient features that form a strong crystal framework upon melt loss or crystallisation, preserving the delicate melt microtextures as they are not overprinted by post-melt deformation.

The processes operating in the ØSZ differs as post-melt deformation does occur here; however, it is isolated to areas of lower melt volume. Pre-melting, the shear zone started to deform and the high temperature deformation is preserved in the shear zone microstructure. Syn-melt grain growth is promoted in the centre of the ØSZ; as melt migrates through the system, it is driven towards the centre of the shear zone (Chapter 3). As the shear zone crystallises and cools, the centre of the ØSZ has crystallised to form a strong solid framework with a relatively coarse grain size; in contrast, the shear zone edges have a finer grain size and form a weaker crystal framework. The finer shear zone edges are easier to deform and strain localises to them, deforming at lower temperatures and higher stresses and overprinting melt textures to form paired shear zones at the ØSZ boundaries (e.g. Mancktelow and Pennacchioni, 2005, Pennacchioni and Mancktelow, 2007, Smith et al., 2015). This style of post-melt deformation localising to fine-grained quartz rich domains is not solely a feature of the ØSZ. It has been observed in the migmatites from the Aravalli-Dehli Fold Belt, India, where the fine-grained layers act as rheologically weak zones, deforming post-melt (Prakash et al., 2018). This suggests the rheological weakness in such shear zones is not isolated to the period of melting.

When considering the idealised models for shear zone activity and thickness through time (summarised in Fossen and Cavalcante, 2017; Figure 2.1), the WGR shows characteristics of Type 2 shear zones, where strain localises to the centre of the shear zone. For the Nupen Peninsula this process occurs during the progressive organisation of the migmatite to form the mylonite-like units, localising strain and activity from the diffuse melt zone to the central mylonite-like areas. The ØSZ is far more complex and doesn't follow an idealised model for shear zone thickness. This is due to partial melting and post-melt deformation localising strain into different areas which conflicts with the idealised models described in Figure 2.1. However the pre-

and syn-melt deformation in the ØSZ suggests strain is progressively localised towards the centre as partial melt uses the shear zone as a migration pathway. This suggests the pre- and syn-melt evolution may have been characteristic of a Type 2 shear zone but the idealised model is not appropriate for post-melt evolution of the shear zone.

From the examples in this thesis it suggests syn-melt shear zones are likely to form Type 2 shear zones as partial melt localises strain towards the centre. It suggests there are more complexities in melt-free shear zones where pre-existing heterogeneities are likely to influence the initial shear zone thickness and shear zone activity as it evolves.

The main driving forces for the different styles of syn-melt deformation are (1) the size of melt region and (2) the mechanisms controlling grain size. At Nupen, the organisation of the migmatites resulted in pinning of grain growth, which ultimately led to grain size reduction. In the ØSZ, the melting process allowed grain growth in areas that were subject to greater melt infiltration (shear zone centre); a grain size heterogeneity therefore formed to permit localisation of post-melt deformation. In the next section I address if these grain-scale variations between the two field areas affect the seismic response and if so, can seismic properties be used to infer melting and deformation styles in actively melting crust.

6.2 Application to seismic data from the Himalaya-Tibet orogen

As discussed in Chapters 2 and 5, geophysical methods used to determine the presence and volume of melt can yield different predictions (e.g. Himalaya-Tibet orogen). In this section I describe evidence for partial melt in the Himalaya-Tibet orogen, where various seismic properties have been used to infer the presence of a partial melt layer or zone in the crust. In order to illustrate the uncertainty and impact induced by the realistic variation in melt volumes, geometries and composition, I compare the seismic properties used to infer melt in the Himalaya-Tibet orogen to seismic properties calculated at different stages from the evolution of partial melt in the ØSZ and Nupen Peninsula.

6.2.1 Evidence for partial melt in orogenic crust

Exposed leucogranites provide clear evidence that Indian crust of the Himalaya underwent partial melting during the Eocene to Miocene (Molnar, 1984, Beaumont, 2004). Geophysical studies over the last ∼30 years suggest a partially molten or fluid-rich layer is present in the middle to lower crust beneath the Himalaya and southern Tibet (Nelson et al., 1996, Schilling and Partzsch, 2001, Unsworth et al., 2005, Klemperer, 2006, Caldwell et al., 2009). The palaeo-melt evidence from leucogranites has been linked to active melting by tectonic models where middle crustal material flows out from beneath the plateau and is exhumed (Grujic et al., 1996, Nelson et al., 1996, Clark and Royden, 2000, Beaumont, 2004, Beaumont et al., 2006, Klemperer, 2006). Table 6.1 sumarises the geophysical data used to identify areas of partial melting across the Himalaya-Tibet orogen (for additional information see Section 2.4).

Vp/Vs from receiver functions is one of the most common methods used to estimate melt fraction. For example, Kind et al. (2002) used teleseismic earthquake records and receiver functions to calculate Vp/Vs, allowing identification of melt accumulations in the Himalaya-Tibet orogen. From the melt models developed in Chapter 5 (no fabric, crystal fabric and prolate ellipsoids in the shape fabric model), Vp/Vs is not necessarily sensitive to melt volume variations. Unless, as is often assumed, melt is oblate or layered, the change of Vp/Vs is minimal and can, in fact, reduce if the melt body is at an angle to the seismic wave propagation direction (Figure 5.5). Thus, Vp/Vs is unsuitable for prediction of melt volume unless the geometric properties of the melt body can be independently assessed. However, this assessment is rarely made and melt bodies are assumed to be either vertical or horizontal in the crust, depending on the setting of the melt magma conduit under a volcano (Hammond and Kendall, 2016) or a migmatitic lower crustal layer, respectively (see Section 5.3.4 for further discussion).

The variability in predictions of melt volume from these seismic and magnetotelluric (MT) studies (Table 6.1) illustrates the enormous variability in

Table 6.1: Summary of geophysical data identifying areas of partial melt across the Himalaya-Tibet orogen

Method	Response	Melt	Location	Literature source
Vp	5.6-5.8 km/s	7-12%	Lhasa block	Yang et al. (2003)
Vs	3.5 km/s	-	Qiangtang terrane	Rapine et al. (2003)
	3.7 km/s	-	Lhasa block	"
	2.9-3.3 km/s	3-7%	NW Himalaya	Caldwell et al. (2009)
	2.9-3.3 km/s	-	Northern Tibet	Yang et al. (2012)
	2.9-3.3 km/s	-	Lhasa block	"
AVs	<5%	2%	Northern Tibet	Chen et al. (2009)
	∼6%	2%	Qiangtang terrane	Hacker et al. (2014)
	∼9%	-	Lhasa block	"
MT	3 Ωm	6-12%	Tibetan Plateau	Schilling and Partzsch (2001)
	3 Ωm	5-14%	Southern Tibet	Unsworth et al. (2005)
	10 Ωm	2-4%	NW Himalaya	"
	3-10 Ωm	<25%	Southern Tibet	Hashim et al. (2013)

interpretations of partial melt. The examples shown here yield melt volumes from 2-25% (Figure 2.13, Table 6.1). Furthermore, the calculated volumes are not consistent along strike, nor do they increase toward either the north or south (Figure 2.13). All of the geophysical studies in Table 6.1 involve vertical profiles through the crust that are used to identify areas of velocity reduction, anisotropy increase and/or resistivity reduction, which in turn identify areas of partial melting or fluids in the Himalaya-Tibet orogen. Vp, Vs, AVs and Vp/Vs are all used in various teleseismic receiver function studies, whilst Vs and radial AVs are used in surface wave studies. In the next two sections I present data for these seismic properties at different structural phases from the evolution of the ØSZ and Nupen Peninsula (Figures 6.1 and 6.2). In the fourth section I simulate the seismic response from the examples shown here and compare melt predictions (Figures 6.3, 6.4, 6.5).

6.2.2 Seismic evolution of the Øksfjord shear zone

According to the model developed in Chapter 3, the ØSZ underwent a complex deformation and melting history from initially deforming with no melt, followed by

syn-melt deformation and finally strain partitioning to the shear zone edges during post-melt deformation (Figure 3.9). Figure 6.1 shows the seismic properties calculated at the four major structural evolution phases where the crystal fabric model represents melt trapped in isolated pockets and the shape fabric model with oblate ellipsoid inclusions represents an interconected melt network (Section 5.2). All seismic properties are modelled to represent a vertical profile intersecting the ∼45° dipping shear zone.

Initially I consider the seismic properties for a pre-melt shear zone where strain preferentially localises into the centre of the shear zone (Figure 6.1a). This stage is represented by the crystal fabric model with 0% melt as the model considers anisotropic solid rock properties (Section 5.2). The teleseismic response from the non-melt shear zones shows an increase in velocity towards the centre of the shear zone. The increase in velocity in the melt-free system is due to the development of anisotropy and thus the orientation of the shear zone and (possibly more importantly) the mineralogy of the rock. The relationship between the way the CPO develops and the single crystal anisotropy varies a lot from mineral to mineral and in this case the development of a strongly foliated fabric results in a velocity increase. This suggests melt-free shear zones may not form low-velocity layers (LVLs) and instead may be identified in areas of velocity increase.

Figure 6.1b shows the effect of a syn-melt ØSZ on a vertical seismic profile where both the shear zone and transition zone are actively melting with up to 15% melt volume. This stage is represented by both the crystal fabric and shape fabric models; the crystal fabric model is used to calculate results for a non-connected melt texture where the melt is trapped in pockets, and the shape fabric model with oblate ellipsoids is used to calculate seismic properties for an interconnected melt network that has developed to form layers (Section 5.2). The seismic response is far greater when considering the interconnected melt network; seismic velocities and Vp/Vs decrease whilst there is a greater anisotropy than the non-melt case. For the non-connected melt network, there is a slight velocity decrease and anisotropy increase but it is evident that the crystal fabric of the solid rock plays a greater role in the seismic response than the melt volume. This suggests when observing LVLs, an

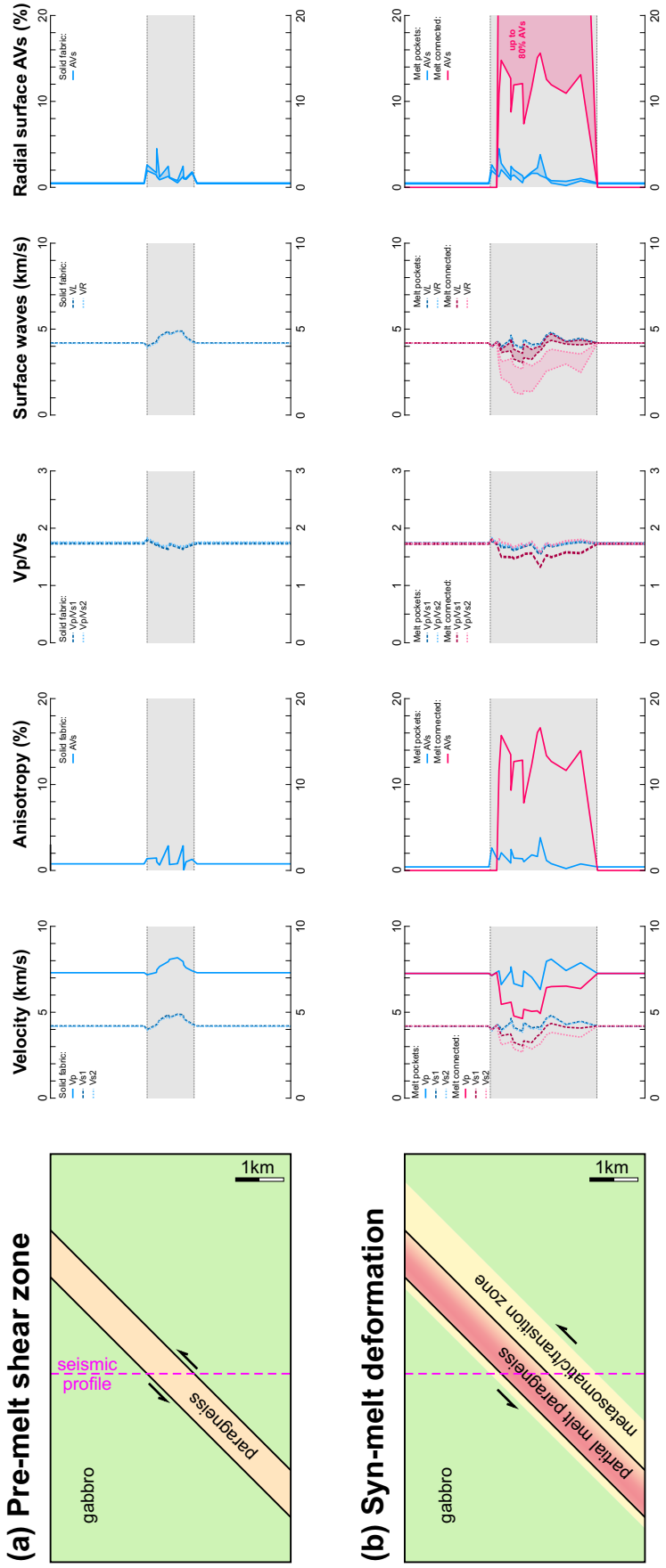
Radial surface AVs (%)
Surface waves (km/s)
Vp/Vs
Anisotropy (%)
Velocity (km/s)
Solid fabric:
Melt pockets:
Melt connected:
up to 80% AVs
(a) Pre-melt shear zone
(b) Syn-melt deformation
1km
seismic profile
paragneiss
gabbro
partial melt paragneiss
metasomatic/transition zone

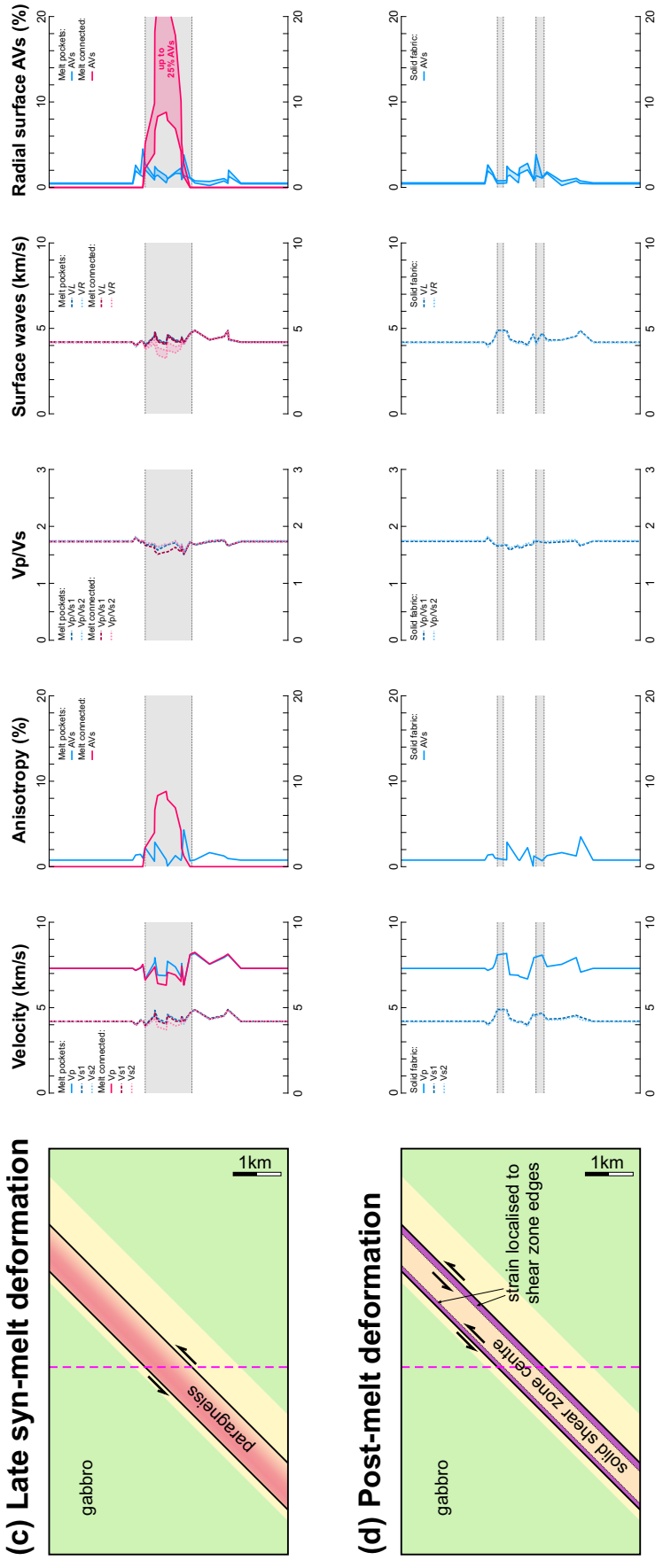

Figure 6.1: Synthesis of geological and seismic results for the ~45° dipping ØSZ under different melting and/or deformation conditions. Seismic results show Vp, Vs, AVs and Vp/Vs for teleseismic waves and Love (VL) and Rayleigh (VR) for surface waves along a vertical profile through the dipping shear zone. The crystal fabric model is used to calculate seismic properties for the solid shear zones (a, d). For the partial melt shear zones (b, c), the crystal fabric model is used to calculate results for a non-connected melt texture where the melt is trapped in pockets, and the shape fabric model with oblate ellipsoids is used to calculate seismic properties for an interconnected melt network developed to form layers. (a) Non-melt shear zone where the grain size decreases towards the shear zone centre, this is the 'typical' structure for a non-melt shear zone. (b) Syn-melt shear zone where the maximum melt volume is used to calculate seismic results for melt pockets and an interconnected network. (c) Late syn-melt shear zone where there is <1% melt in the shear zone. (d) Post-melt shear zone where strain has partitioned to the shear zone edges.

interconnected melt network will produce an increase in AVs and reduction in Vp/Vs, but if the melt is trapped in pores it is unlikely to produce the expected seismic anomaly for active melting.

Next I consider the seismic response for late syn-melt deformation where there is less than 1% melt located in the shear zone (Figure 6.1c). This stage is represented by both the crystal fabric model for isolated melt pockets and shape fabric model with oblate inclusions for an interconnected melt network. The interconnected melt network gives the expected results of Vp, Vs and Vp/Vs reduction and AVs increase, but the melt volume is not enough to overcome the strong crystal fabric resulting in velocity increase in some samples. However, the AVs increase and Vp/Vs reduction would be sufficient to identify a partial melt zone in the crust. If the melt is isolated, the solid crystal fabric dominates the seismic response and it would make it difficult to identify partial melt in the actively deforming crust.

Figure 6.1d shows the seismic properties for the post-melt ØSZ where strain has localised to the paired shear zones at the edges. This stage is represented by the solid crystal fabric model. For this case, the seismic velocities are faster in the shear zones due to the well developed foliation. However, the Vp, Vs1, Vs2, Love (VL) and Rayleigh (VR) wave velocities increase relative to each other meaning there is no significant reduction in Vp/Vs or increase in AVs.

The modelled seismic response for the different stages of the ØSZ-type is varied when considering the contectivity of the melt. I propose the crystal fabric of the solid rock plays a key role on the seismic response if the melt volume is <1% or not connected. Where melt volume is >1% and forms an interconnected network, one would observe a velocity and Vp/Vs reduction and AVs increase. Melt-free shear zones will exhibit a velocity increase relative to the background velocity but Vp/Vs and AVs may be unaffected.

6.2.3 Seismic evolution of the Nupen Peninsula

The Nupen Peninsula represents a small area of partial melting from the much larger (U)HP WGR (Chapter 4, Figure 4.11). Figure 6.2 shows the seismic properties

calculated at three possible structural evolution phases during deformation of the shear zones. As previously shown for the ØSZ, the crystal fabric model with 0% melt is used to calculate seismic properties for the crystallised migmatites and shear zones as observed today; this model therefore considers the anisotropic solid rock properties (Figure 6.2a; Section 5.2). For the partial melt shear zones, the crystal fabric model is used to calculate results for a non-connected melt texture where the melt is trapped in pockets, whilst the shape fabric model with oblate ellipsoids is used to calculate seismic properties for an interconnected melt network that has developed to form layers (Figure 6.2 b, c; Section 5.2). All seismic properties are modelled to represent a vertical profile intersecting the $\sim$15° dipping shear zone inferred from when partial melting occurred during exhumation of the Baltica Plate (Figure 4.1a).

Initially I consider the seismic properties for the crystallised Nupen Peninsula where strain is likely to localise into the fine-grained mylonite-like shear zones within the migmatized gneiss (Figure 6.2a). The teleseismic response from the crystallised Nupen Peninsula show an increase in velocity into the mylonite-like zones where there is a well developed foliated fabric. This corroborates the suggestion from ØSZ and Figure 6.1a that well-developed fabric from a non-melt shear zones could be identified when there is a velocity increase so that it does not form LVLs.

Figure 6.2b shows the seismic response for the shear zones acting as melt escape pathways and as a result have a high melt fraction of up to 20%. Generally, velocities decrease and anisotropy increases into the shear zones but this effect is exaggerated when modelling an interconnected melt network. Vp/Vs is considered to decrease in areas of partial melt, which is the case for Vp/Vs1 but for Vp/Vs2 it increases. This is due to a large decrease in Vp in the presence of partial melt compared to Vs2, which does not decrease as greatly. The seismic response is far greater when we consider the interconnected melt network; seismic velocities and Vp/Vs decrease whilst there is a greater anisotropy than the non-melt case. For the non-connected melt network, there is a slight velocity decrease and anisotropy increase but it is evident that the crystal fabric of the solid rock plays a greater role in the seismic response than the melt volume. This suggests when observing LVLs, AVs increase and Vp/Vs reductions can help to

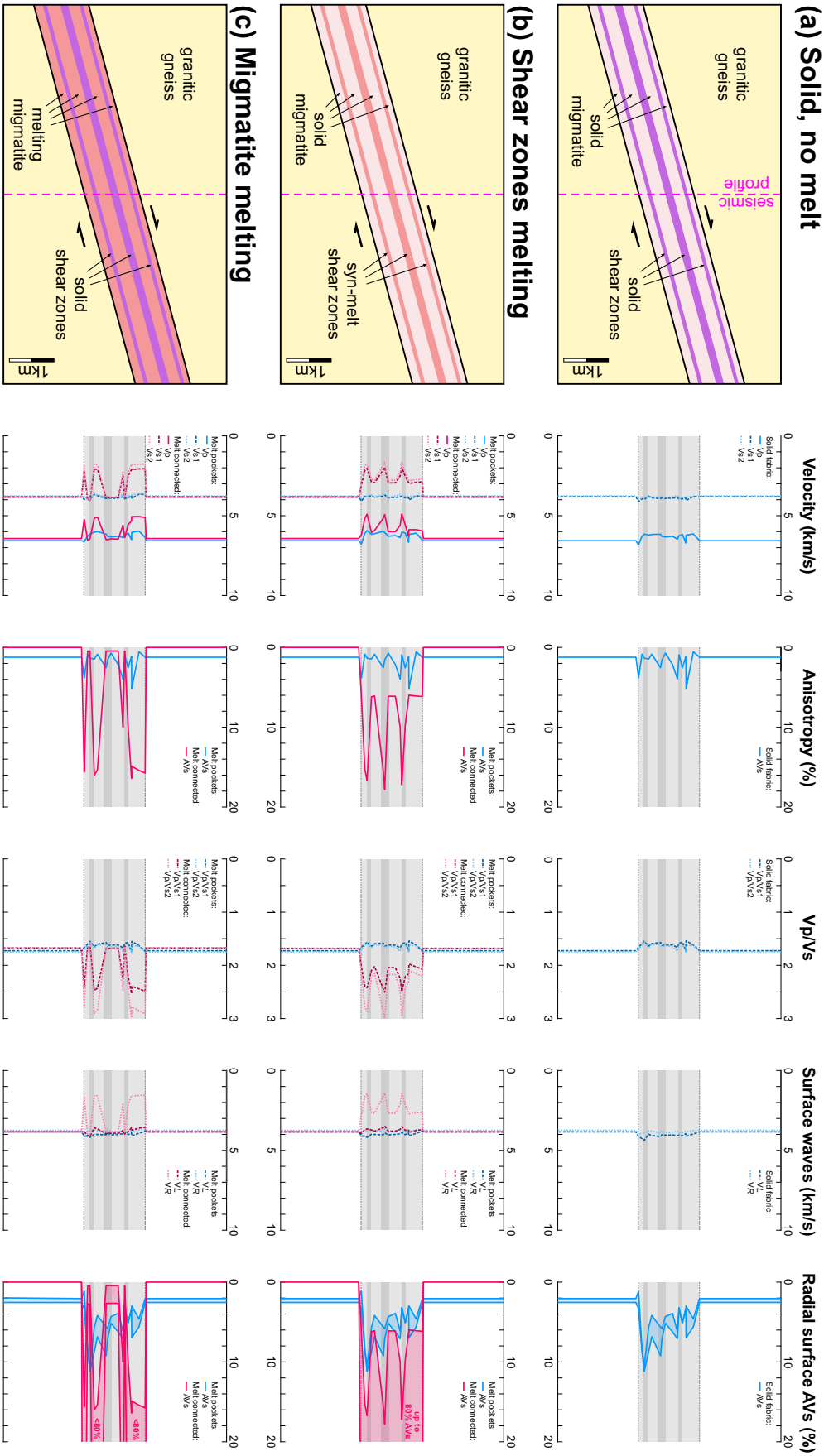

Figure 6.2: Synthesis of geological and seismic results for the Nupen Peninsula. Full caption opposite.

identify areas where there is an interconnected melt network but if the melt is trapped in pores it is unlikely to produce the expected seismic anomaly for active melting.

When considering the surface wave response, there is a decrease in the slower VR and increase in radial surface AVs when melt is present. The seismic response is far greater in the seismic example from WGR than the ØSZ. This is due to the restored shear zones being much shallower and therefore the horizontal shear wave splitting is far greater when Vs polarises vertically, as is the case with Rayleigh waves. The maximum AVs for interconnected melt is in excess of 100%. This is unrealistically high as the model does not consider the anisotropic solid rock properties, but it emphasises that there would be a dramatic effect on the seismic properties when considering a shallow dipping interconnected melt network.

Next I consider the seismic response for low melt (<1% melt) shear zones and higher melt (>15% melt) migmatites (Figure 6.2c). For this case, the seismic response is similar to that of Figure 6.2b but there is a reduction of seismic velocities and Vp/Vs, and increase in AVs in the shear zones relative to the migmatite. As shown for higher melt shear zones, AVs is very high for surface waves in an interconnected melt network, even when considering <1% melt for the shear zones. This emphasises the effect of melt layers that are near horizontal.

Similarly to the results from the ØSZ, I propose the connection of melt has the biggest effect on seismic response for the Nupen Peninsula when we consider a shallowly dipping syn-melt shear zone. If melt is isolated or trapped in pockets, the

Figure 6.2: Synthesis of geological and seismic results for the ∼15° restored dip of the Nupen Peninsula under different melting and/or deformation conditions. Seismic results show Vp, Vs, AVs and Vp/Vs for teleseismic waves and Love (VL) and Rayleigh (VR) for surface waves along a vertical profile through the dipping shear zone. The crystal fabric model is used to calculate seismic properties for the solid shear zones (a). For the partial melt shear zones (b, c), the crystal fabric model is used to calculate results for a non-connected melt texture where the melt is trapped in pockets, and the shape fabric model with oblate ellipsoids is used to calculate seismic properties for an interconnected melt network developed to form layers. (a) Non-melt Nupen Peninsula showing the seismic properties for the non-melt, crystallised section we observe in the field today. (b) Syn-melt shear zones where the maximum melt volume is within the mylonite-like shear zones, seismic results are calculated for melt pockets and an interconnected network. (c) Melt free shear zones where the melt fraction is higher outside the mylonite-like shear zones.

seismic velocities and Vp/Vs will be greater and the AVs will be much lower than that for the connected melt network. This response has also been observed for electrical conductivity. If the melt is connected, the electrical conductivity will be much greater than if melt is trapped in isolated pockets (Schilling and Partzsch, 2001). Thus, it is important to consider the geological behaviour of partial melt in the mid to lower crust when interpreting the geophysical and especially seismic response.

6.2.4 Estimating melt fractions from low-velocity layers

In order to illustrate the considerable uncertainty and impact induced by the realistic variation in melt geometries, I simulate melt fractions using the seismic responses from literature for the Himalaya-Tibet orogeny. Yang et al. (2003) observed an LVL beneath the Lhasa block in the Himalaya-Tibet orogen where Vp from teleseismic receiver functions was reduced to 5.6-5.8 km/s (Figure 2.13). From this low Vp response, they predicted 7-12% melt was interconnected and distributed along grain boundaries forming melt films in quartz-rich felsic rocks. Here I present the seismic melt models described in this thesis to corroborate the melt volumes predicted by Yang et al. (2003). For this I use examples from both the ØSZ and Nupen Peninsula to show how mineral composition can affect the seismic properties (Figure 6.3). The ØSZ represents a case study for biotite-dehydration melting whereas the Nupen Peninsula represents granitic wet melting. The seismic models shown here are: (1) the shape fabric model with oblate ellipsoids, used to calculate seismic properties for an interconnected melt network that has developed to form layers; (2) the shape fabric model with prolate ellipsoid, used to simulate the effect of melt tubes; and (3) the crystal fabric model, used to calculate results for a non-connected melt texture where the melt is trapped in pockets (Section 5.2).

The model that best matches the assumptions of Yang et al. (2003), interconnected partial melt in quartz-rich felsic rocks, is the shape fabric model with oblate inclusions where melting is via the granitic-wet melt reaction as is the case for the Nupen Peninsula (Figure 6.3b). This model predicts a melt volume of 3-5% from a 5.6-5.8 km/s Vp reduction; however, if the rock composition of the LVL is more pelitic and leads to

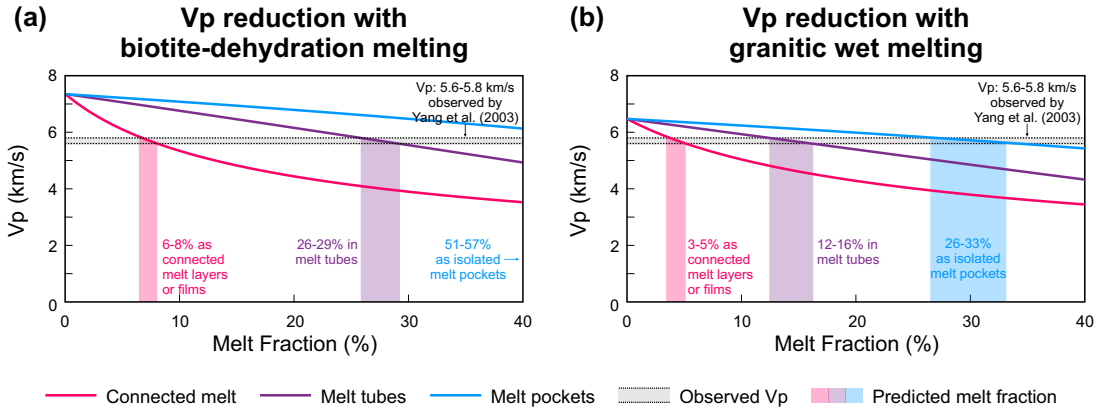

Figure 6.3: Comparison of modelled velocity reduction with data from Southern Tibet after Yang et al. (2003). Modelled Vp results for teleseismic waves (Z direction) between 0 and 40% melt for (a) biotite-dehydration melting and (b) granitic wet melting are compared with observed 5.6-5.8 km/s Vp reduction by Yang et al. (2003) yielding model-dependent melt fractions from 6 to 57%.

biotite-dehydration melting, 6-8% interconnected partial melt would be responsible for the velocity reduction (Figure 6.3a). If the melt was trapped in isolated melt pockets, 26-33% partial melt would be required via granitic-wet melting and a very high melt volume of 51-57% from biotite-dehydration melting (Figure 6.3). These high melt volumes would make it unlikely for melt to remain trapped in isolated pockets as the solid rock framework breaks down at approximately 40% melt (Rosenberg and Handy, 2005). From the seismic model predictions, it is likely 3-8% partial melt is present beneath the Lhasa block with the exact volume depending on the melt composition and strength of the foliated fabric in the solid rock. This value is lower than the 7-12% melt volume estimated by Yang et al. (2003).

In addition to Vp, LVLs are also observed via shear waves, specifically vertical polarisd shear waves (i.e. Rayleigh waves or Vs_v). Hacker et al. (2014) predicted 2% partial melt was present beneath the Qiantang terrane using the seismic data from Rapine et al. (2003), Chen et al. (2009) and Yang et al. (2012; see Hacker et al., 2014; for additional sources). I apply the seismic models from this thesis to calculate partial melt volumes for interconnected melt, melt tubes and isolated melt pockets from the LVL with 2.9-3.3 km/s Rayleigh wave velocity (VR) from Caldwell et al. (2009) and Yang et al. (2012) and the 4-9% radial AVs from Chen et al. (2009; Figure 6.4).

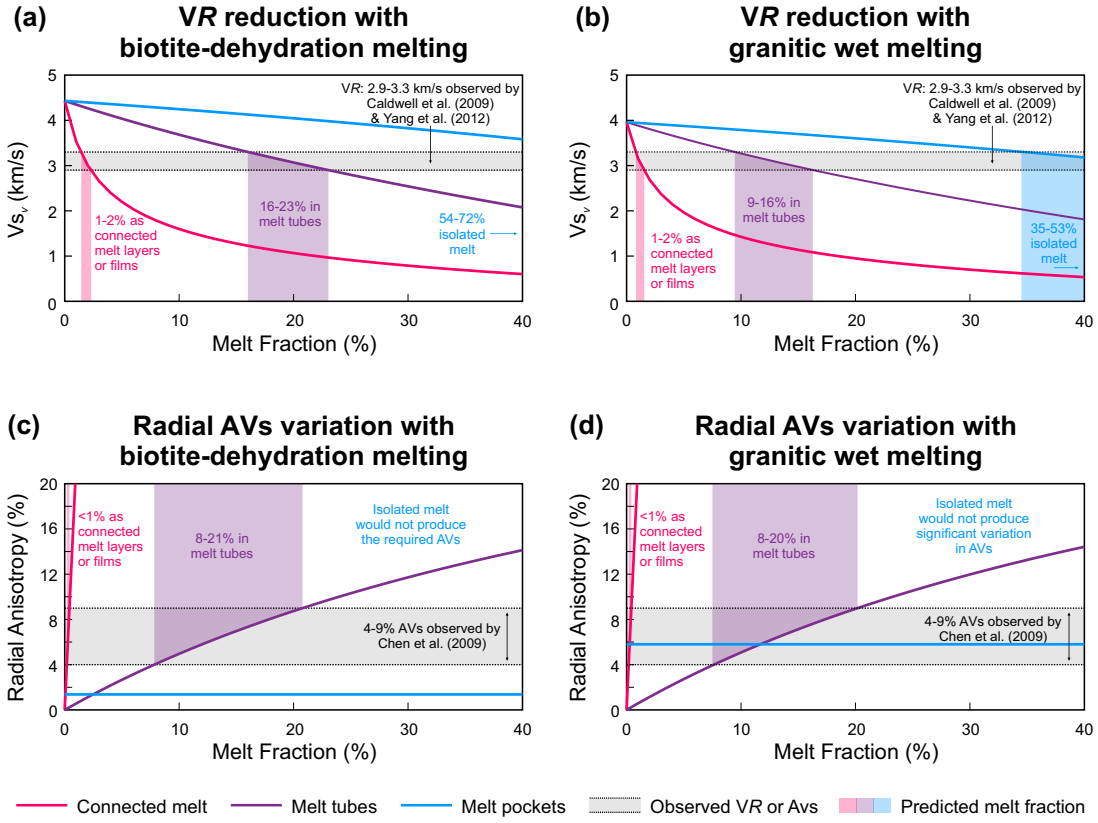

Figure 6.4: Comparison of modelled Rayleigh wave (VR) reduction with data from the northwest Himalaya and Tibet after Caldwell et al. (2009) and Yang et al. (2012), and surface wave anisotropy (AVs) increase with data from Tibet after Chen et al. (2009). Modelled Vs results for vertically polarising shear waves (X and Y directions) between 0 and 40% melt for (a, c) biotite-dehydration melting and (b, d) granitic wet melting are compared with observed 2.9-3.3 km/s VR reduction by Caldwell et al. (2009) and Yang et al. (2012), and 4-9% AVs by Chen et al. (2009) yielding model-dependent melt fractions from <1 to 72%.

The melt prediction for 2.9-3.3 km/s Rayleigh waves suggests 1-2% melt is present if it is distributed in a connected system across the Tibet Plateau and northwest Himalaya (Figure 6.4a, b). This is considerably lower than the predictions from reduction in Vp, 3-8% melt (Figure 6.3), but it highlights the strong effect partial melt has on VR. Similarly to Vp, isolated melt pockets yield unrealistically high melt volumes of up to 72% if the system is pelitic (Figure 6.4a, b). For the observed AVs values of 9% for the Lhasa block and reducing to ∼4% in the northern Songpan-Ganze terrane, the interconnected melt model predicts <1% melt is present whereas melt distributed in tubes produces the same melt fraction for biotite-dehydration and granitic wet melting systems of 8-∼20%.

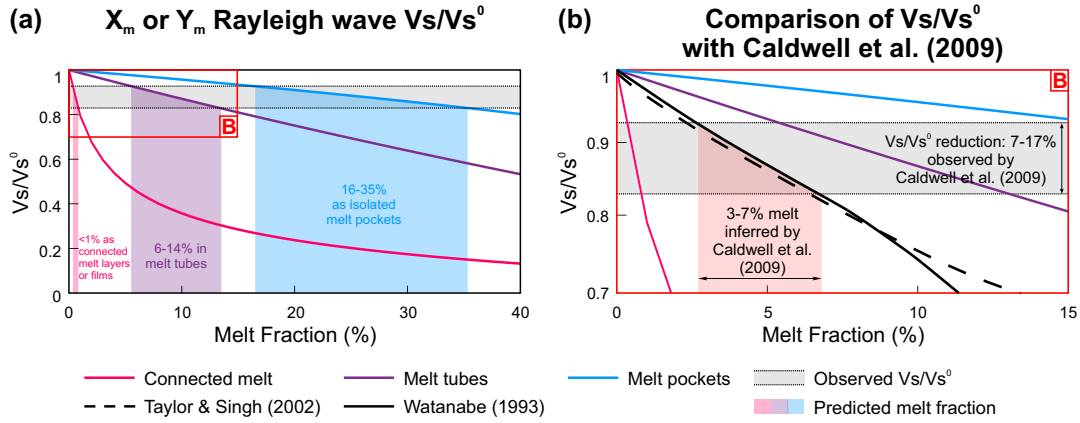

Figure 6.5: Comparison of modelled velocity reduction with data from the northwest Himalaya after Caldwell et al. (2009). a) Modelled Rayleigh Vs/Vs^0 for all model variations between 0 and 40% melt in the X1 direction; b) Comparison with Caldwell et al. (2009) to show model variations against those calculated by Taylor and Singh (2002) and Watanabe (1993).

Additionally, model results from this study are compared with the Rayleigh wave velocity reduction (Vs/Vs^0) results from Caldwell et al. (2009; Figure 6.5) for the northwest Himalaya. The comparison clearly shows that when geological factors like CPO or melt shape are considered, Vs/Vs^0 can vary greatly. Caldwell et al. (2009) identified a 7-17% velocity decrease, from which they inferred a 3-7% melt volume using models from Taylor and Singh (2002) and Watanabe (1993). Taylor and Singh (2002) model horizontal aligned oblate ellipsoids with a $\alpha = 0.1$, I use an α of 0.01 in my models as this is the minimum aspect ratio observed in the field. Watanabe (1993) used randomly orientated triangular melt tubes. These models are plotted in Figure 6.5b together with my models. When the observed results are considered in terms of my models, the isolated melt pockets estimate the largest melt volume (15-34%) for the 7 to 17% Vs reduction observed by Caldwell et al. (2009). However, the interconnected melt modelling estimates a much smaller melt fraction of 1 to 2% for the same 7 to 17% Vs reduction. I can therefore explain the 7 to 17% velocity decrease observed by Caldwell et al. (2009) from either much smaller or much larger melt volumes. When the results for Love waves are considered (Figure 5.5), the effect of isotropic orientated melt on Vs is clear as the model for an interconnected melt network yields an 8-18% melt fraction for the 7 to 17% Vs reduction. Thus, simultaneous use of Love and Rayleigh waves could help resolve more accurate melt volumes.

6.3 Prospects for partial melt quantification from seismic imaging

The comparisons shown in the previous sections emphasise the importance of the different geological parameters and their effect on seismic properties. The results shown in Section 6.2.4 indicate <1-5% interconnected melt is present beneath Tibet and the northwest Himalaya if the crust is granitic; however, the melt volume rises to 8% if the crust is pelitic. We do not know the precise geology underneath active mountain belts and the two analogue examples from SIP and WGR show enormous variation in their syn-melt deformation styles. The melt volume and interconnectivity anlaysed through the microtextures of these former partial melt samples shows partial melting is not as simple as being static at triple junctions or freely moving along all grain boundaries. The examples from SIP and WGR suggest syn-melt deformation influences melt to form an interconnected network rather than being trapped in pockets. This behaviour plays a significant role in the predicted seismic response as interconnected melt dramatically reduces the seismic velocities when compared to isolated melt pockets.

Figures 5.6, 6.1 and 6.2 show the importance of melt body orientation, adding a complexity and uncertainty to the seismic behaviour that is not shown in the seismic comparisons in Figures 6.3, 6.4, 6.5. The observations call for robust assessment of the geometric (e.g. melt orientation, Love and Rayleigh wave disparity) and geological (e.g. solid rock and melt shape) properties of the studied crustal volume to aid the interpretation of partial melt from seismic data. I explore some of these ideas further in Chapter 7.

Chapter 7

Conclusions and future work

7.1 Conclusions

The presence of partial melt in the middle to lower crust is likely to cause a dramatic strength reduction making it rheologically weak. The aim of this thesis has been to identify the styles and mechanisms of partial melt deformation on rock microstructures, and to assess the effect of partial melt on the seismic response of the middle to lower crust. The following conclusions have been made from this research.

1. Microstructural evidence from areas of syn-melt deformation in the Seiland Igneous Province (SIP) and Western Gneiss Region (WGR) indicate partial melt forms an interconnected network even at low melt volumes, thus maximising the weakening effect of partial melt. However the response to syn-melt deformation was not the same for both field areas.

2. The Øksfjord shear zone (ØSZ) in the SIP underwent localised partial melting related to synintrusive deep crustal shearing during the opening of the Iapetus Ocean between Siberia and Baltica. The quartz phase in the ØSZ records the complex deformation sequence from pre-melt high temperature, low stress deformation, to syn-melt deformation where the melt phase infiltrates grain boundaries to form an interconnected network, and finally a post-melt deformation phase at lower temperatures and higher stresses. During melting the strain is absorbed by the melt phase, I have proposed that melt is unlikely

to remain static during deformation and the connectivity and movement of melt through the shear zone is likely to be strongly controlled by the imposed deformation. Upon crystallisation of the melt the rock is strong relative to low melt or melt-free areas, subsequent deformation localises to these weaker areas and resulted in the formation of paired shear zones at the edges of the ØSZ. In effect, melt migration towards the shear zone centre ultimately led to strengthening of the shear zone core, with post-crystallisation deformation focusing along shear zone margins where significant heterogeneities are present.

3. The Nupen Peninsula in the WGR represents a small portion of the pervasive melting across the high pressure area of WGR. The Nupen Peninsula is particularly interesting as the apparent mylonite units are simply the result of progressive organisation of the solid and melt phases to form a strongly foliated, fine grained fabric. There is a lack of post-melt deformation at Nupen as the melt textures are well preserved and the mylonite-like unit lacks the deformation fabric of a typical mylonitie. Due to the extensive partial melting over the WGR, it is likely that upon crystallisation and/or extraction of the melt, strain relocalised to the new melt pathway and the crystallised migmatite was strong inhibiting post-melt deformation.

4. The comparison of the two case studies has highlighted key controls that permit the different styles of syn-melt deformation: the size of melt region; and the mechanisms controlling grain size. At Nupen, the organisation of the partial melt resulted in pinning of grain growth which ultimately led to grain size reduction and the formation of the mylonite-like units. In the ØSZ the pre-melt deformation and melting process allowed grain growth in areas that were subject to greater melt infiltration (shear zone centre) resulting in a grain size heterogeneity that localised post melt deformation to the shear zone edges.

5. Analytical seismic modelling based on geological parameters and field examples demonstrates that partial melt greatly effects the seismic response from the middle and lower crust. The seismic models can be used for melt volumes from 0 to 40%

after which the solid crystal framework starts to break down. The four models are applicable to different partial melt styles or settings:

(a) The 'no fabric' model is an end member model to demonstrate the isotropic effects of the stiffness tensor and is not applicable to a geological setting.

(b) The 'shape fabric' model has end member variants of oblate ellipsoidal melt and prolate ellipsoidal melt. Oblate ellipsoids represent layers of melt parallel to foliation and can be used as an analogue for an interconnected melt network. Prolate ellipsoids are tubes of melt that which could represent magma tubes thus are more applicable to a volcanic setting.

(c) The 'layered fabric' model is an end member of oblate ellipsoidal melts thus represents foliation parallel melt layers.

(d) The 'crystal fabric' model is the only model that accounts for the anisotropic properties of the solid rock. Melt is modelled as isolated spheres, therefore this model is appropriate when melt volume is low and is not connected and the solid rock CPO is the more dominant factor.

6. The chemistry of continental deformation systems are far more complex than MORs. Here I have shown results for two different melting styles; biotite-dehydration and granitic-wet melting. In reality these systems are far more complex than two melt reactions and the reaction systems may change across relatively small areas with variations in mineralogy, pressure, temperature and water. When predicting the melt volume from seismic properties it is important to consider different chemistries and also predict the chemistry at depth using exhumed areas in the deforming region.

7. Seismic properties do not vary linearly with melt fraction; mineral composition, shape and alignment of melt, and the crystal fabric of the solid phase impact resulting in huge variations of seismic properties. There is a lot of uncertainty regarding the geological parameters beneath active mountain belts so we must use multiple sources of seismic data (e.g. Love and Rayleigh waves, P-wave tomography and shear wave splitting from local and remote events, azimuthal as

well as radial anisotropy etc.) to refine the model parameters and find a (more) unique solution. In addition, combining seismic studies with magnetotellurics will highlight where LVLs correspond to areas of high conductivity, supporting the location of areas of fluid or melt. Interpretation of such geophysical data should always be underpinned by robust modelling of the underlying geological parameters (mineral composition, melt shape, and fabric/melt body orientation with respect to the wave propagation direction).

7.2 Future work

The data and findings presented in this thesis provide scope for several additional studies and highlight areas of research that are required in order to further our understanding of syn-melt deformation processes. Future work based on this thesis should focus on the following topics.

7.2.1 Partial melt shear zones

It is apparent that partial melt shear zones are incredibly diverse, but the majority of research into such shear zones focusses on the metamorphic petrology. Further study of the microstructures and crystallographic response of partial melt shear zones will aid our understanding of the deformation processes at play and in turn the rheological implications. One key implication from this study is the scale of melting and its affect on the syn-melt deformation processes. Therefore I think it is important to explore this further by microstructural analysis of both narrow migmatitic shear zones (e.g. Emosson, Variscan shear zone, Aiguilles-Rouges massif, western Alps; Genier et al., 2008) and wider diffuse shear zones (e.g. Cadomian belt, western France; Brown and Solar, 1998b).

7.2.2 Deformation experiments

I have studied partial melt in the continental crust using field, microstructures and seismic modelling. However there is a jump between the real rock data and the

seismic modelling. This gap would normally be bridged by rock deformation experiments where acoustic emissions or ultrasonics would be measured during syn-melt deformation experiments to calibrate partial melting with the seismic response. However these experiments are not possible in the partial melt regime; it would take months to years to reach the pressures and temperatures required to deform and partially melt these rocks ductilely without forming cracks that would contaminate the acoustic response. Therefore it is necessary to use an analogue material to comprehensively understand the link between partial melting, deformation and the seismic response.

7.2.2.1 Analogue ice experiments

Glacier ice and high-grade metamorphic rocks deform according to the same non-linear flow laws. We are able to directly measure strain rate associated with deformation structures in glaciers, this is not possible with high grade rocks (Wilson et al., 2014). As a result, ice is a very good analogue for crystalline crustal rocks and the results from this research can also be applied to rock deformation in the mid to lower crust aiding the understand large-scale plate tectonic processes such as mountain building, orogenic collapse and escape tectonics (Kohlstedt et al., 2009, Brown et al., 2011, Jamieson et al., 2011). A major challenge is that geophysical, and especially seismic, methods cannot reliably determine the degree of melting at depth beneath these tectonically active areas e.g. The Himalayas (Karato, 2010, Jamieson and Beaumont, 2013, Levine et al., 2013, Hammond and Kendall, 2016; Chapter 5). This follow on project would bridge the current gap in knowledge between the microstructural and modelling work via the use of ice as an analogue for rock. Experiments that would take years using rocks can be conducted under much shorter timescales with ice, thus allowing us to fill a missing link in our understanding of partially molten deforming crustal rocks. This study would not only benefit our understanding of mid to lower crustal melting processes but is also applicable to the study of deforming ice sheets and glaciers.

Understanding the strength and stability of ice is becoming significantly more important topic with our increased awareness of dramatic global climate change, the

surge and collapse events in glaciers and ice sheets becoming increasingly more common. Laboratory deformation experiments on ice are the only way to accurately constrain the effects of temperature changes and deformation rates on ice masses. A fundamentally important feedback process in the deformation of ice is the creation and segregation of melt (i.e. water), which enhances rates of plastic flow and leads to flow-induced deformation causing further melt segregation. The flow of ice is ultimately related to grain- and subgrain-scale processes, which control the distribution of deformation across ice masses. Ice streams are significant features of the Antarctic (accounting for 10% of ice volume), they are bound by shear margins that form the boundary between fast- and slow-moving ice. Shear margins regularly change position on the 10-100 year timescale, with their locations primarily controlled by internal ice sheet dynamics and surface meltwater. The addition of partial melt and other phases (e.g. air bubbles, hydrates, clay, rock powder) affect ice rheology and dramatically reduce the strength. Ongoing deformation of ice leads to preferred orientation of ice grains, leading to strong anisotropic fabrics forming, which can be measured by using seismic wave propagation techniques in the field, and if properly calibrated it can be directly related to fabric orientation. As such, in order to model glacial dynamics, we must fully understand the grain-scale mechanics of ice sheet deformation.

7.2.2.2 Syn-melt deformation textures

To further develop the research of syn-melt deformation textures from this thesis, high temperature syn-melt deformation experiments should be conducted to aid understanding of the deformation conditions required to form such microstructures. This work should focus on deformation experiments on natural and synthetic migmatite samples to improve our understanding and prediction of shear zone and mid-lower continental dynamics. In these experiments the melt textures can be quantified upon crystallisation as it is known that melting occurred during one event or melt flux. This quantification will develop better models for seismic velocity and anisotropy and will allow faster recognition of rheologically weak crust, feeding into

research that models continental dynamics and lithospheric strength.

Alternatively deformation experiments on rock should focus on the transition from the low to intermediate melt systems where the mechanical behaviour switches from being controlled by the solid framework to the melt-solid aggregate. Darcy-type experiments by Pec et al. (2017) investigate melt migration in samples of MORB composition. The current work focuses on melting along spreading centres, subduction zones and hotspots, but these experiments could be conducted on quartz-feldspathic rocks to incorporate continental mid to lower crustal melting into their study. The melt migration experiments will help us understand the conditions where felsic melts form an interconnected network which in turn would result in a dramatic strength decrease in the mid to lower continental crust.

7.2.3 Seismic properties

Using the experience gained in the present study, future seismic modelling efforts should aim to combine the crystal fabric approach with melt body shapes, orientations, and connectivity. It is also desirable to develop a model for cuspate melt inclusions in order to increase the accuracy when modelling low melt volumes prior to the formation of a connected melt network. Nevertheless, the models presented here are geologically realistic and can be used to inform geophysical data interpretation and other modelling efforts.

The use of Himalayan migmatite and leucogranite samples could provide a better comparison with Himalayan seismic data. A profile through the Greater Himalayan sequence could be used as an analogue for the seismic response observed beneath the Lhasa Block in Tibet. For example the profile by Parsons et al. (2016) through the Annapurna-Dhaulagiri Himalaya in central Nepal shows evidence for partial melting in the lowermost unit of the Upper Greater Himalayan sequence, and seismic melt modelling through this section of the metamorphic may provide an insight into the present day partial melting beneath the Lhasa block.

Shear zones are very effective at accommodating strain in the Earth's crust and mantle. The future microstructural, experimental and seismic studies proposed here

will further aid our understanding of the effect of partial melt in the crust. Microstructural and experimental studies of grain-scale melting processes will help to highlight how the volume and distribution of partial melt effects the dominant deformation mechanisms which can influence the strength of the lithosphere. Application of these grain-scale properties from Himalayan samples to seismic studies from the orogeny will inform our understanding of the present day partial melt distribute and as a consequence the strength of the crust.

Appendices

Appendix A

Crystallographic preferred orientations

A.1 CPO for the Øksfjord shear zone, SIP

The following pages contain the CPO pole figures for samples that contain quartz, plagioclase, K-feldspar, biotite, amphibole and pyroxene. The CPO are represented in the XZ plane of the kinematic reference frame for each individual sample. All pole figures are displayed with the same colour scale for each mineral to allow easy comparison of CPO strength. Contours show multiples of uniform distribution.

The following pole figures relate to samples discussed in Chapter 3 from the Øksfjord Shear Zone in the Seiland Igneous Province, northern Norway.

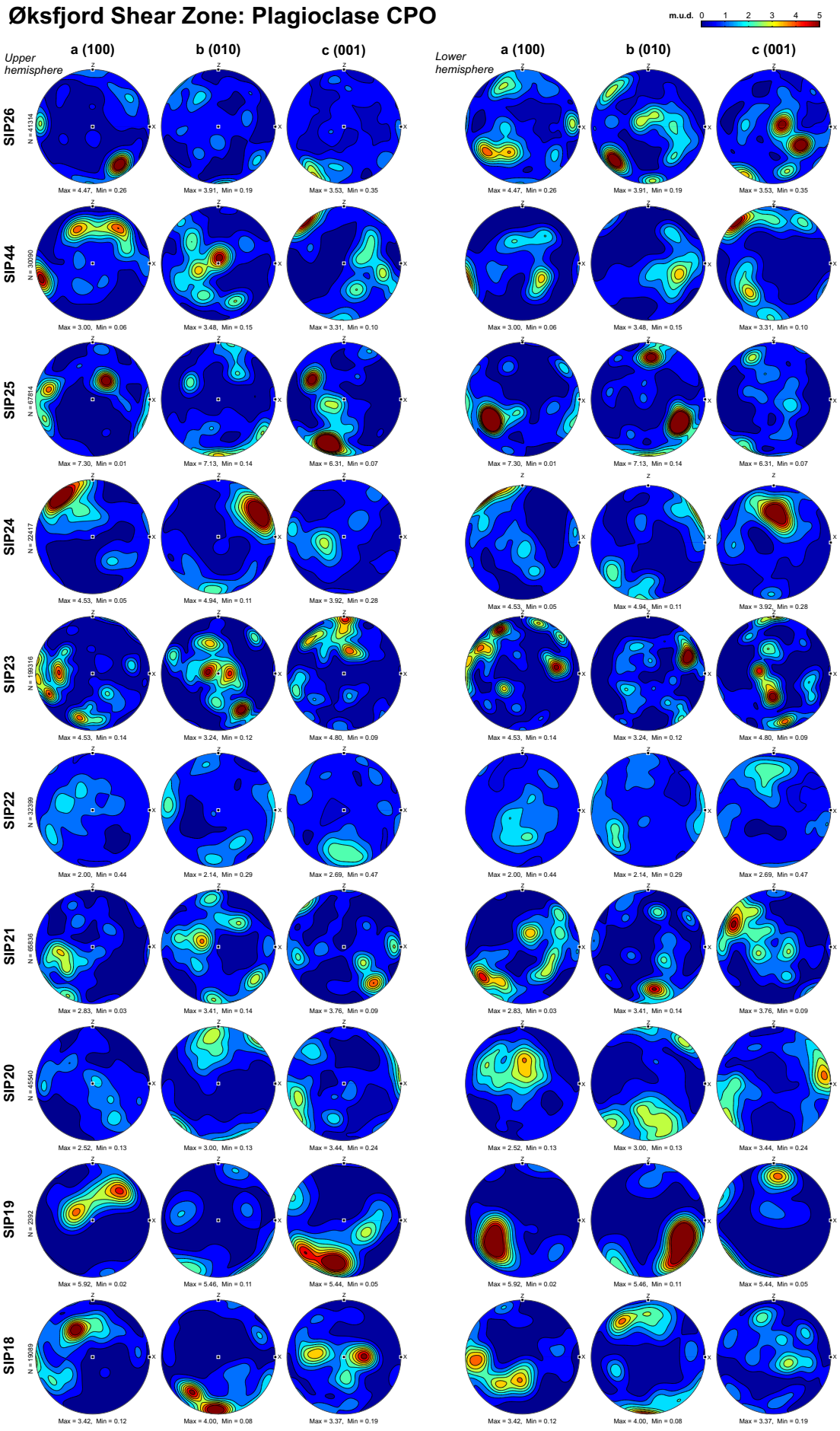
Øksfjord Shear Zone: Plagioclase CPO
m.u.d. 0 1 2 3 4 5
Upper hemisphere
Lower hemisphere
a (100)
b (010)
c (001)
SIP26
N = 41514
Max = 4.47, Min = 0.26
Max = 3.91, Min = 0.19
Max = 3.53, Min = 0.35
SIP44
N = 30900
Max = 3.00, Min = 0.06
Max = 3.48, Min = 0.15
Max = 3.31, Min = 0.10
SIP25
N = 67814
Max = 7.30, Min = 0.01
Max = 7.13, Min = 0.14
Max = 6.31, Min = 0.07
SIP24
N = 22417
Max = 4.53, Min = 0.05
Max = 4.94, Min = 0.11
Max = 3.92, Min = 0.28
SIP23
N = 199316
Max = 4.53, Min = 0.14
Max = 3.24, Min = 0.12
Max = 4.80, Min = 0.09
SIP22
N = 32398
Max = 2.00, Min = 0.44
Max = 2.14, Min = 0.29
Max = 2.69, Min = 0.47
SIP21
N = 66836
Max = 2.83, Min = 0.03
Max = 3.41, Min = 0.14
Max = 3.76, Min = 0.09
SIP20
N = 45540
Max = 2.52, Min = 0.13
Max = 3.00, Min = 0.13
Max = 3.44, Min = 0.24
SIP19
N = 2392
Max = 5.92, Min = 0.02
Max = 5.46, Min = 0.11
Max = 5.44, Min = 0.05
SIP18
N = 19269
Max = 3.42, Min = 0.12
Max = 4.00, Min = 0.08
Max = 3.37, Min = 0.19

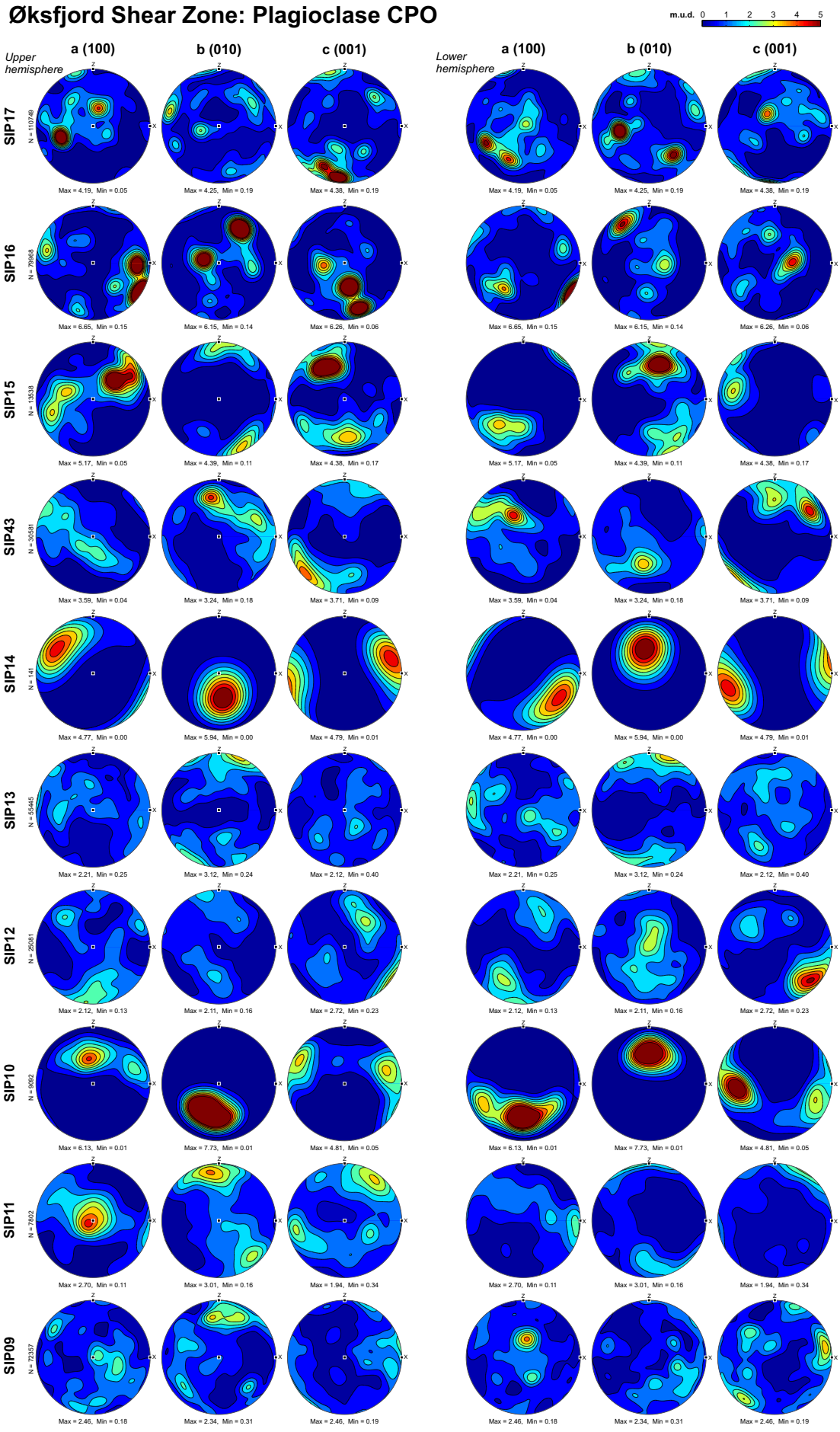
Øksfjord Shear Zone: Plagioclase CPO
m.u.d. 0 1 2 3 4 5
Upper hemisphere
Lower hemisphere
a (100)
b (010)
c (001)
SIP17
N = 110749
Max = 4.19, Min = 0.05
Max = 4.25, Min = 0.19
Max = 4.38, Min = 0.19
SIP16
N = 79988
Max = 6.65, Min = 0.15
Max = 6.15, Min = 0.14
Max = 6.26, Min = 0.06
SIP15
N = 13538
Max = 5.17, Min = 0.05
Max = 4.39, Min = 0.11
Max = 4.38, Min = 0.17
SIP43
N = 30581
Max = 3.59, Min = 0.04
Max = 3.24, Min = 0.18
Max = 3.71, Min = 0.09
SIP14
N = 141
Max = 4.77, Min = 0.00
Max = 5.94, Min = 0.00
Max = 4.79, Min = 0.01
SIP13
N = 55445
Max = 2.21, Min = 0.25
Max = 3.12, Min = 0.24
Max = 2.12, Min = 0.40
SIP12
N = 25081
Max = 2.12, Min = 0.13
Max = 2.11, Min = 0.16
Max = 2.72, Min = 0.23
SIP10
N = 9062
Max = 6.13, Min = 0.01
Max = 7.73, Min = 0.01
Max = 4.81, Min = 0.05
SIP11
N = 7802
Max = 2.70, Min = 0.11
Max = 3.01, Min = 0.16
Max = 1.94, Min = 0.34
SIP09
N = 72357
Max = 2.46, Min = 0.18
Max = 2.34, Min = 0.31
Max = 2.46, Min = 0.19

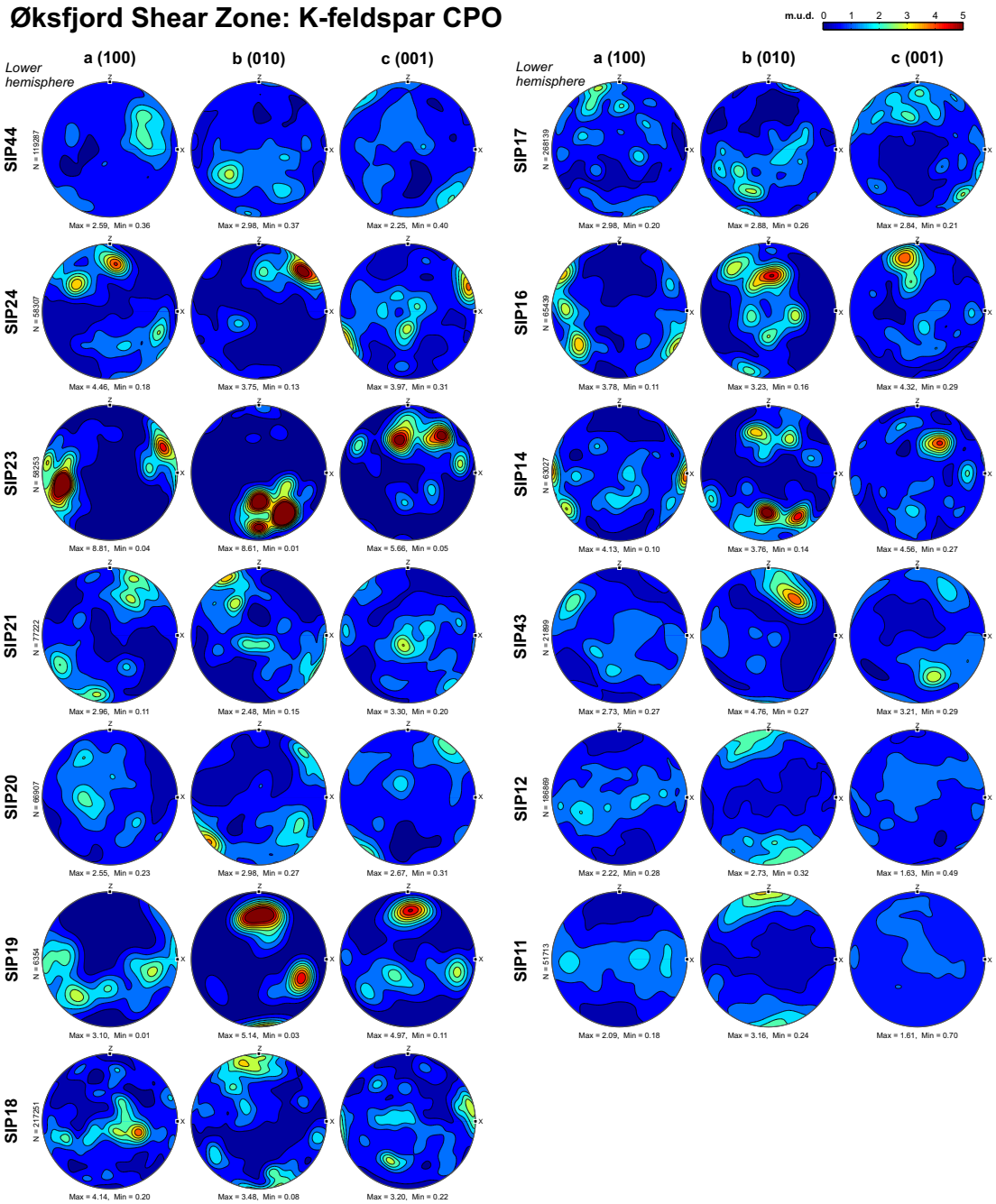
Øksfjord Shear Zone: K-feldspar CPO
m.u.d. 0 1 2 3 4 5
Lower hemisphere
a (100)
b (010)
c (001)
SIP44 N = 119287 Max = 2.59, Min = 0.36 Max = 2.98, Min = 0.37 Max = 2.25, Min = 0.40
SIP24 N = 58307 Max = 4.46, Min = 0.18 Max = 3.75, Min = 0.13 Max = 3.97, Min = 0.31
SIP23 N = 59253 Max = 8.81, Min = 0.04 Max = 8.61, Min = 0.01 Max = 5.66, Min = 0.05
SIP21 N = 77222 Max = 2.96, Min = 0.11 Max = 2.48, Min = 0.15 Max = 3.30, Min = 0.20
SIP20 N = 68907 Max = 2.55, Min = 0.23 Max = 2.98, Min = 0.27 Max = 2.67, Min = 0.31
SIP19 N = 6354 Max = 3.10, Min = 0.01 Max = 5.14, Min = 0.03 Max = 4.97, Min = 0.11
SIP18 N = 217251 Max = 4.14, Min = 0.20 Max = 3.48, Min = 0.08 Max = 3.20, Min = 0.22
Lower hemisphere
a (100)
b (010)
c (001)
SIP17 N = 268139 Max = 2.98, Min = 0.20 Max = 2.88, Min = 0.26 Max = 2.84, Min = 0.21
SIP16 N = 65439 Max = 3.78, Min = 0.11 Max = 3.23, Min = 0.16 Max = 4.32, Min = 0.29
SIP14 N = 63027 Max = 4.13, Min = 0.10 Max = 3.76, Min = 0.14 Max = 4.56, Min = 0.27
SIP43 N = 21899 Max = 2.73, Min = 0.27 Max = 4.76, Min = 0.27 Max = 3.21, Min = 0.29
SIP12 N = 186869 Max = 2.22, Min = 0.28 Max = 2.73, Min = 0.32 Max = 1.63, Min = 0.49
SIP11 N = 51713 Max = 2.09, Min = 0.18 Max = 3.16, Min = 0.24 Max = 1.61, Min = 0.70

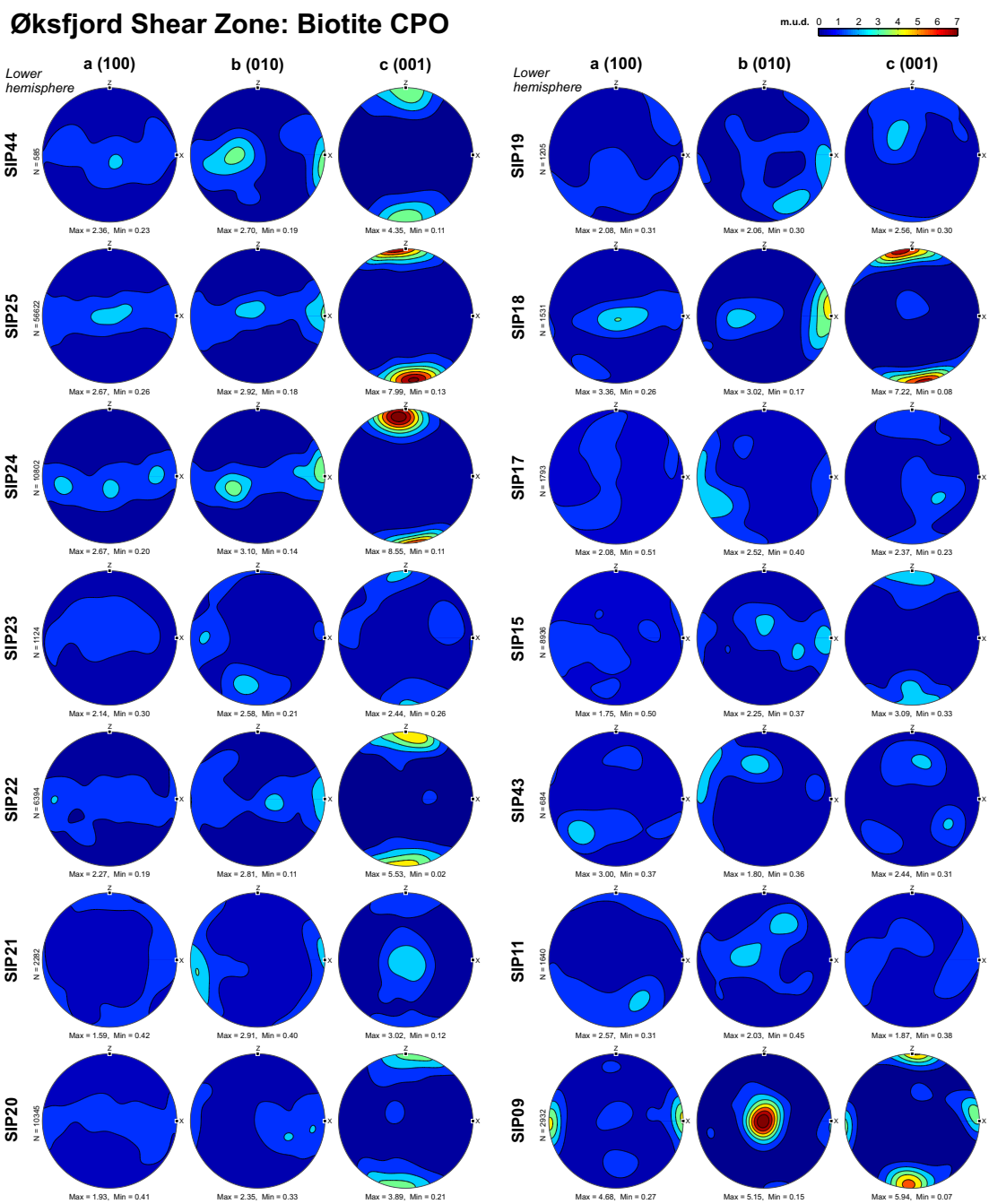
Øksfjord Shear Zone: Biotite CPO
m.u.d. 0 1 2 3 4 5 6 7
Lower hemisphere
a (100)
b (010)
c (001)
SIP44 N = 586 Max = 2.36, Min = 0.23 Max = 2.70, Min = 0.19 Max = 4.35, Min = 0.11
SIP25 N = 56622 Max = 2.67, Min = 0.26 Max = 2.92, Min = 0.18 Max = 7.99, Min = 0.13
SIP24 N = 10802 Max = 2.67, Min = 0.20 Max = 3.10, Min = 0.14 Max = 8.55, Min = 0.11
SIP23 N = 1124 Max = 2.14, Min = 0.30 Max = 2.58, Min = 0.21 Max = 2.44, Min = 0.26
SIP22 N = 6394 Max = 2.27, Min = 0.19 Max = 2.81, Min = 0.11 Max = 5.53, Min = 0.02
SIP21 N = 2282 Max = 1.59, Min = 0.42 Max = 2.91, Min = 0.40 Max = 3.02, Min = 0.12
SIP20 N = 10345 Max = 1.93, Min = 0.41 Max = 2.35, Min = 0.33 Max = 3.89, Min = 0.21
Lower hemisphere
a (100)
b (010)
c (001)
SIP19 N = 1205 Max = 2.08, Min = 0.31 Max = 2.06, Min = 0.30 Max = 2.56, Min = 0.30
SIP18 N = 1531 Max = 3.36, Min = 0.26 Max = 3.02, Min = 0.17 Max = 7.22, Min = 0.08
SIP17 N = 1793 Max = 2.08, Min = 0.51 Max = 2.52, Min = 0.40 Max = 2.37, Min = 0.23
SIP15 N = 8936 Max = 1.75, Min = 0.50 Max = 2.25, Min = 0.37 Max = 3.09, Min = 0.33
SIP43 N = 684 Max = 3.00, Min = 0.37 Max = 1.80, Min = 0.36 Max = 2.44, Min = 0.31
SIP11 N = 1640 Max = 2.57, Min = 0.31 Max = 2.03, Min = 0.45 Max = 1.87, Min = 0.38
SIP09 N = 2932 Max = 4.68, Min = 0.27 Max = 5.15, Min = 0.15 Max = 5.94, Min = 0.07

Øksfjord Shear Zone: Orthopyroxene CPO

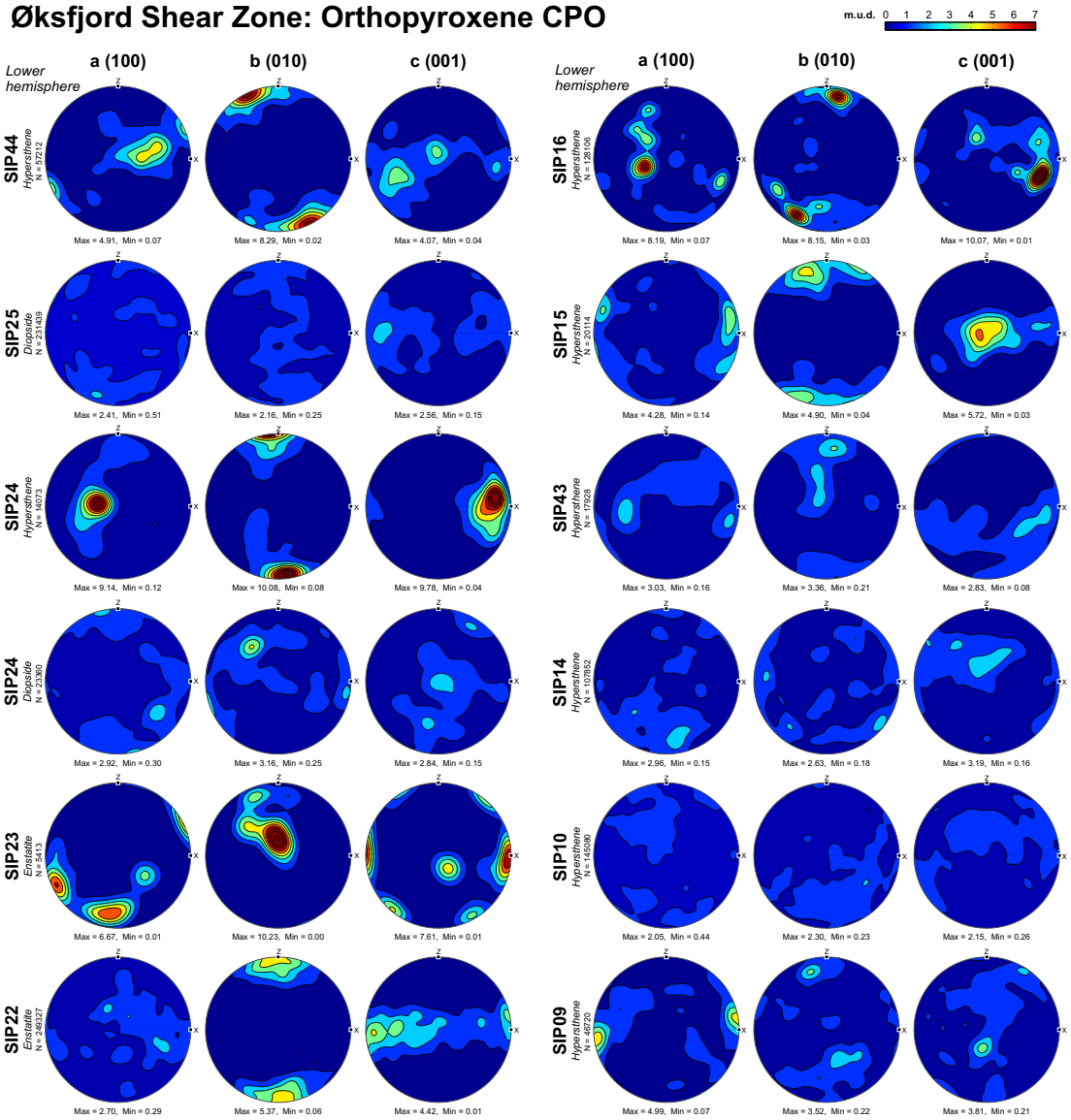

Øksfjord Shear Zone: Clinopyroxene CPO

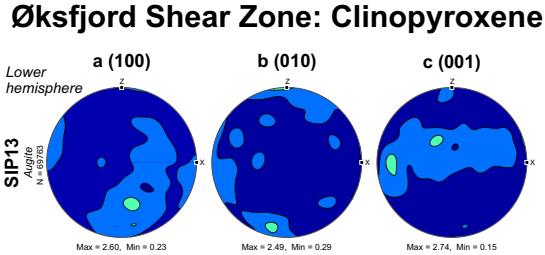

Øksfjord Shear Zone: Hornblende CPO

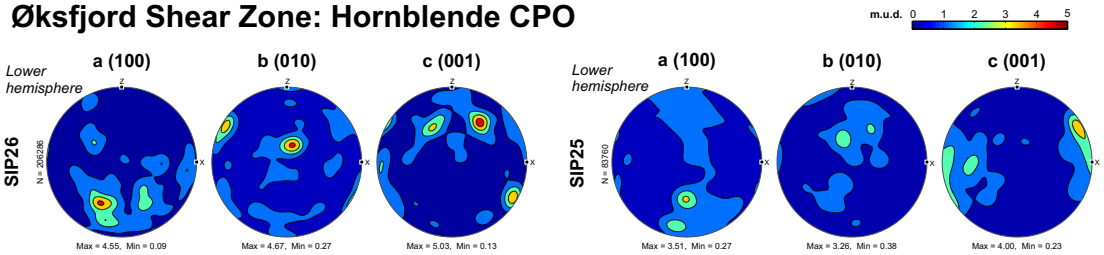

A.2 CPO for the Nupen Peninsula, WGR

The following pole figures of quartz, plagioclase, K-feldspar, biotite and amphibole relate to samples discussed in Chapter 4 from the Nupen Peninsula in the Western Gneiss Region, west Norway. As for the previous pole figures, the CPO are represented in the XZ plane of the kinematic reference frame for each individual sample. All pole figures are displayed with the same colour scale for each mineral to allow easy comparison of CPO strength. Contours show multiples of uniform distribution.

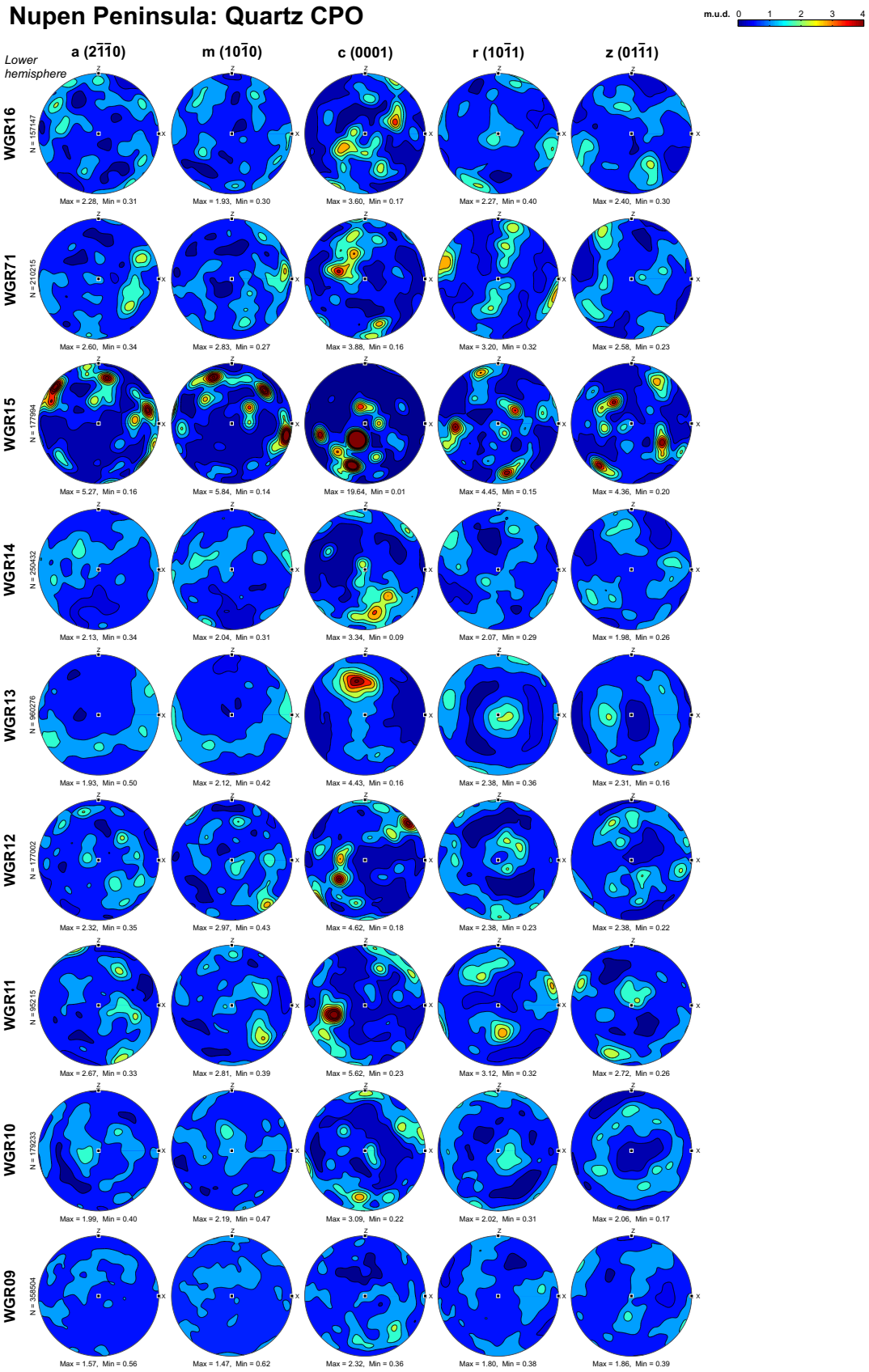
Nupen Peninsula: Quartz CPO
m.u.d. 0 1 2 3 4
Lower hemisphere
a (2$\bar{1}\bar{1}$0)
m (10$\bar{1}$0)
c (0001)
r (10$\bar{1}$1)
z (01$\bar{1}$1)
WGR16 N = 157147
Max = 2.28, Min = 0.31
Max = 1.93, Min = 0.30
Max = 3.60, Min = 0.17
Max = 2.27, Min = 0.40
Max = 2.40, Min = 0.30
WGR71 N = 210215
Max = 2.60, Min = 0.34
Max = 2.83, Min = 0.27
Max = 3.88, Min = 0.16
Max = 3.20, Min = 0.32
Max = 2.58, Min = 0.23
WGR15 N = 177994
Max = 5.27, Min = 0.16
Max = 5.84, Min = 0.14
Max = 19.64, Min = 0.01
Max = 4.45, Min = 0.15
Max = 4.36, Min = 0.20
WGR14 N = 250432
Max = 2.13, Min = 0.34
Max = 2.04, Min = 0.31
Max = 3.34, Min = 0.09
Max = 2.07, Min = 0.29
Max = 1.98, Min = 0.26
WGR13 N = 960276
Max = 1.93, Min = 0.50
Max = 2.12, Min = 0.42
Max = 4.43, Min = 0.16
Max = 2.38, Min = 0.36
Max = 2.31, Min = 0.16
WGR12 N = 177002
Max = 2.32, Min = 0.35
Max = 2.97, Min = 0.43
Max = 4.62, Min = 0.18
Max = 2.38, Min = 0.23
Max = 2.38, Min = 0.22
WGR11 N = 452115
Max = 2.67, Min = 0.33
Max = 2.81, Min = 0.39
Max = 5.62, Min = 0.23
Max = 3.12, Min = 0.32
Max = 2.72, Min = 0.26
WGR10 N = 179233
Max = 1.99, Min = 0.40
Max = 2.19, Min = 0.47
Max = 3.09, Min = 0.22
Max = 2.02, Min = 0.31
Max = 2.06, Min = 0.17
WGR09 N = 358504
Max = 1.57, Min = 0.56
Max = 1.47, Min = 0.62
Max = 2.32, Min = 0.36
Max = 1.80, Min = 0.38
Max = 1.86, Min = 0.39

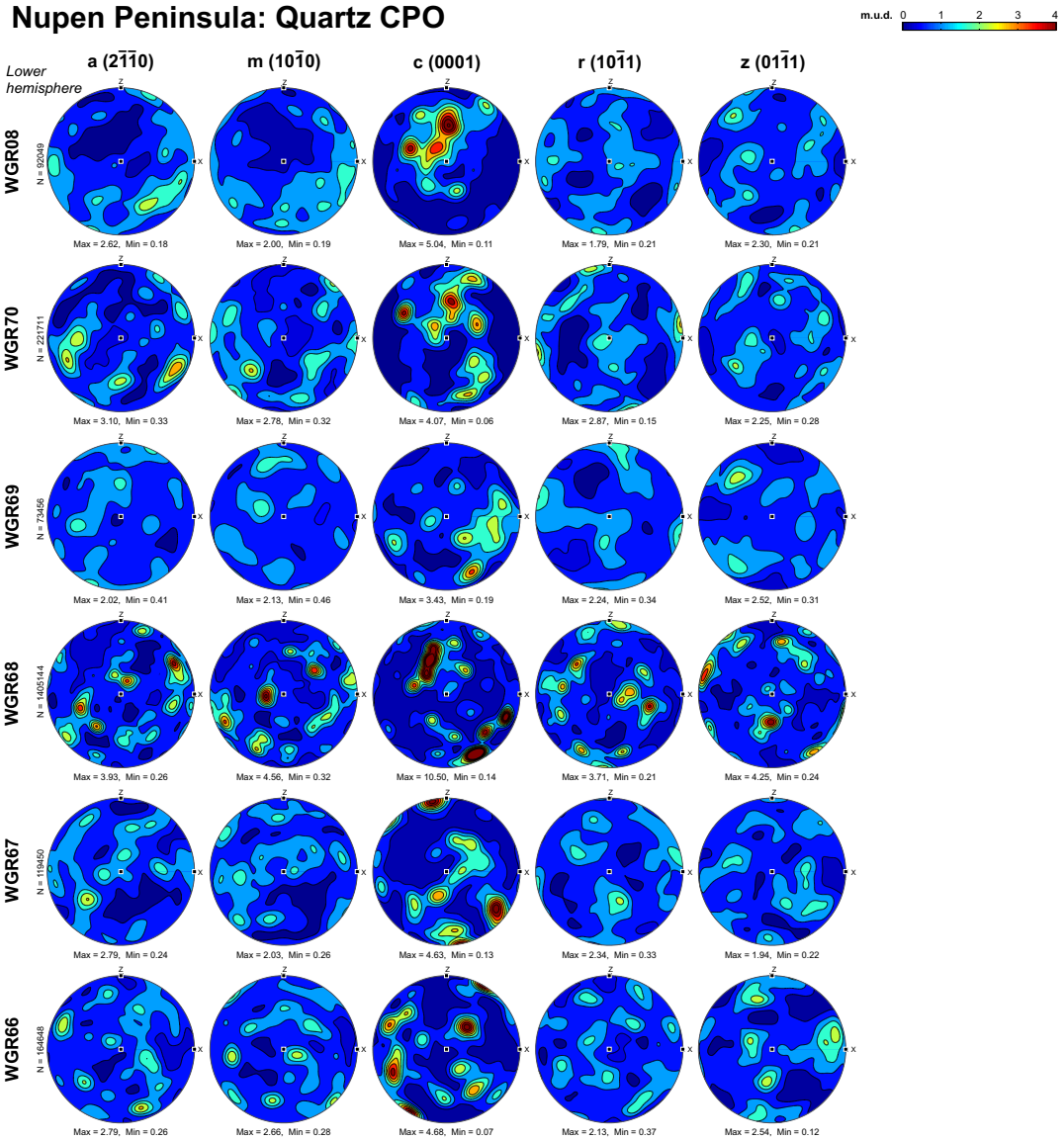
Nupen Peninsula: Quartz CPO
m.u.d. 0 1 2 3 4
Lower hemisphere
a (2$\bar{1}\bar{1}$0)
m (10$\bar{1}$0)
c (0001)
r (10$\bar{1}$1)
z (01$\bar{1}$1)
WGR08
N = 92049
Max = 2.62, Min = 0.18
Max = 2.00, Min = 0.19
Max = 5.04, Min = 0.11
Max = 1.79, Min = 0.21
Max = 2.30, Min = 0.21
WGR70
N = 221711
Max = 3.10, Min = 0.33
Max = 2.78, Min = 0.32
Max = 4.07, Min = 0.06
Max = 2.87, Min = 0.15
Max = 2.25, Min = 0.28
WGR69
N = 73456
Max = 2.02, Min = 0.41
Max = 2.13, Min = 0.46
Max = 3.43, Min = 0.19
Max = 2.24, Min = 0.34
Max = 2.52, Min = 0.31
WGR68
N = 1405144
Max = 3.93, Min = 0.26
Max = 4.56, Min = 0.32
Max = 10.50, Min = 0.14
Max = 3.71, Min = 0.21
Max = 4.25, Min = 0.24
WGR67
N = 119450
Max = 2.79, Min = 0.24
Max = 2.03, Min = 0.26
Max = 4.63, Min = 0.13
Max = 2.34, Min = 0.33
Max = 1.94, Min = 0.22
WGR66
N = 164648
Max = 2.79, Min = 0.26
Max = 2.66, Min = 0.28
Max = 4.68, Min = 0.07
Max = 2.13, Min = 0.37
Max = 2.54, Min = 0.12

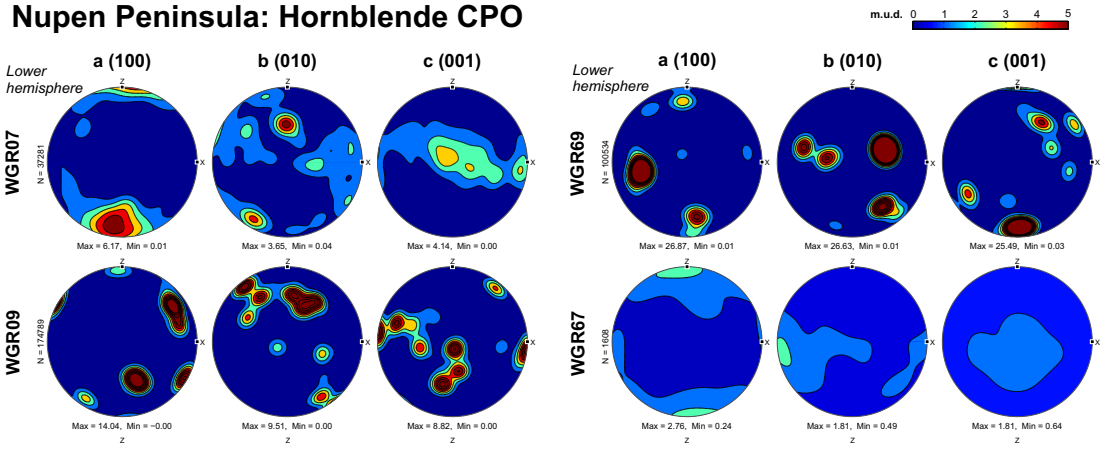
Nupen Peninsula: Hornblende CPO
m.u.d. 0 1 2 3 4 5
Lower hemisphere
a (100)
b (010)
c (001)
WGR07
N = 37281
Max = 6.17, Min = 0.01
Max = 3.65, Min = 0.04
Max = 4.14, Min = 0.00
WGR09
N = 174789
Max = 14.04, Min = −0.00
Max = 9.51, Min = 0.00
Max = 8.82, Min = 0.00
Lower hemisphere
a (100)
b (010)
c (001)
WGR69
N = 100534
Max = 26.87, Min = 0.01
Max = 26.63, Min = 0.01
Max = 25.49, Min = 0.03
WGR67
N = 1608
Max = 2.76, Min = 0.24
Max = 1.81, Min = 0.49
Max = 1.81, Min = 0.64

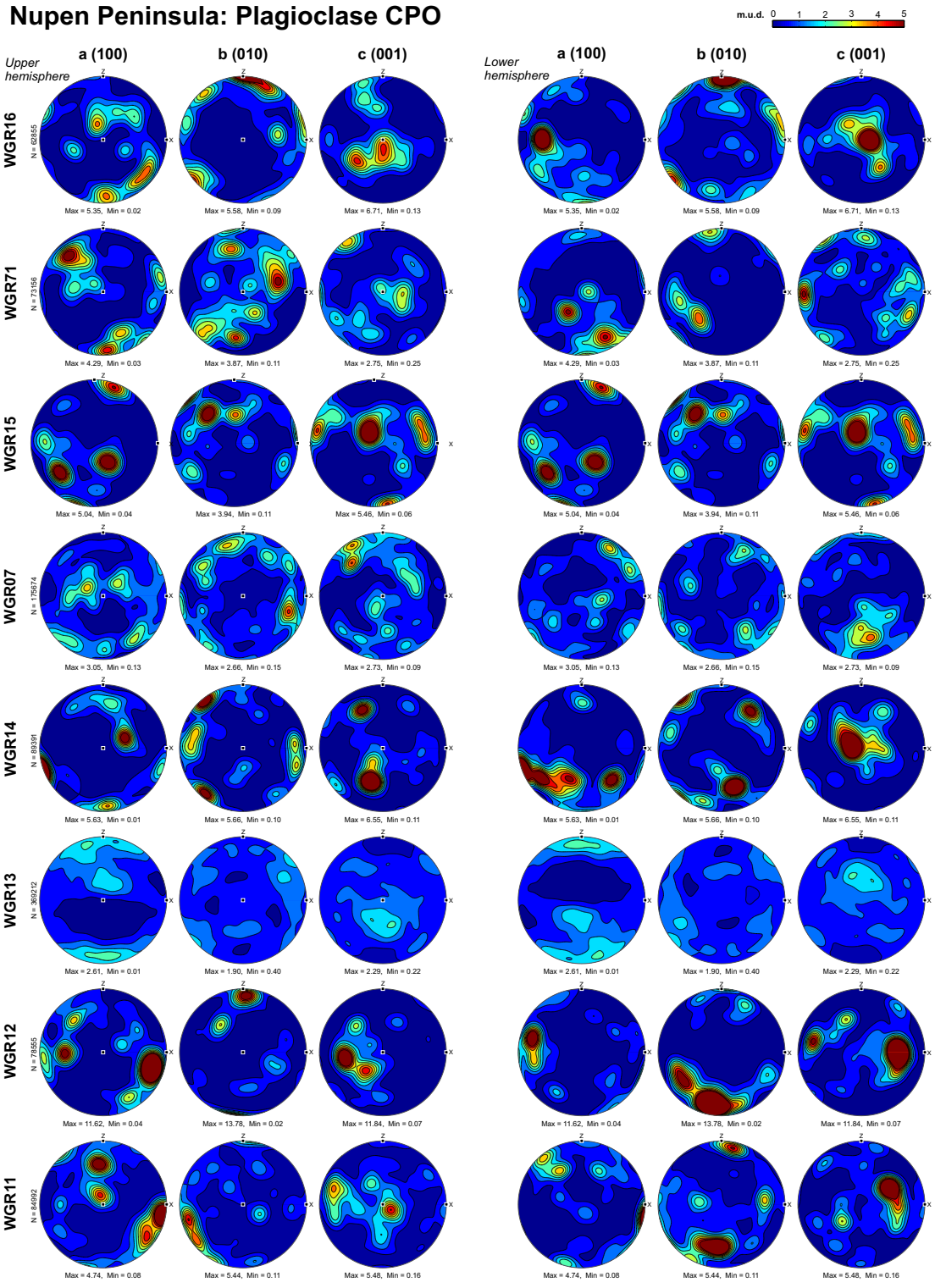
Nupen Peninsula: Plagioclase CPO
m.u.d. 0 1 2 3 4 5
Upper hemisphere
Lower hemisphere
a (100)
b (010)
c (001)
WGR16
N = 62655
Max = 5.35, Min = 0.02
Max = 5.58, Min = 0.09
Max = 6.71, Min = 0.13
WGR71
N = 73156
Max = 4.29, Min = 0.03
Max = 3.87, Min = 0.11
Max = 2.75, Min = 0.25
WGR15
Max = 5.04, Min = 0.04
Max = 3.94, Min = 0.11
Max = 5.46, Min = 0.06
WGR07
N = 175674
Max = 3.05, Min = 0.13
Max = 2.66, Min = 0.15
Max = 2.73, Min = 0.09
WGR14
N = 89391
Max = 5.63, Min = 0.01
Max = 5.66, Min = 0.10
Max = 6.55, Min = 0.11
WGR13
N = 309212
Max = 2.61, Min = 0.01
Max = 1.90, Min = 0.40
Max = 2.29, Min = 0.22
WGR12
N = 79555
Max = 11.62, Min = 0.04
Max = 13.78, Min = 0.02
Max = 11.84, Min = 0.07
WGR11
N = 84992
Max = 4.74, Min = 0.08
Max = 5.44, Min = 0.11
Max = 5.48, Min = 0.16

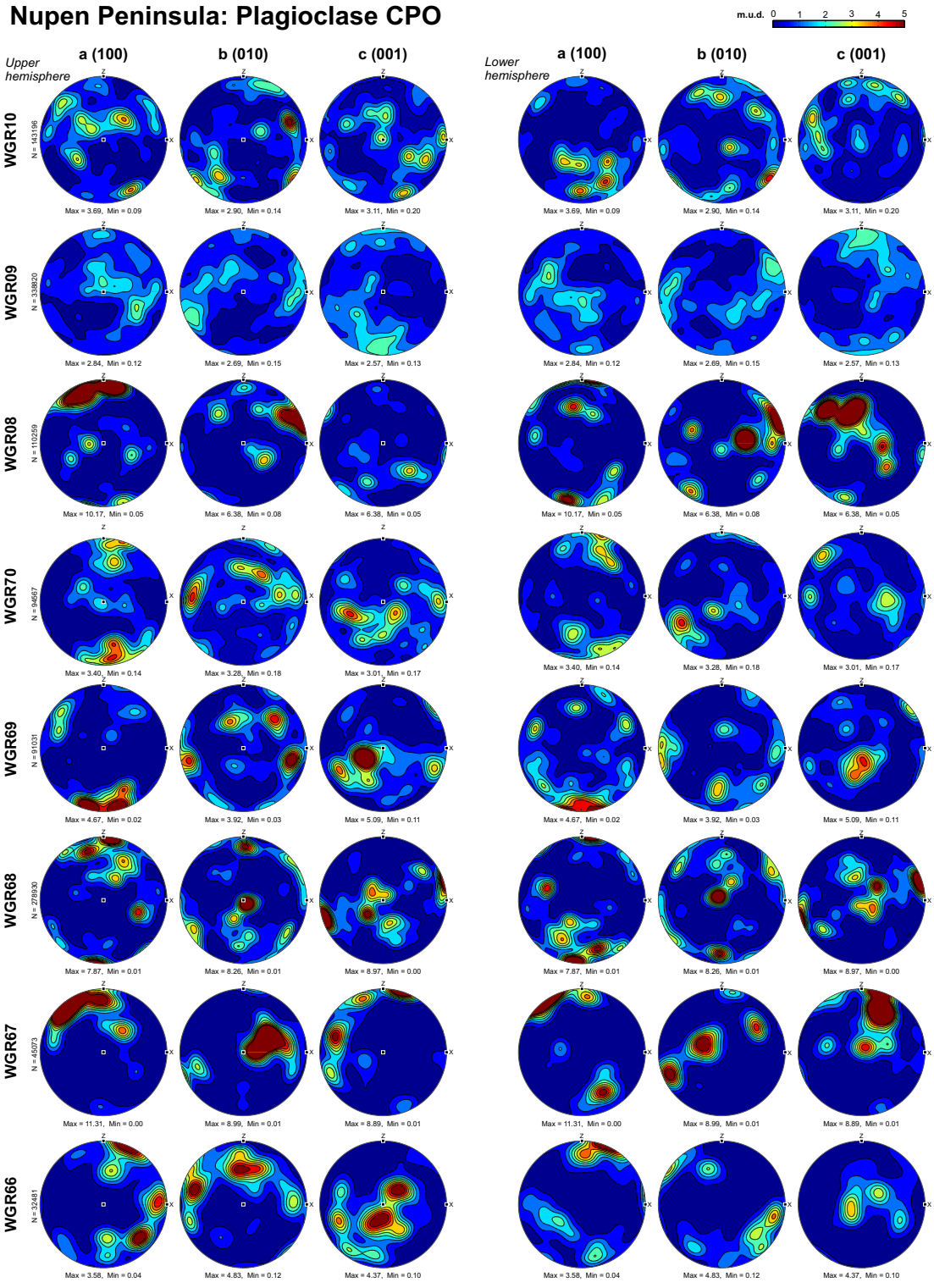
Nupen Peninsula: Plagioclase CPO
m.u.d. 0 1 2 3 4 5
Upper hemisphere
Lower hemisphere
a (100)
b (010)
c (001)
WGR10
N = 143196
Max = 3.69, Min = 0.09
Max = 2.90, Min = 0.14
Max = 3.11, Min = 0.20
WGR09
N = 338920
Max = 2.84, Min = 0.12
Max = 2.69, Min = 0.15
Max = 2.57, Min = 0.13
WGR08
N = 110259
Max = 10.17, Min = 0.05
Max = 6.38, Min = 0.08
Max = 6.38, Min = 0.05
WGR70
N = 94567
Max = 3.40, Min = 0.14
Max = 3.28, Min = 0.18
Max = 3.01, Min = 0.17
WGR69
N = 91031
Max = 4.67, Min = 0.02
Max = 3.92, Min = 0.03
Max = 5.09, Min = 0.11
WGR68
N = 278930
Max = 7.87, Min = 0.01
Max = 8.26, Min = 0.01
Max = 8.97, Min = 0.00
WGR67
N = 45073
Max = 11.31, Min = 0.00
Max = 8.99, Min = 0.01
Max = 8.89, Min = 0.01
WGR66
N = 32481
Max = 3.58, Min = 0.04
Max = 4.83, Min = 0.12
Max = 4.37, Min = 0.10

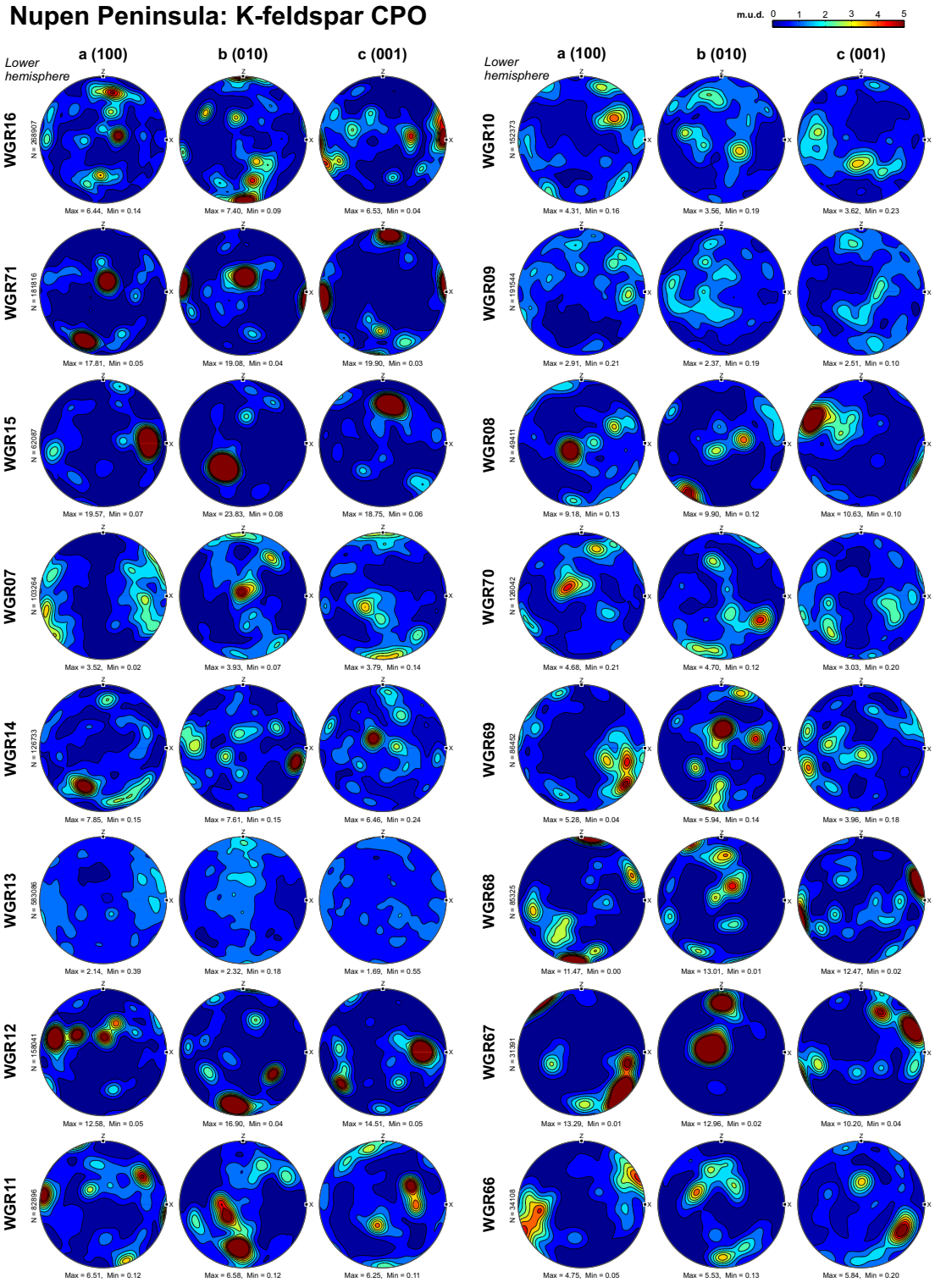
Nupen Peninsula: K-feldspar CPO
m.u.d. 0 1 2 3 4 5
Lower hemisphere
a (100)
b (010)
c (001)
WGR16
N = 286907
Max = 6.44, Min = 0.14
Max = 7.40, Min = 0.09
Max = 6.53, Min = 0.04
WGR71
N = 181616
Max = 17.81, Min = 0.05
Max = 19.08, Min = 0.04
Max = 19.90, Min = 0.03
WGR15
N = 62087
Max = 19.57, Min = 0.07
Max = 23.83, Min = 0.08
Max = 18.75, Min = 0.06
WGR07
N = 103264
Max = 3.52, Min = 0.02
Max = 3.93, Min = 0.07
Max = 3.79, Min = 0.14
WGR14
N = 126733
Max = 7.85, Min = 0.15
Max = 7.61, Min = 0.15
Max = 6.46, Min = 0.24
WGR13
N = 353086
Max = 2.14, Min = 0.39
Max = 2.32, Min = 0.18
Max = 1.69, Min = 0.55
WGR12
N = 159041
Max = 12.58, Min = 0.05
Max = 16.90, Min = 0.04
Max = 14.51, Min = 0.05
WGR11
N = 229896
Max = 6.51, Min = 0.12
Max = 6.58, Min = 0.12
Max = 6.25, Min = 0.11
Lower hemisphere
a (100)
b (010)
c (001)
WGR10
N = 152373
Max = 4.31, Min = 0.16
Max = 3.56, Min = 0.19
Max = 3.62, Min = 0.23
WGR09
N = 191544
Max = 2.91, Min = 0.21
Max = 2.37, Min = 0.19
Max = 2.51, Min = 0.10
WGR08
N = 49411
Max = 9.18, Min = 0.13
Max = 9.90, Min = 0.12
Max = 10.63, Min = 0.10
WGR70
N = 126042
Max = 4.68, Min = 0.21
Max = 4.70, Min = 0.12
Max = 3.03, Min = 0.20
WGR69
N = 86482
Max = 5.28, Min = 0.04
Max = 5.94, Min = 0.14
Max = 3.96, Min = 0.18
WGR68
N = 85325
Max = 11.47, Min = 0.00
Max = 13.01, Min = 0.01
Max = 12.47, Min = 0.02
WGR67
N = 31991
Max = 13.29, Min = 0.01
Max = 12.96, Min = 0.02
Max = 10.20, Min = 0.04
WGR66
N = 34108
Max = 4.75, Min = 0.05
Max = 5.53, Min = 0.13
Max = 5.84, Min = 0.20

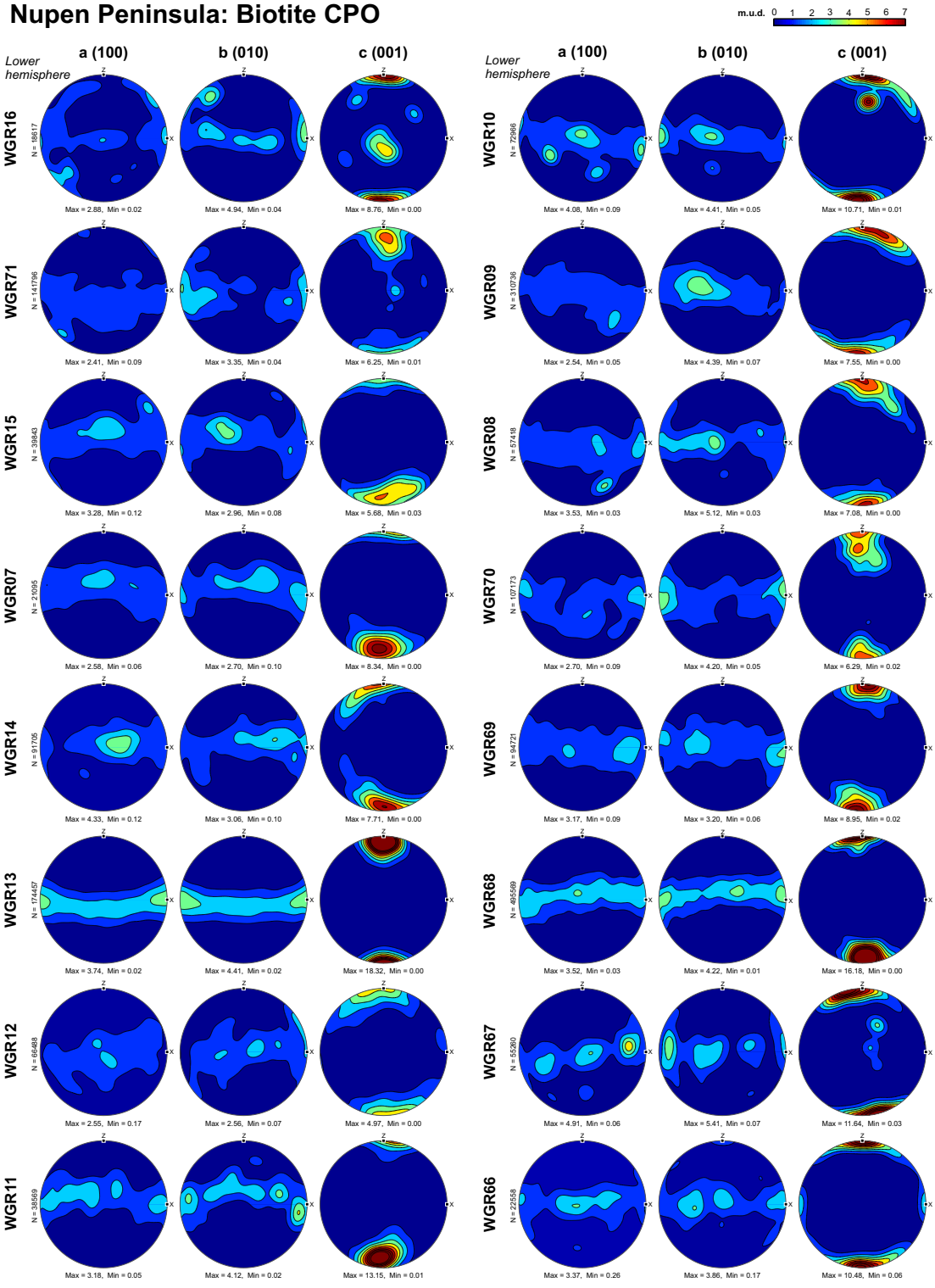
Nupen Peninsula: Biotite CPO
m.u.d. 0 1 2 3 4 5 6 7
Lower hemisphere
a (100)
b (010)
c (001)
WGR16 N = 19817 Max = 2.88, Min = 0.02 Max = 4.94, Min = 0.04 Max = 8.76, Min = 0.00
WGR71 N = 147796 Max = 2.41, Min = 0.09 Max = 3.35, Min = 0.04 Max = 6.25, Min = 0.01
WGR15 N = 39843 Max = 3.28, Min = 0.12 Max = 2.96, Min = 0.08 Max = 5.68, Min = 0.03
WGR07 N = 21095 Max = 2.58, Min = 0.06 Max = 2.70, Min = 0.10 Max = 8.34, Min = 0.00
WGR14 N = 91705 Max = 4.33, Min = 0.12 Max = 3.06, Min = 0.10 Max = 7.71, Min = 0.00
WGR13 N = 174457 Max = 3.74, Min = 0.02 Max = 4.41, Min = 0.02 Max = 18.32, Min = 0.00
WGR12 N = 66488 Max = 2.55, Min = 0.17 Max = 2.56, Min = 0.07 Max = 4.97, Min = 0.00
WGR11 N = 38569 Max = 3.18, Min = 0.05 Max = 4.12, Min = 0.02 Max = 13.15, Min = 0.01
Lower hemisphere
a (100)
b (010)
c (001)
WGR10 N = 72966 Max = 4.08, Min = 0.09 Max = 4.41, Min = 0.05 Max = 10.71, Min = 0.01
WGR09 N = 310736 Max = 2.54, Min = 0.05 Max = 4.39, Min = 0.07 Max = 7.55, Min = 0.00
WGR08 N = 57418 Max = 3.53, Min = 0.03 Max = 5.12, Min = 0.03 Max = 7.08, Min = 0.00
WGR70 N = 107173 Max = 2.70, Min = 0.09 Max = 4.20, Min = 0.05 Max = 6.29, Min = 0.02
WGR69 N = 94721 Max = 3.17, Min = 0.09 Max = 3.20, Min = 0.06 Max = 8.95, Min = 0.02
WGR68 N = 495569 Max = 3.52, Min = 0.03 Max = 4.22, Min = 0.01 Max = 16.18, Min = 0.00
WGR67 N = 55260 Max = 4.91, Min = 0.06 Max = 5.41, Min = 0.07 Max = 11.64, Min = 0.03
WGR66 N = 22558 Max = 3.37, Min = 0.26 Max = 3.86, Min = 0.17 Max = 10.48, Min = 0.06

Appendix B

Stress and strain rate data

B.1 Stress and strain rate data for the Øksfjord shear zone, SIP

Table B.1: Microstructural data for quartz-bearing samples in the ØSZ. J-index and rms grain size are calculated from EBSD data; melt volume is calculated from optical microscopy and image analysis; differential stress is calculated via the Cross et al. (2017) palaeopiezometer and strain rates are calculated after Tokle et al. (2019).

Sample number	D rms grain size (μm)	σ Differential stress (MPa)	$\dot{\varepsilon}$, Strain rate via flow law (s^{-1})	ϕ, Crystallised melt volume (%)
SIP24	21.39	67.54	2.6×10^{-11}	4
SIP23	37.84	45.08	5.2×10^{-12}	8
SIP21	42.78	41.32	3.6×10^{-12}	13
SIP20	45.45	39.58	3.1×10^{-12}	15
SIP19	50.97	36.49	2.2×10^{-12}	14
SIP18	50.01	36.99	2.3×10^{-12}	13
SIP17	17.63	77.48	4.5×10^{-11}	7
SIP16	20.70	69.14	2.6×10^{-11}	4
SIP15	31.70	51.11	8.5×10^{-12}	5
SIP43	26.58	57.91	1.4×10^{-11}	4
SIP12	30.12	52.99	9.9×10^{-12}	4
SIP11	31.65	51.16	8.6×10^{-12}	2

Appendix C

Seismic melt modelling

C.1 Seismic melt code

The `Seismic_melts` toolbox provides a workflow to produce seismic data from an EBSD dataset with a specified melt volume. `Seismic_melts` is a modelling approach to assess the combined impact of various melt and solid phase properties on seismic velocities and anisotropy. The modelling is based on crystallographic preferred orientation data and elastic stiffness tensors, allowing quantification of the variation of seismic velocities with varying melt volumes, shapes, orientations, and matrix anisotropy (see Chapter 5; Lee et al., 2017). The software is run in MatLab utilising functions within the MTEX (*mtex-toolbox.github.io*; Mainprice et al., 2011) and MSAT (*github.com/andreww/MSAT*; Walker and Wookey, 2012) toolboxes.

The `SeismicMelts` script follows the workflow in Figure C.1, first it loads an EBSD data file in channel text file (.ctf) format ('SIP20.ctf' is the example sample). If a mineral phase is not present in the `get_phase_data` database, an error message will be given. Mineral phases can be added to the database if the crystal symmetry, elastic stiffness matrix (GPa) and density (g/m^3) are known (Table C.1 shows the constants used in this thesis). Individual elastic stiffness tensors are calculated for each mineral phase, these are then combined into an aggregate elastic stiffness tensor with the elastic stiffness tensor for melt accourding to the specified melt model. We have developed four melt models that incorporate shape and crystal fabrics to model the seismic properties

Table C.1: Density (ρ) and elastic constants (K, G, C_{ij}) for the mineral phases used in the seismic melt modelling in Chapters 5 and 6.

Mineral phase	ρ (g/m^3)	K (GPa)	G (GPa)	**Subscript in *ij* in modulus C_{ij}** (GPa)												**Ref.**
Trigonal (-3)				*11*	*22*	*33*	*44*	*55*	*66*	*12*	*13*	*23*	*14*	*24*	*56*	
Quartz	2.65	37.41	44.3	86.8	86.8	105.75	58.2	58.2	39.88	7.04	11.91	11.91	-18.04	18.04	-18.04	*a*
Ilmenite	3.79	212	132	472	472	382	106	106	152	168	70	70	-27	27	-27	*b*
Calcite	3.58	73.3	32	144	144	84	33.5	33.5	33.5	53.9	51.1	51.1	-20.5	20.5	-20.5	*c*
Monoclinic (12/m1)				*11*	*22*	*33*	*44*	*55*	*66*	*12*	*13*	*23*	*15*	*25*	*35*	*46*	
K-Feldspar	2.56	54	27	62.5	172	124.4	14.3	22.3	37.4	42.8	35.8	24.1	-15.4	-14.3	-11.5	-2.8	*d*
Hornblende	3.12	87	43	116	159.7	197.6	57.4	31.8	36.8	44.9	61.4	65.5	4.3	-2.5	10	-6.2	*c*
Augite	3.4	95.4	59	181.6	150.7	217.8	69.7	51.1	55.8	73.4	72.4	33.9	19.9	16.6	24.6	4.3	*e*
Diopside	3.29	108	65.1	204	175	238	67.5	58.8	70.5	84.4	81	57	17	7	43	7.3	*f*
Biotite	3.06	37.53	15.36	186	186	186	5.86	5.8	76.8	32.4	11.6	11.6					*g*
Muscovite	2.79	-	-	181	178.4	58.6	16.5	19.5	72	48.8	25.6	21.2					*e*
Triclinic (-1)				*11*	*22*	*33*	*44*	*55*	*66*	*12*	*13*	*23*	*15*	*25*	*35*	*46*	
Albite An_{0-10}	2.62	-	-	74	131	128	17.3	29.6	32	36.4	39.4	31	-6.6	-12.8	-20	-2.5	*f*
Oligoclase An_{25}	2.65	-	-	91.66	95.44	92.85	28.08	27.92	27.98	36.61	36.14	36.75	-0.86	-0.83	-1.29	-0.09	*d*
Andesine An_{38}	2.56	70.7	33.6	96.2	189.4	171.9	23.6	33.1	1.4	46.1	38.4	15.4	-0.2	-5.1	7.2	-4.8	*d*
Labradorite An_{67}	2.72	-	-	99.4	158	150	21.7	34.5	37.1	62.8	48.7	26.7	-2.5	-10.7	-12.4	-5.4	*f*
Bytownite An_{85}	2.73	-	-	120.4	91.6	163.7	23.3	32.8	35	56.6	49.9	26.3	3.2	5.4	1.7	0.9	*d*
Anorthosite An_{90-100}	2.76	-	-	124	205	156	23.5	40.4	41.5	66	50	42	-19	-7	-18	-1	*f*
Orthorhombic (2/m)				*11*	*22*	*33*	*44*	*55*	*66*	*12*	*13*	*23*	*15*	*25*	*35*	*46*	
Enstatite	3.12	108	76.8	223	171	216	83	79	87	73	56	50	17	7	43	7.3	*b*
Hypersthene	3.38	102.2	60.7	223	165.4	205.7	83.1	76.4	78.5	70.1	57.3	49.6					*h*
Sillimanite	3.24	-	-	287.3	231.9	388.4	122.4	80.7	89.3	158.6	83.4	94.7					*i*
Cubic (m-3m)				*11*	*22*	*33*	*44*	*55*	*66*	*12*	*13*	*23*					
Almandine	3.58	177	94.3	287.4	287.4	287.4	91.6	91.6	91.6	105	105	105					*j*
Pyrope	3.57	-	-	296.2	296.2	296.2	91.6	91.6	91.6	111.1	111.1	111.1					*k*
Isotropic (O)				*11*	*22*	*33*	*44*	*55*	*66*	*12*	*13*	*23*					
Melt	2.25-2.65	16.1	0.01	16.1	16.1	16.1	0.01	0.01	0.01	15.967	15.967	15.967					

Reference key: [a]McSkimin et al. (1965); [b]Weidner and Ito (1985); [c]Hearmon (1979); [d]Aleksandrov et al. (1974); [e]Aleksandrov and Ryzhova (1961); [f]Bass (1995); [g]Belikov (1967); [h]Kress et al. (1988); [i]Verma (1960); [j]O'Neill et al. (1989); [k]O'Neill et al. (1991).

of mid to lower crustal melt (Figure 5.1): (a) 'no fabric', `ISO`; (b) 'shape fabric', `SHP`; (c) 'layered fabric', `BAC`; and (d) 'crystal fabric', `CPO`. For detailed methodology for how each melt model calculates the aggregate elastic stiffness tensor, see Chapter 5.

The source code for `Seismic_melts` is available from the following GitHub repository: *github.com/ earall/ seismic_melts*.

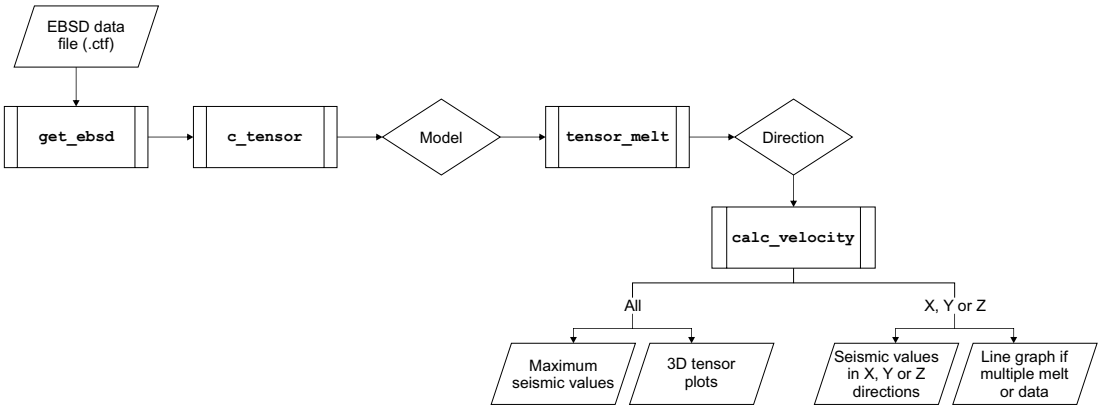

Figure C.1: 'Seismic_melts' function flow chart from loading the EBSD data to calculating elastic stiffness tensors to calculating seismic properties and displaying output values or a figure.

C.2 Seismic tensors

The following pages contain the seismic tensors for all samples in the ØSZ and Nupen Peninsula. Seismic properties for the solid crystal fabric model are shown here. Calculated seismic results are shown for waves propagating in the X_m, Y_m and Z_m directions.

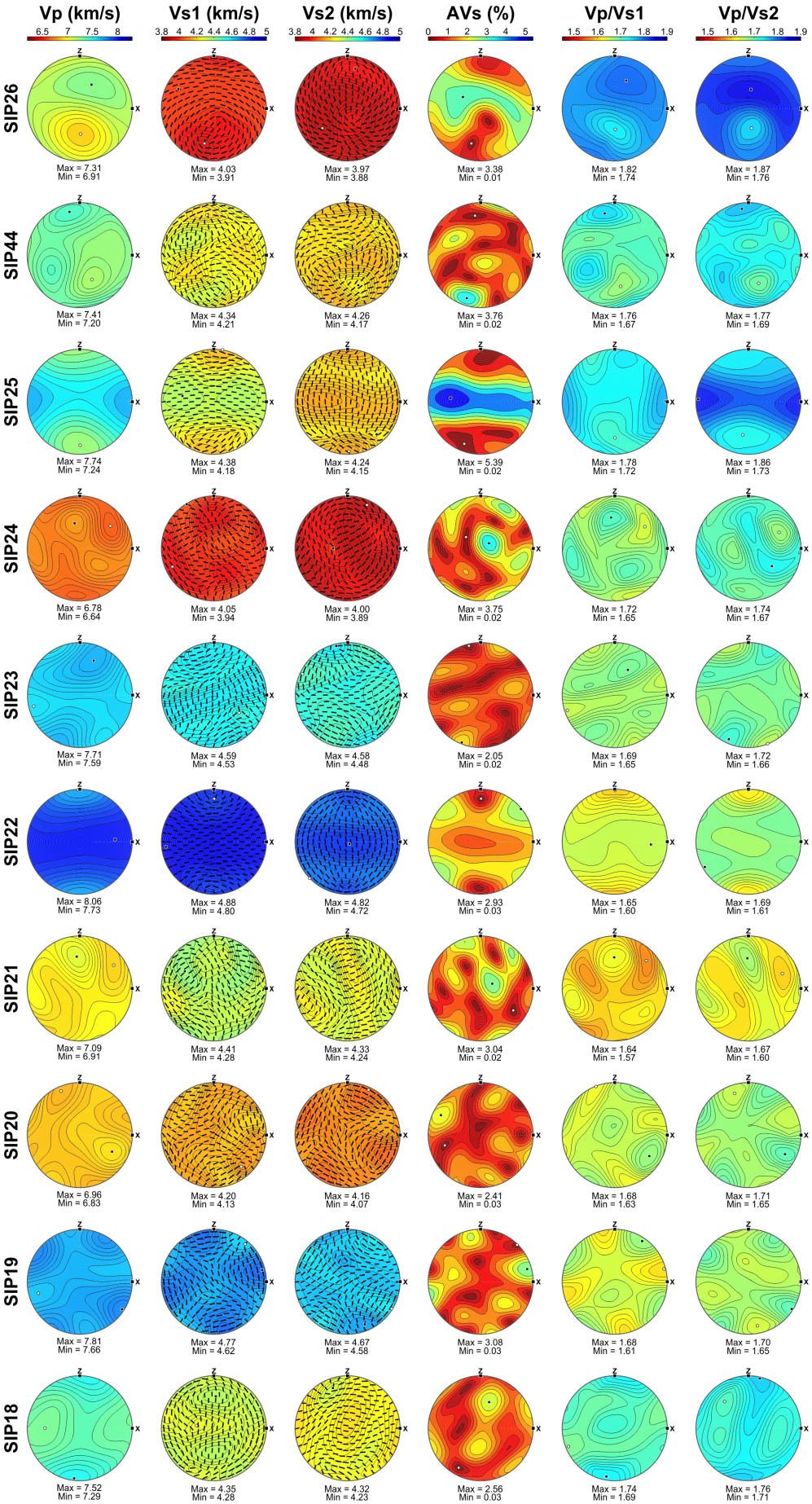
Vp (km/s)
6.5 7 7.5 8
Vs1 (km/s)
3.8 4 4.2 4.4 4.6 4.8 5
Vs2 (km/s)
3.8 4 4.2 4.4 4.6 4.8 5
AVs (%)
0 1 2 3 4 5
Vp/Vs1
1.5 1.6 1.7 1.8 1.9
Vp/Vs2
1.5 1.6 1.7 1.8 1.9
SIP26
Max = 7.31 Min = 6.91
Max = 4.03 Min = 3.91
Max = 3.97 Min = 3.88
Max = 3.38 Min = 0.01
Max = 1.82 Min = 1.74
Max = 1.87 Min = 1.76
SIP44
Max = 7.41 Min = 7.20
Max = 4.34 Min = 4.21
Max = 4.26 Min = 4.17
Max = 3.76 Min = 0.02
Max = 1.76 Min = 1.67
Max = 1.77 Min = 1.69
SIP25
Max = 7.74 Min = 7.24
Max = 4.38 Min = 4.18
Max = 4.24 Min = 4.15
Max = 5.39 Min = 0.02
Max = 1.78 Min = 1.72
Max = 1.86 Min = 1.73
SIP24
Max = 6.78 Min = 6.64
Max = 4.05 Min = 3.94
Max = 4.00 Min = 3.89
Max = 3.75 Min = 0.02
Max = 1.72 Min = 1.65
Max = 1.74 Min = 1.67
SIP23
Max = 7.71 Min = 7.59
Max = 4.59 Min = 4.53
Max = 4.58 Min = 4.48
Max = 2.05 Min = 0.02
Max = 1.69 Min = 1.65
Max = 1.72 Min = 1.66
SIP22
Max = 8.06 Min = 7.73
Max = 4.88 Min = 4.80
Max = 4.82 Min = 4.72
Max = 2.93 Min = 0.03
Max = 1.65 Min = 1.60
Max = 1.69 Min = 1.61
SIP21
Max = 7.09 Min = 6.91
Max = 4.41 Min = 4.28
Max = 4.33 Min = 4.24
Max = 3.04 Min = 0.02
Max = 1.64 Min = 1.57
Max = 1.67 Min = 1.60
SIP20
Max = 6.96 Min = 6.83
Max = 4.20 Min = 4.13
Max = 4.16 Min = 4.07
Max = 2.41 Min = 0.03
Max = 1.68 Min = 1.63
Max = 1.71 Min = 1.65
SIP19
Max = 7.81 Min = 7.66
Max = 4.77 Min = 4.62
Max = 4.67 Min = 4.58
Max = 3.08 Min = 0.03
Max = 1.68 Min = 1.61
Max = 1.70 Min = 1.65
SIP18
Max = 7.52 Min = 7.29
Max = 4.35 Min = 4.28
Max = 4.32 Min = 4.23
Max = 2.56 Min = 0.03
Max = 1.74 Min = 1.69
Max = 1.76 Min = 1.71

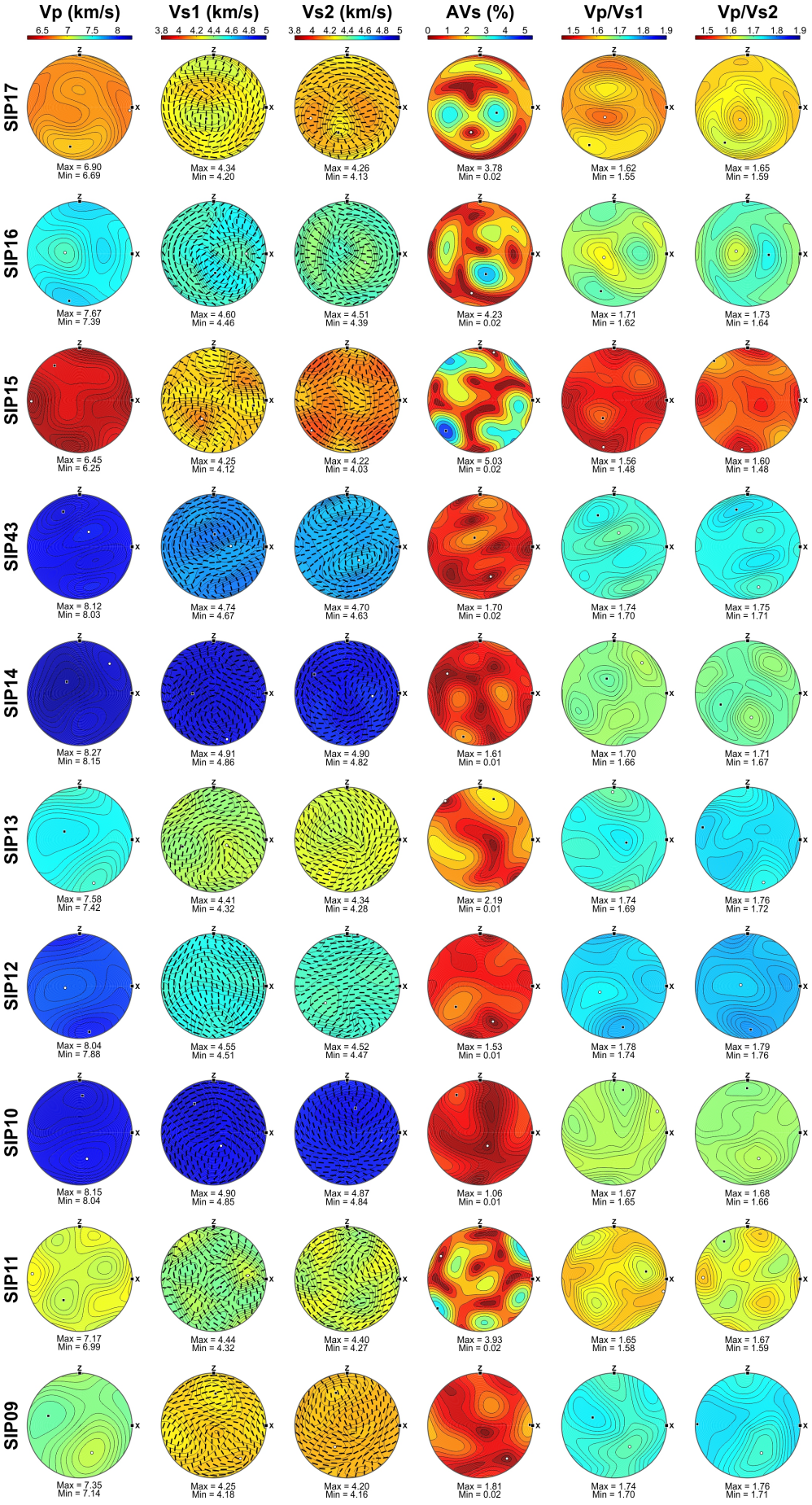
Vp (km/s)
6.5 7 7.5 8
Vs1 (km/s)
3.8 4 4.2 4.4 4.6 4.8 5
Vs2 (km/s)
3.8 4 4.2 4.4 4.6 4.8 5
AVs (%)
0 1 2 3 4 5
Vp/Vs1
1.5 1.6 1.7 1.8 1.9
Vp/Vs2
1.5 1.6 1.7 1.8 1.9
SIP17
Max = 6.90 Min = 6.69
Max = 4.34 Min = 4.20
Max = 4.26 Min = 4.13
Max = 3.78 Min = 0.02
Max = 1.62 Min = 1.55
Max = 1.65 Min = 1.59
SIP16
Max = 7.67 Min = 7.39
Max = 4.60 Min = 4.46
Max = 4.51 Min = 4.39
Max = 4.23 Min = 0.02
Max = 1.71 Min = 1.62
Max = 1.73 Min = 1.64
SIP15
Max = 6.45 Min = 6.25
Max = 4.25 Min = 4.12
Max = 4.22 Min = 4.03
Max = 5.03 Min = 0.02
Max = 1.56 Min = 1.48
Max = 1.60 Min = 1.48
SIP43
Max = 8.12 Min = 8.03
Max = 4.74 Min = 4.67
Max = 4.70 Min = 4.63
Max = 1.70 Min = 0.02
Max = 1.74 Min = 1.70
Max = 1.75 Min = 1.71
SIP14
Max = 8.27 Min = 8.15
Max = 4.91 Min = 4.86
Max = 4.90 Min = 4.82
Max = 1.61 Min = 0.01
Max = 1.70 Min = 1.66
Max = 1.71 Min = 1.67
SIP13
Max = 7.58 Min = 7.42
Max = 4.41 Min = 4.32
Max = 4.34 Min = 4.28
Max = 2.19 Min = 0.01
Max = 1.74 Min = 1.69
Max = 1.76 Min = 1.72
SIP12
Max = 8.04 Min = 7.88
Max = 4.55 Min = 4.51
Max = 4.52 Min = 4.47
Max = 1.53 Min = 0.01
Max = 1.78 Min = 1.74
Max = 1.79 Min = 1.76
SIP10
Max = 8.15 Min = 8.04
Max = 4.90 Min = 4.85
Max = 4.87 Min = 4.84
Max = 1.06 Min = 0.01
Max = 1.67 Min = 1.65
Max = 1.68 Min = 1.66
SIP11
Max = 7.17 Min = 6.99
Max = 4.44 Min = 4.32
Max = 4.40 Min = 4.27
Max = 3.93 Min = 0.02
Max = 1.65 Min = 1.58
Max = 1.67 Min = 1.59
SIP09
Max = 7.35 Min = 7.14
Max = 4.25 Min = 4.18
Max = 4.20 Min = 4.16
Max = 1.81 Min = 0.02
Max = 1.74 Min = 1.70
Max = 1.76 Min = 1.71

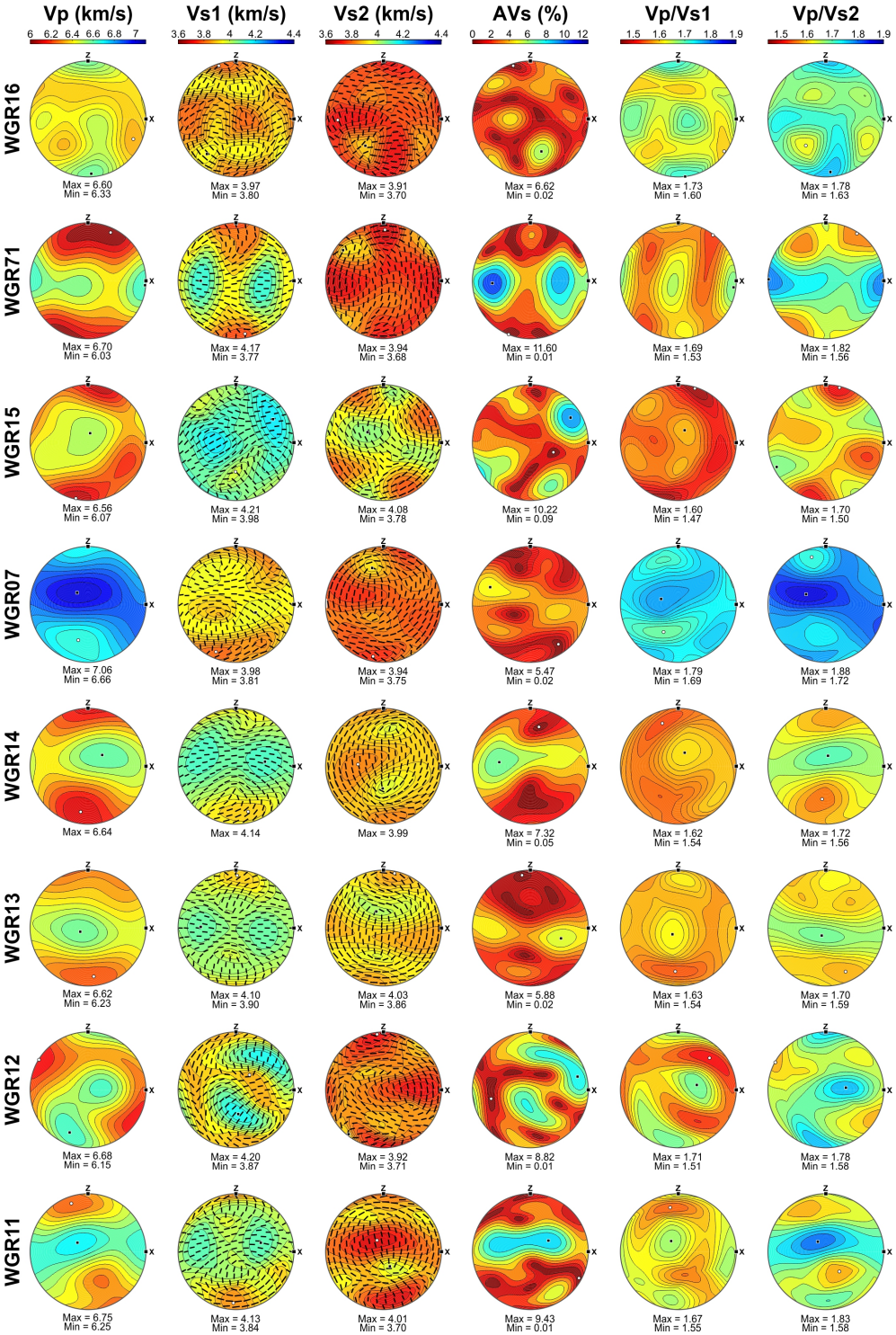
Vp (km/s)
6 6.2 6.4 6.6 6.8 7
Vs1 (km/s)
3.6 3.8 4 4.2 4.4
Vs2 (km/s)
3.6 3.8 4 4.2 4.4
AVs (%)
0 2 4 6 8 10 12
Vp/Vs1
1.5 1.6 1.7 1.8 1.9
Vp/Vs2
1.5 1.6 1.7 1.8 1.9
WGR16
Max = 6.60 Min = 6.33
Max = 3.97 Min = 3.80
Max = 3.91 Min = 3.70
Max = 6.62 Min = 0.02
Max = 1.73 Min = 1.60
Max = 1.78 Min = 1.63
WGR71
Max = 6.70 Min = 6.03
Max = 4.17 Min = 3.77
Max = 3.94 Min = 3.68
Max = 11.60 Min = 0.01
Max = 1.69 Min = 1.53
Max = 1.82 Min = 1.56
WGR15
Max = 6.56 Min = 6.07
Max = 4.21 Min = 3.98
Max = 4.08 Min = 3.78
Max = 10.22 Min = 0.09
Max = 1.60 Min = 1.47
Max = 1.70 Min = 1.50
WGR07
Max = 7.06 Min = 6.66
Max = 3.98 Min = 3.81
Max = 3.94 Min = 3.75
Max = 5.47 Min = 0.02
Max = 1.79 Min = 1.69
Max = 1.88 Min = 1.72
WGR14
Max = 6.64
Max = 4.14
Max = 3.99
Max = 7.32 Min = 0.05
Max = 1.62 Min = 1.54
Max = 1.72 Min = 1.56
WGR13
Max = 6.62 Min = 6.23
Max = 4.10 Min = 3.90
Max = 4.03 Min = 3.86
Max = 5.88 Min = 0.02
Max = 1.63 Min = 1.54
Max = 1.70 Min = 1.59
WGR12
Max = 6.68 Min = 6.15
Max = 4.20 Min = 3.87
Max = 3.92 Min = 3.71
Max = 8.82 Min = 0.01
Max = 1.71 Min = 1.51
Max = 1.78 Min = 1.58
WGR11
Max = 6.75 Min = 6.25
Max = 4.13 Min = 3.84
Max = 4.01 Min = 3.70
Max = 9.43 Min = 0.01
Max = 1.67 Min = 1.55
Max = 1.83 Min = 1.58

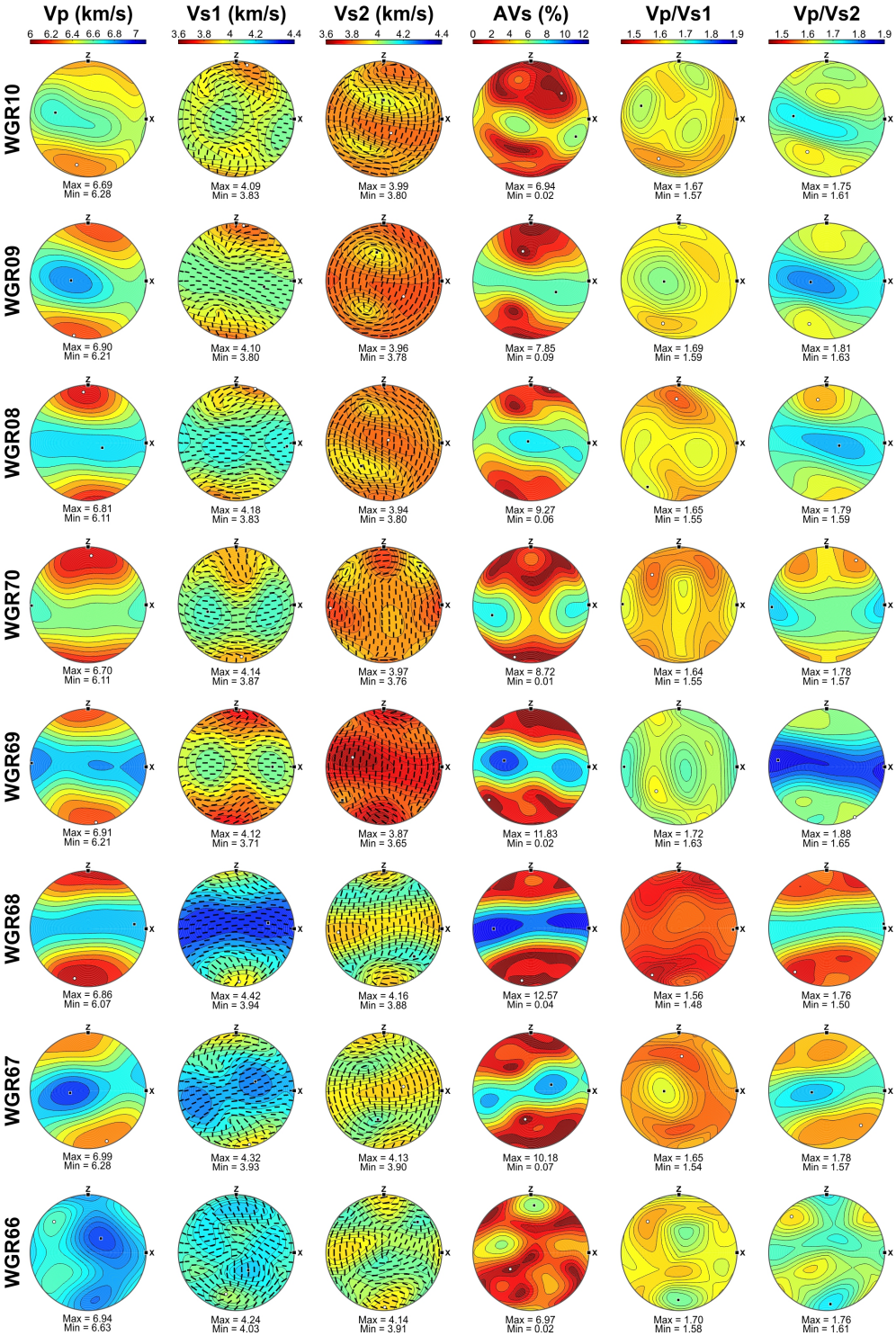
Vp (km/s)
6 6.2 6.4 6.6 6.8 7
Vs1 (km/s)
3.6 3.8 4 4.2 4.4
Vs2 (km/s)
3.6 3.8 4 4.2 4.4
AVs (%)
0 2 4 6 8 10 12
Vp/Vs1
1.5 1.6 1.7 1.8 1.9
Vp/Vs2
1.5 1.6 1.7 1.8 1.9
WGR10
Max = 6.69 Min = 6.28
Max = 4.09 Min = 3.83
Max = 3.99 Min = 3.80
Max = 6.94 Min = 0.02
Max = 1.67 Min = 1.57
Max = 1.75 Min = 1.61
WGR09
Max = 6.90 Min = 6.21
Max = 4.10 Min = 3.80
Max = 3.96 Min = 3.78
Max = 7.85 Min = 0.09
Max = 1.69 Min = 1.59
Max = 1.81 Min = 1.63
WGR08
Max = 6.81 Min = 6.11
Max = 4.18 Min = 3.83
Max = 3.94 Min = 3.80
Max = 9.27 Min = 0.06
Max = 1.65 Min = 1.55
Max = 1.79 Min = 1.59
WGR70
Max = 6.70 Min = 6.11
Max = 4.14 Min = 3.87
Max = 3.97 Min = 3.76
Max = 8.72 Min = 0.01
Max = 1.64 Min = 1.55
Max = 1.78 Min = 1.57
WGR69
Max = 6.91 Min = 6.21
Max = 4.12 Min = 3.71
Max = 3.87 Min = 3.65
Max = 11.83 Min = 0.02
Max = 1.72 Min = 1.63
Max = 1.88 Min = 1.65
WGR68
Max = 6.86 Min = 6.07
Max = 4.42 Min = 3.94
Max = 4.16 Min = 3.88
Max = 12.57 Min = 0.04
Max = 1.56 Min = 1.48
Max = 1.76 Min = 1.50
WGR67
Max = 6.99 Min = 6.28
Max = 4.32 Min = 3.93
Max = 4.13 Min = 3.90
Max = 10.18 Min = 0.07
Max = 1.65 Min = 1.54
Max = 1.78 Min = 1.57
WGR66
Max = 6.94 Min = 6.63
Max = 4.24 Min = 4.03
Max = 4.14 Min = 3.91
Max = 6.97 Min = 0.02
Max = 1.70 Min = 1.58
Max = 1.76 Min = 1.61

Appendix D

Sample data

The samples collected during fieldwork for this thesis are held in the author's collection, please contact Amicia Lee if you wish to use any samples from this thesis.

Table D.1: Sample locations and University of Leeds catalogue reference number for Øksfjord shear zone samples.

Sample number	**Location** (decimal deg.)		**Catalogue reference**
SIP 09	70.0704	22.3660	67098
SIP 10	70.0720	22.3610	67099
SIP 11	70.0731	22.3629	67100
SIP 12	70.0727	22.3599	67101
SIP 13	70.0733	22.3524	67102
SIP 14	70.0744	22.3461	67103
SIP 15	70.0752	22.3413	67104
SIP 16	70.0754	22.3403	67105
SIP 17	70.0755	22.3401	67106
SIP 18	70.0761	22.3378	67108
SIP 19	70.0762	22.3337	67109
SIP 20	70.0764	22.3333	67110
SIP 21	70.0772	22.3297	67111
SIP 22	70.0774	22.3282	67112
SIP 23	70.0774	22.3281	67113
SIP 24	70.0777	22.3234	67114
SIP 25	70.0778	22.3223	67115
SIP 26	70.0781	22.3186	67116
SIP 43	70.0748	22.3440	67117
SIP 44	70.0780	22.3213	67118

Table D.2: Sample locations and University of Leeds catalogue reference number for Western Gneiss Region samples.

Sample number	**Location** (decimal deg.)		**Catalogue reference**
WGR 07	62.2261	05.5350	67215
WGR 08	62.2316	05.5350	67216
WGR 09	62.2315	05.5342	67217
WGR 10	62.2309	05.5332	67218
WGR 11	62.2294	05.5328	67219
WGR 12	62.2285	05.5324	67220
WGR 13	62.2284	05.5312	67221
WGR 14	62.2278	05.5304	67222
WGR 15	62.2268	05.5314	67223
WGR 16	62.2227	05.5362	67224
WGR 66	62.2343	05.5436	67225
WGR 67	62.2339	05.5418	67226
WGR 68	62.2337	05.5407	67227
WGR 69	62.2333	05.5382	67228
WGR 70	62.2329	05.5371	67229
WGR 71	62.2327	05.5289	67230

References

Abdelmalak, M. M., Faleide, J. I., Planke, S., Gernigon, L., Zastrozhnov, D., Shephard, G. E., and Myklebust, R. (2017). The T-Reflection and the Deep Crustal Structure of the Vøring Margin, Offshore mid-Norway. *Tectonics*, 36(11):2497–2523.

Akselsen, J. (1982). Precambrian and Caledonian tectonometamorphic evolution of northeastern Seiland, Finnmark, North Norway. *Norges Geologiske Undersøkelse Bulletin*, 373(1977):45–61.

Aleksandrov, K. S., Alchikov, V. V., Belikov, B. P., Zaslavskii, B. I., and Krupnyi, A. I. (1974). Velocities of elastic waves in minerals at atmospheric pressure and increasing of precision of elastic constants by means of EVM. *Izvestiya Academy of Sciences, USSR, Geophysics*, Series 10:15–24.

Aleksandrov, K. S. and Ryzhova, T. V. (1961). The elastic properties of rock-forming minerals, I: pyroxenes and amphiboles. *Izvestiya Academy of Sciences, USSR, Geophysics*, Series 9:1339–1344.

Andersen, T. B. (1998). Extensional tectonics in the Caledonides of southern Norway, an overview. *Tectonophysics*, 285(3-4):333–351.

Andersen, T. B., Jamtveit, B., Dewey, J. F., and Swensson, E. (1991). Subduction and eduction of continental crust: major mechanisms during continentcontinent collision and orogenic extensional collapse, a model based on the south Norwegian Caledonides. *Terra Nova*, 3(3):303–310.

Anderson, D. L. (1989). Elasticity and Solid-state Geophysics. In *Theory of the Earth*, chapter 6, pages 103–128. Blackwell Scientific Publications, Boston.

Andreasson, P. G. and Lagerblad, B. (1980). Occurrence and significance of inverted metamorphic gradients in the western Scandinavian Caledonides. *Journal of the Geological Society*, 137(3):219–230.

Arnold, J., Jacoby, W. R., Schmeling, H., and Schott, B. (2001). Continental collision and the dynamic and thermal evolution of the Variscan orogenic crustal root numerical models. *Journal of Geodynamics*, 31:273–291.

Arzi, A. A. (1978). Critical phenomena in the rheology of partially melted rocks. *Tectonophysics*, 44(1-4):173–184.

Ashworth, J. R. (1972). Myrmekites of exsolution and replacement origins. *Geological Magazine*, 109(1):45–62.

Ashworth, J. R., editor (1985). *Migmatites*. Blackie, Glasgow.

Ashworth, J. R. and McLellan, E. L. (1985). Textures. In Ashworth, J. R., editor, *Migmatites*, chapter 5, pages 180–203. Blackie, Glasgow.

Austrheim, H. and Boundy, T. M. (1994). Pseudotachylytes Generated During Seismic Faulting and Eclogitization of the Deep Crust. *Science*, 265(5168):82–83.

Auzanneau, E., Vielzeuf, D., and Schmidt, M. W. (2006). Experimental evidence of decompression melting during exhumation of subducted continental crust. *Contributions to Mineralogy and Petrology*, 152(2):125–148.

Bachmann, F., Hielscher, R., and Schaeben, H. (2010). Texture Analysis with MTEX - Free and Open Source Software Toolbox. *Solid State Phenomena*, 160:63–68.

Backus, G. E. (1962). Long-Wave Elastic Anisotropy Produced by Horizontal Layering. *Journal of Geophysical Research: Solid Earth*, 67(11):4427–4440.

Bai, D., Unsworth, M. J., Meju, M. A., Ma, X., Teng, J., Kong, X., Sun, Y., Sun, J., Wang, L., Jiang, C., Zhao, C., Xiao, P., and Liu, M. (2010). Crustal deformation of the eastern Tibetan plateau revealed by magnetotelluric imaging. *Nature Geoscience*, 3(5):358–362.

Baird, G. B. and Hudleston, P. J. (2007). Modeling the influence of tectonic extrusion and volume loss on the geometry, displacement, vorticity , and strain compatibility of ductile shear zones. *Journal of Structural Geology*, 29:1665–1678.

Bao, X., Sandvol, E., Ni, J., Hearn, T., and Chen, Y. J. (2011). High resolution regional seismic attenuation tomography in eastern Tibetan Plateau and adjacent regions. *Geophysical Research Letters*, 38:1–5.

Bao, X., Song, X., Xu, M., Wang, L., Sun, X., and Mi, N. (2013). Crust and upper mantle structure of the North China Craton and the NE Tibetan Plateau and its tectonic implications. *Earth and Planetary Science Letters*, 369-370:129–137.

Bao, X., Sun, X., Xu, M., Eaton, D. W., Song, X., Wang, L., Ding, Z., Mi, N., Li, H., Yu, D., Huang, Z., and Wang, P. (2015). Two crustal low-velocity channels beneath SE Tibet revealed by joint inversion of Rayleigh wave dispersion and receiver functions. *Earth and Planetary Science Letters*, 415:16–24.

Barbey, P. (2007). Diffusion-controlled biotite breakdown reaction textures at the solid/ liquid transition in the continental crust. *Contributions to Mineralogy and Petrology*, 154(6):707–716.

Barth, N. C., Hacker, B. R., Seward, G. G. E., Walsh, E. O., Young, D., and Johnston, S. (2010). Strain within the ultrahigh-pressure Western Gneiss region of Norway recorded by quartz CPOs. *Geological Society, London, Special Publications*, 335:663–685.

Bass, J. D. (1995). Elasticity of minerals, glasses, and melts. In Ahrens, T. J., editor, *Mineral Physics and Crystallography: A Handbook of Physical Constants*, volume 2, pages 45–63. American Geophysical Union, Washington DC.

Bastow, I. D., Pilidou, S., Kendall, J. M., and Stuart, G. W. (2010). Melt-induced seismic anisotropy and magma assisted rifting in Ethiopia: Evidence from surface waves. *Geochemistry, Geophysics, Geosystems*, 11:1–19.

Beaumont, C. (2004). Crustal channel flows: 1. Numerical models with applications to the tectonics of the Himalayan-Tibetan orogen. *Journal of Geophysical Research: Solid Earth*, 109(B6):B06406.

Beaumont, C., Jamieson, R. A., Nguyen, M. H., and Lee, B. (2001). Himalayan tectonics explained by extrusion of a low-viscosity crustal channel coupled to focused surface denudation. *Nature*, 414(December):738–742.

Beaumont, C., Nguyen, M. H., Jamieson, R. A., and Ellis, S. (2006). Crustal flow modes in large hot orogens. *Geological Society, London, Special Publications*, 268(1):91–145.

Behrens, H. and Nowak, M. (1997). The mechanisms of water diffusion in polymerized silicate melts. *Contributions to Mineralogy and Petrology*, 126(4):377–385.

Behrmann, J. H. and Platt, J. P. (1982). Sense of nappe emplacement from quartz c-axis fabrics; an example from the Betic Cordilleras (Spain). *Earth and Planetary Science Letters*, 59(1):208–215.

Belikov, B. P. (1967). Plastic constants of rock-forming minerals and their effect on the elasticity of rocks. In *Physical and mechanical properties of rocks*, pages 124–140. Academy of Sciences of the USSR, Israel Program for Scientific Translations, Jerusalem.

Bercovici, D. and Ricard, Y. (2012). Mechanisms for the generation of plate tectonics by two-phase grain-damage and pinning. *Physics of the Earth and Planetary Interiors*, 202-203:27–55.

Berger, A. and Kalt, A. (1999). Structures and Melt Fractions as Indicators of Rheology in Cordierite-Bearing Migmatites of the Bayerische Wald (Variscan Belt, Germany). *Journal of Petrology*, 40(11):1699–1719.

Bird, P. C., Cartwright, J. A., and Davies, T. L. (2015). Basement reactivation in the development of rift basins: an example of reactivated Caledonide structures in the West Orkney Basin. *Journal of the Geological Society*, 172:77–85.

Blackman, D. K. and Kendall, J. M. (1997). Sensitivity of teleseismic body waves to mineral texture and melt in the mantle beneath a mid-ocean ridge. *Philosophical Transactions of the Royal Society of London A: Mathematical, Physical and Engineering Sciences*, 355(1723):217–231.

Blenkinsop, T. G. (2000). *Deformation microstructures and mechanisms in minerals and rocks*. Kluwer Academic Publishers, Dordrecht.

Blumenfeld, P., Mainprice, D., and Bouchez, J. L. (1986). C-slip in quartz from subsolidus deformed granite. *Tectonophysics*, 127(1-2):97–115.

Bottinga, Y. and Weill, D. F. (1970). Densities of liquid silicate systems calculated from partial molar volumes of oxide components. *American Journal of Science*, 269:169–182.

Bouchez, J. L. (1977). Plastic deformation of quartzites at low temperature in an area of natural strain gradient. *Tectonophysics*, 39(1-3):25–50.

Bouchez, J. L., Delas, C., Gleizes, G., and Nédélec, A. (1992). Submagmatic microfractures in granites. *Geology*, 20(1):35–38.

Bouchez, J. L., Lister, G. S., and Nicolas, A. (1983). Fabric asymmetry and shear sense in movement zones. *Geologische Rundschau*, 72(2):401–419.

Brown, M. (1973). The definition of metatexis, diatexis and migmatite. *Proceedings of the Geologists' Association*, 84(4):371–382.

Brown, M. (1994). The generation, segregation, ascent and emplacement of granite magma: the migmatite-to-crustally-derived granite connection in thickened orogens. *Earth-Science Reviews*, 36(1-2):83–130.

Brown, M. (2001a). Crustal melting and granite magmatism: key issues. *Physics and Chemistry of the Earth, Part A: Solid Earth and Geodesy*, 26(4-5):201–212.

Brown, M. (2001b). Orogeny, migmatites and leucogranites: A review. *Journal of Earth System Science*, 110(4):313–336.

Brown, M. (2007). Crustal melting and melt extraction, ascent and emplacement in orogens: mechanisms and consequences. *Journal of the Geological Society*, 164(4):709–730.

Brown, M. (2012). Introduction to a virtual special issue on crustal melting. *Journal of Metamorphic Geology*, 30(5):453–456.

Brown, M., Averkin, Y. A., McLellan, E. L., and Sawyer, E. W. (1995). Melt segregation in migmatites. *Journal of Geophysical Research: Solid Earth*, 100(B8):15655.

Brown, M. and Dallmeyer, R. D. (1996). Rapid Variscan exhumation and the role of magma in core complex formation: southern Brittany metamorphic belt, France. *Journal of Metamorphic Geology*, 14(3):361–379.

Brown, M. and Korhonen, F. J. (2009). Some Remarks on Melting and Extreme Metamorphism of Crustal Rocks. In *Physics and Chemistry of the Earth's Interior*, chapter 4, pages 67–87. Springer New York.

Brown, M., Korhonen, F. J., and Siddoway, C. S. (2011). Organizing melt flow through the crust. *Elements*, 7(4):261–266.

Brown, M. and Solar, G. S. (1998a). Granite ascent and emplacement during contractional deformation in convergent orogens. *Journal of Structural Geology*, 20(9-10):1365–1393.

Brown, M. and Solar, G. S. (1998b). Shear-zone systems and melts: feedback relations and self-organization in orogenic belts. *Journal of Structural Geology*, 20(2/3):211–227.

Bruhn, D., Groebner, N. J., and Kohlstedt, D. L. (2000). An interconnected network of core-forming melts produced by shear deformation. *Nature*, 403(6772):883–886.

Bucher, K. and Grapes, R. (2011). Metamorphic Rocks. In *Petrogenesis of Metamorphic Rocks*, chapter 2, pages 21–56. Springer-Verlag, Berlin.

Burg, J.-P. and Laurent, P. (1978). Strain analysis of a shear zone in a granodiorite. *Tectonophysics*, 47(1):15–42.

Burg, J.-P. and Vigneresse, J.-L. (2002). Non-linear feedback loops in the rheology of cooling-crystallizing felsic magma and heating-melting felsic rock. *Geological Society, London, Special Publications*, 200(1):275–292.

Büsch, W., Schneider, G., and Mehnert, K. R. (1974). Initial melting at grain boundaries. Part II: melting in rocks of granodioritic, quartzdioritic and tonalitic composition. *Neues Jahrbuch für Mineralogie, Monatshefte*, 8:345–370.

Butler, R. W. H., Bond, C. E., Shipton, Z. K., Jones, R. R., and Casey, M. (2008). Fabric anisotropy controls faulting in the continental crust. *Journal of the Geological Society*, 165:449–452.

Caldwell, W. B., Klemperer, S. L., Rai, S. S., and Lawrence, J. F. (2009). Partial melt in the upper-middle crust of the northwest Himalaya revealed by Rayleigh wave dispersion. *Tectonophysics*, 477(1-2):58–65.

Carreras, J., Czeck, D. M., Druguet, E., and Hudleston, P. J. (2010). Structure and development of an anastomosing network of ductile shear zones. *Journal of Structural Geology*, 32(5):656–666.

Carswell, D. A., Brueckner, H. K., Cuthbert, S. J., Mehta, K., and Brien, P. J. O. (2003). The timing of stabilisation and the exhumation rate for ultra-high pressure rocks in the Western Gneiss Region of Norway. *Journal of Metamorphic Geology*, 21(6):601–612.

Carter, K. E. and Dworkin, S. I. (1990). Channelized fluid flow through shear zones during fluid-enhanced dynamic recrystallization, Northern Apennines, Italy. *Geology*, 18:720–723.

Cartwright, I. and Barnicoat, A. C. (2003). Geochemical and stable isotope resetting in shear zones from Täschalp: constraints on fluid flow during exhumation in the Western Alps. *Journal of Metamorphic Geology*, 21:143–161.

Cavalcante, G. C. G., Viegas, G., Archanjo, C. J., and da Silva, M. E. (2016). The influence of partial melting and melt migration on the rheology of the continental crust. *Journal of Geodynamics*, 101:186–199.

Cesare, B., Ferrero, S., Salvioli-Mariani, E., Pedron, D., and Cavallo, A. (2009). "Nanogranite" and glassy inclusions: The anatectic melt in migmatites and granulites. *Geology*, 37(7):627–630.

Chauvet, A., Kienast, J. R., Pinardon, J. L., and Brunel, M. (1992). Petrological Constraints and Pt Path of Devonian Collapse Tectonics within the Scandian Mountain Belt (Western Gneiss Region, Norway). *Journal of the Geological Society*, 149:383–400.

Chen, Y., Badal, J., and Zhang, Z. (2009). Journal of Asian Earth Sciences Radial anisotropy in the crust and upper mantle beneath the Qinghai-Tibet Plateau and surrounding regions. *Journal of Asian Earth Sciences*, 36(4-5):289–302.

Christensen, N. I. (1996). Poisson's ratio and crustal seismology. *Journal of Geophysical Research: Solid Earth*, 101(B2):3139–3156.

Clark, M. K. and Royden, L. H. (2000). Topographic ooze: Building the eastern margin of Tibet by lower crustal flow. *Geology*, 28(8):703–706.

Clemens, J. D. and Holness, M. B. (2000). Textural evolution and partial melting of arkose in a contact aureole: a case study and implications. *Visual Geosciences*, 5(4):1–14.

Clerc, C., Jolivet, L., and Ringenbach, J.-c. (2015). Ductile extensional shear zones in the lower crust of a passive margin. *Earth and Planetary Science Letters*, 431:1–7.

Clerc, C., Ringenbach, J.-c., Jolivet, L., and Ballard, J.-f. (2018). Rifted margins: Ductile deformation, boudinage, continentward-dipping normal faults and the role of the weak lower crust. *Gondwana Research*, 53:20–40.

Cobbold, P. R. (1977a). Description and origin of banded deformation structures. I. Regional strain, local perturbations, and deformation bands. *Canadian Journal of Earth Sciences*, 14:1721–1731.

Cobbold, P. R. (1977b). Description and origin of banded deformation structures. II. Rheology and the growth of banded perturbations. *Canadian Journal of Earth Sciences*, 14(2510-2523).

Cooper, R. F. and Kohlstedt, D. L. (1986). Rheology and structure of olivine-basalt partial melts. *Journal of Geophysical Research: Solid Earth*, 91(B9):9315.

Corfu, F. and Andersen, T. B. (2002). U-Pb ages of the Dalsfjord complex, SW Norway, and their bearing on the correlation of allochthonous crystalline segments of the Scandinavian Caledonides. *International Journal of Earth Sciences*, 91(6):955–963.

Cornwell, D. G., Maguire, P. K. H., England, R. W., and Stuart, G. W. (2010). Imaging detailed crustal structure and magmatic intrusion across the Ethiopian Rift using a dense linear broadband array. *Geochemistry, Geophysics, Geosystems*, 11:1–21.

Cottle, J. M., Larson, K. P., and Kellett, D. A. (2015). How does the mid-crust accommodate deformation in large, hot collisional orogens? A review of recent research in the Himalayan orogen. *Journal of Structural Geology*, 78:119–133.

Cross, A. J., Prior, D. J., Stipp, M., and Kidder, S. (2017). The recrystallized grain size piezometer for quartz: An EBSD-based calibration. *Geophysical Research Letters*, 44:6667–6674.

Daines, M. J. and Kohlstedt, D. L. (1997). Influence of deformation on melt topology in peridotites conditions. *Journal of Geophysical Research: Solid Earth*, 102(B5):10257–10271.

Degli Alessandrini, G., Menegon, L., Malaspina, N., Dijkstra, A. H., and Anderson, M. W. (2017). Creep of mafic dykes infiltrated by melt in the lower continental crust (Seiland Igneous Province, Norway). *Lithos*, 274-275:169–187.

Dell'Angelo, L. N. and Tullis, J. (1988). Experimental deformation of partially melted granitic aggregates. *Journal of Metamorphic Geology*, 6:495–515.

Dell'Angelo, L. N., Tullis, J., and Yund, R. A. (1987). Transition from dislocation creep to melt-enhanced diffusion creep in fine-grained granitic aggregates. *Tectonophysics*, 139:325–332.

Drury, M. R., Humphreys, F. J., and White, S. H. (1985). Large strain deformation studies using polycrystalline magnesium as a rock analogue. Part II: dynamic recrystallisation mechanisms at high temperatures. *Physics of the Earth and Planetary Interiors*, 40(3):208–222.

Drury, M. R. and Urai, J. L. (1990). Deformation-related recrystallization processes. *Tectonophysics*, 172(3-4):235–253.

Durney, D. W. (1972). Solution-transfer, an important geological deformation mechanism. *Nature*, 235(5337):315.

Elliott, D. (1973). Diffusion Flow Laws in Metamorphic Rocks. *Geological Society of America Bulletin*, 84(August):2645–2664.

Elvevold, S., Reginiussen, H., Krogh, E. J., and Bjørklund, F. (1994). Reworking of deep-seated gabbros and associated contact metamorphism paragneisses in the southeastern part of the Seiland Igneous Province, northern Norway. *Journal of Metamorphic Geology*, 12:539–556.

Engvik, A. K., Andersen, T. B., and Wachmann, M. (2007). Inhomogeneous deformation in deeply buried continental crust, an example from the eclogite-facies province of the Western Gneiss Region, Norway. *Norsk Geologisk Tidsskrift*, 87(4):373–389.

Eshelby, J. D. (1957). The Determination of the Elastic Field of an Ellipsoidal Inclusion, and Related Problems. *Proceedings of the Royal Society of London A: Mathematical, Physical and Engineering Sciences*, 241(1226):376–396.

Evans, B., Renner, J., and Hirth, G. (2001). A few remarks on the kinetics of static grain growth in rocks. *International Journal of Earth Sciences*, 90(1):88–103.

Faul, U. H., Toomey, D. R., and Waff, H. S. (1994). Intergranular basaltic melt is distributed in thin, elogated inclusions. *Geophysical Research Letters*, 21(1):29–32.

Fossen, H. (2010). Extensional tectonics in the North Atlantic Caledonides: a regional view. *Geological Society, London, Special Publications*, 335:767–793.

Fossen, H. and Cavalcante, G. C. G. (2017). Shear zones - A review. *Earth-Science Reviews*, 171(May):434–455.

Frederiksen, A. W. and Bostock, M. G. (2000). Modelling teleseismic waves in dipping anisotropic structures. *Geophysical Journal International*, 141:401–412.

Fu, Y. V., Li, A., and Chen, Y. J. (2010). Crustal and upper mantle structure of southeast Tibet from Rayleigh wave tomography. *Journal of Geophysical Research: Solid Earth*, 115(B12):1–16.

Fusseis, F., Handy, M. R., and Schrank, C. (2006). Networking of shear zones at the brittle-to-viscous transition (Cap de Creus, NE Spain). *Journal of Structural Geology*, 28:1228–1243.

Ganzhorn, A.-C., Labrousse, L., Prouteau, G., Leroy, C., Vrijmoed, J. C., Andersen, T. B., and Arbaret, L. (2014). Structural, petrological and chemical analysis of syn-kinematic migmatites: insights from the Western Gneiss Region, Norway. *Journal of Metamorphic Geology*, 32(6):647–673.

Gapais, D. and Barbarin, B. (1986). Quartz fabric transition in a cooling syntectonic granite (Hermitage Massif, France). *Tectonophysics*, 125(4):357–370.

Garapić, G., Faul, U. H., and Brisson, E. (2013). High-resolution imaging of the melt distribution in partially molten upper mantle rocks: evidence for wetted two- grain boundaries. *Geochemistry, Geophysics, Geosystems*, 14(3):556–566.

Gardner, R., Piazolo, S., Evans, L., and Daczko, N. (2017). Patterns of strain localization in heterogeneous, polycrystalline rocks a numerical perspective. *Earth and Planetary Science Letters*, 463:253–265.

Genier, F., Bussy, F., Epard, J.-l., and Baumgartner, L. (2008). Water-assisted migmatization of metagraywackes in a Variscan shear zone, Aiguilles-Rouges massif, western Alps. *Lithos*, 102:575–597.

Gleason, G. C., Bruce, V., and Green, H. W. (1999). Experimental investigation of melt topology in partially molten quartzo-feldspathic aggregates under hydrostatic and non-hydrostatic stress. *Journal of metamorphic Geology*, 17:705–722.

Gleason, G. C. and Tullis, J. (1995). A flow law for dislocation creep of quartz aggregates determined with the molten salt cell. *Tectonophysics*, 247(1-4):1–23.

Goes, S., Armitage, J., Harmon, N., Smith, H., and Huismans, R. (2012). Low seismic velocities below mid-ocean ridges: Attenuation versus melt retention. *Journal of Geophysical Research: Solid Earth*, 117(12):1–19.

Goes, S. and van der Lee, S. (2002). Thermal structure of the North American uppermost mantle inferred from seismic tomography. *Journal of Geophysical Research: Solid Earth*, 107(B3):2050.

Gordon, S. M., Whitney, D. L., Teyssier, C., and Fossen, H. (2013). U-Pb dates and trace-element geochemistry of zircon from migmatite, Western Gneiss Region, Norway: Significance for history of partial melting in continental subduction. *Lithos*, 170-171:35–53.

Gordon, S. M., Whitney, D. L., Teyssier, C., Fossen, H., and Kylander-Clark, A. R. C. (2016). Geochronology and geochemistry of zircon from the northern Western Gneiss Region: Insights into the Caledonian tectonic history of western Norway. *Lithos*, 246-247:134–148.

Gottstein, G. and Mecking, H. (1985). Recrystallization. In *Preferred orientation in deformed metal and rocks: an introduction to modern texture analysis*, pages 183–218. Academic Press, New York.

Grujic, D., Casey, M., Davidson, C., Hollister, L. S., Kündig, R., Pavlis, T., and Schmid, S. (1996). Ductile extrusion of the Higher Himalayan Crystalline in Bhutan: evidence from quartz microfabrics. *Tectonophysics*, 260(1-3):21–43.

Guillope, M. and Poirier, J.-P. (1979). Dynamic recrystallisation during creep of single crystalline halite: an experimental study. *Journal of Geophysical Research: Solid Earth*, 84(2):5557–5567.

Hacker, B. R. (2007). Ascent of the ultrahigh-pressure Western Gneiss Region, Norway. *Geological Society of America, Special Papers*, 419:171–184.

Hacker, B. R., Andersen, T. B., Johnston, S., Kylander-Clark, A. R. C., Peterman, E. M., Walsh, E. O., and Young, D. (2010). High-temperature deformation during continental-margin subduction & exhumation: The ultrahigh-pressure Western Gneiss Region of Norway. *Tectonophysics*, 480(1-4):149–171.

Hacker, B. R., Andersen, T. B., Root, D. B., Mehl, L., Mattinson, J. M., and Wooden, J. L. (2003). Exhumation of high-pressure rocks beneath the Solund Basin, Western Gneiss Region of Norway. *Journal of Metamorphic Geology*, 21(6):613–629.

Hacker, B. R. and Gans, P. B. (2005). Continental collisions and the creation of ultrahigh-pressure terranes: Petrology and thermochronology of nappes in the central Scandinavian Caledonides. *Bulletin of the Geological Society of America*, 117(1-2):117–134.

Hacker, B. R., Ritzwoller, M. H., and Xie, J. (2014). Partially melted, mica-bearing crust in Central Tibet. *Tectonics*, 33(7):1408–1424.

Hammond, J. O. S. (2014). Constraining melt geometries beneath the Afar Depression, Ethiopia from teleseismic receiver functions: The anisotropic H- κ stacking technique. *Geochemistry, Geophysics, Geosystems*, 15(4):1316–1322.

Hammond, J. O. S. and Kendall, J. M. (2016). Constraints on melt distribution from seismology: A case study in Ethiopia. *Geological Society, London, Special Publications*, 420:SP420–14.

Hammond, W. C. and Humphreys, E. D. (2000a). Upper mantle seismic wave attenuation: Effects of realistic partial melt distribution. *Journal of Geophysical Research: Solid Earth*, 105(B5):10987–10999.

Hammond, W. C. and Humphreys, E. D. (2000b). Upper mantle seismic wave velocity: Effects of realistic partial melt geometries. *Journal of Geophysical Research: Solid Earth*, 105(B5):10975–10986.

Handy, M. R., Mulch, A., Rosenau, M., and Rosenberg, C. L. (2001). The role of fault zones and melts as agents of weakening, hardening and differentiation of the continental crust: a synthesis. *Geological Society, London, Special Publications*, 186(1):305–332.

Harte, B., Pattison, D. R. M., and Linklater, C. M. (1991). Field relations and petrography of partially melted pelitic and semi-pelitic rocks. In *Equilibrium and Kinetics in Contact Metamorphism: the Ballachulish Igneous Complex and its Aureole*, pages 181–210. Springer, Heidelberg.

Hasalová, P., Schulmann, K., Lexa, O., Štípská, P., Hrouda, F., Ulrich, S., Haloda, J., and Týcová, P. (2008a). Origin of migmatites by deformation-enhanced melt infiltration of orthogneiss: a new model based on quantitative microstructural analysis. *Journal of Metamorphic Geology*, 26(1):29–53.

Hasalová, P., Štípská, P., Powell, R., Schulmann, K., Janoušek, V., and Lexa, O. (2008b). Transforming mylonitic metagranite by open-system interactions during melt flow. *Journal of Metamorphic Geology*, 26:55–80.

Hashim, L., Gaillard, F., Champallier, R., and Le, N. (2013). Experimental assessment of the relationships between electrical resistivity, crustal melting and strain localization beneath the Himalayan-Tibetan Belt. *Earth and Planetary Science Letters*, 373:20–30.

Hearmon, R. F. S. (1979). The elastic constants of crystals and other anisotropic materials. *Landolt-Börnstein Tables*, 3(11):1–244.

Henry, P., Le Pichon, X., and Goffe, B. (1997). Kinematic, thermal and petrological model of the Himalayas: constraints related to metamorphism within the underthrust Indian crust and topographic elevation. *Tectonophysics*, 273:31–56.

Hibbard, M. J. (1979). Myrmekite as a marker between preaqueous and postaqueous phase saturation in granitic systems. *Geological Society of America Bulletin*, 90(11):1047–1062.

Hibbard, M. J. (1987). Deformation of incompletely crystallized magma systems: granitic gneisses and their tectonic implications. *Journal of Geology*, 95(4):543–561.

Hirn, A., Sapin, M., Lépine, J. C., Diaz, J., and Mei, J. (1997). Increase in melt fraction along a south-north traverse below the Tibetan Plateau: evidence from seismology. *Tectonophysics*, 273:17–30.

Hirth, G. and Kohlstedt, D. L. (1995a). Experimental constraints on the dynamics of the partially molten upper mantle: 2. Deformation in the dislocation creep regime. *Journal of Geophysical Research: Solid Earth*, 100:15441–15449.

Hirth, G. and Kohlstedt, D. L. (1995b). Experimental constraints on the dynamics of the partially molten upper mantle: Deformation in the diffusion creep regime. *Journal of Geophysical Research: Solid Earth*, 100:1981–2001.

Hirth, G., Teyssier, C., and Dunlap, W. J. (2001). An evaluation of quartzite flow laws based on comparisons between experimentally and naturally deformed rocks. *International Journal of Earth Sciences*, 90(1):77–87.

Hirth, G. and Tullis, J. (1992). Dislocation creep regimes in quartz aggregates. *Journal of Structural Geology*, 14(2):145–159.

Hollister, L. S. and Crawford, M. L. (1986). Melt-enhanced deformation: A major tectonic process. *Geology*, 14(July):558–561.

Holness, M. B. (2006). Melt-solid dihedral angles of common minerals in natural rocks. *Journal of Petrology*, 47(4):791–800.

Holness, M. B., Cesare, B., and Sawyer, E. W. (2011). Melted rocks under the microscope: Microstructures and their interpretation. *Elements*, 7(4):247–252.

Holness, M. B., Cheadle, M. J., and McKenzie, D. P. (2005). On the use of changes in dihedral angle to decode late-stage textural evolution in cumulates. *Journal of Petrology*, 46(8):1565–1583.

Holness, M. B. and Clemens, J. D. (1999). Partial melting of the Appin Quartzite driven by fracture-controlled H2O infiltration in the aureole of the Ballachulish Igneous Complex, Scottish Highlands. *Contributions to Mineralogy and Petrology*, 136(1-2):154–168.

Holness, M. B. and Sawyer, E. W. (2008). On the pseudomorphing of melt-filled pores during the crystallization of migmatites. *Journal of Petrology*, 49(7):1343–1363.

Holtz, F., Scaillet, B., Behrens, H., Schulze, F., and Pichavant, M. (1996). Water contents of felsic melts: application to the rheological properties of granitic magmas. *Earth and Environmental Science Transactions of The Royal Society of Edinburgh*, 87(1-2):57–64.

Holtzman, B. K. and Kendall, J. M. (2010). Organized melt, seismic anisotropy, and plate boundary lubrication. *Geochemistry, Geophysics, Geosystems*, 11(12):1–29.

Holtzman, B. K., Kohlstedt, D. L., Zimmerman, M. E., Heidelbach, F., Hiraga, T., and Hustoft, J. (2003). Melt Segregation and Strain Partitioning: Implications for Seismic Anisotropy and Mantle Flow. *Science*, 301(August):1227–1230.

Holyoke, C. W. and Rushmer, T. (2002). An experimental study of grain scale melt segregation mechanisms in two common crustal rock types. *Journal of Metamorphic Geology*, 20(5):493–512.

Hu, S., He, L., and Wang, J. (2000). Heat flow in the continental area of China: a new data set. *Earth and Planetary Science Letters*, 179:407–419.

Hull, J. (1988). Thickness-displacement relationships for deformation zones. *Journal of Structural Geology*, 10(4):431–435.

Hunter, R. H. (1987). Textural equilibrium in layered igneous rocks. In *Origins of igneous layering*, pages 473–503. Springer, Dordrecht.

Jackson, I., Fitz Gerald, J. D., Faul, U. H., and Tan, B. H. (2002). Grain-size-sensitive seismic wave attenuation in polycrystalline olivine. *Journal of Geophysical Research: Solid Earth*, 107(B12):ECV 5–1–ECV 5–16.

Jamieson, R. A. and Beaumont, C. (2013). On the origin of orogens. *Bulletin of the Geological Society of America*, 125(11):1671–1702.

Jamieson, R. A., Unsworth, M. J., Harris, N. B. W., Rosenberg, C. L., and Schulmann, K. (2011). Crustal Melting and the Flow of Mountains. *Elements*, 7(4):253–260.

Jessell, M. W. (1987). Grain-boundary migration microstructures in a naturally deformed quartzite. *Journal of Structural Geology*, 9(8):1007–1014.

Ji, S., Shao, T., Michibayashi, K., Oya, S., Satsukawa, T., Wang, Q., Zhao, W., and Salisbury, M. H. (2015). Magnitude and symmetry of seismic anisotropy in mica-and amphibole-bearing metamorphic rocksand implications for tectonic interpretationof seismic data from the southeastTibetan Plateau. *Journal of Geophysical Research: Solid Earth*, 160(9):6404–6430.

Johannes, W., Ehlers, C., Kriegsman, L. M., and Mengel, K. (2003). The link between migmatites and S-type granites in the Turku area, southern Finland. *Lithos*, 68(3-4):69–90.

Jurewicz, S. R. and Watson, E. B. (1985). The distribution of partial melt in a granitic system: The application of liquid phase sintering theory. *Geochimica et Cosmochimica Acta*, 49(5):1109–1121.

Karato, S., Paterson, M. S., and Fitz Gerald, J. D. (1986). Rheology of synthetic olivine aggregates: influence of grain size and water. *Journal of Geophysical Research: Solid Earth*, 91(B8):8151–8176.

Karato, S.-i. (2010). Rheology of the deep upper mantle and its implications for the preservation of the continental roots: A review. *Tectonophysics*, 481(1-4):82–98.

Karato, S.-i. (2012). *Deformation of earth materials: an introduction to the rheology of solid earth*. Cambridge University Press.

Karato, S.-i. and Jung, H. (1998). Water, partial melting and the origin of the seismic low velocity and high attenuation zone in the upper mantle. *Earth and Planetary Science Letters*, 157:193–207.

Keay, S., Lister, G. S., and Buick, I. (2001). The timing of partial melting, Barrovian metamorphism and granite intrusion in the Naxos metamorphic core complex, Cyclades, Aegean Sea, Greece. *Tectonophysics*, 342(3-4):275–312.

Kelemen, P. B., Hirth, G., Shimizu, N., Spiegelman, M., and Dick, H. J. (1997). A Review of Melt Migration Processes in the Adiabatically Upwelling Mantle beneath Oceanic Spreading Ridges. *Philosophical Transactions of the Royal Society of London A: Mathematical, Physical and Engineering Sciences*, 355(1723):283–318.

Kildal, E. S. (1970). Geologisk kart over Noreg Måløy: Trondheim. *Norges Geologiske Undersøking*, scale 1:25.

Kind, R., Yuan, X., Saul, J., Nelson, K. D., Sobolev, S. V., Mechie, J., Zhao, W., Kosarev, G., Ni, J. F., Achauer, U., and Jiang, M. (2002). Seismic Images of Crust and Upper Mantle Beneath Tibet: Evidence for Eurasian Plate Subduction. *Science*, 298(November):1219–1222.

Kjøll, H. J., Andersen, T. B., Corfu, F., Labrousse, L., Tegner, C., Abdelmalak, M. M., and Planke, S. (2019). Timing of break-up and thermal evolution of a pre-Caledonian Neoproterozoic exhumed magma-rich rifted margin. *Tectonics*.

Klemperer, S. L. (2006). Crustal flow in Tibet: geophysical evidence for the physical state of Tibetan lithosphere, and inferred patterns of active flow. *Geological Society, London, Special Publications*, 268(1):39–70.

Kohlstedt, D. L. (2002). Partial Melting and Deformation. *Reviews in Mineralogy and Geochemistry*, 51(1):121–135.

Kohlstedt, D. L. and Zimmerman, M. E. (1996). Rheology of partially molten mantle rocks. *Annual Review of Earth and Planetary Sciences*, 24(1):41–62.

Kohlstedt, D. L., Zimmerman, M. E., and Mackwell, S. J. (2009). Stress-driven melt segregation in partially molten feldspathic rocks. *Journal of Petrology*, 51(1-2):9–19.

Krabbendam, M., Wain, A., and Andersen, T. B. (2000). Pre-Caledonian granulite and gabbro enclaves in the Western Gneiss Region, Norway: indications of incomplete transition at high pressure. *Geological Magazine*, 137(3):235–255.

Kress, V. C., Williams, Q., and Carmichael, I. S. E. (1988). Ultrasonic investigation of melts in the system Na20-A1203-Si02. *Geochimica et Cosmochimica Acta*, 52(2):283–293.

Kretz, R. (1966). Interpretation of the shape of mineral grains in metamorphic rocks. *Journal of Petrology*, 7(1):68–94.

Kriegsman, L. M. (2001). Partial melting, partial melt extraction and partial back reaction in anatectic migmatites. *Lithos*, 56(1):75–96.

Krogh, E. J. (1980). Geochemistry and petrology of glaucophane-bearing eclogites and associated rocks from Sunnfjord, Western Norway. *Lithos*, 13(4):355–380.

Krogh, E. J. and Elvevold, S. (1990). A Precambrian age for an early gabbro-monzonitic intrusive on the Øksfjord peninsula, Seiland Igneous Province, northern Norway. *Norsk Geologisk Tidsskrift*, 70(4):267–273.

Kruhl, J. H. (1996). Prism- and basal-plane parallel subgrain boundaries in quartz: a microstructural geothermobaromether. *Journal of Metamorphic Geology*, 14:581–589.

Kushiro, I. (1976). Changes in Viscosity and Structure of Melt of NaA1SiO Composition at High Pressures. *Journal of Geology*, 81(35):6347–6350.

Kylander-Clark, A. R. C., Hacker, B. R., and Mattinson, J. M. (2008). Slow exhumation of UHP terranes: Titanite and rutile ages of the Western Gneiss Region, Norway. *Earth and Planetary Science Letters*, 272(3-4):531–540.

Labrousse, L., Jolivet, L., Agard, P., Hebert, R., and Andersen, T. B. (2002). Crustal-scale boudinage and migmatization of gneiss during their exhumation in the UHP Province of Western Norway. *Terra Nova*, 14(4):263–270.

Labrousse, L., Jolivet, L., Andersen, T. B., Agard, P., and Maluski, H. (2004). Pressure-temperature-time deformation history of the exhumation of ultra-high pressure rocks in the Western Gneiss Region, Norway. *Geological Society of America, Special Papers*, 380:155–183.

Labrousse, L., Prouteau, G., and Ganzhorn, A.-C. (2011). Continental exhumation triggered by partial melting at ultrahigh pressure. *Geology*, 39(12):1171–1174.

Law, R. D., Schmid, S. M., and Wheeler, J. (1990). Simple shear deformation and quartz crystallographic fabrics: a possible natural example from the Torridon area of NW Scotland. *Journal of Structural Geology*, 12(1):29–45.

Lee, A. L., Torvela, T., Lloyd, G. E., and Walker, A. M. (2018). Melt organisation and strain partitioning in the lower crust. *Journal of Structural Geology*, 113:188–199.

Lee, A. L., Walker, A. M., Lloyd, G. E., and Torvela, T. (2017). Modeling the impact of melt on seismic properties during mountain building. *Geochemistry, Geophysics, Geosystems*, 18(3):1090–1110.

Lee, V. W., Mackwell, S. J., and Brantley, S. L. (1991). The effect of fluid chemistry on wetting textures in novaculite. *Journal of Geophysical Research: Solid Earth*, 96(B6):10023–10037.

Lejeune, A.-M. and Richet, P. (1995). Rheology of crystal-bearing silicate melts: An experimental study at high viscosities. *Journal of Geophysical Research: Solid Earth*, 100(B3):4215.

Lemonnier, C., Perrier, F., Avouac, J.-p., Chitrakar, G., Kalfe, B., Sapkota, S., Gautam, U., Tiwari, D., and Bano, M. (1999). Electrical structure of the Himalaya of Central Nepal: high conductivity around the mid-crustal ramp along the MHT. *Geophysical Research Letters*, 26(21):3261–3264.

Levine, J. S. F., Mosher, S., and Siddoway, C. S. (2013). Relationship between syndeformational partial melting and crustal-scale magmatism and tectonism across the Wet Mountains, central Colorado. *Lithosphere*, 5(5):456–476.

Lin, G., Amelung, F., Lavallee, Y., and Okubo, P. G. (2014). Seismic evidence for a crustal magma reservoir beneath the upper east rift zone of Kilauea volcano, Hawaii. *Geology*, 42(3):187–190.

Lindh, A. and Wahlgren, C.-H. (1985). Migmatite formation at subsolidus conditions-an alternative to anatexis. *Journal of Maps*, 3:1–12.

Lister, G. S. and Dornsiepen, U. F. (1982). Fabric transitions in the Saxony granulite terrain. *Journal of Structural Geology*, 4(1):81–92.

Lister, G. S. and Hobbs, B. E. (1980). The simulation of fabric development during plastic deformation and its application to quartzite: the influence of deformation history. *Journal of Structural Geology*, 2(3):355–370.

Llorens, M.-G., Gomez-Rivas, E., Ganzhorn, A.-C., Griera, A., Steinbach, F., Roessiger, J., Labrousse, L., Walte, N. P., Weikusat, I., and Bons, P. D. (2019). The effect of dynamic recrystallisation on the rheology and microstructures of partially molten rocks. *Journal of Structural Geology*, 118(April 2018):224–235.

Lloyd, G. E. (1987). Atomic number and crystallographic contrast images with the SEM: a review of backscattered electron techniques. *Mineralogical Magazine*, 51:3–19.

Lloyd, G. E., Butler, R. W. H., Casey, M., and Mainprice, D. (2009). Mica, deformation fabrics and the seismic properties of the continental crust. *Earth and Planetary Science Letters*, 288(1-2):320–328.

Lloyd, G. E., Butler, R. W. H., Casey, M., Tatham, D. J., and Mainprice, D. (2011a). Constraints on the seismic properties of the middle and lower continental crust. *Geological Society, London, Special Publications*, 360:7–32.

Lloyd, G. E. and Freeman, B. (1994). Dynamic recrystallization of quartz under greenschist conditions. *Journal of Structural Geology*, 16(6):867–881.

Lloyd, G. E., Halliday, J. M., Butler, R. W. H., Casey, M., Kendall, J. M., Wookey, J., and Mainprice, D. (2011b). From crystal to crustal: petrofabric-derived seismic modelling of regional tectonics. *Geological Society, London, Special Publications*, 360(Deformation Mechanisms, Rheology and Tectonics: Microstructures, Mechanics and Anisotropy):49–78.

Lloyd, G. E. and Knipe, R. J. (1992). Deformation mechanisms accommodating faulting of quartzite under upper crustal conditions. *Journal of Structural Geology*, 14(2):127–143.

Luan, F. C. and Paterson, M. S. (1992). Preparation and deformation of synthetic aggregates of quartz. *Journal of Geophysical Research: Solid Earth*, 97(B1):301–320.

Lutro, O., Robinson, P., and Solli, A. (1997). Proterozoic geology and Scandian overprinting in the Western Gneiss Region. *Norges Geologiske Undersøkelse*, 97:86.

Lutro, O. and Tveten, E. (1998). Geologisk kart over Noreg Årdal: Trondheim. *Norges Geologiske Undersøking*, scale 1:25.

Mainprice, D. (1997). Modelling the anisotropic seismic properties of partially molten rocks found at mid-ocean ridges. *Tectonophysics*, 279:161–179.

Mainprice, D., Bachmann, F., Hielscher, R., and Schaeben, H. (2015). Descriptive tools for the analysis of texture projects with large datasets using MTEX: strength, symmetry and components. *Geological Society, London, Special Publications*, 409(1):251–271.

Mainprice, D., Bouchez, J. L., Blumenfeld, P., and Tubià, J. M. (1986). Dominant c slip in naturally deformed quartz: Implications for dramatic plastic softening at high temperature. *Geology*, 14(10):819–822.

Mainprice, D., Hielscher, R., and Schaeben, H. (2011). Calculating anisotropic physical properties from texture data using the MTEX open-source package. *Geological Society, London, Special Publications*, 360:175–192.

Mainprice, D. and Humbert, M. (1994). Methods of calculating petrophysical properties. *Surveys in Geophysics*, 15:575–592.

Makovsky, Y., Klemperer, S. L., Ratschbacher, L., and Alsdorf, D. (1999). Midcrustal reflector on IDEPTH wide-angle profiles: An ophiolitic slab beneath the India-Asia suture in southern Tibet? *Tectonics*, 18(5):793–808.

Mancktelow, N. S. and Pennacchioni, G. (2005). The control of precursor brittle fracture and fluid rock interaction on the development of single and paired ductile shear zones. *Journal of Structural Geology*, 27:645–661.

Mavko, G. M. (1980). Velocity and attenuation in partially molten rocks. *Journal of Geophysical Research: Solid Earth*, 85(B10):5173–5189.

McKenzie, D. P. (1984). The generation and compaction of partially molten rock. *Journal of Petrology*, 25:713–765.

McSkimin, H. J., Andreatch, P., and Thurston, R. N. (1965). Elastic Moduli of Quartz versus Hydrostatic Pressure at 25 and 195.8C. *Journal of Applied Physics*, 36(5):1624–1632.

Means, W. D. (1995). Shear zones and rock history. *Tectonophysics*, 247:157–160.

Means, W. D. and Xia, Z. G. (1981). Deformation of crystalline materials in thinsection. *Geology*, 9(11):538–543.

Meek, U., Piazolo, S., and Daczko, N. R. (2019). The field and microstructural signatures of deformationassisted melt transfer: insights from magmatic arc lower crust, New Zealand. *Journal of Metamorphic Geology*.

Mehnert, K. R. (1968). *Migmatites and the origin of granitic rocks*. Elsevier, Amsterdam.

Mehnert, K. R., Büsch, W., and Schneider, G. (1973). Initial melting at grain boundaries of quartz and feldspar in gneisses and granulites. *Neues Jahrbuch für Mineralogie, Monatshefte*, 4:165–183.

Mei, S., Bai, W., Hiraga, T., and Kohlstedt, D. L. (2002). Influence of melt on the creep behavior of olivine-basalt aggregates under hydrous conditions. *Earth and Planetary Science Letters*, 201:491–507.

Menegon, L., Nasipuri, P., Stünitz, H., Behrens, H., and Ravna, E. K. (2011). Dry and strong quartz during deformation of the lower crust in the presence of melt. *Journal of Geophysical Research: Solid Earth*, 116(10):B10410.

Milsom, J. (2003). Field geophysics. In *The geological field guide series, vol. 25*. John Wiley and Sons.

Min, Z. and Wu, F. T. (1987). Nature of the upper crust beneath central Tibet. *Earth and Planetary Science Letters*, 84:204–210.

Molnar, P. (1984). Structure and tectonics of the Himalaya: Constraints and implications of geophysical data. *Annual Review of Earth and Planetary Sciences*, 12(1):489–518.

Morales, L. F. G., Lloyd, G. E., and Mainprice, D. (2014). Fabric transitions in quartz via viscoplastic self-consistent modeling part I: Axial compression and simple shear under constant strain. *Tectonophysics*, 636:52–69.

Morgan, S. S. and Law, R. D. (2004). Unusual transition in quartzite dislocation creep regimes and crystal slip systems in the aureole of the Eureka ValleyJoshua FlatBeer Creek pluton, California: a case for anhydrous conditions created by decarbonation reactions. *Tectonophysics*, 384:209–231.

Nachlas, W. O. and Hirth, G. (2015). Experimental constraints on the role of dynamic recrystallization on resetting the Ti-in-quartz thermobarometer. *Journal of Geophysical Research: Solid Earth*, 120:8120–8137.

Nelson, K. D., Zhao, W., Brown, L. D., Kuo, J., Che, J., Liu, X., Klemperer, S. L., Makovsky, Y., Meissner, R., Mechie, J., and Kind, R. (1996). Partially molten middle crust beneath southern Tibet: synthesis of project INDEPTH results. *Science*, 274(5293):1684–1688.

Nicolas, A. and Ildefonse, B. (1996). Flow mechanism and viscosity in basaltic magma chambers. *Geophysical Research Letters*, 23(16):2013–2016.

Nicolas, A. and Poirier, J. P. (1976). *Crystalline plasticity and solid state flow in metamorphic rocks*. John Wiley & Sons.

Nishikawa, O., Saiki, K., and Wenk, H. R. (2004). Intra-granular strains and grain boundary morphologies of dynamically recrystallized quartz aggregates in a mylonite. *Journal of Structural Geology*, 26(1):127–141.

Nishikawa, O. and Takeshita, T. (2000). Progressive lattice misorientation and microstructureal development in quartz veins deformed under subgreenshist conditions. *Journal of Structural Geology*, 22(2):259–276.

Nixon, R. D., Davis, R. F., Carolina, N., and Carolina, N. (1992). DiffusionAccommodated Grain Boundary Sliding and Dislocation Glide in the Creep of Sintered Alpha Silicon Carbide. *Journal of the American Ceramic Society*, 75(7):1786–1795.

O'Connell, R. J. and Budiansky, B. (1977). Viscoelastic properties of fluid-saturated cracked solids. *Journal of Geophysical Research: Solid Earth*, 82(36):5719–5735.

Ohno, I., Harada, K., and Yoshitomi, C. (2006). Temperature variation of elastic constants of quartz across the α - β transition. *Physics and Chemistry of Minerals*, 33(1):1–9.

Olgaard, D. L. and Evans, B. (1988). Grain growth in synthetic marbles with added mica and water. *Contributions to Mineralogy and Petrology*, 100(2):246–260.

Oliver, J. (1962). A summary of observed seismic surface wave dispersion. *Bulletin of the Seismological Society of America*, 52(1):81–86.

O'Neill, B., Bass, J. D., Rossman, G. R., Geiger, C. A., and Langer, K. (1991). Elastic Properties of Pyrope. *Physics and Chemistry of Minerals*, 17:617–621.

O'Neill, B., Bass, J. D., Smyth, J. R., and Vaughan, M. T. (1989). Elasticity of a Grossular-Pyrope-Almandine. *Journal of Geophysical Research*, 94(B12):819–824.

Ord, A. and Christie, J. M. (1984). Flow stresses from microstructures in mylonitic quartzites of the Moine Thrust zone, Assynt area, Scotland Geological setting. *Journal of Structural Geology*, 6(6):639–654.

Otani, M. and Wallis, S. (2006). Quartz lattice preferred orientation patterns and static recrystallization: Natural examples from the Ryoke belt, Japan. *Geology*, 34(7):561–564.

Paquet, J., Francois, P., and Nedelec, A. (1981). Effect of partial melting on rock deformation: Experimental and natural evidences on rocks of granitic compositions. *Tectonophysics*, 78(1-4):545–565.

Parsons, A. J., Law, R. D., Lloyd, G. E., Phillips, R. J., and Searle, M. P. (2016). Thermo-kinematic evolution of the Annapurna-Dhaulagiri Himalaya, central Nepal: The Composite Orogenic System. *Geochemistry, Geophysics, Geosystems*, 17:1511–1539.

Passchier, C. W. (1982). Pseudotachylyte and the development of ultramylonite bands in the Saint-Barthelemy Massif, French Pyrenees. *Journal of Structural Geology*, 4(1).

Passchier, C. W. and Trouw, R. A. J. (2005). *Microtectonics*. Springer, Berlin, Heidelberg, New York.

Paterson, M. S. (2001). A granular flow theory for the deformation of partially molten rock. *Tectonophysics*, 335:51–61.

Pearce, M. A. and Wheeler, J. (2011). Grain growth and the lifetime of diffusion creep deformation. *Geological Society of London, Special Publications*, 360:257–272.

Pec, M., Holtzman, B. K., Zimmerman, M. E., and Kohlstedt, D. L. (2017). Reaction Infiltration Instabilities in Mantle Rocks: an Experimental Investigation. *Journal of Petrology*, 58(5):979–1004.

Pennacchioni, G. and Cesare, B. (1997). Ductile-brittle transition in pre-Alpine amphibolite facies mylonites during evolution from water-present to water-deficient conditions (Mont Mary nappe, Italian Western Alps). *Journal of Metamorphic Geology*, 15:777–791.

Pennacchioni, G. and Mancktelow, N. S. (2007). Nucleation and initial growth of a shear zone network within compositionally and structurally heterogeneous granitoids under amphibolite facies conditions. *Journal of Structural Geology*, 29:1757–1780.

Petford, N., Cruden, A. R., McCaffrey, K. J. W., and Vigneresse, J.-L. (2000). Granite magma formation, transport and emplacement in the Earth's crust. *Nature*, 408(6813):669–673.

Petford, N. and Koenders, M. A. (1998). Granular flow and viscous fluctuations in low Bagnold number granitic magmas. *Journal of the Geological Society*, 155:873–881.

Phillips, E. R. (1974). Myrmekite - one hundred years later. *Lithos*, 7(3):181–194.

Phillips, E. R. (1980). On polygenetic myrmekite. *Geological Magazine*, 117(1):29–36.

Phillips, T. B., Jackson, C. A.-l., Bell, R. E., and Duffy, O. B. (2016). Reactivation of intrabasement structures during rifting: A case study from offshore southern Norway. *Journal of Structural Geology*, 91:54–73.

Platt, J. P., Behr, W. M., and Cooper, F. J. (2015). Metamorphic core complexes: windows into the mechanics and rheology of the crust. *Journal of the Geological Society*, 172:9–27.

Platt, J. P. and Behrmann, J. H. (1986). Structures and fabrics in a crustal-scale shear zone, Betic Cordillera, SE Spain. *Journal of Structural Geology*, 8(1):15–33.

Poirier, J. P. (1980). Shear localization and shear instability in materials in the ductile field. *Journal of Structural Geology*, 2(1):135–142.

Poirier, J.-P. (1985). *Creep of crystals: high-temperature deformation processes in metals, ceramics and minerals*. Cambridge University Press.

Prakash, A., Piazolo, S., Saha, L., Bhattacharya, A., and Kumar, D. (2018). Deformation behavior of migmatites: insights from microstructural analysis of a garnet-sillimanite-mullite-quartz-feldspar-bearing anatectic migmatite at Rampura-Agucha, Aravalli-Delhi Fold Belt, NW India. *International Journal of Earth Sciences*, 107(6):2265–2292.

Preston, R. J. (2006). Magma Density spreadsheet: www.gabbrosoft.org.

Prior, D. J., Boyle, A. P., Brenker, F., Cheadle, M. C., Day, A., Lopez, G., Peruzzo, L., Potts, G. J., Reddy, S., Spiess, R., Timms, N. E., Trimby, P., Wheeler, J., and Zetterström, L. (1999). The application of electron backscatter diffraction and orientation contrast imaging in the SEM to textural problems in rocks. *American Mineralogist*, 84:1741–1759.

Ramsay, D. M. and Sturt, B. A. (1986). The contribution of the Finnmarkian orogeny to the framework of the Scandinavian Caledonides. In Fettes, D. J. and Harris, A. L., editors, *Synthesis of the Caledonian rocks of Britain*, pages 221–246. Springer, Dordrecht.

Ramsay, D. M., Sturt, B. A., Jansen, Ø., Andersen, T. B., and Sinha-Roy, S. (1985). The tectonostratigraphy of western Porsangerhalvøya, Finnmark, north Norway. In Gee, D. G. and Sturt, B. A., editors, *The Caledonide Orogen: Scandinavia and related areas*, pages 611–619. John Wiley, Chichester, UK.

Ramsay, J. G. and Graham, R. H. (1970). Strain variation in shear belts. *Canadian Journal of Earth Sciences*, 7(3):786–813.

Ramsay, J. G. and Huber, M. I. (1987). Ductile and Brittle Shear Zones. In *The techniques of modern structural geology. Volume 2: Folds and Fractures*, pages 595–640. Academic Press Limited.

Rapine, R., Tilmann, F., West, M., Ni, J., and Rodgers, A. (2003). Crustal structure of northern and southern Tibet from surface wave dispersion analysis. *Journal of Geophysical Research: Solid Earth*, 108(2120):1–11.

Reginiussen, H., Ravna, E. K., and Berglund, K. (1995). Mafic dykes from Øksfjord, Seiland Igneous Province, northern Norway: geochemistry and palaeotectonic significance. *Geological Magazine*, 132(6):667–681.

Renner, J., Evans, B., and Hirth, G. (2000). On the rheologically critical melt fraction. *Earth and Planetary Science Letters*, 181(4):585–594.

Richet, P., Lejeune, A.-M., Holtz, F., and Roux, J. (1996). Water and the viscosity of andesite melts. *Chemical Geology*, 128(1-4):185–197.

Richter, B., Stünitz, H., and Heilbronner, R. (2016). Stresses and pressures at the quartz-to-coesite phase transformation in shear deformation experiments. *Journal of Geophysical Research: Solid Earth*, 121(11):8015–8033.

Rivers, M. L. and Carmichael, I. S. E. (1987). Ultrasonic Studies of Silicate Melts. *Journal of Geophysical Research: Solid Earth*, 92(B9):9247–9270.

Roberts, D. (1973). Geologisk kart over Norge, berggrunnskart. Hammerfest 1: 250 000. *Norges Geologiske Undersøkelse Bulletin*, 61:1–49.

Roberts, D. (1974). Hammerfest: beskrivelse til det 1: 250.000 berggrunnsgeologiske kart. *Norges Geologiske Undersøkelse*, 301:1–66.

Roberts, D. (2003). The Scandinavian Caledonides: Event chronology, palaeogeographic settings and likely modern analogues. *Tectonophysics*, 365(1-4):283–299.

Roberts, D. and Gee, D. G. (1985). An introduction to the structure of the Scandinavian Caledonides. *The Caledonide Orogen: Scandinavia and related areas*, 1:55–68.

Roberts, R. J., Corfu, F., Torsvik, T. H., Ashwal, L. D., and Ramsay, D. M. (2006). Short-lived mafic magmatism at 560-570 Ma in the northern Norwegian Caledonides: U-Pb zircon ages from the Seiland Igneous Province. *Geological Magazine*, 143:887–903.

Robertson, S. (1999). BGS Rock Classification Scheme Volume 2 - Classification of metamorphic rocks. *British Geological Survey Research Report, RR 9902*, 2:1–24.

Robin, P.-Y. F. (1979). Theory of metamorphic segregation and related processes. *Geochimica et Cosmochimica Acta*, 43(10):1587–1600.

Robins, B. and Often, M. (1996). Field Trip Guidebook: The Seiland Igneous Province, North Norway, IGCP Project 336. *Norges Geologiske Undersøkelse Report*, 96(127):1–30.

Root, D. B., Hacker, B. R., Gans, P. B., Ducea, M. N., Eide, E. A., and Mosenfelder, J. L. (2005). Discrete ultrahigh-pressure domains in the Western Gneiss Region, Norway: Implications for formation and exhumation. *Journal of Metamorphic Geology*, 23(1):45–61.

Rosenberg, C. L. and Handy, M. R. (2001). Mechanisms and orientation of melt segregation paths during pure shearing of a partially molten rock analog (norcamphor–benzamide). *Journal of Structural Geology*, 23(12):1917–1932.

Rosenberg, C. L. and Handy, M. R. (2005). Experimental deformation of partially melted granite revisited: Implications for the continental crust. *Journal of Metamorphic Geology*, 23(1):19–28.

Rosenberg, C. L. and Riller, U. (2000). Partial-melt topology in statically and dynamically recrystallized granite. *Geology*, 28(1):7–10.

Rutter, E. H. (1983). Pressure solution in nature, theory and experiment. *Journal of the Geological Society*, 140:725–740.

Rutter, E. H. (1997). The influence of deformation on the extraction of crustal melts: a consideration of the role of melt-assisted granular flow. In Holness, M. B., editor, *Deformation-enhanced Fluid Transport in the Earth's Crust and Mantle*, chapter 4, pages 82–110. The Mineralogical Society.

Rutter, E. H. and Neumann, D. H. K. (1995). Experimental deformation of partially molten Westerly granite under fluid-absent conditions, with implications for the extraction of granitic magmas. *Journal of Geophysical Research: Solid Earth*, 100:15697–15715.

Ryerson, F. J., Weed, H. C., and Piwinskii, A. J. (1988). Rheology of subliquidus magmas: 1. Picritic compositions. *Journal of Geophysical Research: Solid Earth*, 93:3421–3436.

Sawyer, E. (1996). Melt segregation and magma flow in migmatites: implications for the generation of granite magmas. *Earth and Environmental Science Transactions of the Royal Society of Edinburgh*, 87(1-2):85–94.

Sawyer, E. W. (1991). Disequilibrium Melting and the Rate of Melt-Residuum Separation During Migmatization of Mafic Rocks from the Grenville Front, Quebec. *Journal of Petrology*, 32(4):701–738.

Sawyer, E. W. (1994). Melt segregation in the continental crust. *Geology*, 22:1019–1022.

Sawyer, E. W. (1999). Criteria for the Recognition of Partial Melting. *Physics and Chemistry of the Earth, Part A: Solid Earth and Geodesy*, 24(3):269–279.

Sawyer, E. W. (2001). Melt segregation in the continental crust: distribution and movement of melt in anatectic rocks. *Journal of Metamorphic Geology*, 19(3):291–309.

Sawyer, E. W. (2008). *Atlas of Migmatites*. NRC Research Press, 2008., vol. 9 edition.

Sawyer, E. W., Cesare, B., and Brown, M. (2011). When the continental crust melts. *Elements*, 7(4):229–234.

Schärer, U. and Labrousse, L. (2003). Dating the exhumation of UHP rocks and associated crustal melting in the Norwegian Caledonides. *Contributions to Mineralogy and Petrology*, 144(6):758–770.

Schilling, F. R. and Partzsch, G. M. (2001). Quantifying Partial Melt Fraction in the Crust Beneath the Central Andes and the Tibetan Plateau. *Physics and Chemistry of the Earth, Part A: Solid Earth and Geodesy*, 26(4-5):239–246.

Schmeling, H. (1985). Numerical models on the influence of partial melt on elastic, anelastic and electric properties of rocks. Part I: elasticity and anelasticity. *Physics of the Earth and Planetary Interiors*, 41:34–57.

Schmid, S. M. and Casey, M. (1986). Complete Fabric Analysis of Some Commonly Observed Quartz C-Axis Patterns. In Hobbs, B. and Heard, H., editors, *Mineral and Rock Deformation: Laboratory Studies, The Paterson Volume. Geophysical Monograph Series*, volume 36, pages 263–286.

Schneider, C. A., Rasband, W. S., and Eliceiri, K. W. (2012). NIH Image to ImageJ: 25 years of image analysis. *Nature Methods*, 9(7):671–675.

Scholz, C. H. (1988). The brittle-plastic transition and the depth of seismic faulting. *Geologische Rundschau*, 77(1):319–328.

Scholz, C. H. (2002). *The mechanics of earthquakes and faulting*. Cambridge University Press, Cambridge, UK, 2nd edition.

Schott, B. and Schmeling, H. (1998). Delamination and detachment of a lithospheric root. *Tectonophysics*, 296:225–247.

Schulmann, K., Martelat, J.-E., Ulrich, S., Lexa, O., Štípská, P., and Becker, J. K. (2008). Evolution of microstructure and melt topology in partially molten granitic mylonite: Implications for rheology of felsic middle crust. *Journal of Geophysical Research: Solid Earth*, 113(B10406):1–20.

Schulze, F., Behrens, H., Holtz, F., Roux, J., and Johannes, W. (1996). The influence of h2o on the viscosity of a haplogranitic melt. *American Mineralogist*, 81(9-10):1155–1165.

Searle, M. P. (2013). Crustal melting, ductile flow, and deformation in mountain belts: Cause and effect relationships. *Lithosphere*, 5(6):547–554.

Sederholm, J. J. (1907). Om granit och gneis: deras uppkomst, uppträdande och utbredning inom urberget i Fennoskandia. *Bulletin de la Commission geologique de Finlande*, 23:1–110.

Shearer, P. M. (2009). Surface waves and normal modes. In *Introduction to seismology*, pages 215–240. Cambridge University Press, second edition.

Sheehan, A. F., Torre, T. L., Monsalve, G., Abers, G. A., and Hacker, B. R. (2014). Physical state of Himalayan crust and uppermost mantle: Constraints from seismic attenuation and velocity tomography. *Journal of Geophysical Research: Solid Earth*, 119(1):567–580.

Shigematsu, N. (1999). Dynamic recrystallization in deformed plagioclase during progressive shear deformation. *Tectonophysics*, 305(4):437–452.

Sibson, R. H. (1977). Fault rocks and fault mechanisms. *Journal of the Geological Society*, 133:191–213.

Sibson, R. H. (1983). Continental fault structure and the shallow earthquake source. *Journal of the Geological Society*, 140(5):741–767.

Simpson, C. and Wintsch, R. P. (1989). Evidence for deformation-induced K-feldspar replacement by myrmekite. *Journal of Metamorphic Geology*, 7(2):261–275.

Slagstad, T., Melezhik, V. A., Kirkland, C. L., Zwaan, K. B., Roberts, D., Gorokhov, I. M., and Fallick, A. E. (2006). Carbonate isotope chemostratigraphy suggests revisions to the geological history of the West Finnmark Caledonides, northern Norway. *Journal of the Geological Society*, 163(2):277–289.

Smith, J. R., Piazolo, S., Daczko, N. R., and Evans, L. (2015). The effect of pre-tectonic reaction and annealing extent on behaviour during subsequent deformation: insights from paired shear zones in the lower crust of Fiordland, New Zealand. *Journal of Metamorphic Geology*, 33:557–577.

Spear, F. S., Kohn, M. J., and Cheney, J. T. (1999). P -T paths from anatectic pelites. *Contributions to Mineralogy and Petrology*, 134:17–32.

Spiegelman, M., Kelemen, P. B., and Aharonov, E. (2001). Causes and consequences of flow organization during melt transport: The reaction infiltration instability in compactible media. *Journal of Geophysical Research: Solid Earth*, 106(B2):2061–2077.

Stein, S. and Wysession, M. (2003). *An introduction to seismology, earthquakes, and earth structure*. John Wiley and Sons.

Stephens, M. B. and Gee, D. G. (1989). Terranes and polyphase accretionary history in the Scandinavian Caledonides. *Geological Society of America, Special Papers*, 230:17–30.

Stipp, M., Stünitz, H., Heilbronner, R., and Schmid, S. M. (2002). The eastern Tonale fault zone: a 'natural laboratory' for crystal plastic deformation of quartz over a temperature range from 250 to 700C. *Journal of Structural Geology*, 24:1861–1884.

Stipp, M. and Tullis, J. (2003). The recrystallized grain size piezometer for quartz. *Geophysical Research Letters*, 30(21):1–5.

Stixrude, L. and Lithgow-Bertelloni, C. (2005). Mineralogy and elasticity of the oceanic upper mantle: Origin of the low-velocity zone. *Journal of Geophysical Research: Solid Earth*, 110(3):1–16.

Stork, A. L., Stuart, G. W., Henderson, C. M., Keir, D., and Hammond, J. O. S. (2013). Uppermost mantle (Pn) velocity model for the Afar region, Ethiopia: An insight into rifting processes. *Geophysical Journal International*, 193(1):321–328.

Straume, Å. K. and Austrheim, H. (1999). Importance of fracturing during retrometamorphism of eclogites. *Journal of Metamorphic Geology*, 17(6):637–652.

Streit, J. E. and Cox, S. F. (2002). Evolution of fracture networks in shear zones: Insights from see-through experiments on biphenyl aggregates. *Journal of Structural Geology*, 24(1):107–122.

Stuart, C., Daczko, N., and Piazolo, S. (2017). Local partial melting of the lower crust triggered by hydration through melt–rock interaction: an example from fiordland, new zealand. *Journal of Metamorphic Geology*, 35(2):213–230.

Stuart, C. A., Piazolo, S., and Daczko, N. R. (2016). Mass transfer in the lower crust: Evidence for incipient meltassisted flow along grain boundaries in the deep arc granulites of Fiordland, New Zealand. *Geochemistry, Geophysics, Geosystems*, 17:3733–3753.

Stuart, C. A., Piazolo, S., and Daczko, N. R. (2018). The recognition of former melt flux through high-strain zones. *Journal of Metamorphic Geology*, 36(8):1049–1069.

Sturt, B. A., Pringle, R., and Ramsay, D. M. (1978). The Finnmarkian phase of the Caledonian orogeny. *Journal of Structural Geology*, 135(6):591–610.

Tandon, G. P. and Weng, G. J. (1984). The Effect of Aspect Ratio of Inclusions on the Elastic Properties of Unidirectionally Aligned Composites. *Polymer Composites*, 5(4):327–333.

Tatham, D. J., Lloyd, G. E., Butler, R. W. H., and Casey, M. (2008). Amphibole and lower crustal seismic properties. *Earth and Planetary Science Letters*, 267:118–128.

Taylor, M. A. J. and Singh, S. C. (2002). Composition and microstructure of magma bodies from effective medium theory. *Geophysical Journal International*, 149(1):15–21.

Terry, M. P., Robinson, P., Hamilton, A., and Jercinovic, M. J. (2000). Monazite geochronology of UHP and HP metamorphism, deformation, and exhumation, Nordøyane, Western Gneiss Region, Norway. *American Mineralogist*, 85(11-12):1651–1664.

Teyssier, C. and Whitney, D. L. (2002). Gneiss domes and orogeny. *Geology*, 30(12):1139–1142.

Tikoff, B., Blenkinsop, T., Kruckenberg, S. C., Morgan, S., Newman, J., and Wojtal, S. (2013). A perspective on the emergence of modern structural geology: Celebrating the feedbacks between historical-based and process-based approaches. *The Geological Society of America Special Paper*, 500:65–119.

Tokle, L., Hirth, G., and Behr, W. M. (2019). Flow laws and fabric transitions in wet quartzite. *Earth and Planetary Science Letters*, 505:152–161.

Torvela, T., Moreau, J., Butler, R. W. H., Korja, A., and Heikkinen, P. J. (2013). The mode of deformation in the orogenic mid-crust revealed by seismic attribute analysis. *Geochemistry, Geophysics, Geosystems*, 14(4):1069–1086.

Toy, V. G., Prior, D. J., and Norris, R. J. (2008). Quartz fabrics in the Alpine Fault mylonites: Influence of pre-existing preferred orientations on fabric development during progressive uplift. *Journal of Structural Geology*, 30(5):602–621.

Tucker, R. D., Krogh, T. E., and Råheim, A. (1990). Proterozoic evolution and age-province boundaries in the central part of the Western Gneiss Region, Norway: Results of U-Pb dating of accessory minerals from Trondheimsfjord to Geiranger. *Mid-Proterozoic Laurentia-Baltica*, 38:149–173.

Tucker, R. D., Robinson, P., Solli, A., Gee, D. G., Thorsnes, T., Krogh, T. E., Nordgulen, Ø., and Bickford, M. E. (2004). Thrusting and extension in the Scandian Hinterland, Norway: New U-Pb ages and tectonostratigraphic evidence. *American Journal of Science*, 304(6):477–532.

Tullis, J. and Yund, R. A. (1991). Diffusion creep in feldspar aggregates: experimental evidence. *Journal of Structural Geology*, 13(9):987–1000.

Tungatt, P. D. and Humphreys, F. J. (1984). The plastic deformation and dynamic recrystallization of polycrystalline sodium nitrate. *Acta Metallurgica*, 32(10):1625–1635.

Turner, F. J. (1941). The development of pseudo-stratification by metamorphic differentiation in the schists of otago, new zealand. *American Journal of Science*, 239(1):1–16.

Tveten, E., Lutro, O., and Thorsnes, T. (1998). Geologisk kart over Noreg Ulsteinvik: Trondheim. *Norges Geologiske Undersøkelse*, scale 1:25.

Twiss, R. J. (1977). Theory and applicability of a recrystallized grain size paleopiezometer. In *Stress in the Earth*, pages 227–244. Birkhäuser, Basel.

Unsworth, M. J. (2010). Magnetotelluric studies of active continent-continent collisions. *Surveys in Geophysics*, 31(2):137–161.

Unsworth, M. J., Jones, A. G., Wei, W., Marquis, G., Gokarn, S. G., Spratt, J. E., and Team, I.-M. (2005). Crustal rheology of the Himalaya and Southern Tibet inferred from magnetotelluric data. *Nature*, 438(7064):78–81.

Urai, J. L., Means, W. D., and Lister, G. S. (1986). Dynamic recrystallization of minerals. *Mineral and rock deformation: laboratory studies*, 36:161–199.

van der Molen, I. and Paterson, M. S. (1979). Experimental Deformation of Partially-Melted Granite. *Contributions to Mineralogy and Petrology*, 70:299–318.

Vanderhaeghe, O. (2001). Melt segregation, pervasive melt migration and magma mobility in the continental crust: The structural record from pores to orogens. *Physics and Chemistry of the Earth, Part A: Solid Earth and Geodesy*, 26(4-5):213–223.

Vanderhaeghe, O. (2009). Migmatites, granites and orogeny: Flow modes of partially-molten rocks and magmas associated with melt/solid segregation in orogenic belts. *Tectonophysics*, 477(3-4):119–134.

Vanderhaeghe, O. and Teyssier, C. (2001). Partial melting and flow of orogens. *Tectonophysics*, 342:451–472.

Verma, R. K. (1960). Elasticity of Some High-Density Crystals. *Journal of Geophysical Research*, 65(2):757–766.

Vernon, R. H. (1968). Microstructures of high-grade metamorpbic rocks at broken hill, Australia. *Journal of Petrology*, 9(1):1–22.

Vernon, R. H. (1986). K-Feldspar megacrysts in granites-phenocrysts, not porphyroblasts. *Earth-Science Reviews*, 23:1–63.

Vernon, R. H. (1991). Questions about myrmekite in deformed rocks. *Journal of Structural Geology*, 13(9):979–985.

Vernon, R. H. (2011). Microstructures of melt-bearing regional metamorphic rocks. *GSA Memoirs*, 207(01):1–11.

Vernon, R. H. and Collins, W. J. (1988). Igneous microstructures in migmatites. *Geology*, 16(January 2009):1126–1129.

Vidale, R. (1974). Metamorphic differentiation layering in pelitic rocks of dutchess county, new york. *Geochemical Transport and Kinetics*, 1:273.

Viegas, L. G. F., Archanjo, C. J., and Vauchez, A. (2013). Fabrics of migmatites and the relationships between partial melting and deformation in high-grade transpressional shear zones: The Espinho Branco anatexite (Borborema Province, NE Brazil). *Journal of Structural Geology*, 48:45–56.

Vigneresse, J.-L., Barbey, P., and Cuney, M. (1996). Rheological Transitions During Partial Melting and Crystallization with Application to Felsic Magma Segregation and Transfer. *Journal of Petrology*, 37(6):1579–1600.

Vigneresse, J.-L. and Tikoff, B. (1999). Strain partitioning during partial melting and crystallizing felsic magmas. *Tectonophysics*, 312(2-4):117–132.

Vinnik, L. P. (1977). Detection of waves converted from P to SV in the mantle. *Physics and Chemistry of the Earth's Interior*, 15(October 1976):39–45.

Vitale, S. and Mazzoli, S. (2008). Heterogeneous shear zone evolution: The role of shear strain hardening/softening. *Journal of Structural Geology*, 30(11):1383–1395.

Walker, A. M., Forte, A. M., Wookey, J., Nowacki, A., and Kendall, J. M. (2011). Elastic anisotropy of D" predicted from global models of mantle flow. *Geochemistry, Geophysics, Geosystems*, 12(10):1–22.

Walker, A. M. and Wookey, J. (2012). MSAT-A new toolkit for the analysis of elastic and seismic anisotropy. *Computers and Geosciences*, 49:81–90.

Walsh, E. O. and Hacker, B. R. (2004). The fate of subducted continental margins: Two-stage exhumation of the high-pressure to ultrahigh-pressure Western Gneiss Region, Norway. *Journal of Metamorphic Geology*, 22(7):671–687.

Walsh, E. O., Hacker, B. R., Gans, P. B., Grove, M., and Gehrels, G. (2007). Protolith ages and exhumation histories of (ultra)high-pressure rocks across the Western Gneiss Region, Norway. *Bulletin of the Geological Society of America*, 119(3-4):289–301.

Walsh, J. B. (1969). New analysis of attenuation in partially melted rock. *Journal of Geophysical Research: Solid Earth*, 74(17):4333–4337.

Walte, N. P., Bons, P. D., and Passchier, C. W. (2005). Deformation of melt-bearing systems - Insight from in situ grain-scale analogue experiments. *Journal of Structural Geology*, 27(9):1666–1679.

Walte, N. P., Bons, P. D., Passchier, C. W., and Koehn, D. (2003). Disequilibrium melt distribution during static recrystallization. *Geology*, 31(11):1009–1012.

Watanabe, T. (1993). Effects of water and melt on seismic velocities and their application to characterization of seismic reflectors. *Geophysical Research Letters*, 20(24):2933–2936.

Waters, D. J. (2001). The significance of prograde and retrograde quartz-bearing intergrowth microstructures in partially melted granulite-facies rocks. *Lithos*, 56(1):97–110.

Watt, G. R. and Harley, S. L. (1993). Accessory phase controls on the geochemistry of crustal melts and restites produced during water-undersaturated partial melting. *Contributions to Mineralogy and Petrology*, 114(4):550–566.

Wei, W., Unsworth, M. J., Jones, A., Booker, J., Tan, H., Nelson, K. D., Chen, L., Li, S., Solon, K., Bedrosian, P., Jin, S., and Deng, M. (2001). Detection of Widespread Fluids in the Tibetan Crust by Magnetotelluric Studies. *Science*, 292(5517):716–719.

Weidner, D. J. and Ito, E. (1985). Elasticity of MgSiO3 in the ilmenite phase. *Experimental Techniques*, 40:65–70.

Weinberg, R. F., Veveakis, E., and Regenauer-Lieb, K. (2015). Compaction-driven melt segregation in migmatites. *Geology*, 43(6):471–474.

Wheeler, J. (1992). Importance of Pressure Solution and Coble Creep in the Deformation of Polymineralic Rocks. *Journal of Geophysical Research: Solid Earth*, 97(B4):4579–4586.

White, S. (1979). Grain and sub-grain size variations across a mylonite zone. *Contributions to Mineralogy and Petrology*, 70(2):193–202.

Williams, M. L., Melis, E. A., Kope, C. F., and Hanmer, S. (2000). Microstructural tectonometamorphic processes and the development of gneissic layering: a mechanism for metamorphic segregation. *Journal of Metamorphic Geology*, 18(1):41–58.

Wilson, C. J. L. (1975). Preferred orientation in Quartz Ribbon mylonites. *Bulletin of the Geological Society of America*, 86(7):968–974.

Wilson, C. J. L., Peternell, M., Piazolo, S., and Luzin, V. (2014). Microstructure and fabric development in ice: Lessons learned from in situ experiments and implications for understanding rock evolution. *Journal of Structural Geology*, 61:50–77.

Wimmenauer, W. and Bryhni, I. (2007). A systematic nomenclature for metamorphic rocks: 6 Migmatites and related rocks. A proposal on behalf of the IUGS Subcommission on the Systematics of Metamorphic Rocks. *Recommendations*, pages 1–5.

Wu, S. and Groshong, R. H. (1991). Strain analysis using quartz deformation bands. *Tectonophysics*, 190(2-4):269–282.

Wyllie, P. J. (1977). Crustal anatexis: An experimental review. *Tectonophysics*, 43(1-2):41–71.

Xie, J., Ritzwoller, M. H., Shen, W., Yang, Y., Zheng, Y., and Zhou, L. (2013). Crustal radial anisotropy across eastern Tibet and the Western Yangtze Craton. *Journal of Geophysical Research: Solid Earth*, 118:4226–4252.

Xu, Q., Zhao, J., Pei, S., and Liu, H. (2013). Imaging lithospheric structure of the eastern Himalayan syntaxis: New insights from receiver function analysis. *Journal of Geophysical Research: Solid Earth*, 118:2323–2332.

Yakymchuk, C. and Brown, M. (2014). Behaviour of zircon and monazite during crustal melting. *Journal of the Geological Society*, 171(4):465–479.

Yang, X., Ma, J., Jin, Z., Gao, S., and Ma, S. (2003). Partial melting and its implications for understanding the seismic velocity structure within the southern Tibetan crust. *Acta Geologica SinicaEnglish Edition*, 77(1):64–71.

Yang, Y., Ritzwoller, M. H., Zheng, Y., Shen, W., and Levshin, A. L. (2012). A synoptic view of the distribution and connectivity of the mid-crustal low velocity zone beneath Tibet. *Journal of Geophysical Research: Solid Earth*, 117(B04303):1–20.

Yao, H., Beghein, C., and Hilst, R. D. V. D. (2008). Surface wave array tomography in SE Tibet from ambient seismic noise and two-station analysis II. Crustal and upper-mantle structure. *Geophysical Journal International*, 173:205–219.

Yuguchi, T. and Nishiyama, T. (2008). The mechanism of myrmekite formation deduced from steady-diffusion modeling based on petrography: Case study of the Okueyama granitic body, Kyushu, Japan. *Lithos*, 106(3-4):237–260.

Zhang, Z. and Klemperer, S. L. (2010). Crustal structure of the Tethyan Himalaya, southern Tibet: new constraints from old wide-angle seismic data. *Geophysical Journal International*, 181:1247–1260.

Zhao, L.-f., Xie, X.-b., He, J.-k., Tian, X., and Yao, Z.-x. (2013). Crustal flow pattern beneath the Tibetan Plateau constrained by regional Lg-wave Q tomography. *Earth and Planetary Science Letters*, 383:113–122.